UNIVERSIDADE DE LISBOA

INSTITUTO SUPERIOR TÉCNICO

Nonlinear Crosstalk in MB-OFDM Metropolitan Optical Networks

Pedro Emanuel Domingos da Cruz

Supervisor: Doctor Adolfo da Visitação Tregeira Cartaxo

Co-supervisors:

Doctor Tiago Manuel Ferreira Alves

Doctor Paulo Sérgio de Brito André

Thesis approved in public session to obtain the PhD Degree in Electrical and Computer Engineering

Jury final classification: Pass with Distinction

2018

UNIVERSIDADE DE LISBOA

INSTITUTO SUPERIOR TÉCNICO

Nonlinear Crosstalk in MB-OFDM Metropolitan Optical Networks

Pedro Emanuel Domingos da Cruz

Supervisor: Doctor Adolfo da Visitação Tregeira Cartaxo
Co-supervisors:
Doctor Tiago Manuel Ferreira Alves
Doctor Paulo Sérgio de Brito André

Thesis approved in public session to obtain the PhD Degree in Electrical and Computer Engineering

Jury final classification: Pass with Distinction

Jury

Chairperson: Doctor José António Marinho Brandão Faria, Instituto Superior Técnico, Universidade de Lisboa
Members of the Committee:
Doctor Adolfo da Visitação Tregeira Cartaxo, Escola de Tecnologias e Arquitetura, ISCTE - Instituto Universitário de Lisboa
Doctor Jorge Manuel Torres Pereira, Instituto Superior Técnico, Universidade de Lisboa
Doctor Maria do Carmo Raposo de Medeiros, Faculdade de Ciências e Tecnologia, Universidade de Coimbra
Doctor Henrique Manuel de Castro Faria Salgado, Faculdade de Engenharia, Universidade do Porto
Doctor Fernando Duarte Nunes, Instituto Superior Técnico, Universidade de Lisboa
Doctor João Pedro Castilho Pereira Santos Gomes, Instituto Superior Técnico, Universidade de Lisboa

Funding Institutions
Fundação para a Ciência e a Tecnologia

2018

Ph. D. thesis accomplished under the supervision of

Dr. Adolfo da Visitação Tregeira Cartaxo

Full Professor
of the Department of Information Science and Technology
of ISCTE - Instituto Universitário de Lisboa

Dr. Tiago Manuel Ferreira Alves

Fundação para a Ciência e a Tecnologia (FCT) Investigator

Dr. Paulo Sérgio de Brito André

Associate Professor
of the Department of Electrical and Computer Engineering
of Instituto Superior Técnico

This work was supported by FCT from Portugal through projects
MORFEUS-PTDC/EEI-TEL/2573/2012 and AMEN - UID/EEA/50008/2013, and
Contracts SFRH/BD/85940/2012 and IF/01225/2015/CP1310/CT0001.

Acknowledgments

First of all, I would like to thank my supervisor, Prof. Dr. Adolfo Cartaxo, for all the help, support and advices in the last years. It all started in 2012 with the M. Sc. thesis. Since then I have learned a lot in the field of telecommunications in general and in the field of optical communications in particular. He has always been available to answer my questions and to teach me on several issues I faced throughout this work. His thoroughness has greatly improved my way of writing, working and thinking.

I also would like to thank my co-supervisor, Dr. Tiago Alves, for being always available to answer my questions, and for all the guidance, important advices and companionship during the course of this thesis. He has been a crucial part in the improvement of several aspects of this work. He also has been essential in teaching me how to tackle all the problems I faced with the laboratory equipment.

Additionally, I would like to thank my co-supervisor, Prof. Dr. Paulo André, for his advices during the course of this thesis.

I would like to thank my close family, especially my parents, Manuel Cruz and Maria Manuela Cruz, for all the love, understanding and support they always gave me and keep on giving. They are present in the good and bad moments and will always be my example to follow until the last day of my life. I would also like to thank my two younger sisters, Margarida Cruz and Mariana Cruz, for all the love they have given me since the day they were born. This work is dedicated to them.

I would also like to express my gratitude to Instituto de Telecomunicações for providing me access to their facilities.

A special thanks goes to Dr. Filipe Carvalho, for the advices and companionship in the first two years of this Ph. D.. Also to Eng. Fabricio Rossi, which is also finishing his Ph. D. and has been a great friend since the first moment when he arrived from Brazil.

A special thanks goes also to my friends David Ferreira, Miguel Fragoso and Isabel Simões, for all the good moments and companionship they have given me throughout the years.

I also wish to thank Fundação para a Ciência e a Tecnologia (FCT) from Portugal which sup-

ported this work through contracts SFRH/BD/85940/2012 and IF/01225/2015/CP1310/CT0001, and projects MORFEUS-PTDC/EEI-TEL/2573/2012 and AMEN-UID/EEA/50008/2013.
To all I have not mentioned and have been important in certain moments of my life, many thanks.

Pedro Cruz

Resumo

Esta tese descreve a investigação do impacto dos efeitos não-lineares da fibra óptica induzidos pelo efeito Kerr na transmissão de sinais multi-banda com multiplexagem ortogonal por divisão na frequência (MB-OFDM) em redes metro-acesso, considerando detecção directa (DD) com sinais assistidos por portadoras virtuais (VCs).

A análise do sistema MB-OFDM é feita sem e com transmissão por fibra óptica. O estudo da degradação induzida pela não-linearidade da fibra é centrado no efeito da mistura de quatro ondas (FWM), que é o efeito não-linear dominante. A potência de FWM é avaliada através de um método teórico (TM) proposto e validado que analisa o impacto dos produtos de FWM do tipo VC-VC-banda no desempenho do sistema. Usando o TM, são obtidos os valores máximos permitidos para as potências médias à entrada da fibra com um esquema referido como esquema base, considerando transmissão em fibra monomodo convencional (SSMF) com diferentes comprimentos e considerando sinais MB-OFDM com multiplexagem por divisão no comprimento de onda (WDM) com diferentes bandas de guarda entre canais WDM.

São propostos esquemas MB-OFDM assistidos por VCs e usando DD com elevada tolerância à FWM, considerando dois espaçamentos entre bandas diferentes. É avaliado o aumento do número de utilizadores ou o aumento da cobertura da rede óptica de distribuição (ODN) potenciado pelo relaxamento do impacto da FWM. São também apresentadas as melhorias de balanço de potência (PB) obtidas por estes esquemas para diferentes coberturas na rede e diferentes níveis capacidade da rede. Para um espaçamento entre bandas de 3,125 GHz e um débito binário de dados de 10 Gb/s por utilizador, foi demonstrado que o melhor esquema apresenta uma melhoria de PB que atinge 3 dB. Essa melhoria permite duplicar o número de utilizadores da rede ou aumentar o alcance da ODN em cerca de 12 km. Com um espaçamento entre bandas de 6,25 GHz e um débito binário de dados de 25 Gb/s por utilizador, a melhoria do PB supera 4 dB, permitindo duplicar o número de utilizadores e aumentar simultaneamente o alcance da ODN em 5 km.

São comparados e avaliados experimentalmente dois esquemas MB-OFDM assistidos por VCs

e usando DD: o esquema base e um esquema com alta tolerância à FWM. Os resultados de desempenho dos dois esquemas são avaliados em função da potência média total lançada em cada segmento de fibra, para transmissão com um canal e com vários canais e para propagação com um segmento de fibra e com vários segmentos de fibra.

Palavras-chave: multiplexagem ortogonal por divisão na frequência, multi-banda, mistura de quatro ondas, redes metro-acesso, transmissão não-linear.

Abstract

This thesis reports the investigation of the impact of the optical fibre nonlinear effects induced by the Kerr effect on the transmission of multi-band (MB)-orthogonal frequency-division multiplexing (OFDM) signals along metro-access networks using virtual carrier (VC)-assisted direct-detection (DD).

The MB-OFDM system is analysed without and with optical fibre transmission. The study of the degradation induced by the fibre nonlinearity is focused on the four wave mixing (FWM) effect, which is the dominant nonlinear effect. The FWM power is evaluated through a proposed and validated theoretical method (TM) which analyses the impact of the VC-VC-band FWM products on the system performance. The maximum allowed average powers obtained with the TM for a scheme referred to as the baseline scheme are compared considering standard single mode fibre (SSMF) transmission with different number of fibre spans and wavelength division multiplexing (WDM)-MB-OFDM signals with different channel gaps between WDM channels.

VC-assisted DD MB-OFDM schemes with high tolerance to the FWM effect are proposed considering two different frequency slot widths. The increase of the number of users or the optical distribution network coverage potentiated by relaxing the FWM impact is assessed. The power budget (PB) improvements provided by these schemes are also presented for different user distances and capacity levels. For a channel grid of 3.125 GHz and a data bit rate per-user of 10 Gb/s, a PB improvement of 3 dB is achieved, which allows to double the number of users or to extend the optical distribution network (ODN) reach by about 12 km. With a 6.25 GHz channel grid and a data bit rate per-user of 25 Gb/s, the PB improvement surpasses 4 dB, enabling to double the number of users and simultaneously extend the ODN coverage by 5 km.

Two VC-assisted MB-OFDM schemes are assessed and compared experimentally: the baseline scheme and a scheme with higher FWM tolerance. The performance of both schemes is evaluated and compared as a function of the total average power launched into each SSMF span, for single-channel and multi-channel transmission and for single-span and multi-span propagation.

Keywords: orthogonal frequency-division multiplexing, multi-band, four wave mixing, metro-access networks, nonlinear transmission.

Contents

List of Figures

List of Tables

List of Acronyms

ADC	analogue-to-digital converter.
AGA	analytical Gaussian approach.
AM	analytical model.
ASE	amplified spontaneous emission.
AWG	arbitrary waveform generator.
AWGN	additive white Gaussian noise.
BER	bit error ratio.
BG	band gap.
BPF	band-pass filter.
BPSK	binary phase shift keying.
BS	band selector.
CB	channel bandwidth.
CG	channel gap.
CO	coherent detection.
CP	cyclic prefix.
CW	continuous wave.
DAC	digital-to-analogue converter.
DBP	digital back-propagation.
DC	direct-current.
DD	direct-detection.
DEC	direct error counting.

DFT discrete Fourier transform.

DG degenerate.

DP dual-parallel.

DSB double sideband.

DSO digital storage oscilloscope.

DSP digital signal processing.

EA electrical amplifier.

EAM electro-absorption modulator.

EDFA erbium doped fibre amplifier.

EGA exhaustive Gaussian approach.

ESNR electrical signal-to-noise ratio.

EVM error vector magnitude.

FEC forward error correction.

FFT fast Fourier transform.

FWM four wave mixing.

G Gaussian.

GVD group velocity dispersion.

HC hybrid coupler.

HT Hilbert transform.

ICI intercarrier interference.

IDFT inverse discrete Fourier transform.

IFFT inverse fast Fourier transform.

ISI intersymbol interference.

LPE low-pass equivalent.

LPF low-pass filter.

MARIN	metro and access ring integrated network.
MB	multi-band.
MCM	multi-carrier modulation.
MEB	MORFEUS extraction block.
MI	modulation index.
MIB	MORFEUS insertion block.
MLL	maximum link loss.
MORFEUS	Metro Networks based on Multi-band Orthogonal Frequency Division Multiplexing Signals.
MSSI	mid-span spectral inversion.
MZM	Mach-Zehnder modulator.
NDG	non-degenerate.
NDG1	non-degenerate product of type 1.
NDG2	non-degenerate product of type 2.
NL	noise loading.
NLSE	nonlinear Schrödinger equation.
NS	numerical simulation.
OBPR	optical carrier-to-band power ratio.
ODN	optical distribution network.
OFDM	orthogonal frequency-division multiplexing.
OFDMA	orthogonal frequency-division multiple access.
OLT	optical line termination.
ONU	optical network unit.
OSA	optical spectrum analyser.
OSNR	optical signal-to-noise ratio.
OTF	optical transfer function.
PAPR	peak-to-average power ratio.

PB	power budget.
PCTW	phase-conjugated twin wave.
PD	photodiode.
PIN	p-type-intrinsic-n-type.
PMD	polarization mode dispersion.
PON	passive optical network.
PS	pilot subcarrier.
PSD	power spectral density.
QAM	quadrature amplitude modulation.
QPSK	quadrature phase shift keying.
RF	radio frequency.
RMS	root-mean-square.
ROADM	reconfigurable optical add-drop multiplexer.
Rx	receiver.
SB	single-band.
SBS	stimulated Brillouin scattering.
SG	super-Gaussian.
SMF	single mode fibre.
SNR	signal-to-noise ratio.
SPM	self phase modulation.
SRS	stimulated Raman scattering.
SSB	single sideband.
SSBI	signal-signal beat interference.
SSFM	split-step Fourier method.
SSMF	standard single mode fibre.
STM	simplified theoretical method.
TAP	threshold average power.

TDM	time division multiplexing.
TDMA	time division multiple access.
TIA	trans-impedance amplifier.
TM	theoretical method.
TS	training symbol.
Tx	transmitter.
UBPL	upper bound of the power limit.
UC	unwanted carrier.
UD	ultradense.
UDWDM	ultradense wavelength division multiplexing.
VBG	virtual carrier-to-band gap.
VBPR	virtual carrier-to-band power ratio.
VC	virtual carrier.
VOA	variable optical attenuator.
WDM	wavelength division multiplexing.
WSS	wavelength selective switch.
XPM	cross phase modulation.

List of Symbols

α	optical fibre loss coefficient.
β	propagation constant of the optical fibre.
β_0	propagation constant at frequency ν_0.
β_1	propagation delay.
β_2	first-order GVD coefficient.
β_3	second-order GVD coefficient.
δ	number of slots inside the WDM channel not occupied with OFDM bands.
Δ_{aux}	amplitude coefficient at the SSBI mitigation algorithm.
$\Delta\beta$	phase mismatch between the interacting waves involved in the FWM generation.
Δ_d	stored amplitude coefficient at the SSBI mitigation algorithm.
Δf	frequency spacing between different subcarriers.
Δf_b	frequency spacing between the central frequencies of consecutive OFDM bands.
Δf_{sc}	OFDM subcarrier spacing.
Δf_v	frequency spacing between consecutive VCs.
Δ_i	increment factor at the SSBI mitigation algorithm.
$\Delta\lambda$	spectral width of the optical signals to be photodetected.
$\Delta\nu_{ch}$	WDM channel spacing.
$\Delta\nu_{ik}$	frequency difference between optical frequencies ν_i and ν_k.
$\Delta\nu_{jk}$	frequency difference between optical frequencies ν_j and ν_k.
$\Delta\nu_m$	frequency slot width.
$\Delta\tau$	PMD-induced signal-broadening in the time domain.
$\varepsilon_{\mathrm{CP}}$	CP overhead.
$\varepsilon_{\mathrm{FEC}}$	FEC overhead.
$\varepsilon_{\mathrm{TS}}$	TS overhead.

η_B	bandwidth efficiency.
η_{FWM}	FWM efficiency that regulates the strength of the generated mixing product.
η_s	spectral efficiency of the WDM-MB-OFDM signal.
γ	fibre nonlinearity coefficient.
λ	optical wavelength.
λ_0	optical wavelength at frequency ν_0.
λ_m	optical wavelength of the m-th wave.
λ_n	optical wavelength of the n-th wave.
ν	optical frequency.
ν_0	reference optical frequency.
$\nu_{\text{BS},n}$	BS central frequency when selecting the pair band-VC n.
$\nu_{b,n,l}$	central optical frequency of the l-th band of the n-th channel.
ν_i	optical frequency of the optical signal i involved in FWM generation.
ν_j	optical frequency of the optical signal j involved in FWM generation.
ν_k	optical frequency of the optical signal k involved in FWM generation.
ν_n	optical frequency of the optical signal n generated by the FWM process.
$\nu_{sc,n,l,m}$	optical frequency of the m-th subcarrier of the l-th band of the n-th channel.
$\nu_{v,n,l}$	optical frequency of the l-th VC of the n-th channel.
ϕ_{SPM}	SPM-induced nonlinear phase shift.
ϕ_{XPM}	XPM-induced nonlinear phase shift.
$\sigma^{(i)}_{(I,Q)}[k]$	standard deviation of the I or Q components of the received k-th OFDM subcarrier of the i-th OFDM symbol.
φ_v	VC initial phase.
$\chi^{(1)}$	linear susceptibility.
$\chi^{(2)}$	second-order nonlinear susceptibility.
$\chi^{(3)}$	third-order nonlinear susceptibility.
A	slowly varying envelope of the optical field.
A_e	effective core area of the fibre.
A_v	VC amplitude.

$B_{-20\,\mathrm{dB}}$	-20 dB bandwidth of an optical filter.
$B_{-20\,\mathrm{dB,BS}}$	BS −20 dB bandwidth.
$B_{-3\,\mathrm{dB}}$	-3 dB bandwidth of an optical filter.
$B_{-3\,\mathrm{dB,BS}}$	BS −3 dB bandwidth.
$B_{-3\,\mathrm{dB,WSS}}$	WSS −3 dB bandwidth.
$B_{-3\,\mathrm{dB,WSS,c}}$	equivalent −3 dB bandwidth of the WSS after WSS concatenation.
$B_{-6\,\mathrm{dB,HC1}}$	−6 dB bandwidth of HC1.
$B_{-6\,\mathrm{dB,HC2}}$	−6 dB bandwidth of HC2.
B_{BS}	ideal BS bandwidth.
B_d	BS parameter for bandwidth increment/shrinkage.
B_E	BPF bandwidth.
$BER^{(i)}[k]$	BER of the k-th OFDM subcarrier of the i-th OFDM symbol.
$BER[k]$	BER of the k-th subcarrier averaged over the OFDM symbols.
B_i	bandwidth of the OFDM signal that suffers from distortion interference.
$B_{\mathrm{MB\text{-}OFDM}}$	MB-OFDM signal bandwidth.
B_N	reference bandwidth.
B_{OTF}	OTF bandwidth.
B_w	bandwidth of each OFDM band.
B_{WDM}	WDM channel bandwidth.
c	speed of light in a vacuum.
c_n	normalized subcarrier complex amplitude.
D	GVD parameter.
D_{DG}	degeneracy factor for the DG products.
D_g	degeneracy factor.
$\hat{D}$	operator that accounts for the fibre dispersion and attenuation effects.
D_{NDG}	degeneracy factor for the NDG products.
$d_{n,m}$	walk-off parameter between the n-th and m-th optical waves.
D_{PMD}	PMD parameter.

$e_{BS,d}(t)$	LPE of the distortion-impaired optical signal at the BS output.
$\mathbf{e}_{BS,n}(t)$	LPE of the signal at the BS output.
$e_{BS,n,\parallel}(t)$	optical field, at the BS output, of the n-th OFDM signal and n-th VC in the parallel polarization.
$e_{DSB,H}(t)$	optical field of the HT of the DSB signal.
$e_{DSB}(t)$	optical field of the DSB signal.
E_i	optical field of the CW laser.
$e_{MZM,d}(t)$	LPE of the output electrical field of a chirpless MZM after a Taylor series third-order expansion.
$e_{MZM,l}(t)$	linearised output electrical field of a chirpless MZM.
$e_{MZM}(t)$	output electrical field of a chirpless MZM.
$\mathbf{e}_{NL}(t)$	LPE of the field after NL.
$e_o(t)$	optical field at the DP-MZM output.
$\mathrm{erf}(\cdot)$	error function.
$\mathrm{erfc}(\cdot)$	complementary error function.
$e_{SSB,d}(t)$	LPE of the distortion-impaired optical signal at the SSB filter output.
$e_{SSB,\parallel}(t)$	OFDM signal field at the SSB filter output in the parallel polarization.
$e_{SSB}(t)$	optical field of the SSB signal.
EVM_D	distortion-impaired EVM.
$\langle EVM_D \rangle$	average EVM of the OFDM band due to distortion.
$EVM_{\mathrm{FWM},n,l}$	average EVM due to the FWM effect, in decibel, of the l-th band of the n-th channel.
EVM_{L}	EVM not impaired by the fibre nonlinearity.
EVM_{NL}	EVM impaired by the fibre nonlinearity.
$\mathbb{E}\{\cdot\}$	expected value of a function.
f	frequency.
$f_{b,1}$	central frequency of the first OFDM band of the MB-OFDM signal.
$f_{b,n}$	up-converter frequency applied to the n-th OFDM signal.
$f_{\mathrm{BS},n}$	LPE of the BS central frequency when selecting the pair band-VC n.
f_c	central frequency of the SG filter.
f_d	BS parameter for frequency detuning.

f_m	frequency of the m-th subcarrier.
$f_{\max}$	MB-OFDM signal highest frequency.
$f_{\max,\mathrm{BS}}$	maximum frequency of the BS passband.
$f_{\min}$	MB-OFDM signal lowest frequency.
$f_{\min,\mathrm{BS}}$	minimum frequency of the BS passband.
$f_{r,n}$	central frequency of the received n-th OFDM signal after photodetection.
$f_{v,n}$	n-th VC frequency.
$f_{v,n-1}$	frequency of VC $n-1$.
$f_{v,n+1}$	frequency of VC $n+1$.
$f_{\mathrm{WSS},d}$	WSS detuning frequency.
$f_{\mathrm{WSS,ini}}$	LPE of the initial WSS central frequency.
$f_{\mathrm{WSS,opt}}$	LPE of the optimum WSS central frequency.
g	number of empty frequency slots occupied by the CG.
h	step size of the SSFM.
$H_{BPF}(f)$	BPF transfer function.
$H_{BS,n}(f)$	transfer function of the LPE of the BS.
$h_{BS,n}(t)$	impulse response of the LPE of the BS.
$H_{ch}(k)$	channel loading transfer function for subcarrier k.
$H_{eq}(k)$	equalizer transfer function for subcarrier k.
$H_{HT}(f)$	HT transfer function.
H_{SG}	amplitude response of a SG-shape filter.
H_{SMF}	SMF transfer function.
I_a	number of amplitude iterations used to adjust the amplitude of the reconstructed SSBI term before each training iteration.
I_e	number of training iterations used to estimate the SSBI.
$I_{m,n}$	I component of the ideal m-th QAM symbols of the n-th OFDM symbol.
$\widetilde{I}_{m,n}$	I component of the measured m-th QAM symbols of the n-th OFDM symbol.
$i_{n,PIN}(t)$	noise-dependent photocurrent.

$i_{PIN}(t)$	photocurrent at the PIN-PD output.
$i_{PIN,d}(t)$	photocurrent of the distortion-impaired signal at the PIN-PD output.
$i_{s,BPF}(t)$	signal at the BPF output.
$i_{s,PIN}(t)$	signal-dependent photocurrent.
L_e	effective length of the fibre.
L_f	fibre length of the transmission link.
L_{sp}	length of fibre span.
M	subcarrier QAM order.
$m^{(i)}_{(I,Q)}[k]$	mean of the I or Q components of the received k-th OFDM subcarrier of the i-th OFDM symbol.
$m_{(I,Q)}[k]$	mean of the I or Q component of the k-th OFDM subcarrier of the received OFDM symbols.
N_B	number of bands of the MB-OFDM signal.
N_c	number of columns of QAM symbols in the constellation.
N_{ch}	number of WDM channels.
N_{DG}	number of VC-VC-band FWM products of type DG.
$N^{(i)}_{E,(l,c)}[k]$	number of erroneous bits of the k-th OFDM subcarrier of the i-th OFDM symbol when falling in the (l,c) decision region.
$\hat{N}$	operator that accounts for the fibre nonlinearity effects.
$n_{I,\parallel}(t)$	I noise component in the parallel polarization.
$n'_{I,\parallel}(t)$	filtered I noise component in the parallel polarization.
$n_{I,\parallel}(t)$	I noise component in the perpendicular polarization.
$n'_{I,\parallel}(t)$	filtered I noise component in the perpendicular polarization.
N_{IS}	number of information OFDM symbols within a period of transmission.
N_l	number of rows of QAM symbols in the constellation.
N_{NDG1}	number of VC-VC-band FWM products of type NDG1.
N_{NDG2}	number of VC-VC-band FWM products of type NDG2.
n_{NL}	nonlinear refractive index coefficient.
$n_{Q,\parallel}(t)$	Q noise component in the parallel polarization.

$n'_{Q,\parallel}(t)$	filtered Q noise component in the parallel polarization.
$n_{Q,\parallel}(t)$	Q noise component in the perpendicular polarization.
$n'_{Q,\parallel}(t)$	filtered Q noise component in the perpendicular polarization.
N_r	number of signal runs.
N_s	number of OFDM symbols per signal run.
N_{sc}	number of OFDM subcarriers per OFDM symbol.
N_{sp}	number of fibre spans in the metro network.
N_{sym}	number of OFDM symbols that contribute to the EVM evaluation.
N_{TS}	number of training OFDM symbols within a period of transmission.
OSNR_{req}	OSNR that leads to a BER of 10^{-3}.
p_b	mean power of all the OFDM bands.
$p_{b,n}$	mean power of the n-th OFDM band.
$p_{BS,n}$	mean power of the optical field, at the BS output, of the n-th OFDM signal and n-th VC in the parallel polarization.
$P_{b,w}$	maximum allowed average power of the worst pair band-VC.
P_D	distortion power affecting a certain OFDM subcarrier.
$P_{\mathrm{FWM},i}$	average power of the FWM product at frequency ν_i.
$P_{\mathrm{FWM},j}$	average power of the FWM product at frequency ν_j.
$P_{\mathrm{FWM},k}$	average power of the FWM product at frequency ν_k.
$P_{\mathrm{FWM},n}$	average power of the FWM product at frequency ν_n.
$P^{(\mathrm{DG})}_{\mathrm{FWM},n}$	average power of the DG product at frequency ν_n.
$P^{(\mathrm{NDG1})}_{\mathrm{FWM},n}$	average power of the NDG1 product at frequency ν_n.
$P^{(\mathrm{NDG2})}_{\mathrm{FWM},n}$	average power of the NDG2 product at frequency ν_n.
$P^{(i)}_{I,(l,c)}[k]$	probability of the I component of the received k-th OFDM subcarrier of the i-th OFDM symbol to fall in the (l,c) decision region.
P_{in}	power launched into a SSMF span.
$P_{in,\mathrm{ONU}}$	average power at the ONU input.
P_m	average power of the m-th WDM channel.
P_n	average power of the n-th WDM channel.
$p_{n,BPF}$	noise mean power at the BPF output.

$p_{n,NL}$	optical noise mean power after NL.
$p_{n,PIN}$	noise power at the PIN-PD output.
p_o	optical carrier mean power.
P_{out}	power at the SSMF span output.
$P_{out,\text{EDFA}}$	average power at the EDFA output.
P_p	average power per pair band-VC.
$P^{(i)}_{Q,(l,c)}[k]$	probability of the Q component of the received k-th OFDM subcarrier of the i-th OFDM symbol to fall in the (l,c) decision region.
p_{RF}	mean power of the RF MB-OFDM signal.
P_S	signal power of a certain OFDM subcarrier.
$p_{s,BPF}$	mean power of the signal at the BPF output.
P_{sc}	OFDM subcarrier average power.
$p_{s,NL}$	optical signal mean power after NL.
p_{SSB}	mean power of the signal at the SSB filter output.
P_t	total average power launched into each SSMF span.
p_v	mean power of all the VCs.
P_{VC}	VC average power.
$p_{v,n}$	mean power of the n-th VC.
$P_{v,w}$	average power of the VC close to the worst band.
Q_F	tail distribution function of the standard normal distribution.
$Q_{m,n}$	Q component of the ideal m-th QAM symbols of the n-th OFDM symbol.
$\widetilde{Q}_{m,n}$	Q component of the measured m-th QAM symbols of the n-th OFDM symbol.
R_b	overall bit rate of each OFDM band.
R_d	data bit rate of each OFDM band.
$\Re\{\cdot\}$	real part of a signal.
$R_{n,PIN}(\tau)$	auto-correlation function of the noise-dependent photocurrent.
S	dispersion slope.
s_{ADC}	ADC oversampling factor.

S_{ASE}	PSD of the ASE noise along one polarization direction.
$s_{b,n,H}(t)$	HT of the n-th OFDM signal.
$s_{b,n}(t)$	n-th OFDM signal.
$s_{e,n}(t)$	normalized signal at the n-th OFDM Tx output.
$s_e(t)$	unnormalized RF MB-OFDM signal.
S_f	optical filter selectivity.
$S_{f,\mathrm{BS}}$	BS selectivity.
$\mathrm{sgn}(f)$	signum function.
$S_I(f)$	noise PSD of the I component.
$s_{I,n}(t)$	low-pass filtered I component of the OFDM signal n.
$S_{n,PIN}(f)$	noise PSD at the PIN-PD output.
$s_n(t)$	n-th complex baseband OFDM signal.
$S_Q(f)$	noise PSD of the Q component.
$s_{Q,n}(t)$	low-pass filtered Q component of the OFDM signal n.
$\tilde{s}_n(t)$	normalized n-th complex baseband OFDM signal.
$s_{v,n,H}(t)$	HT of the n-th VC signal.
$s_{v,n}(t)$	n-th VC signal.
$S_{\mathrm{WSS}}(f)$	WSS amplitude response.
T	time measured in a retarded frame of reference moving at the group velocity v_g.
t	time.
T_c	ADC sampling interval.
T_{cp}	CP time.
T_p	Period of transmission of a set of training and information OFDM symbols.
T_s	OFDM symbol duration including CP.
t_s	OFDM symbol duration without CP.
T_{sp}	time spreading of the transmission link caused by fibre chromatic dispersion.
V_1	bias voltage of the upper MZM of the DP-MZM.
$v_1(t)$	electrical signal applied to the upper MZM of the DP-MZM.
V_2	bias voltage of the lower MZM of the DP-MZM.

$v_2(t)$	electrical signal applied to the lower MZM of the DP-MZM.
V_3	bias voltage of the outer MZM of the DP-MZM.
V_b	MZM bias voltage.
v_g	group velocity.
$v_-(t)$	lower sideband of the RF MB-OFDM signal.
V_π	MZM switching voltage.
$v_+(t)$	upper sideband of the RF MB-OFDM signal.
V_{RMS}	RMS voltage of the electrical signals applied to the MZM arms.
$V_{RMS,req}$	required RMS voltage of the MB-OFDM signal.
$V_{RMS,s_{b,n}}$	RMS voltage of the n-th OFDM signal.
V_{RMS,s_e}	RMS voltage of the unnormalized RF MB-OFDM signal.
V_{RMS,s_n}	RMS voltage of the n-th complex baseband OFDM signal.
$V_{RMS,s_{v,n}}$	RMS voltage of the n-th VC signal.
$v(t)$	RF MB-OFDM signal.
$w_m(t)$	waveform of the m-th subcarrier.
$\mathrm{WSS}_{\mathrm{max}}^{1\,\mathrm{dB}}$	maximum number of concatenated WSSs after a 1 dB EVM degradation.
$\mathrm{WSS}_{\mathrm{max}}^{2\,\mathrm{dB}}$	maximum number of concatenated WSSs after a 2 dB EVM degradation.
$x[k]$	k-th sample of the OFDM signal.
$X_{m,n}$	m-th mapped symbol of the n-th MCM symbol.
$x(t)$	MCM signal in the time domain.
$y_{(I,Q),n}^{(i)}[k]$	amplitude of the I or Q component of the received k-th OFDM subcarrier of the i-th OFDM symbol in the n-th signal run.
z	propagation distance along the fibre.

Chapter 1

Introduction

In this chapter, the motivation and scope of the thesis are explained in section 1.1. In section 1.2, the objectives and organization of the thesis are presented. In section 1.3, the main contributions of the thesis are summarized.

1.1 Motivation and scope of the thesis

A huge increase of the traffic demand has been witnessed in the last years, and forecasts anticipate that the increase will be nearly threefold over the next 5 years, with twice the current broadband speeds by 2021 [1]. In order to address the huge traffic demand, the capacity of optical fibre networks reached several dozens of Tb/s and wavelength division multiplexing (WDM) systems have been deployed to meet the capacity requirements [2, 3]. Optical fibre networks are commonly segmented in three tiers [4]: long-haul, metropolitan (metro) and access networks. Long-haul networks may achieve distances of one thousand kilometres or more, whereas metropolitan networks may reach a few hundreds of kilometres and interconnect long-haul and access networks. Providing connectivity between metro networks and the end users (that is, business or residential customers) are access networks with distances no longer than a few tens of kilometres. Forecasts anticipate that metro traffic is growing faster than long-haul traffic and will account for 35% of the total end-user traffic by 2021, a 13% increase when compared with the metro traffic in 2016 [1]. Therefore, extending the transmission capacity of metro networks has become essential to support that traffic growth [5–8]. In the same way, access networks are expected to experience a huge increase of traffic coming mainly from mobile devices, video and gaming services [1].

The expected growth in metro traffic over the following years highlights the need for metro networks to present higher capacity, but also flexibility, scalability, dynamic reconfiguration, transparency [6,8,9] in order to avoid demanding requirements on the optoelectronic components and to avoid requiring new infrastructure, which will affect the deployment potentials. All these features have to be integrated in a cost-effective metro network solution. Transponders are one of the major cost contributions of a metro network. Therefore, a low-cost solution can only be obtained if structures employing complex transmitters or receivers are avoided, technology with limited bandwidth is applied and the expensive components are shared by several users. Integrated in this effort, this thesis is focused on the investigation of the nonlinear impairments of high bit-rate and spectrally-efficient orthogonal frequency-division multiplexing (OFDM) signals deployed in metro-access networks with low-cost receivers, and proposes solutions to improve the tolerance to those impairments.

1.1.1 Integrated metro-access networks

The huge traffic demand is pushing current metro and access networks towards metro-access integration, which consists in having a single hybrid optical network (integrated metro-access network) that allows network operators to reduce capital and operational expenditures, to facilitate broadband access for a large number of customers and to increase the energy efficiency of next generation optical networks [9–11]. Merging metro and access networks also enables an all-optical solution where several services and standards are provided and coexist with each other [12].

Different solutions for integrated metro-access networks have been proposed in the last years to cope with the foreseen traffic demand [13–17]. One of the first proposals was the metro and access ring integrated network (MARIN) [13]. MARIN is a hybrid WDM/time division multiple access (TDMA) solution in which the integration is based on interconnecting dense WDM rings to form an all-optical mesh network [13]. Another architecture, based on a hybrid WDM/TDMA approach, was proposed using a long-reach passive optical network (PON) [14]. This network, known as PIEMAN, uses dense WDM in the metro segment and time division multiplexing (TDM) in the access segment. It is a semi-PON in the sense that it requires an active node with optical amplifiers between the metro and access segments to achieve the desired reach and split per wavelength [14]. A different approach, based on ring and tree topology to improve the network resilience, has been proposed in the SARDANA project [15]. This metro-access architecture employs a bidirectional WDM ring merged with TDM-PON trees in the access

part of the network. The metro and access parts are interconnected through cascadable optical passive add/drop remote nodes [15].

More recently, with the advent of OFDM, solutions using multiple-access based on OFDM have emerged [18]. In [16], a structure with single fibre access trees connected to an orthogonal frequency-division multiple access (OFDMA) single fibre ring was proposed. An updated version of this metro-access network employing OFDMA was shown in [17], which considers polarization multiplexing to transmit the downstream and upstream signals.

In the work presented in this thesis, the integrated metro-access network employs a structure where the metro segment relies on the use of WDM channels. The traffic coming from the optical line termination (OLT) travels through a ring towards the access segments. The interface between the access segments and the metro segment consists on a node with add/drop capabilities. The node transparently routes the traffic from/to a subset of users that are attached to it through PON trees. Each user is connected to the network by an optical network unit (ONU). The access network based on PON trees has the advantage of not requiring active components, such as optical amplifiers, hence reducing the overall cost of the network.

Compared with conventional metro and access networks, the integrated metro-access network employs a single network infrastructure covering a larger geographical area. Moreover, it provides savings in terms of the aggregation equipment typically deployed between the access and metro networks. Fig. 1.1 illustrates the integrated metro-access network concept.

1.1.2 Optical networks employing OFDM

In order to conciliate the bandwidth requirements needed to cope with the traffic increase, the use of transmission techniques with high spectral efficiency and flexible provisioning of high capacity to the end-users are highly desirable. In the past few years, OFDM has received remarkable attention as a promising technology with the aforementioned features [18–20]. Transmission of OFDM signals through optical fibre has been proposed for a variety of telecommunication networks, including access [18, 21, 22], metro [23] and long-haul [24]. OFDM provides: 1) high capacity to the users together with high spectral efficiency [18, 25–28]; 2) resilience to linear fibre effects, such as group-velocity dispersion and polarization-mode dispersion [19, 29]; and 3) flexible bandwidth allocation [19, 30, 31].

Optical OFDM systems are often divided in two different categories: coherent detection (CO)-OFDM and direct-detection (DD)-OFDM [19]. CO-OFDM has shown great robustness against

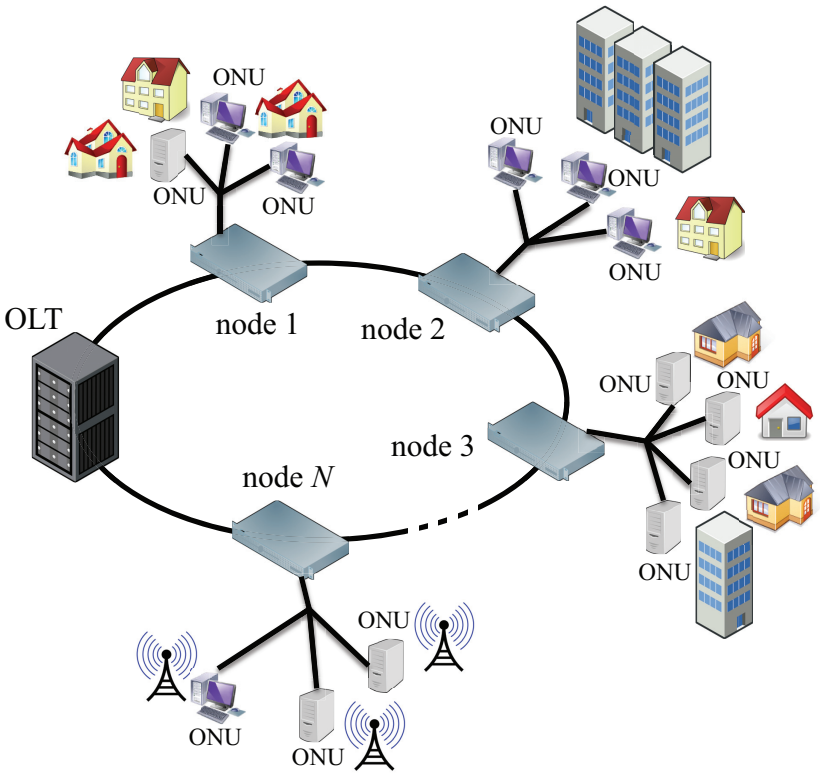

Figure 1.1: Integrated metro-access network.

fibre dispersion impairments and, when combined with polarization division multiplexing, can further increase the spectral efficiency and relax the bandwidth requirements of the electronic components [32]. Unfortunately, these great benefits are accompanied by high-cost installations, including narrow-linewidth laser sources, local oscillators, hybrid couplers, several photodetectors at the receiver side, and extra signal processing accounting for the phase and frequency offset estimations. On the other hand, DD-OFDM can be deployed with low-cost distributed feedback lasers with moderate-linewidth. In addition, there is no need for local oscillators and hybrid couplers at the receiver as it only requires a single photodetector. Therefore, DD-OFDM is quite convenient to be implemented in systems where cost is of primary concern. As metropolitan and access networks are cost-sensitive, DD-OFDM systems are preferred in detriment of CO-OFDM systems [33, 34].

Although optical OFDM systems have been widely studied in the past decade, the concept of multi-band (MB)-OFDM (transmission of several OFDM electrical signals in each WDM channel) for application in next generation metro networks and spectrally-efficient PONs is quite recent [9, 25, 34–43]. When compared with single-band (SB)-OFDM systems, MB-OFDM presents higher flexibility in capacity allocation and granularity at the sub-wavelength level as main strengths [25]. Due to the sharp shape of the OFDM spectrum, it is possible to transmit simultaneously several OFDM bands in each wavelength channel with reduced guard band be-

tween them, and traffic switching from the metro to the access network can be performed at the band level rather than at the wavelength level. Moreover, services generated from different sources in the network can be aggregated in the same wavelength in different OFDM bands [9]. Additionally, the deployment of MB-OFDM signals also allows to overcome the frequency limitations of the digital-to-analogue converters (DACs) and analogue-to-digital converters (ADCs) when data rate increases by dividing the overall data rate into multiple OFDM bands [25].

In order to conciliate the advantages of MB transmission with the low-cost implementation provided by DD, solutions employing MB-OFDM with DD have been proposed recently. In [38], a high-speed ($>$ 100 Gb/s) MB-OFDM system using a DD optical OFDM superchannel (several OFDM bands) with dual carriers at both sides of the superchannel (to assist the DD process) is proposed for long-haul networks. Each carrier assists the detection of half of the superchannel OFDM bands. This system employs an optical multi-band receiving method which performs the detection by just considering one band. Although it presents high spectral efficiency, it is quite challenging to implement this MB-OFDM system in flexible metro-access networks due to the huge requirements for the receiver front-end bandwidth associated with the dual-band filter employed to assist the photodetection. A variant of the MB-OFDM DD long-haul system proposed in [38] is presented in [34]. This optical OFDM superchannel employs multiple carriers (could be more than two), targeting ultra-high capacity with relaxed electrical receiver bandwidth requirements.

A different solution for DD MB-OFDM systems is to use a carrier close to each OFDM band to assist the band detection [9, 44]. This carrier [referred as virtual carrier (VC)] can be electrically generated together with each OFDM band to avoid phase mismatch in the photodetection process. The inclusion of the VC just close to each OFDM band allows the detection of each band individually with minimum required electrical receiver (photodetector, amplifier and analogue-to-digital converter) bandwidth, nearly the same as the OFDM signal bandwidth. As a consequence, the electronic part of the receiver presents reduced cost, which is essential in metro-access networks. The main limitation of minimizing the frequency gap between the VC and the OFDM band is the presence of additional distortion which may interfere significantly with the OFDM signal. This distortion is usually known as the signal-signal beat interference (SSBI) and is originated from the square-law of the photodetector [44]. Nevertheless, this limitation can be minimized either by increasing the power of each VC compared with the power of the corresponding OFDM band or by using digital signal processing (DSP) algorithms at the receiver side to reconstruct and remove the SSBI term from the photodetected signal [9, 32, 45]. A simplified MB-OFDM signal spectrum with N OFDM bands and N VCs, considering the

VCs at a higher frequency than the corresponding OFDM bands, is shown in Fig. 1.2.

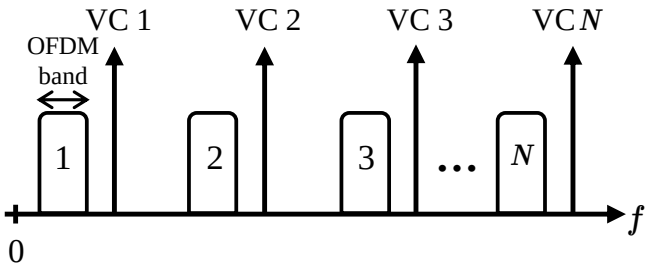

Figure 1.2: Simplified MB-OFDM signal spectrum with N OFDM bands and N VCs, with the VCs at a higher frequency than the corresponding OFDM band.

1.1.3 Nonlinear crosstalk in spectrally-efficient networks

High spectral-efficiency can be achieved by employing high order modulation formats and/or by reducing the frequency spacing between WDM channels [46]. Increasing the modulation formats' order requires high signal-to-noise ratios (SNRs) to keep a certain performance level. Thus, more and more power is launched into the fibre [47]. Reducing the frequency spacing between different channels may induce inter-channel interference, which is a form of linear crosstalk, and could degrade substantially the network performance. It is well known that launching optical signals with high power into the fibre results in signal distortions coming mainly from the dependence of the fibre refractive index on light intensity [47–50]. This is known as the Kerr effect, and is responsible for fibre nonlinearities such as the four wave mixing (FWM) effect. This form of nonlinear crosstalk sets an upper bound on the SNR and limits the capacity of optical fibre-based networks [47, 49, 50]. In the context of metro-access networks, the launched power limitation translates into power budget reduction and, consequently, in lower network capacity and/or smaller network coverage.

Given that linear fibre impairments can nowadays be fully compensated using digital equalization algorithms [51], it is without surprise that the subject of increasing the tolerance of optical networks to fibre-induced nonlinearities has become a hot topic [46,47,51–59]. The most common techniques employed for nonlinearity mitigation are digital back-propagation (DBP) [46, 51–54], mid-span spectral inversion (MSSI) [55–57] and phase-conjugated twin waves (PCTWs) [47, 58, 59]. In the end, these techniques are all based on the general concept of channel inversion and result from tradeoffs between computational cost, latency and spectral efficiency. In OFDM-based networks, fibre nonlinearity compensation is mainly focused on applications considering high data-rate CO-OFDM transmission [57,58,60], instead of DD-OFDM-based solutions [61,62]. With CO-OFDM transmission, it was shown that FWM is the dominant fibre nonlinear effect

responsible for signal quality degradation [83, 84]. However, the influence of the nonlinear fibre effects on the performance of high data-rate DD-OFDM-based networks still requires further investigation. A study of this kind is of particular relevance as DD-OFDM-based systems may suffer from additional types of fibre-induced degradation coming from the transmission of radio frequency (RF) carriers (used to assist the direct-detection) in each WDM channel.

1.2 Objectives and organization of the thesis

This thesis deals with the investigation of the nonlinear crosstalk induced by the Kerr effect on the transmission of MB-OFDM signals along metro-access networks. Following this investigation, MB-OFDM schemes showing enhanced tolerance to this fibre-induced nonlinear effect are proposed. The degradation induced by the fibre nonlinearity is characterized considering DD-OFDM transmission in order to keep the system complexity and cost as low as possible, as required by metro-access networks. This work was developed within the National Project "Metro networks based on multi-band orthogonal frequency-division multiplexing signals" (MORFEUS-PTDC/EEI-TEL/2573/2012).

Particularly, the main objectives of this thesis are the following:

1. Analysis of the degradation induced by optical fibre nonlinear effects on MB-OFDM signals transmitted along metro networks and validation of such analysis using numerical simulation,

2. Proposal, assessment and demonstration of MB-OFDM schemes for metro-access networks with high tolerance to the Kerr effect,

3. Experimental demonstration of a MB-OFDM network employing a MB-OFDM scheme with high tolerance to the Kerr effect.

This thesis is composed by 7 chapters. Additionally, 7 appendixes provide support to these chapters.

In chapter 2, the MB-OFDM signals employing VC-assisted DD in metro-access networks are introduced and discussed. First, the analytical formulation of multi-carrier modulation (MCM) signals (in which OFDM signals are a particular case) is presented. The operations associated with OFDM signal generation are discussed, and the main OFDM signal parameters are

explained. The analytical characterization of VC-assisted MB-OFDM signals in the electrical domain is analysed and the generation of single sideband (SSB)-MB-OFDM signals in the optical domain is discussed. The operations involving OFDM signal demodulation are also analysed. Additionally, the elements of the metro-access network which employs VC-assisted DD-SSB-MB-OFDM signals are described.

In chapter 3, the performance of VC-assisted DD-SSB-MB-OFDM signals in back-to-back operation (that is, without optical fibre transmission) is assessed. Particularly, the DD-MB-OFDM system in optical back-to-back operation is described and the characteristics of the bandwidth-limited components, namely, the wavelength selective switch (WSS), band selector (BS) and hybrid coupler (HC), are presented. Additionally, the main parameters which rule the design of MB-OFDM signals are discussed, namely, the virtual carrier-to-band gap (VBG), the band gap (BG) and the central frequency of the first OFDM band of the MB-OFDM signal. The limitations provided by non-ideal band selector filtering are also analysed. The performance analysis in back-to-back operation is assessed through numerical simulation with different number of OFDM subcarriers, different BS shapes, considering different WDM channel spacings and the bandwidth-narrowing effect caused by successive filtering of the WSSs.

In chapter 4, a theoretical method (TM) to evaluate the FWM power in ultradense wavelength division multiplexing (UDWDM) VC-assisted MB-OFDM systems using DD is proposed and validated. Preliminary analysis has shown that the FWM is dominant over other nonlinear effects, such as self phase modulation (SPM) and cross phase modulation (XPM), and that the dominant FWM products are the ones generated from the mixing between two VCs and an OFDM band (VC-VC-band products). Hence, the TM also assumes that the VC-VC-band products are dominant over other FWM-induced products. Additionally, a simplified theoretical method (STM) with reduced complexity that provides the maximum allowed average power at the fibre input for the worst pair band-VC of the WDM-MB-OFDM signal is also proposed. The structure of the WDM-MB-OFDM signal considered in the analysis is identified. The TM and STM results are validated by comparison with numerical simulation and the maximum allowed average powers obtained with the TM and STM are compared for standard single mode fibre (SSMF) transmission with different number of fibre spans and WDM-MB-OFDM signals with different frequency gaps between WDM channels.

In chapter 5, VC-assisted DD MB-OFDM schemes with high tolerance to the FWM effect are proposed considering two different frequency slot widths. The limits and compromises when designing new VC-assisted schemes are analysed and discussed. The best schemes are selected

from a set of alternative MB-OFDM schemes chosen with high potential to increase the tolerance to the FWM effect. The increase of the number of users or the optical distribution network (ODN) coverage potentiated by relaxing the impact of the FWM effect on the proposed VC-assisted DD MB-OFDM metro-access network is assessed. Additionally, the power budget (PB) improvements provided by these new schemes are shown for different user distances and considering two different capacity levels.

In chapter 6, the experimental assessment of VC-assisted DD WDM-MB-OFDM schemes is performed. Two different MB-OFDM schemes are presented and compared: one is referred as the baseline scheme and the other is the scheme showing high tolerance to the FWM effect, as demonstrated in chapter 5. The main parameters of the two schemes are discussed. The experimental setup for both schemes is explained and the laboratory equipment and components are listed and briefly discussed. Maximum allowed average powers using the TM for the two schemes are compared. The performance is assessed experimentally for both schemes and compared as a function of the total average power launched into each SSMF span, for single-channel and multi-channel transmission (to each channel, a MB-OFDM signal is attributed). Single-span and multi-span propagation is also employed.

In chapter 7, a summary of all the work performed and the main conclusions are presented, as well as suggestions for future work.

1.3 Main contributions

In the author's opinion, the main contributions of this thesis are the following:

1. Development of a simulation tool in MATLAB® for assessment of the performance of VC-assisted DD WDM-MB-OFDM signals with linear and nonlinear fibre transmission.

2. Performance analysis of VC-assisted DD SSB-MB-OFDM systems impaired by the noise of the electrical receiver. A preliminary study of this analysis resulted in the publication [63].

3. Development of a TM to evaluate the FWM power of VC-assisted DD WDM-MB-OFDM signals. A detailed description of this method resulted in the publication [37].

4. Proposal and demonstration of VC-assisted DD MB-OFDM schemes with high tolerance to the FWM effect considering different frequency slot widths. A detailed description of this work resulted in the publication [64].

5. Implementation of an experimental setup for the proof-of-concept of a WDM-MB-OFDM metro network employing a VC-assisted DD MB-OFDM scheme with high tolerance to the FWM effect.

6. Development of an analytical model for performance evaluation of amplified spontaneous emission (ASE) noise-impaired DD-SSB-MB-OFDM systems. Development of another analytical model for performance evaluation of distortion-impaired DD-SSB-OFDM systems with a single pair band-VC. A detailed description of both models resulted in the publications [65, 66] and in the publication [67], respectively, and can be found in Appendix B.

7. Development of a DSP-based iterative algorithm for SSBI mitigation. Improvements have been made to the algorithm previously presented in [68]. A detailed description of this algorithm can be found in Appendix C.

8. Development of a method for evaluating the bit error ratio (BER) using the exhaustive Gaussian approach (EGA) for crossed [32-quadrature amplitude modulation (QAM) and 128-QAM] and squared (16-QAM, 64-QAM and 256-QAM) constellations. A detailed description of this model resulted in the publication [69] and can be found in Appendix E.

9. Evaluation of the impact of inter-band nonlinear crosstalk on the performance of VC-assisted DD-SSB-MB-OFDM signals in metro networks, considering single-band and single-channel transmission. A detailed description of this work resulted in the publication [70] and can be found in Appendix G.

A complete list of all the publications developed within this Ph. D. thesis is presented in Appendix A.

Chapter 2

VC-assisted DD-MB-OFDM signals in integrated metro-access networks

2.1 Introduction

The multi-band (MB)-orthogonal frequency-division multiplexing (OFDM) signals employing virtual carrier (VC)-assisted direct-detection (DD) are discussed in detail in this chapter in the context of integrated metro-access networks. The most important concepts associated with this type of signals are introduced and the solutions employed in the transmitter and receiver sides are analysed for a better understanding of the VC-assisted DD-MB-OFDM transmission concept.

This chapter is structured as follows. In section 2.2, the analytical formulation of multi-carrier modulation (MCM) signals is presented. The OFDM signal generation and the OFDM signal parameters are also presented. In section 2.3, the analytical characterization of VC-assisted MB-OFDM signals is performed and the generation of single sideband (SSB)-MB-OFDM signals in the optical domain is discussed. The operations involving OFDM signal demodulation are also analysed. In section 2.4, the elements of the integrated metro-access network employing VC-assisted DD-MB-OFDM signals are described. In section 2.5, the main conclusions are summarized.

2.2 OFDM signals

In this section, the analytical formulation of MCM signals is presented. The operations associated with OFDM signal generation are also presented, together with the main OFDM signal parameters.

2.2.1 Analytical formulation of multi-carrier modulation signals

OFDM signals are a special class of MCM signals [48]. In a MCM signal, the main data stream is divided into several low-rate data streams. The binary input data is mapped onto these low-rate data streams, usually known as subcarriers, using simple modulation formats such as quadrature amplitude modulation (QAM). The MCM signals are formed by a sequence of MCM symbols, where each MCM symbol has N_{sc} subcarriers, corresponding to a group of N_{sc} QAM-mapped symbols. The MCM signal in the time domain, $x(t)$, can be expressed as [48]:

$$x(t) = \sum_{n=-\infty}^{+\infty} \sum_{m=1}^{N_{sc}} X_{m,n}\, w_m(t - nT_s) \tag{2.1}$$

with

$$w_m(t) = \begin{cases} \exp\left(j2\pi f_m t\right), & 0 < t \leq T_s \\ 0, & \text{otherwise} \end{cases} \tag{2.2}$$

where $X_{m,n}$ is the m-th mapped symbol of the n-th MCM symbol, $w_m(t)$ is the waveform of the m-th subcarrier, N_{sc} is the number of subcarriers within each MCM symbol, T_s is the MCM symbol duration and f_m is the m-th subcarrier frequency.

With OFDM signalling, the subcarriers are overlapped in the frequency domain (spectrum) to increase the spectral efficiency when compared with classical MCM signalling [48]. The overlapping can be performed if orthogonality between the different subcarriers is ensured. The orthogonality condition depends on the symbol duration and is defined as [48]:

$$\Delta f = \frac{\rho}{T_s},\ \forall \rho \in \mathbb{N}^+ \tag{2.3}$$

where Δf is the frequency spacing between different subcarriers, and ρ is a positive integer. For consecutive subcarriers, $\rho = 1$ in order to have the maximum spectral efficiency. By considering, at the receiver side, an optimum detector for each subcarrier, the subcarriers can be recovered without intercarrier interference (ICI), in spite of strong spectral overlapping [48].

For the transmission channel to affect each OFDM subcarrier as a flat channel, a high number of subcarriers are required [48]. This means that several modulators (one for each subcarrier) are required to generate the OFDM signal, which increases considerably the system complexity and cost. The impact of this drawback can be minimized by implementing OFDM signals using inverse discrete Fourier transform (IDFT) [48]. To understand the IDFT implementation, let us assume that an OFDM signal composed by one OFDM symbol ($n = 1$) is being sampled with a sampling period of T_s/N_{sc}. The k-th sample of $x(t)$, $x[k]$, can be written as:

$$x[k] = \sum_{m=1}^{N_{sc}} X_{m,1} \cdot \exp\left[j2\pi \frac{f_m(k-1)T_s}{N_{sc}}\right] \tag{2.4}$$

where $k \in \{1, 2, \ldots, N_{sc}\}$. By defining $f_m = (m-1)/T_s$, which takes into account the orthogonality condition presented in Eq. 2.3, Eq. 2.4 can be rewritten as:

$$x[k] = \sum_{m=1}^{N_{sc}} X_{m,1} \cdot \exp\left[j2\pi \frac{(m-1)(k-1)}{N_{sc}}\right] \tag{2.5}$$

which satisfies:

$$x[k] = \sum_{m=1}^{N_{sc}} X_{m,1} \cdot \exp\left[j2\pi \frac{f_m(k-1)T_s}{N_{sc}}\right] = \sum_{m=1}^{N_{sc}} X_{m,1} \cdot \exp\left[j2\pi \left(f_m + \frac{N_{sc}}{T_s}\right) \frac{(k-1)T_s}{N_{sc}}\right] \tag{2.6}$$

that is, it is a periodical function of f_m with period N_{sc}/T_s. Different subcarrier indexing conventions can be used for index k, as long as the frequency components of the subcarriers span one period of N_{sc}/T_s. In this work, the following indexing conventions are employed: $k \in \{1, 2, \ldots, N_{sc}\}$ or $k \in \{-N_{sc}/2 + 1, -N_{sc}/2 + 2, \ldots, N_{sc}/2\}$. In the same way, OFDM signal demodulation at the receiver side can be performed using the discrete Fourier transform (DFT) [48]. IDFT/DFT implementation for OFDM signal generation/demodulation enables the use of the efficient inverse fast Fourier transform (IFFT)/fast Fourier transform (FFT) algorithm which implements IDFT/DFT with reduced complexity, and allows the use of a large number of subcarriers without resorting to a high number of complex modulators.

2.2.2 OFDM signal generation

The OFDM signal is composed by several OFDM symbols, with each one carrying N_{sc} subcarriers. This signal is transmitted through an optical channel that adds distortion and time delays, causing amplitude and phase errors. In order to mitigate these effects, the transmission channel function has to be measured so that, at the receiver side, effective demodulation and

compensation of the channel effects are accomplished. There are several ways of measuring the transmission channel to ensure effective demodulation at the receiver, yet the most common are either pilot subcarriers (PSs) or training symbols (TSs). The main difference between these two techniques is the location of the training data that, at the receiver, is used to estimate the channel response. The PS technique considers training subcarriers integrated with data subcarriers in each OFDM symbol, whereas the TS scheme considers OFDM symbols completely filled with training subcarriers where no information data is sent. In this work, the TS technique is the one chosen for channel estimation.

In dispersive channels, such as the ones considering optical fibre transmission, the signal spreads along time. This can be problematic if a certain OFDM symbol crosses its boundary and causes interference with another OFDM symbol. One way to tackle this issue out is by inserting a time gap between consecutive OFDM symbols, usually known as guard interval. The insertion of a guard interval was proposed to solve the channel dispersion-induced intersymbol interference (ISI) because, as a result of channel dispersion, the distorted OFDM symbol is longer than the original symbol before transmission. The guard interval is effective only if the condition of ISI-free OFDM transmission holds, that is, the guard interval duration needs to be longer than the time spreading. By preceding each OFDM symbol with a guard interval in which no signal is transmitted mitigates ISI; however, this results in ICI. To avoid ICI, the guard interval is filled with an identical copy of a portion of the OFDM signal. One way to mitigate ICI is by using a cyclic prefix [48], where a copy of a portion of the final part of the OFDM symbol is inserted at the guard interval located at the beginning of that OFDM symbol. Usually, a small cyclic prefix (much less than the OFDM symbol duration) is enough to compensate for the time spreading induced by a few hundreds of kilometres of optical fibre. For illustration purposes, Fig. 2.1 shows the time waveform of the in-phase component of an OFDM symbol with cyclic prefix.

Fig. 2.2 depicts the block diagram of the OFDM signal generator. The binary input data is split into parallel bitstreams (one for each subcarrier) and each parallel bitstream is mapped using QAM symbol mapping. The QAM symbols are grouped into blocks with length N (with all subcarriers carrying information, $N = N_{sc}$) that are sent to the IFFT block. At the IFFT block input, the symbols are divided into two groups with $N/2$ symbols each and a zero-padding sequence with length N is placed in-between the two groups of symbols. The zero-padding is a sequence of null symbols employed to oversample the OFDM signal. This oversampling allows to separate in frequency the baseband OFDM signal from the high-frequency aliasing components generated by the IFFT. Spectrally, these null symbols appear at the edges of the OFDM signal

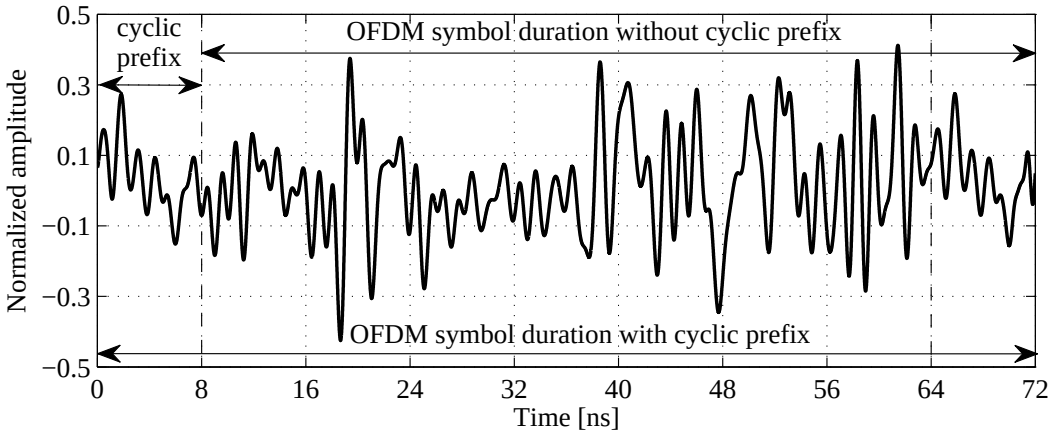

Figure 2.1: Time waveform of the in-phase component of an OFDM symbol with cyclic prefix. The cyclic prefix duration is 8 ns.

spectrum as null subcarriers. After the IFFT operation, a guard interval filled with a cyclic prefix (CP) is introduced at the beginning of each OFDM symbol. Afterwards, a parallel-to-series conversion is performed to form the digital OFDM signal composed by complex-valued samples. The complex-valued signal is separated into two different real-valued signals: a signal with the in-phase (I) components, and another signal with the quadrature (Q) components. Each one of these signals is fed to a sample-and-hold digital-to-analogue converter (DAC) to form an analogue waveform. The analogue signals are then filtered by a low-pass filter (LPF) to suppress the aliasing generated by the digital-to-analogue conversion process. After low-pass filtering, the signals are up-converted to a specified frequency and combined to generate the OFDM signal. Mathematically, the n-th OFDM signal, $s_{b,n}(t)$, can be expressed as:

$$s_{b,n}(t) = s_{I,n}(t)\cos(2\pi f_{b,n}t) - s_{Q,n}(t)\sin(2\pi f_{b,n}t) \tag{2.7}$$

where $s_{I,n}(t)$ is the low-pass filtered in-phase component of the OFDM signal n, $s_{Q,n}(t)$ is the low-pass filtered quadrature component of the OFDM signal n, and $f_{b,n}$ is the up-converter frequency applied to the n-th OFDM signal.

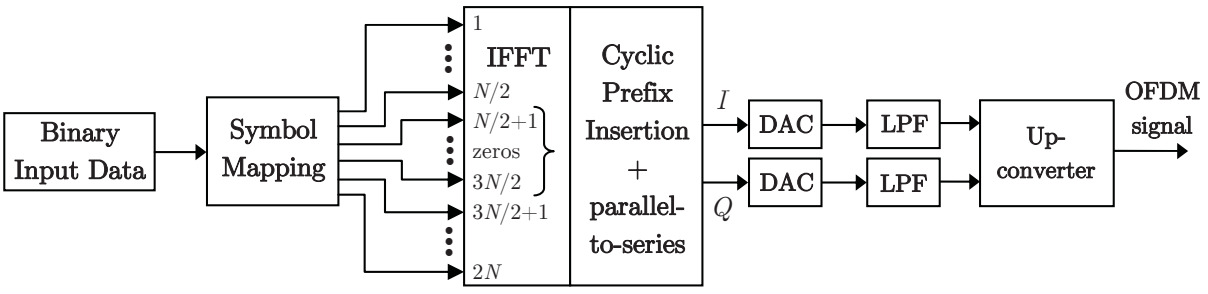

Figure 2.2: Block diagram of the OFDM signal generator.

Fig. 2.3(a) and Fig. 2.3(b) show a partial representation of the time waveforms of the in-phase and quadrature signals after digital-to-analogue conversion, respectively. Fig. 2.3(c) shows the power spectral density (PSD) of the in-phase baseband signal with bandwidth of 1 GHz, before and after low-pass filtering. The LPF is a third-order super-Gaussian (SG) filter with −3 dB bandwidth equal to 1.75 GHz (75% larger than the bandwidth of the baseband OFDM signal). The expression for the amplitude response of a n-th order SG-shape low-pass filter, is based on the expression for the amplitude response of a n-th order SG-shape band-pass filter, $H_{SG}(f)$, which is given by:

$$H_{SG}(f) = \exp\left[-2^{2n}\log_e(\sqrt{2})\left(\frac{f-f_c}{B_{-3\,\mathrm{dB}}}\right)^{2n}\right] \tag{2.8}$$

where f_c is the central frequency of the SG band-pass filter and $B_{-3\,\mathrm{dB}}$ is the −3 dB bandwidth of the SG band-pass filter. A SG low-pass filter is expressed by Eq. 2.8 with the difference of considering 1) $f_c = 0$ and 2) half of the −3 dB bandwidth of the band-pass filter ($B_{-3\,\mathrm{dB}}/2$). Fig. 2.3(d) shows a partial representation of the time waveform of the OFDM signal up-converted to 5 GHz. Fig. 2.3(a), Fig. 2.3(b) and Fig. 2.3(d) show that the OFDM signals have similar shape in time and present high peak levels. The high peaks are attributed to the independent phases of the subcarriers that often combine constructively [71]. This translates into a high peak-to-average power ratio (PAPR), which is known to be one of the major drawbacks of OFDM signals [48, 71]. Fig. 2.3(c) shows that aliasing components with considerable power are present at the DAC output, and that after low-pass filtering, the aliasing components are adequately filtered.

2.2.3 OFDM signal parameters

In this work, it is considered that each OFDM signal (or band) transports a 10 Gb/s information data rate and also that a frequency slot of 3.125 GHz is reserved for each band. Along with the information data, additional overheads need to be accounted in the total data rate to be transmitted. These overheads are due to forward error correction (FEC), OFDM TSs and CP [72]. Hence, the overall bit rate of each band, R_b, which accounts all the overheads, can be written as:

$$R_b = R_d\,(1+\varepsilon_{\mathrm{FEC}})\,(1+\varepsilon_{\mathrm{TS}})\,(1+\varepsilon_{\mathrm{CP}}) \tag{2.9}$$

with R_d standing for the information data rate, and $\varepsilon_{\mathrm{FEC}}$, $\varepsilon_{\mathrm{TS}}$ and $\varepsilon_{\mathrm{CP}}$ representing the overheads for FEC, OFDM TSs and CP, respectively. The FEC overhead $\varepsilon_{\mathrm{FEC}}$ is 7%, which accepts a maximum tolerable pre-FEC bit error ratio (BER) of 3.8×10^{-3} [73].

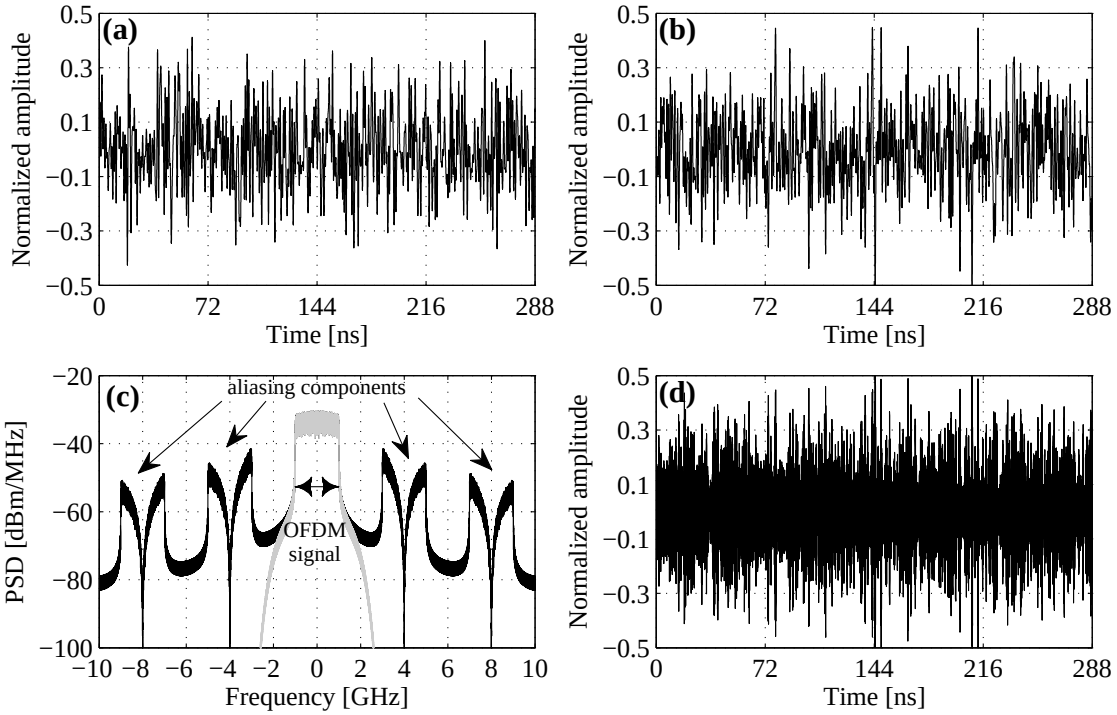

Figure 2.3: Partial representation of the time waveforms of the (a) in-phase signal after digital-to-analogue conversion and the (b) quadrature signal after digital-to-analogue conversion. (c) PSD of the in-phase baseband signal with bandwidth of 1 GHz, before (black) and after (grey) low-pass filtering. The LPF is a third-order super-Gaussian filter with −3 dB bandwidth equal to 1.75 GHz (75% larger than the bandwidth of the OFDM signal). (d) Partial representation of the time waveform of the OFDM signal up-converted to 5 GHz.

The CP overhead is determined by the time spreading occurring at the transmission channel, that is caused by group velocity dispersion (GVD). The CP time needs to be longer than the time spreading to compensate for that impairment. To obtain the required CP time, T_{cp}, the time spreading needs to be estimated. The time spreading, T_{sp}, of two signal frequencies separated by $\Delta\lambda$ and suffering an accumulated dispersion of $D(\lambda) \cdot L_f$ is given by:

$$T_{sp} = D(\lambda) \cdot L_f \cdot \Delta\lambda \tag{2.10}$$

where $D(\lambda)$ is the GVD parameter at wavelength λ, L_f is the fibre length of the transmission channel, and $\Delta\lambda$ is the spectral width of the optical signal to be demodulated at the receiver side (signal composed by the OFDM band and the corresponding VC). In the subsequent chapters, it is considered the following: 1) transmission over standard single mode fibre (SSMF) at 1550 nm, which leads to a GVD parameter close to 17 $\text{ps} \cdot \text{nm}^{-1} \cdot \text{km}^{-1}$; 2) SSMF reaches on the order of a few hundreds of kilometres; and 3) maximum spectral widths of the optical signal to be photodetected of a few GHz. For instance, with a maximum SSMF reach of 400 km and maximum spectral width of 3.125 GHz (0.025 nm), T_{sp} is equal to 0.17 ns. The OFDM symbol

duration without CP, t_s, is given by:

$$t_s = \frac{N_{sc} \log_2 M}{R_b} \tag{2.11}$$

where N_{sc} is the number of OFDM subcarriers per OFDM symbol, and M is the subcarrier QAM order. Let us suppose that $R_b \approx R_d\,(1 + \varepsilon_{\text{FEC}}) = 10.7$ Gb/s. In this situation, with 128 OFDM subcarriers ($N_{sc} = 128$) per OFDM symbol and 16-QAM modulation ($M = 16$) in each subcarrier, t_s is approximately 47.9 ns. By considering T_{cp} equal to the sampling interval T_c, with $T_c = t_s/N_{sc} \approx 0.37$ ns, the condition $T_{cp} > T_{sp}$ is verified. The CP overhead, ε_{CP}, is then given by:

$$\varepsilon_{\text{CP}} = \frac{T_{cp}}{t_s} = \frac{T_c}{t_s} = \frac{1}{N_{sc}}. \tag{2.12}$$

The TS overhead depends on the optical channel stability with respect to linear impairments such as polarization mode dispersion (PMD). The polarization variation along the optical channel is close to one millisecond [48]. This timescale defines the magnitude of the period for transmission of training symbols required to monitor those channel impairments. Knowing the period of transmission of a set of training symbols and information symbols, T_p, the number of training OFDM symbols, N_{TS}, and the number of information OFDM symbols, N_{IS}, within that period can be obtained, as follows:

$$N_{\text{TS}} + N_{\text{IS}} = \frac{T_p}{T_s} \tag{2.13}$$

where T_s is the OFDM symbol duration including CP ($T_s = t_s + T_{cp}$). The TS overhead can be written as:

$$\varepsilon_{\text{TS}} = \frac{T_s N_{\text{TS}}}{T_p - T_s N_{\text{TS}}} = \frac{N_{\text{TS}}}{N_{\text{IS}}}. \tag{2.14}$$

The bandwidth of each OFDM band, B_w, can be also defined using t_s. For $N_{sc} \gg 2$, B_w is approximately given by [48]:

$$B_w \approx \frac{N_{sc}}{t_s} = \frac{R_b}{\log_2 M}. \tag{2.15}$$

Using Eq. 2.12 and Eq. 2.14, Eq. 2.9 can be rewritten as:

$$R_b = R_d\,(1 + \varepsilon_{\text{FEC}}) \left(1 + \frac{N_{\text{TS}}}{N_{\text{IS}}}\right) \left(1 + \frac{1}{N_{sc}}\right). \tag{2.16}$$

As an example, Tab. 2.1 shows R_b and T_p with $N_{sc} \in \{64, 128, 256\}$, $M \in \{16, 256\}$, $N_{\text{TS}} = 100$ and $N_{\text{IS}} = 10000$ ($\varepsilon_{\text{TS}} = 1\%$), $\varepsilon_{\text{FEC}} = 7\%$, $R_d = 10$ Gb/s, and $T_{cp} = T_c$.

Table 2.1: R_b and T_p as a function of $N_{sc} \in \{64, 128, 256\}$ and $M \in \{16, 256\}$.

$M = 16$	N_{sc}	R_b [Gb/s]	T_p [ms]
$N_{\text{TS}} = 100$	64	10.98	0.24
$N_{\text{IS}} = 10000$	128	10.89	0.48
$R_d = 10$ Gb/s	256	10.85	0.96
$M = 256$	N_{sc}	R_b [Gb/s]	T_p [ms]
$N_{\text{TS}} = 100$	64	10.98	0.48
$N_{\text{IS}} = 10000$	128	10.89	0.96
$R_d = 10$ Gb/s	256	10.85	1.91

From inspection of Tab. 2.1, it can be verified that the condition $T_p < 1\,\text{ms}$ is met with $N_{sc} \in \{64, 128\}$ for $M \leq 256$. With $N_{sc} = 64$, the total overhead in percentage, $[(R_b/R_d) - 1] \times 100$, is 9.8%; with $N_{sc} = 128$, the total overhead decreases to almost 9%; and with $N_{sc} = 256$, the total overhead becomes 8.5%.

2.3 VC-assisted direct-detection MB-OFDM signals

In this section, the VC-assisted MB-OFDM signals are characterized analytically, and the generation of SSB-MB-OFDM signals is presented. Additionally, the operations required to perform OFDM signal demodulation are analysed.

2.3.1 Analytical characterization of VC-assisted MB-OFDM signals

The MB-OFDM signal is divided into N_B pairs, and each pair is formed by an OFDM band and a radio frequency (RF) carrier referred also as VC. Hereafter, the OFDM band and respective VCs are referred as a pair band-VC. Each pair band-VC does not interfere in frequency with the neighbouring pairs. The n-th VC signal, $s_{v,n}(t)$, can be expressed as:

$$s_{v,n}(t) = \sqrt{2} \cdot \cos(2\pi f_{v,n} t + \varphi_v) \tag{2.17}$$

where $f_{v,n}$ is the n-th VC frequency and φ_v is the VC initial phase.

In this work, the most used frequency allocation of each pair band-VC is with the VC at a higher frequency than the OFDM band. In some cases, other frequency allocations with the VC at a lower frequency than the OFDM band are addressed. Fig. 2.4 illustrates the MB-OFDM signal spectrum with N_B pairs band-VC, and the most relevant parameters involving the frequency allocation of a MB-OFDM signal: the virtual carrier-to-band gap (VBG) and the band gap (BG). To guarantee that each pair band-VC is within its reserved 3.125 GHz frequency slot, a

frequency spacing of 3.125 GHz between the central frequencies of consecutive OFDM bands is considered, that is, $\Delta f_b = 3.125$ GHz. In this way, the BG can be expressed as follows:

$$\mathrm{BG} = \Delta f_b - B_w. \tag{2.18}$$

Furthermore, by setting the same VBG per pair band-VC, a frequency spacing of 3.125 GHz between consecutive VCs is ensured, that is, $\Delta f_v = 3.125$ GHz.

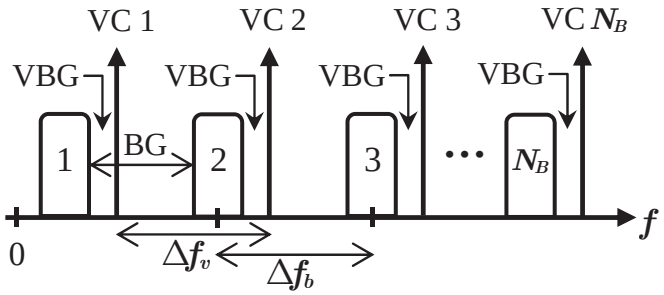

Figure 2.4: Illustration of the MB-OFDM signal spectrum comprising N_B pairs band-VC, with each VC at a higher frequency than the corresponding OFDM band. Δf_v: frequency spacing between consecutive VCs. Δf_b: frequency spacing between central frequencies of consecutive OFDM bands.

Another important parameter when dealing with VC-assisted OFDM signals is the virtual carrier-to-band power ratio (VBPR) (similar to the well-known carrier-to-signal power ratio). The VBPR has a significant impact on the performance of the MB-OFDM signal as it controls the power balance between the OFDM band and the VC within each pair. The VBPR is given by:

$$\mathrm{VBPR} = \frac{p_{v,n}}{p_{b,n}} \tag{2.19}$$

where $p_{v,n}$ and $p_{b,n}$ are the mean power of the n-th VC and the n-th OFDM band, respectively, at the transmitter (Tx) side.

Each pair band-VC is generated by an individual OFDM Tx. Each OFDM Tx is composed by the OFDM signal generator and the VC generator. The normalized signal at the n-th OFDM Tx output, $s_{e,n}(t)$, can be expressed as:

$$s_{e,n}(t) = \frac{s_{b,n}(t)}{V_{RMS,s_{b,n}}} + A_v \cdot \frac{s_{v,n}(t)}{V_{RMS,s_{v,n}}} \tag{2.20}$$

where $V_{RMS,s_{b,n}}$ is the root-mean-square (RMS) voltage of $s_{b,n}(t)$, A_v is the VC amplitude, and $V_{RMS,s_{v,n}}$ is the RMS voltage of $s_{v,n}(t)$. By defining $s_n(t)$ as the n-th complex baseband OFDM signal $[s_n(t) = s_{I,n}(t) + j \cdot s_{Q,n}(t)]$, and taking into account that $V_{RMS,s_{b,n}} = V_{RMS,s_n}/\sqrt{2}$ [V_{RMS,s_n} is the RMS voltage of $s_n(t)$] and that $V_{RMS,s_{v,n}} = 1$ V, the signal $s_{e,n}(t)$ can be

rewritten as:

$$s_{e,n}(t) = \frac{\sqrt{2}}{V_{RMS,s_n}} \cdot s_{b,n}(t) + A_v \cdot s_{v,n}(t). \tag{2.21}$$

The RF MB-OFDM signal, $v(t)$, can be written as a function of $s_{e,n}(t)$ as follows:

$$v(t) = \underbrace{\left[\sum_{n=1}^{N_B} s_{e,n}(t)\right]}_{s_e(t)} \cdot \frac{V_{RMS,req}}{V_{RMS,s_e}} \tag{2.22}$$

where $V_{RMS,req}$ is the required RMS voltage of the MB-OFDM signal, and V_{RMS,s_e} is the RMS voltage of $s_e(t)$, which is equal to $\sqrt{N_B(1+A_v^2)}$. After some calculations, $p_{v,n}$ can be written as:

$$p_{v,n} = \left(\frac{V_{RMS,req}}{V_{RMS,s_e}} A_v\right)^2 \tag{2.23}$$

and $p_{b,n}$ as:

$$p_{b,n} = \left(\frac{V_{RMS,req}}{V_{RMS,s_e}}\right)^2. \tag{2.24}$$

The mean power of $v(t)$, p_{RF}, can be simply expressed as:

$$p_{RF} = N_B \cdot (p_{b,n} + p_{v,n}) = V_{RMS,req}^2. \tag{2.25}$$

Using Eq. 2.23 and Eq. 2.24, the VBPR can be written as:

$$\text{VBPR} = A_v^2. \tag{2.26}$$

2.3.2 Single-sideband MB-OFDM signal generation

The transmission of high-rate MB-OFDM signals along optical fibre must meet two important requirements: 1) high spectral efficiency, and 2) resilience to optical fibre dispersion impairments. Optical fibre transmission can be accomplished considering double sideband (DSB) or SSB transmission. However, only SSB transmission meets the two requirements mentioned above. SSB signals are more spectrally efficient than DSB signals (SSB signals use half of the signal bandwidth). Moreover, there is no need to transmit the two sidebands as the information data can be recovered from one of the sidebands. Furthermore, SSB transmission avoids the destructive beat between the two sidebands after square-law detection. This destructive beat, known as dispersion-induced power fading [74], is caused by the accumulated dispersion of the optical link. For more details on the dispersion-induced impairments, see section F.1.2.

SSB signal generation can be performed by using a conventional electrical-to-optical modulator, such as a Mach-Zehnder modulator (MZM) or an electro-absorption modulator (EAM), followed by an optical filter to suppress one of the sidebands of the DSB signal generated by the modulator. The major drawback of this solution is the requirement of a high selectivity (and thus, expensive) optical filter. SSB signalling can also be accomplished using other architectures, such as the Sieben architecture or by using complex electrical-to-optical modulators, such as the dual-parallel (DP)-MZM, which consists in four phase modulators in parallel and is also referred as a dual-arm MZM or a complex MZM [75]. In this work, the SSB-MB-OFDM signal generation is performed using a DP-MZM and the Hilbert transform (HT). This avoids the use of a high selectivity optical SSB filter. A theoretical study which considers SSB signal generation with a single MZM and an optical SSB filter is presented in Appendix B. The HT transfer function, $H_{HT}(f)$, is given by $H_{HT}(f) = -j \cdot \text{sgn}(f)$, where $\text{sgn}(f)$ is the signum function defined as:

$$\text{sgn}(f) = \begin{cases} 1, & f > 0 \\ 0, & f = 0 \\ -1, & f < 0. \end{cases} \tag{2.27}$$

In order to generate the SSB-MB-OFDM signal in this work, suppression of the lower-side pairs band-VC of the DSB-MB-OFDM signal is performed. A SSB signal with lower-side suppression, $e_{SSB}(t)$, can be obtained using the HT as follows:

$$e_{SSB}(t) = e_{DSB}(t) + j \cdot e_{DSB,H}(t) \tag{2.28}$$

where $e_{DSB}(t)$ is the DSB signal and $e_{DSB,H}(t)$ is the HT of $e_{DSB}(t)$. The SSB-MB-OFDM signal is formed at the MB-OFDM Tx. Fig. 2.5 shows the block diagram of the MB-OFDM Tx. The RF MB-OFDM signal $v(t)$ is applied to one branch of the DP-MZM and the HT of $v(t)$ to the other branch of the DP-MZM. The inner MZMs of the DP-MZM are biased at the minimum point to produce a carrier-suppressed signal. The optical carrier can be suppressed as VCs are instead used to assist the direct-detection. The outer modulator is biased at the quadrature point through a bias voltage, to provide a phase shift of 90 degrees between the DSB signal generated by one inner MZM and the HT of the DSB signal generated by the other inner MZM. The generated SSB-MB-OFDM signal then modulates a continuous wave (CW) laser to obtain the optical signal at the DP-MZM output. The phase noise effect introduced by the CW laser is neglected in this work. A detailed study regarding the limitations of laser phase noise in VC-assisted DD-MB-OFDM networks can be found in [76]. Assuming similar MZM switching voltages (voltage required to switch between the maximum and the minimum of the MZM power

transmission characteristic), the optical field at the DP-MZM output, $e_o(t)$, is given by [75]:

$$e_o(t) = \frac{E_i}{2}\left[\exp\left(-j\pi\frac{V_3}{2V_\pi}\right)\cos\left(\pi\frac{v_1(t)-V_1}{2V_\pi}\right) + \exp\left(j\pi\frac{V_3}{2V_\pi}\right)\cos\left(\pi\frac{v_2(t)-V_2}{2V_\pi}\right)\right] \tag{2.29}$$

where E_i is the optical field at the DP-MZM input (CW laser), V_3 is the bias voltage of the outer MZM, V_π is the switching voltage of the MZMs, $v_1(t)$ and $v_2(t)$ are the electrical signals applied to the upper and lower MZM arms, respectively, and V_1 and V_2 are the bias voltages of the inner MZMs 1 and 2, respectively. In order to bias the inner MZMs at the minimum transmission point, $V_1 = V_2 = V_\pi$ are set. By setting $V_3 = V_\pi/2$, the outputs of the two inner MZMs are set in quadrature to each other and a carrier suppressed SSB-MB-OFDM optical signal is obtained.

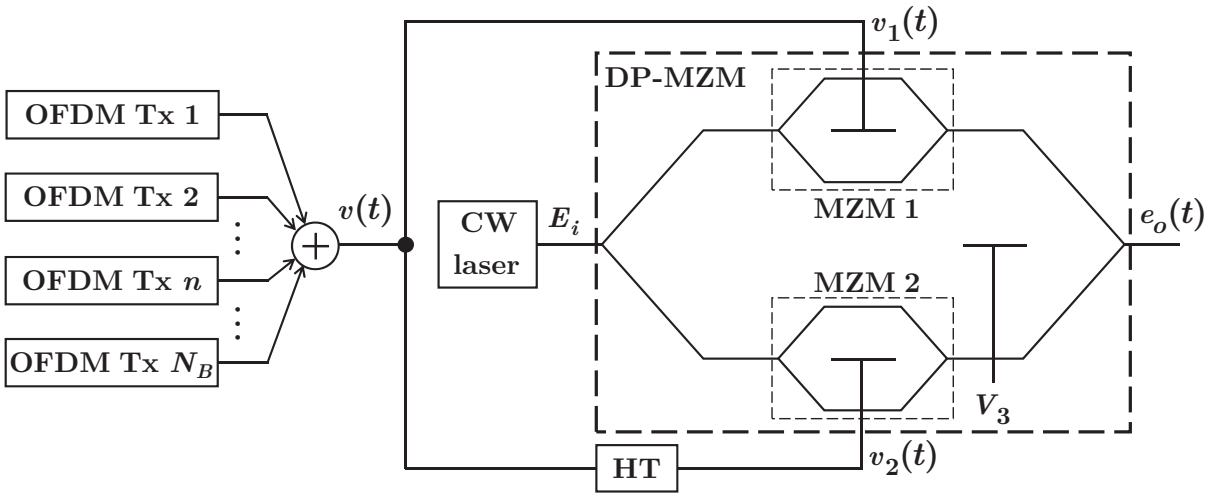

Figure 2.5: Block diagram of the MB-OFDM transmitter. E_i: optical field at the DP-MZM input. $v_1(t)$: electrical signal applied to MZM 1. $v_2(t)$: electrical signal applied to MZM 2. V_3: bias voltage applied to the outer MZM. $e_o(t)$: optical field at the DP-MZM output (optical SSB-MB-OFDM signal).

With the inner MZMs biased at the minimum transmission point ($V_1 = V_2 = V_\pi$) and the outer MZM biased at quadrature point ($V_3 = V_\pi/2$), Eq. 2.29 can then be expressed as:

$$e_o(t) = \frac{E_i}{2}\left[\exp\left(-j\frac{\pi}{4}\right)\sin\left(\pi\frac{v_1(t)}{2V_\pi}\right) + \exp\left(j\frac{\pi}{4}\right)\sin\left(\pi\frac{v_2(t)}{2V_\pi}\right)\right]. \tag{2.30}$$

As shown in Eq. 2.30, the electrical-to-optical conversion performed by the DP-MZM is a nonlinear process, which becomes more nonlinear with the increase of the power of the electrical signals applied to the MZM arms. The modulation index is a parameter that enables to control the impact of the DP-MZM-induced nonlinearity caused by the electrical-to-optical conversion on the system performance. The modulation index (MI) is defined as:

$$\text{MI} = \frac{V_{RMS}}{V_\pi} \tag{2.31}$$

where V_{RMS} is the RMS voltage of the electrical signals applied to the MZM arms. For electrical signals with low modulation index, the electrical-to-optical conversion performed by the DP-MZM can be considered as a linear process. Using the first term of the Taylor's series expansion of Eq. 2.30 to linearise the DP-MZM, the optical field at the DP-MZM output can be approximated as:

$$e_o(t) \approx \frac{E_i}{2}\left\{\exp\left(-j\frac{\pi}{4}\right)\frac{\pi}{2V_\pi}v_1(t) + \exp\left(j\frac{\pi}{4}\right)\frac{\pi}{2V_\pi}v_2(t)\right\}. \tag{2.32}$$

2.3.3 OFDM signal demodulation

After MB-OFDM signal generation performed by the MB-OFDM Tx, the resulting signal is transmitted along an optical fibre link. After fibre transmission, the pair band-VC of interest is selected, converted to the electrical domain and demodulated at the OFDM signal demodulator. Fig. 2.6 shows the block diagram of the OFDM signal demodulator. The pair band-VC to be demodulated is selected by an optical filter. In this work, that filter is named band selector (BS). The non-ideal optical filters used for band selection are modelled by a SG-shape (see Eq. 2.8).

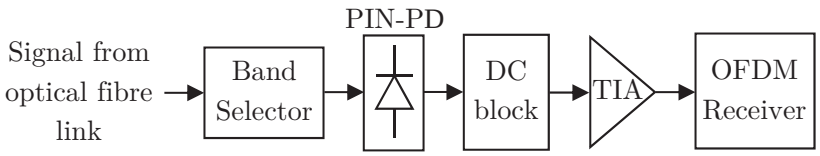

Figure 2.6: Block diagram of the OFDM signal demodulator. DC: direct-current, PIN-PD: p-type-intrinsic-n-type photodiode, TIA: trans-impedance amplifier.

Each pair band-VC is photodetected by a p-type-intrinsic-n-type (PIN)-photodiode (PD). To understand the photodetection operation, let us assume, for the sake of simplicity, that the DP-MZM output transmits one pair band-VC with low modulation index. This means that Eq. 2.32 can be employed to model the optical field at the DP-MZM output. Assuming that the PIN-PD has responsivity of 1 $\mathrm{A}\cdot\mathrm{W}^{-1}$ and is modelled by an ideal square-law operation, the photocurrent at the PIN-PD output, $i_{PIN}(t)$, can be expressed as:

$$i_{PIN}(t) = |e_o(t)|^2 = \left(\frac{E_i\pi}{4V_\pi}\right)^2\left[|v_1(t)|^2 + |v_2(t)|^2\right]. \tag{2.33}$$

Taking into account that $v_1(t) = A\cdot s_{v,n}(t) + B\cdot s_{b,n}(t)$ and $v_2(t) = A\cdot s_{v,n,H}(t) + B\cdot s_{b,n,H}(t)$, where A and B are constants and $s_{v,n,H}(t)$ and $s_{b,n,H}(t)$ are the HT of $s_{v,n}(t)$ and $s_{b,n}(t)$,

respectively, the photocurrent can be rewritten as:

$$i_{PIN}(t) = \left(\frac{E_i\pi}{4V_\pi}\right)^2 \cdot \Bigg[\underbrace{A^2|s_{v,n}(t)|^2 + A^2|s_{v,n,H}(t)|^2}_{\text{(a)}} + \\ + \underbrace{2AB\cdot\Re\{s_{b,n}(t)s^*_{v,n}(t)\} + 2AB\cdot\Re\{s_{b,n,H}(t)s^*_{v,n,H}(t)\}}_{\text{(b)}} + \underbrace{B^2|s_{b,n}(t)|^2 + B^2|s_{b,n,H}(t)|^2}_{\text{(c)}}\Bigg] \quad (2.34)$$

where $\Re\{\cdot\}$ denotes the real part and $\{\cdot\}^*$ stands for the conjugate operation. The terms represented by (a) correspond to the beating between the VCs [which include the direct-current (DC) components]. The terms in (b) represent the beating between the VCs and the OFDM signal and its HT, which are fundamental terms containing linear relation with the OFDM signal. The terms in (c) represent distortion components usually referred as signal-signal beat interference (SSBI). The SSBI produces an unwanted component close to the zero frequency with bandwidth B_w. Fig. 2.7 illustrates the spectrum after photodetection, considering two different VBGs: VBG = B_w and VBG < B_w. With VBG = B_w, the SSBI does not interfere with the OFDM signal. In this case, the VBG accommodates the distortion induced by the SSBI. With VBG < B_w, the SSBI interferes with the OFDM signal, causing performance degradation.

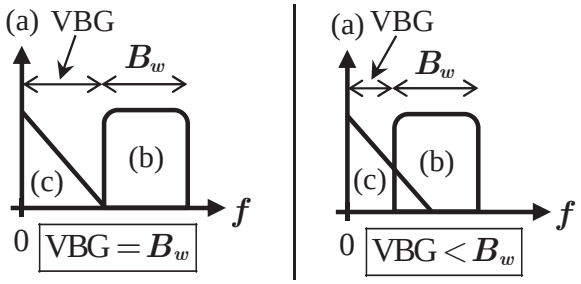

Figure 2.7: Illustration of the spectrum after photodetection with VBG = B_w and VBG < B_w. Components (a), (b) and (c) stand for the DC, OFDM signal and SSBI components, respectively (see Eq. 2.34).

After photodetection, the DC component generated by the photodetection operation is removed by a DC block, and electrical amplification is performed by a trans-impedance amplifier (TIA), which introduces electrical noise with a constant PSD. The electrical noise is mostly thermal noise. After electrical amplification, the received OFDM signal is demodulated by the OFDM receiver. The main blocks of the OFDM receiver are the complementary operations of the OFDM signal generator shown in Fig. 2.2.

Fig. 2.8 depicts the block diagram of the OFDM receiver. The signal at the DC block output is converted to digital by an analogue-to-digital converter (ADC) with oversampling factor of

4. The oversampling allows to sample adequately the photodetected signal. The digital signal is converted to parallel and the samples corresponding to the CP are removed. The frequency domain values of the subcarriers are recovered by applying the FFT. Samples corresponding to the zero-padding and the oversampling are discarded at the sample selection block. To compensate for the amplitude and phase distortions induced by the dispersive transmission channel and other system impairments, an one-tap equalizer is employed. The equalizer is characterized by a transfer function that estimates the inverse of the transmission channel transfer function from the information provided by the TSs. This transfer function is multiplied to the symbols at FFT output. After equalization, the signal performance is evaluated and SSBI estimation is performed in order to mitigate the SSBI components from the detected OFDM signal. SSBI estimation is performed by using an algorithm similar to the one presented in [68]. This algorithm uses the information provided by the TSs to estimate the transmitted OFDM signal and reconstruct the SSBI component to be subtracted to the received signal. Mitigating the SSBI enables reducing the VBPR and simultaneously employing a small VBG to achieve high spectral efficiency, at the expense of an increase on the computation effort. For a detailed description of the SSBI mitigation algorithm, see Appendix C. When the SSBI is adequately mitigated and the feedback loop is no longer required, that is, when the performance improvement provided by successive iterations of the SSBI mitigation algorithm is residual, the almost SSBI-free data symbols are demapped and the recovered bits are combined to form the original high bit-rate stream.

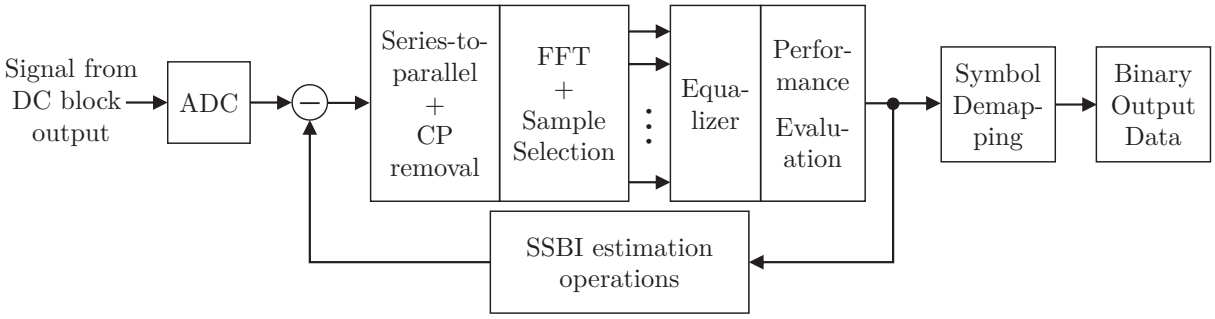

Figure 2.8: Block diagram of the OFDM receiver.

At the OFDM receiver, the signal performance is evaluated using two different figures of merit: the error vector magnitude (EVM) (see Appendix D) and the BER. In this work, the most used figure of merit to evaluate the performance of OFDM signals is the EVM. Nevertheless, the BER is employed in the theoretical study presented in section B.2 in two different ways: the BER is estimated from 1) the electrical signal-to-noise ratio (ESNR), which is the inverse of the EVM, and 2) from the exhaustive Gaussian approach (EGA). The EGA is explained and validated [by comparison with the BER obtained with direct error counting (DEC)] in Appendix E.

2.4 Integrated MB-OFDM metro-access network

The transmitter and receiver sides are connected by an integrated MB-OFDM metro-access network as transmission channel. Fig. 2.9 shows the block diagram of the integrated MB-OFDM metro-access network. This network is based on the MORFEUS network proposed in [9] and aims at delivering one OFDM band to each user of the access network.

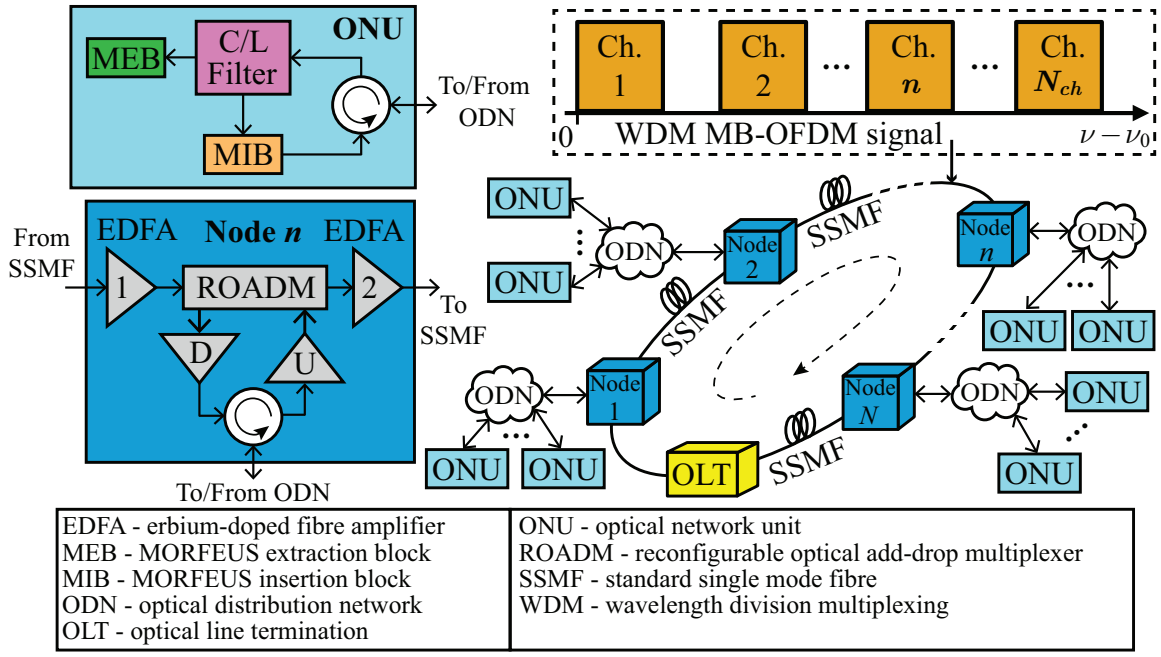

Figure 2.9: Block diagram of the metro-access network. ν is the optical frequency and ν_0 the reference optical frequency.

In the following chapters, only the downstream direction [wavelength division multiplexing (WDM)-MB-OFDM signal generated at the optical line termination (OLT) and a pair band-VC dropped at the optical network unit (ONU)] is considered. However, it is assumed that the downstream and upstream transmission can be accomplished using the C-band and L-band, respectively, and that the upstream also employs a VC-assisted DD MB-OFDM signal similar to the one used in the downstream with each pair band-VC dedicated to a single user [35].

The metro part of the network comprises a ring topology with N nodes interconnected by SSMF spans. The SSMF parameters at the wavelength of 1550 nm are given in Tab. 2.2. Propagation along the SSMF is modelled by the scalar generalized nonlinear Schrödinger equation (NLSE), which is numerically solved using the split-step Fourier method (SSFM) (for more details related to the SSMF parameters, the NLSE and the SSFM, see Appendix F). The OLT is responsible for the generation of the WDM-MB-OFDM signal to be launched into the metro ring. The WDM-MB-OFDM signal is composed by N_{ch} channels, with each channel carrying a carrier-

suppressed SSB-MB-OFDM signal with N_B pairs band-VC. This is accomplished at the OLT by multiplexing the signals of N_{ch} MB-OFDM Tx's. The allocation process of the pairs band-VC to the ONUs is also performed by the OLT, through the control plane of the network. This ensures that the allocation process follows a defined strategy. Each network node is composed by four erbium doped fibre amplifiers (EDFAs), a circulator and one reconfigurable optical add-drop multiplexer (ROADM). The ROADM is able to add and drop WDM channels and to perform power level equalization for all the wavelengths. EDFA 1 compensates for the losses of the preceding SSMF span and EDFA 2 adjusts the optical power level at the input of each span. EDFAs D and U compensate for the power unbalance of the downstream and the upstream paths, respectively.

Table 2.2: SSMF parameters at the wavelength of 1550 nm.

Dispersion parameter, D [ps·nm^{-1}·km^{-1}]	17
Dispersion slope, S [ps·nm^{-2}·km^{-1}]	0.09
Attenuation coefficient, α [dB · km^{-1}]	0.2
Nonlinearity coefficient, γ [W^{-1} · km^{-1}]	1.3

The optical distribution network (ODN) and the ONU comprise the access part of the network. At a given node, a single MB-OFDM signal or a set of MB-OFDM signals is extracted to the ODN. The ODN links the node to each ONU and is emulated by a single SSMF span plus an optical attenuator to account for the ODN splitting ratio. Each ONU is composed by three main blocks: the MORFEUS insertion block (MIB), the MORFEUS extraction block (MEB) and the C/L optical filter. In the communication process, each ONU uses one pair band-VC at the C-band for the downstream direction and one pair band-VC at the L-band for the upstream direction. The separation between the downstream signal coming from the ODN to the MEB and the upstream signal from the MIB to the ODN is accomplished by the C/L optical filter. In the downstream direction, the MEB is responsible for the dropping operation of a given pair band-VC from the MB-OFDM signals that arise at the each ONU. The dropping operation of the MEB is emulated by an OFDM signal demodulator (see Fig. 2.6). The MIB is responsible for generating another pair band-VC in an available slot to be transmitted in the upstream direction.

2.5 Conclusions

Along this chapter, the generation and demodulation of VC-assisted DD-MB-OFDM signals has been explained and the elements of the integrated metro-access network have been described.

The operations required to generate an OFDM signal have been shown and training symbols have been chosen to measure the transmission channel in order to ensure effective demodulation at the receiver side. The main parameters which characterize the OFDM signal have been explained and it has been shown that the overall bit rate depends considerably on the system overheads (due to FEC, TSs and CP) and on the number of OFDM subcarriers.

The analysis of VC-assisted MB-OFDM signals has shown that the frequency allocation of a MB-OFDM signal depends on a set of parameters and the most relevant are the VBG and BG. Regarding the power distribution inside each MB-OFDM signal, the VBPR has been defined (similar to the well-known carrier-to-signal power ratio).

It has been concluded that SSB transmission is preferable when compared with DSB transmission. Considering the generation of SSB-MB-OFDM signals, the DP-MZM together with the HT have been employed to avoid the use of an optical filter with high selectivity after electrical-to-optical conversion. Given that the considered SSB-MB-OFDM generation is not an ideal process, the modulation index has been defined to control the impact of the nonlinearity induced by the DP-MZM (caused by electrical-to-optical conversion) on the system performance. Considering the operations involving OFDM signal demodulation, it has been shown that SSBI poses an important limitation to the performance of the received OFDM signal, and requires mitigation.

Regarding the integrated metro-access network, the elements that compose that network have been described and it has been decided that only the downstream direction will be considered in the analysis performed in the following chapters. This decision is based on the assumption that the upstream transmission employs a signal structure similar to the one employed in the downstream transmission.

Chapter 3

VC-assisted DD-MB-OFDM systems in back-to-back operation

3.1 Introduction

The direct-detection (DD) multi-band (MB)-orthogonal frequency-division multiplexing (OFDM) system performance in back-to-back operation (that is, without optical fibre transmission) is assessed in this chapter. The analysis is performed through numerical simulation with different number of subcarriers, different band selector (BS) shapes, considering different wavelength division multiplexing (WDM) channel spacings and the bandwidth-narrowing effect caused by successive filtering of the wavelength selective switches (WSSs).

This chapter is structured as follows. In section 3.2, the MB-OFDM system in optical back-to-back operation is described and the characteristics of the bandwidth-limited components, namely, the WSS, BS and hybrid coupler (HC), are presented. In section 3.3, the main system parameters which rule the design of MB-OFDM signals are presented. In section 3.4, the performance analysis of the MB-OFDM system in back-to-back operation is accomplished, considering different system parameters. In section 3.5, the main conclusions are summarized.

The work published in [63] is a preliminary study of the analysis presented in this chapter.

3.2 System description

The DD-MB-OFDM system in back-to-back operation is shown in Fig. 3.1 and is based on the network presented in section 2.4. The system of Fig. 3.1 can be seen as a simplified metropolitan (metro) network without fibre transmission. The following simplifications are made: 1) each network node is represented by a lossless reconfigurable optical add-drop multiplexer (ROADM); 2) a single noiseless erbium doped fibre amplifier (EDFA) is employed to set the optical power after the ROADM cascade; 3) the optical distribution network (ODN) losses are emulated by a variable optical attenuator (VOA); 3) optical fibre transmission between nodes is not considered; and 4) transmission of one WDM channel is employed. Although several WDM channels are transmitted in the network, it is assumed that similar performance is experienced among different WDM channels in back-to-back operation. Thus, the analysis can be focused on a single WDM channel, comprising one MB-OFDM signal. In the optical channel, the lossless ROADM cascade represents the non-ideal filtering impairment occurred when selecting the MB-OFDM signal in a sequence of ROADMs. The optical network unit (ONU) is responsible for selecting and demodulating a certain band of the MB-OFDM signal and evaluate its performance. In the MB-OFDM transmitter (Tx), the Hilbert transform (HT) is generated in two different ways: 1) using an ideal HT and 2) using an HC that performs an HT approximation. The electrical noise introduced by the trans-impedance amplifier (TIA) is thermal noise with power spectral density (PSD) of 1 $(\text{pA})^2 \cdot \text{Hz}^{-1}$ [49].

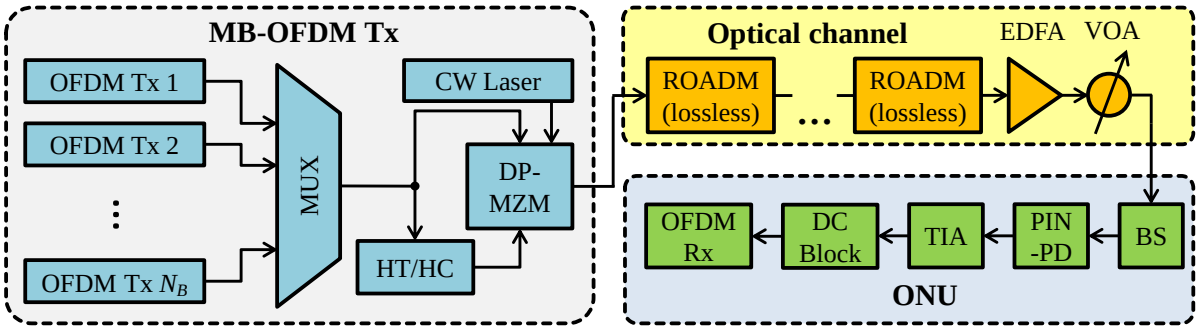

Figure 3.1: DD-MB-OFDM system in back-to-back operation considered in this chapter.

3.2.1 Wavelength selective switches

The key component of the ROADM is the WSS. The use of several WSS-based ROADMs in the metro ring causes passband narrowing due to successive filtering [77]. This passband narrowing implies increased system performance penalty as the number of ROADMs (or nodes) in the

metro ring rises. To accommodate this narrowing effect, not all the passband of a single WSS is used for the MB-OFDM signal. A ROADM with the multiplexing function performed by a WSS and the demultiplexing function performed by a 1×2 passive splitter plus a WSS is considered [78]. In the demultiplexing function, it is preferable to use a passive splitter and a WSS rather than 2 WSSs in order to avoid two filtering actions: 1) when the WDM channel is added to the network, it is filtered only once by the WSS performing the multiplexing function; 2) when the WDM channel passes through a ROADM in the metro ring, it is filtered again only once by the WSS performing the multiplexing function; 3) when the WDM channel is dropped, it passes once through the WSS that performs the demultiplexing function. In this way, the number of passed-through WSSs correspond to the same number of passed-through ROADMs.

The WSS model used in this work is based on the amplitude response presented in [79], which considers that the WSS amplitude response, $S_{\mathrm{WSS}}(f)$, can be expressed as:

$$S_{\mathrm{WSS}}(f) = \frac{1}{2}\sigma\sqrt{2\pi}\left[\mathrm{erf}\left(\frac{\frac{B_{\mathrm{WDM}}}{2} - f}{\sqrt{2}\sigma}\right) - \mathrm{erf}\left(\frac{-\frac{B_{\mathrm{WDM}}}{2} - f}{\sqrt{2}\sigma}\right)\right] \tag{3.1}$$

where B_{WDM} is the WDM channel spacing, $\mathrm{erf}(\cdot)$ is the error function and σ is given by:

$$\sigma = \frac{B_{\mathrm{OTF}}}{2\sqrt{2\log_e(2)}} \tag{3.2}$$

where B_{OTF} is a WSS parameter, corresponding to its optical transfer function (OTF) bandwidth. The OTF bandwidth is a metric which represents how the light beam at the WSS input is focused onto the WSS aperture plane [79]. In this work, three different WDM channel spacings are considered: 12.5, 25 and 50 GHz. In [79], two devices with different OTF bandwidths were considered for a WDM channel spacing of 50 GHz: $B_{\mathrm{OTF}} = 10.4$ GHz and $B_{\mathrm{OTF}} = 11.1$ GHz. In this analysis, $B_{\mathrm{OTF}} = 10.4$ GHz is used as a WSS with less OTF bandwidth presents higher selectivity and less impact due to bandwidth narrowing. In this case, $B_{\mathrm{WDM}}/B_{\mathrm{OTF}} \approx 4.8$. To maintain the same WSS selectivity for $B_{\mathrm{WDM}} = 12.5$ GHz and $B_{\mathrm{WDM}} = 25$ GHz, the ratio $B_{\mathrm{WDM}}/B_{\mathrm{OTF}}$ is kept constant.

Fig. 3.2 depicts the amplitude responses of the WSSs with $B_{\mathrm{WDM}} \in \{12.5, 25, 50\}$ GHz. B_{WDM} is equal to the -6 dB bandwidth of the WSSs. Inspection of Fig. 3.2 shows that all the considered WSSs have high selectivity. The selectivity of an optical filter, S_f, is defined as:

$$S_f = \frac{B_{-3\,\mathrm{dB}}}{B_{-20\,\mathrm{dB}}} \tag{3.3}$$

where $B_{-3\,\mathrm{dB}}$ and $B_{-20\,\mathrm{dB}}$ are the -3 dB bandwidth and -20 dB bandwidth of the filter,

respectively. The 12.5, 25 and 50 GHz WSSs have a selectivity of approximately 0.736, and a −3 dB bandwidth of 11.3, 22.6 and 45.2 GHz, respectively.

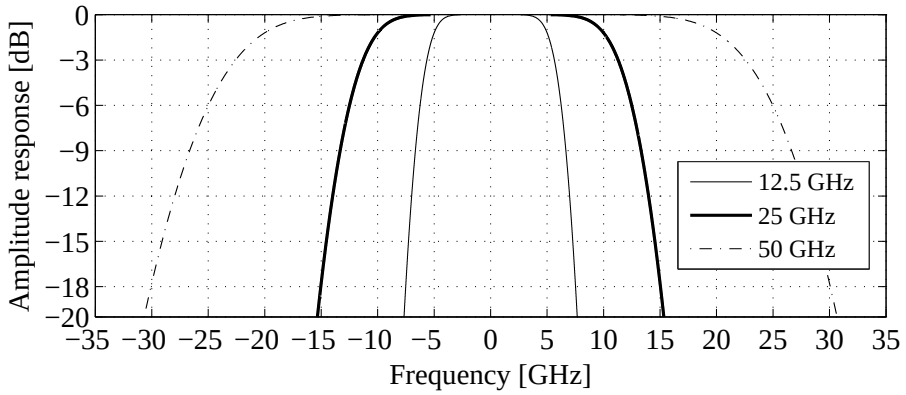

Figure 3.2: Amplitude response of the WSS with $B_{\mathrm{WDM}} \in \{12.5, 25, 50\}$ GHz.

As the number of concatenated WSSs increases, the equivalent WSS transfer function after concatenation presents smaller bandwidth and higher selectivity. Fig. 3.3 illustrates the ratio between the equivalent −3 dB bandwidth of the WSS after WSS concatenation, $B_{-3\,\mathrm{dB,WSS,c}}$, and the −3 dB bandwidth of one WSS, $B_{-3\,\mathrm{dB,WSS}}$, as well as the selectivity of the equivalent WSS, both as a function of the number of concatenated WSSs. By assuming that the minimum acceptable number of WSSs passed through in the metro ring is around 10, Fig. 3.3 shows that the corresponding reduction of the equivalent WSS bandwidth after concatenation is 25%. This indicates that a minimum of 25% of the −3 dB bandwidth of one WSS has to be considered unused to accommodate the WSS concatenation effect without performance penalty. In this way, to ensure a good margin for WSS concatenations, a 30% reduction of the −3 dB bandwidth of one WSS is accounted to accommodate the bandwidth narrowing of concatenating several WSSs. Thus, the maximum bandwidth of the MB-OFDM signal to be transported in a WDM channel corresponds to 70% of the −3 dB bandwidth of one WSS. 70% of the −3 dB bandwidth of one WSS corresponds to 7.9, 15.8, and 31.6 GHz for WDM channel bandwidths of 12.5, 25 and 50 GHz. Hence, the maximum number of bands transported in WDM channels with B_{WDM} of 12.5, 25 and 50 GHz, assuming a 3.125 GHz slot per pair band-virtual carrier (VC), is 2, 5 and 10, respectively.

3.2.2 Ideal and non-ideal architectures

In this chapter, two different architectures of the MB-OFDM system are considered: an ideal architecture and a non-ideal architecture. Both architectures employ the dual-parallel (DP)-Mach-Zehnder modulator (MZM) as electro-optic converter and a p-type-intrinsic-n-type (PIN)-

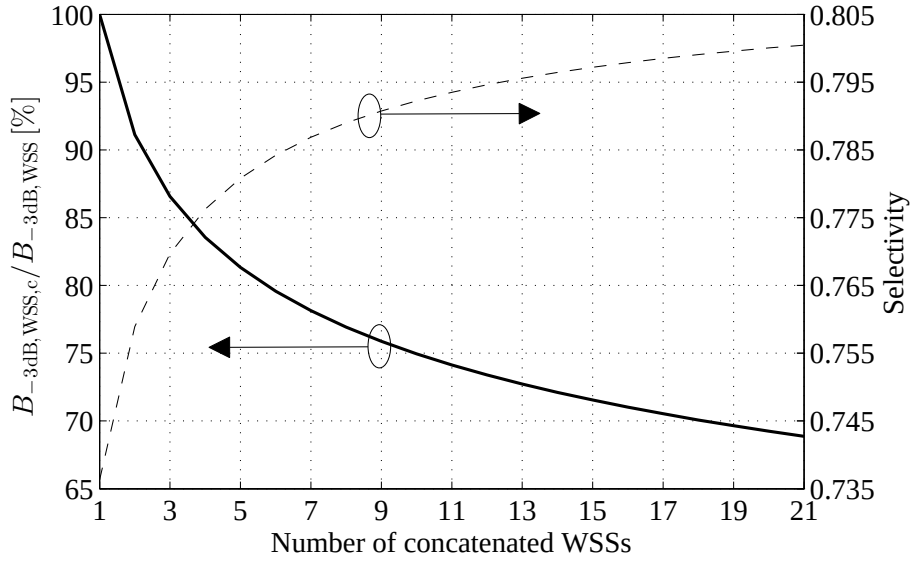

Figure 3.3: -3 dB bandwidth reduction of the concatenated WSS (with respect to the -3 dB bandwidth of one WSS) and the corresponding selectivity, both as a function of the number of concatenated WSSs.

photodiode (PD) (modelled by an ideal square-law operation) as photodetector. The ideal architecture provides the best results as frequency limitations due to BS and HC are not considered. The ideal architecture considers the DP-MZM where one arm has the MB-OFDM signal and the other arm the ideal HT of that MB-OFDM signal. Moreover, the BS at the receiver and other filters are all ideal rectangular transfer function-shaped filters. The non-ideal architecture includes the frequency limitations of the BS and HC. Two different shapes for the BSs are considered: super-Gaussian (SG) filter with $n = 1$ [first-order SG filter hereafter referred as Gaussian (G)-BS] and SG filter with $n = 2$ (second-order SG filter hereafter referred as SG-BS). The amplitude response of a n-th order SG-shape filter is expressed in Eq. 2.8. Fig. 3.4 shows the amplitude response of the G-BS and SG-BS, with $B_{-3\,\mathrm{dB}} = 2$ GHz and $f_c = 5$ GHz, as an example. In terms of selectivity, the SG-BS has a selectivity of 0.62 and the G-BS a selectivity of 0.39. With the non-ideal architecture, one arm of the DP-MZM is driven by the MB-OFDM signal and the other arm by the HT approximation of that MB-OFDM signal, provided by the HC. The HC allows to assess the impairments of non-ideal single sideband (SSB) signal generation. Two different HCs (HC1 and HC2) are considered in the non-ideal architecture. Their amplitude and phase responses were experimentally characterized. Fig. 3.5 shows the amplitude and phase responses of the two different HCs. HC1 has a -6 dB bandwidth of 18.5 GHz and HC2 a -6 dB bandwidth of 35 GHz, and both have a phase response, in the passband, with a phase fluctuation of ± 10 degrees around 90 degrees. Due to the frequency response of the HCs, HC1 can accommodate a maximum of 5 bands, and HC2 a maximum of 10 bands. In this way, for the WDM channels considered in this work, HC1 is used to generate the SSB-MB-OFDM

signal for systems with WDM channel spacings of 12.5 GHz and 25 GHz, and HC2 is employed to generate the SSB-MB-OFDM signal for a channel spacing of 50 GHz.

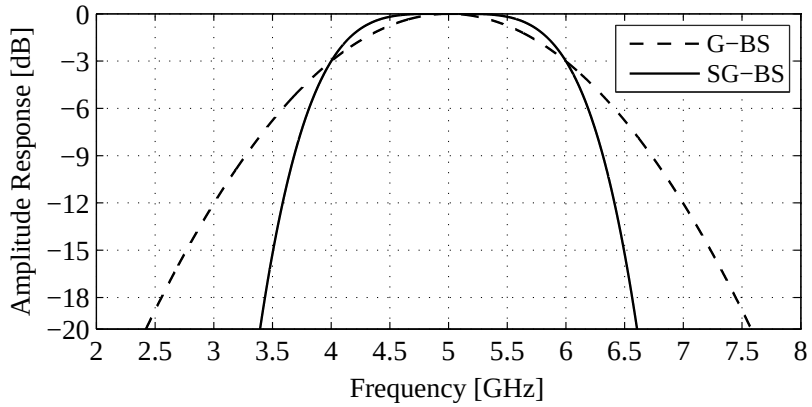

Figure 3.4: Amplitude response of the G-BS and SG-BS, both with a −3 dB bandwidth of 2 GHz and a central frequency of 5 GHz.

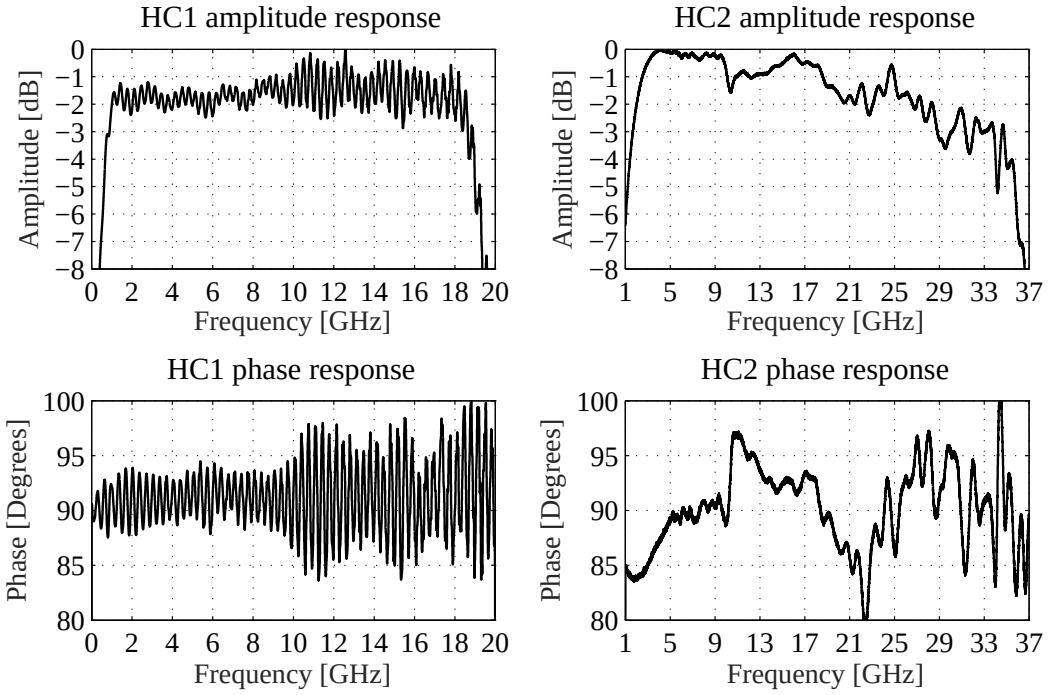

Figure 3.5: Amplitude and phase responses of the two different HCs (HC1 and HC2).

3.3 System parameters

All WDM channels fulfil two main requirements: each OFDM signal (or band) within each WDM channel transports a 10 Gb/s information data rate and a frequency slot of 3.125 GHz is reserved for each band.

In the considered MB-OFDM system, the most relevant frequency allocation parameters are the

virtual carrier-to-band gap (VBG), the band gap (BG), and the central frequency of the first OFDM band ($f_{b,1}$). Fig. 2.4 illustrates the SSB MB-OFDM signal spectrum with N_B pairs band-VC. To ensure a reduced receiver bandwidth after photodetection, the VBG must be negligible when compared with the OFDM signal bandwidth. To avoid significant crosstalk caused by non-ideal BS filtering, the BG needs to be optimized. To prevent significant degradation from the amplitude response of the HCs in lower frequencies, the central frequency of the first OFDM band needs to be adjusted. In this chapter, the frequency disposition of each pair composed by a band and a VC is with the VC at a higher frequency than the OFDM band (as shown in Fig. 2.4).

In this chapter, the VBG is set to be less than 100 MHz (in order to be negligible when compared with the OFDM signal bandwidth) and proportional to the subcarrier frequency spacing $1/t_s$. Following the aforementioned conditions, the VBG is given by twice the subcarrier frequency spacing and can be written as:

$$\text{VBG} = \frac{2}{t_s}. \tag{3.4}$$

If R_b and Δf_b are maintained, the BG depends exclusively of the quadrature amplitude modulation (QAM) order M. Increasing M implies that B_w decreases and BG increases. Hence, increasing M can be considered as an advantage when selecting a OFDM band with a non-ideal BSs, as crosstalk between bands could become insignificant due to the higher frequency gap between consecutive bands. However, the drawback of increasing M is that the required signal-to-noise ratio (SNR) for the OFDM subcarriers to achieve a fixed performance level (for instance, bit error ratio (BER) = 10^{-3}) also increases.

Considering $M < 16$ would lead to negative BG, thus, to undesirable frequency overlapping between consecutive bands. With $M \geq 16$, a positive BG is obtained, thus, it is possible to select individually a pair band-VC. When the BS is an ideal rectangular transfer function-shaped filter, which has a selectivity equal to one, a pair band-VC can always be correctly selected as long as the BG is positive. However, with the use of non-ideal BSs, which do not have a selectivity equal to one, the positive BG condition is not enough, as crosstalk from adjacent bands may occur causing performance degradation. To avoid significant crosstalk after photodetection, the BS must ensure that the neighbouring pairs have been sufficiently filtered. In this way, in order to have a crosstalk level after photodetection not affecting significantly the performance, the BS must induce at least a power attenuation to the neighbouring pairs of 20 dB.

Let us assume that the BS is filtering the pair band-VC n, surrounded by the neighbouring

pairs $n-1$ and $n+1$. The BS parameters are the -3 dB BS bandwidth, $B_{-3\,\mathrm{dB,BS}}$, and the BS central frequency, $\nu_{\mathrm{BS},n}$, which has a low-pass equivalent (LPE) central frequency given by $f_{\mathrm{BS},n} = \nu_{\mathrm{BS},n} - \nu_0$, where ν_0 is the reference optical frequency. The BS parameters can be expressed as:

$$\begin{cases} f_{\mathrm{BS},n} = \dfrac{1}{2} \times \left(f_{v,n} + f_{b,n} - \dfrac{B_w}{2} \right) + f_d \\ B_{-3\,\mathrm{dB,BS}} = B_w + \mathrm{VBG} + B_d \end{cases} \tag{3.5}$$

where $f_{v,n}$ is the frequency of VC n, $f_{b,n}$ is the central frequency of OFDM band n, f_d is the BS parameter for frequency detuning, and B_d is the BS parameter for bandwidth increment/shrinkage. With $f_d = 0$, the BS is centred at the middle of the pair band-VC n; with $B_d = 0$, the -3 dB BS bandwidth is equal to the OFDM signal bandwidth plus the VBG. To avoid significant crosstalk, a minimum attenuation of 20 dB in the $(n-1)$-th VC and in the $(n+1)$-th OFDM band has to be guaranteed. These conditions can be expressed as:

$$\begin{cases} \dfrac{B_{-20\,\mathrm{dB,BS}}}{2} \leq f_{\mathrm{BS},n} - f_{v,n-1} \\ \dfrac{B_{-20\,\mathrm{dB,BS}}}{2} \leq (f_{v,n+1} - B_w - \mathrm{VBG}) - f_{\mathrm{BS},n} \end{cases} \tag{3.6}$$

where $B_{-20\,\mathrm{dB,BS}}$ is the -20 dB BS bandwidth, $f_{v,n-1}$ is the frequency of the $(n-1)$-th VC and $f_{v,n+1}$ the frequency of the $(n+1)$-th VC. After some calculations, Eq. 3.6 is equivalent to:

$$\begin{cases} B_{-20\,\mathrm{dB,BS}} \leq 2\Delta f_b - B_w - \mathrm{VBG} + 2f_d \\ B_{-20\,\mathrm{dB,BS}} \leq 2\Delta f_b - B_w - \mathrm{VBG} - 2f_d. \end{cases} \tag{3.7}$$

With $f_d < 0$, the first condition is more restrictive, whereas with $f_d > 0$, the second condition becomes the most restrictive. In order to avoid filtering considerably the n-th VC, positive f_d values are preferred. With positive f_d values, the following condition has to be verified:

$$B_{-20\,\mathrm{dB,BS}} \leq 2\Delta f_b - B_w - \mathrm{VBG} - 2f_d. \tag{3.8}$$

Taking into account that $S_{f,\mathrm{BS}} = B_{-3\,\mathrm{dB,BS}}/B_{-20\,\mathrm{dB,BS}}$ and that $B_{-3\,\mathrm{dB,BS}} = B_w + \mathrm{VBG} + B_d$, Eq. 3.8 can be rewritten as:

$$B_{-3\,\mathrm{dB,BS}} \leq \left(\frac{S_{f,\mathrm{BS}}}{1 + S_{f,\mathrm{BS}}} \right) (2\Delta f_b + B_d - 2f_d) \tag{3.9}$$

and also as:

$$B_w \leq 2 \left(\frac{S_{f,\mathrm{BS}}}{1 + S_{f,\mathrm{BS}}} \right) (\Delta f_b - f_d) - \mathrm{VBG} - \left(\frac{1}{1 + S_{f,\mathrm{BS}}} \right) B_d. \tag{3.10}$$

From Eq. 3.9 and assuming for simplicity that $f_d = 0$ and $B_d = 0$, the -3 dB bandwidth of the G-BS (with $S_{f,\mathrm{BS}} = 0.39$) and the SG-BS (with $S_{f,\mathrm{BS}} = 0.62$) should not exceed 1.75 GHz and 2.39 GHz, respectively. These values limit the minimum QAM orders that can be employed with the G-BS and the SG-BS to avoid high crosstalk interference: $M = 128$ for the G-BS and $M = 32$ for the SG-BS. Tab. 3.1 shows the compromise between VBG, B_w and BG when $N_{sc} \in \{64, 128, 256\}$ and $M \in \{32, 128\}$. For the sake of illustration, Fig. 3.6 shows the LPE of the MB-OFDM signal spectrum with pairs band-VC $n-1$, n and $n+1$ and main parameters, together with a non-ideal BS filtering the pair band-VC n.

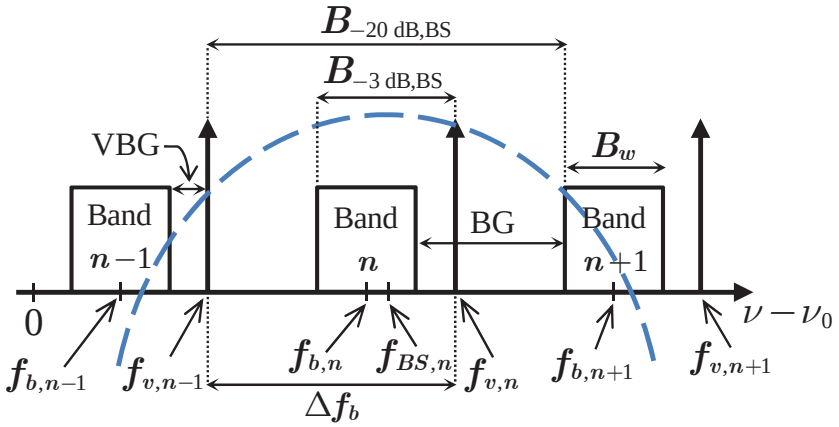

Figure 3.6: Illustration of the LPE of the MB-OFDM signal spectrum with pairs band-VC $n-1$, n and $n+1$ and main parameters, together with a non-ideal BS filtering the pair band-VC n. For simplicity, $B_d = 0$ MHz and $f_d = 0$ MHz are employed. ν is the optical frequency and $\nu - \nu_0$ stands for the LPE frequency.

Table 3.1: VBG, B_w and BG as a function of $N_{sc} \in \{64, 128, 256\}$ and $M \in \{32, 128\}$.

	N_{sc}	R_b [Gb/s]	B_w [GHz]	VBG [MHz]	BG [GHz]
$M = 32$	64	10.98	2.196	68.6	0.929
	128	10.89	2.178	34.0	0.947
	256	10.85	2.170	17.0	0.955
	N_{sc}	R_b [Gb/s]	B_w [GHz]	VBG [MHz]	BG [GHz]
$M = 128$	64	10.98	1.569	49.0	1.556
	128	10.89	1.556	24.3	1.569
	256	10.85	1.550	12.1	1.575

So far, a crosstalk level after photodetection of at least 20 dB has been considered. However, in order to guarantee that the crosstalk from neighbouring pairs do not interfere with the n-th band at all after photodetection, the following condition has to be ensured:

$$\mathrm{BG} \geq B_w + 2 \times \mathrm{VBG}. \tag{3.11}$$

This guarantees that the beating between the n-th VC and the $(n+1)$-th band and the beating between the $(n-1)$-th VC and the n-th band are out-of-band.

To avoid significant degradation due to the HC amplitude responses, the MB-OFDM signal spectrum has to be confined within the HCs passband and closest as possible to the lower frequencies to avoid stronger degradation at higher frequencies. Through inspection of Fig. 3.5, the −6 dB bandwidth of HC1 is $B_{-6\,\mathrm{dB,HC1}} = [0.6, 19.3]$ GHz and the −6 dB bandwidth of HC2 is $B_{-6\,\mathrm{dB,HC2}} = [1.1, 35.9]$ GHz. The MB-OFDM signal lowest frequency $f_{\min}$ and highest frequency $f_{\max}$ are given by:

$$\begin{cases} f_{\min} = f_{b,1} - \dfrac{B_w}{2} \\ f_{\max} = f_{b,1} + (N_B - 1)\,\Delta f_b + \mathrm{VBG} + \dfrac{B_w}{2}. \end{cases} \tag{3.12}$$

Considering $M = 32$ and $N_{sc} = 64$ (the most limiting case where B_w and VBG are the highest in this analysis), $B_w \approx 2.2$ GHz and VBG ≈ 68.6 MHz are obtained. The MB-OFDM signal is confined within the HCs passband if $f_{\min} \geq 0.6$ GHz when employing HC1, and if $f_{\min} \geq 1.1$ GHz when employing HC2. In this chapter, $f_{b,1} = 1.9$ GHz and $f_{b,1} = 2.5$ GHz are chosen for HT generation with HC1 and HC2, respectively. These central frequencies for the first OFDM band ensure that the MB-OFDM signal is confined within the HCs passband.

3.4 Performance analysis in back-to-back operation

The performance analysis in back-to-back operation requires the adjustment of several parameters of the MB-OFDM system, namely the virtual carrier-to-band power ratio (VBPR), the modulation index (MI), and the BS parameters B_d and f_d. The performance is assessed through numerical simulation considering thermal noise introduced by the TIA, fixed QAM order for all the subcarriers and WDM channel spacings of 12.5, 25 and 50 GHz. In the numerical results, a sequence of 100 training symbols is considered to estimate the equalizer transfer function and to mitigate the signal-signal beat interference (SSBI) component with the digital signal processing (DSP)-based SSBI mitigation algorithm. Moreover, a sequence of 100 information symbols is considered to evaluate the performance of the MB-OFDM signal. The average error vector magnitude (EVM) that corresponds to an average BER of 10^{-3}, with additive white Gaussian noise (AWGN) dominance, referred in this chapter as the maximum EVM, is considered as figure of merit for performance evaluation (the average EVM, for different QAM orders, can be seen in Tab. D.1). This average BER accommodates a small margin from the maximum tolerable pre-forward error correction (FEC) BER of 3.8×10^{-3}. With the maximum EVMs, the maximum link loss (MLL) of the MB-OFDM system (emulated in Fig. 3.1 by the VOA) can be obtained

from the average power at the EDFA output, $P_{out,\text{EDFA}}$, and the average power at the ONU input, $P_{in,\text{ONU}}$. By setting $P_{out,\text{EDFA}} = 0$ dBm (ensures that when employing fibre transmission, the nonlinear fibre effects are not dominant [62]), the MLL (in dB) is given by:

$$\text{MLL} = P_{out,\text{EDFA}} - P_{in,\text{ONU}} = -P_{in,\text{ONU}}. \tag{3.13}$$

For MLL evaluation, two different studies are performed. First, the influence of the number of subcarriers of the MB-OFDM signal on the MLL is analysed. Second, the influence of different channel spacings on the performance of the MB-OFDM signal is evaluated.

3.4.1 Number of OFDM subcarriers

In order to identify the compromises between the number of subcarriers of the MB-OFDM signal and its impact on the MLL, two relevant MB-OFDM system parameters, besides of the number of subcarriers, require optimization: the MI and the VBPR. The MI controls the nonlinear DP-MZM operation regime and is defined as the ratio between the root-mean-square (RMS) voltage of the MB-OFDM signal at the DP-MZM input and the voltage required to switch between the maximum and the minimum of the MZM power transmission characteristic. The VBPR balances the power attributed to the pair band-VC, and the power of the SSBI component.

To analyse the subcarriers influence, the MLL is obtained for $N_{sc} \in \{64, 128, 256\}$, considering a MB-OFDM signal with 3 bands. With $N_B = 3$, all different types of inter-band crosstalk due to non-ideal filtering are present: 1) the first-band is mainly limited by the crosstalk caused by the beating between the first-band VC and the residual part of the second-band; 2) the second-band by the beating between the first-band VC and the second-band together with the beating between the second-band VC and the residual part of the third-band; and 3) the third-band by the beating between the second-band VC and the third-band. This indicates that the second-band is the most limited by inter-band crosstalk as it receives the influence of two different crosstalk components. The difference when considering 2 bands is that each band is only limited by one crosstalk component. Three different BSs are considered: ideal (rectangular-shaped) BS, G-BS, and SG-BS. For the non-ideal BSs (G-BS and SG-BS), the minimum acceptable QAM order is employed, that is, $M = 128$ for the G-BS and $M = 32$ for the SG-BS. For the ideal BS, $M = 32$ and $M = 128$ are also employed as a term of comparison.

Tab. 3.2 shows the MLL and the optimum VBPR using an ideal BS, with $M \in \{32, 128\}$. Fig. 3.7 shows the EVMs, using an ideal BS, as a function of the MI and VBPR, for the 3 bands, with

$N_{sc} \in \{64, 128, 256\}$ and with $M \in \{32, 128\}$, for the MLLs of Tab. 3.2. Fig. 3.7 shows that the optimum region does not present an optimum MI. Instead, it consists of a wide region defined by MIs between 1% and 10%, approximately. Therefore, a MI of 5% is employed to ensure the results obtained are within the optimum MI range. The maximum MI, which is the MI that reaches the maximum EVM for the optimum VBPR, indicates that the DP-MZM nonlinearity is no longer irrelevant, degrading the performance. On the other hand, the good EVM results obtained with small MIs are due to the following: 1) a small MI guarantees that the degradation induced by the DP-MZM nonlinearity is negligible, and 2) with small MIs, the signal power after photodetection is still higher than the considered TIA thermal noise power. Tab. 3.2 shows that the influence of the number of subcarriers on the MLL, when using the ideal BS, is insignificant. Inspection of Tab. 3.2 also reveals that the MLL decrease and the optimum VBPR increase as M increases. The MLL decrease with increasing M is a direct consequence of the decrease of the maximum EVM. The optimum VBPR is set by the SSBI mitigation algorithm limitations and the receiver's noise: for VBPRs below the optimum VBPRs presented in Tab. 3.2, the SSBI distortion level is considerably high and the algorithm is not capable to reconstruct and remove completely the SSBI from the original signal; for VBPRs higher than the optimum VBPRs, the system performance is dominantly affected by the receiver's noise. The optimum VBPR increases when increasing M because, the minimum acceptable SNR to achieve the same BER level as increased.

Table 3.2: MLL and optimum VBPR with $N_{sc} \in \{64, 128, 256\}$ and $M \in \{32, 128\}$, using an ideal BS.

	N_{sc}	MLL [dB]	Opt. VBPR [dB]
Ideal BS $N_B = 3$ $M = 32$	64	29	6.5
	128	29	6.5
	256	29	6.0
	N_{sc}	MLL [dB]	Opt. VBPR [dB]
Ideal BS $N_B = 3$ $M = 128$	64	25	8.5
	128	25	8.5
	256	25	8.5

When using non-ideal BSs, the performance of the MB-OFDM system is remarkably influenced by the BS selectivity, which is often a fixed parameter. Besides the BS selectivity, other BS parameters, as the BS central frequency and BS -3 dB bandwidth, influence the performance of the MB-OFDM system. These parameters must be suitably adjusted in order to optimize the system performance. They are chosen to allow selecting the desired OFDM band without imposing high attenuation on the edges of the spectrum of the extracted signal and, simultaneously, to avoid high levels of distortion from adjacent bands after photodetection. The BS optimization process consists on finding the BS -3 dB bandwidth and central frequency that lead to the best

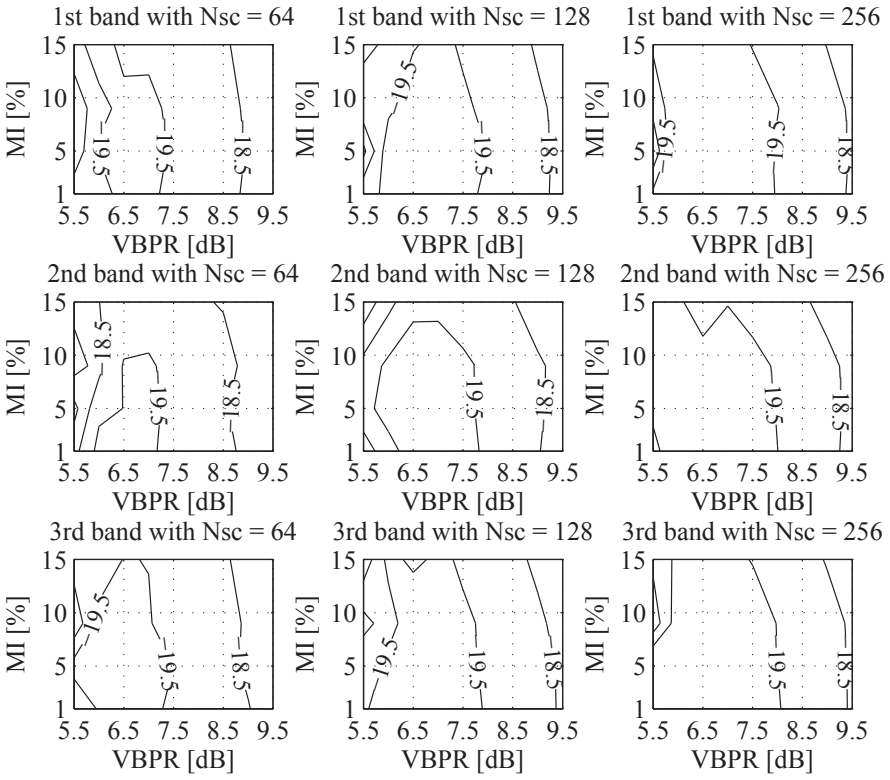

(a)

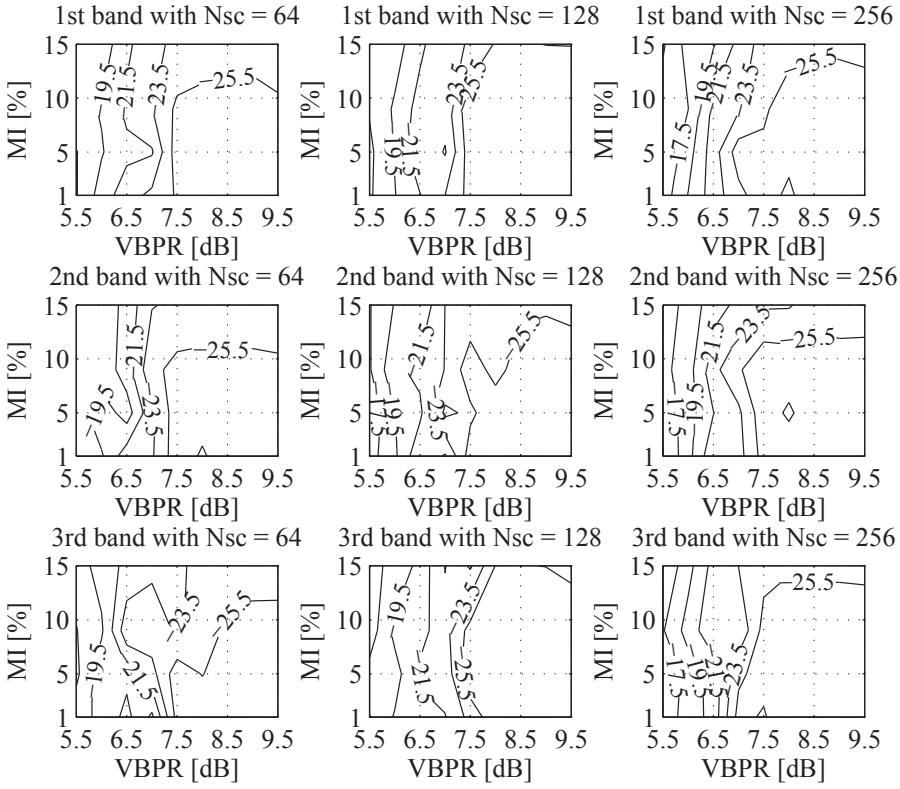

(b)

Figure 3.7: EVMs, using an ideal BS, as a function of the MI and VBPR, for the 3 bands, with $N_{sc} \in \{64, 128, 256\}$ and with (a) $M = 32$ and MLL = 29 dB, and (b) $M = 128$ and MLL = 25 dB.

performance, which is fulfilled through the adjustment of B_d and f_d (see Eq. 3.5).

To obtain the optimum region for the BS -3 dB bandwidth and central frequency, the MI and VBPR are fixed for the two different non-ideal BSs considered in this chapter. The optimum region is defined by the optimum point and the surrounding detuning frequencies f_d and B_d that induce an EVM degradation not exceeding 1 dB from the optimum point. Tab. 3.3 shows the optimum f_d and B_d ranges for the G-BS and SG-BS. For the SG-BS, a MLL = 27 dB is employed, along with MI = 5%, $M = 32$ and VBPR = 8 dB. For the G-BS, a MLL = 20 dB is considered, together with MI = 5%, $M = 128$ and VBPR = 10 dB. A MB-OFDM signal with 3 bands is considered, as well as $N_{sc} \in \{64, 128, 256\}$. The results of Tab. 3.3 are for the second-band, which is the band that imposes more restricted f_d and B_d ranges, as it is the most limited by inter-band crosstalk. Fig. 3.8 shows the EVMs as a function of B_d and f_d for the SG-BS with $M = 32$, and the G-BS with $M = 128$, for the 3 bands and with $N_{sc} \in \{64, 128, 256\}$, with the same MLLs and VBPRs of Tab. 3.3.

Table 3.3: Optimum f_d and B_d ranges for the G-BS and SG-BS, with $N_{sc} \in \{64, 128, 256\}$, MI = 5% and $N_B = 3$.

SG-BS	N_{sc}	f_d [MHz]	B_d [MHz]
$M = 32$	64	$[100, 300]$	$[0, 300]$
MLL = 27 dB	128	$[100, 300]$	$[0, 300]$
VBPR = 8 dB	256	$[50, 300]$	$[0, 300]$
G-BS	N_{sc}	f_d [MHz]	B_d [MHz]
$M = 128$	64	$[50, 200]$	$[-150, 100]$
MLL = 20 dB	128	$[50, 200]$	$[-100, 200]$
VBPR = 10 dB	256	$[100, 300]$	$[-100, 300]$

Tab. 3.3 shows that, for the SG-BS, the optimum B_d and f_d ranges are similar and positive. The reason for the positive f_d range is because the VC is less filtered, when compared with the initial situation that considers $f_d = 0$ MHz. Thus, more power is given to the signal after photodetection, improving the performance. The positive B_d range indicates that the BS has margin to accommodate more crosstalk. For the G-BS, the positive f_d ranges are also because the VC is less filtered, however, negative B_d ranges are shown, especially for the case with $N_{sc} = 64$. The reason for the negative B_d values within the optimum region (a negative B_d means that the BS -3 dB bandwidth is smaller than B_w plus VBG) is due to inter-band crosstalk. When selecting the second-band, as Eq. 3.11 is not verified, inter-band crosstalk exists. Due to the good selectivity of the SG-BS, a considerable attenuation is induced to the VC of the first-band, and the beating between the first-band VC and the second-band produces reduced crosstalk, that is, does not affect significantly the performance of the second-band. For the G-BS, the attenuation induced to the first-band VC is insufficient, and when Eq. 3.11 is not verified, which is the case for

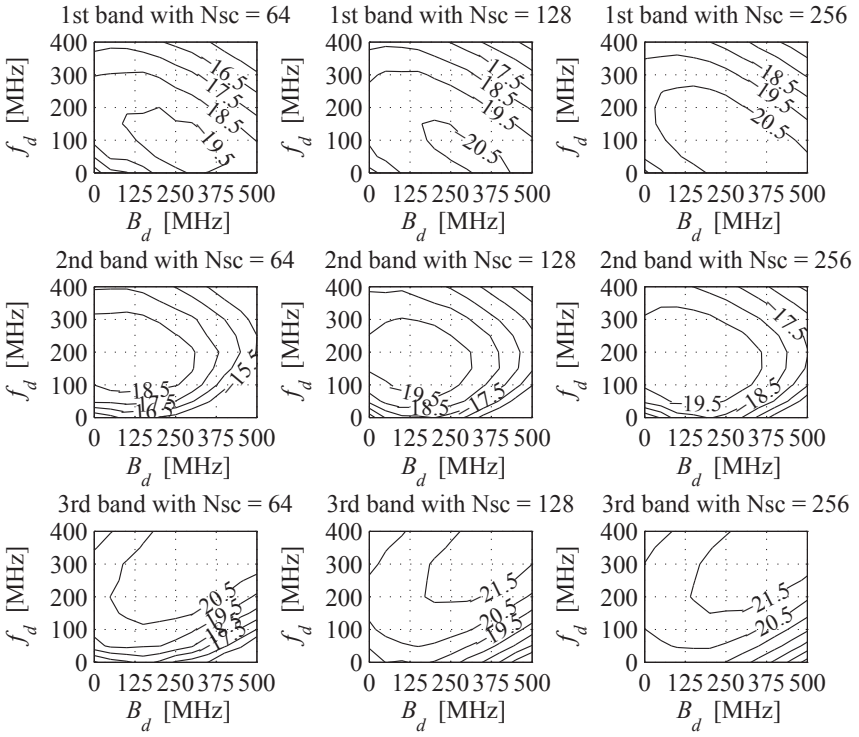

(a)

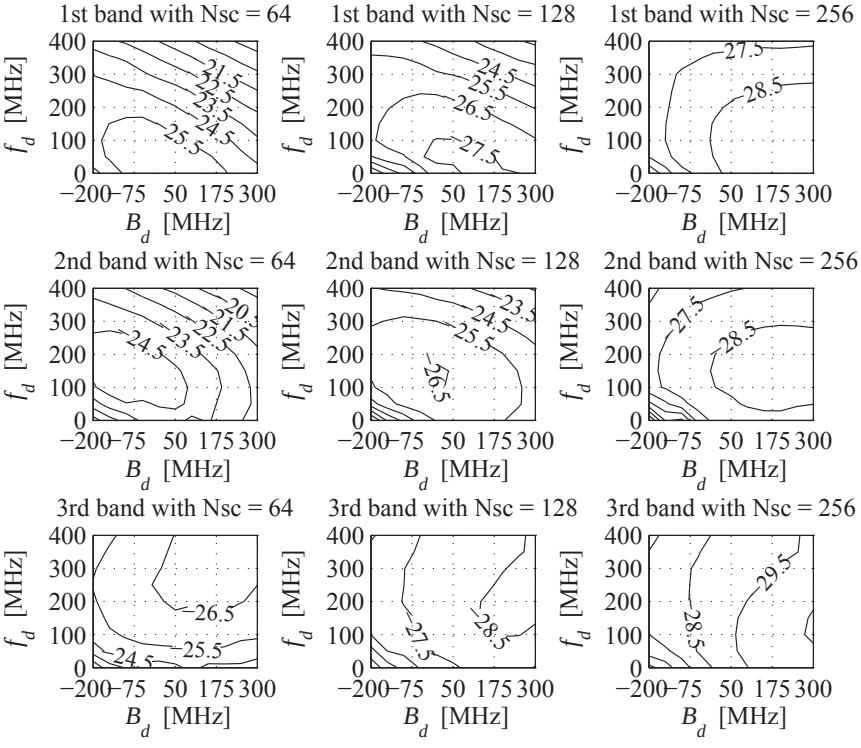

(b)

Figure 3.8: EVMs as a function of B_d and f_d for the (a) SG-BS with $M = 32$ and the (b) G-BS with $M = 128$, for the 3 bands and with $N_{sc} \in \{64, 128, 256\}$. For the SG-BS, the following values are considered: MLL = 27 dB, MI = 5%, and VBPR = 8 dB. For the G-BS, MLL = 20 dB, MI = 5%, and VBPR = 10 dB are used.

$N_{sc} = 64$ and $N_{sc} = 128$, the crosstalk level originated from the beating between the first-band VC and the second-band becomes significant. This crosstalk induces severe distortion to some subcarriers of the second-band, degrading the overall performance. This crosstalk can be reduced with a negative B_d, as this induces more attenuation to the first-band VC, when compared with the situations that consider $B_d = 0$ or a positive B_d. The disadvantage of considering a negative B_d is that the BS is tighter than the OFDM band to be selected, inducing a degradation to the subcarriers at the edges of the OFDM signal spectrum.

After finding the optimum regions of the non-ideal BSs, the MLL is obtained through MI and VBPR optimization. Through inspection of Tab. 3.3, the following values for B_d and f_d are considered: $B_d = 200$ MHz and $f_d = 200$ MHz for the SG-BS, and $B_d = 0$ MHz and $f_d = 100$ MHz for the G-BS.

Tab. 3.4 shows the MLL and the optimum VBPR for the G-BS and SG-BS, with $N_{sc} \in \{64, 128, 256\}$ and with $B_d = 200$ MHz and $f_d = 200$ MHz for the SG-BS, and $B_d = 0$ MHz and $f_d = 100$ MHz for the G-BS. A MI = 5% is considered as optimum MI. The results of Tab. 3.4 are for the second-band, which is the band that presents the highest EVM when compared with the EVMs of the other bands, as it is the most limited by inter-band crosstalk. Fig. 3.9 shows the EVMs, using the SG-BS with $M = 32$ and the G-BS with $M = 128$, as a function of the MI and VBPR, for the 3 bands, with $N_{sc} \in \{64, 128, 256\}$, and considering the MLLs of Tab. 3.4.

Table 3.4: MLL and optimum VBPR for the G-BS and SG-BS, with $N_{sc} \in \{64, 128, 256\}$.

SG-BS	N_{sc}	MLL [dB]	Opt. VBPR [dB]
$M = 32$	64	26	7.0
$B_d = 200$ MHz	128	27	7.0
$f_d = 200$ MHz	256	27	6.5
G-BS	N_{sc}	MLL [dB]	Opt. VBPR [dB]
$M = 128$	64	20	11.0
$B_d = 0$ MHz	128	22	10.0
$f_d = 100$ MHz	256	22	9.5

Tab. 3.4 shows that the number of subcarriers influence the MLL when using non-ideal BSs. With the SG-BS, when selecting the second-band (the most affected by inter-band crosstalk with $N_B = 3$), a compromise exists when finding the optimum region: the BS has to guarantee simultaneously low filtering of the second-band VC and high rejection of the first-band VC and the third-band. First, the second-band VC requires low filtering to avoid power loss for the beating between the second-band VC and the second-band (the signal component after photodetection). Second, the first-band VC requires high rejection to avoid the influence of crosstalk caused by the beating between the first-band VC and the second-band. Third, the third-band requires also high rejection to avoid the influence of crosstalk caused by the beating

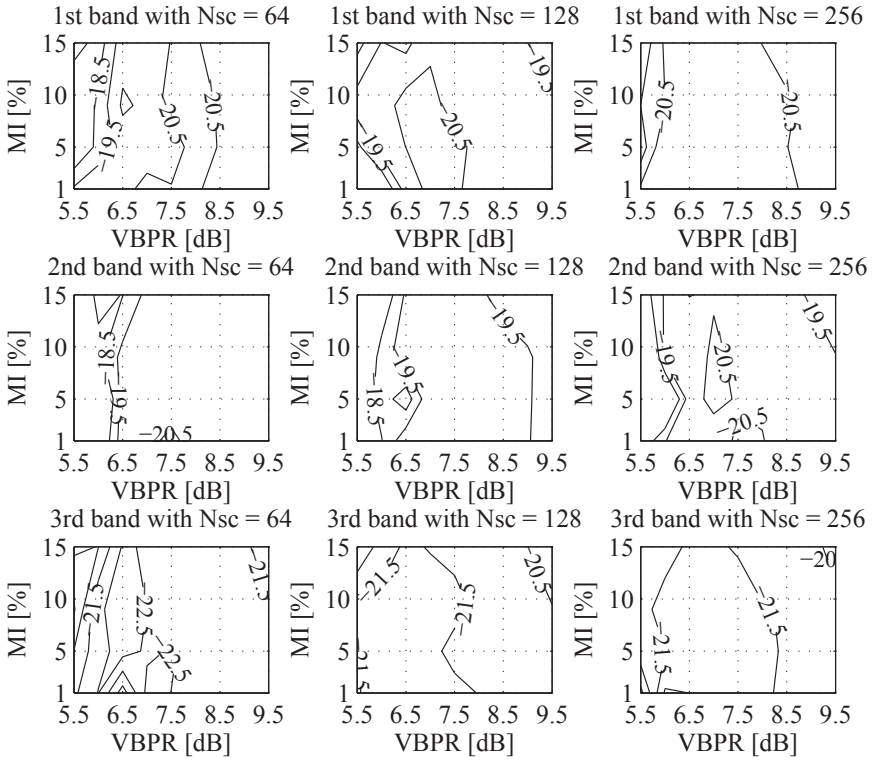

(a)

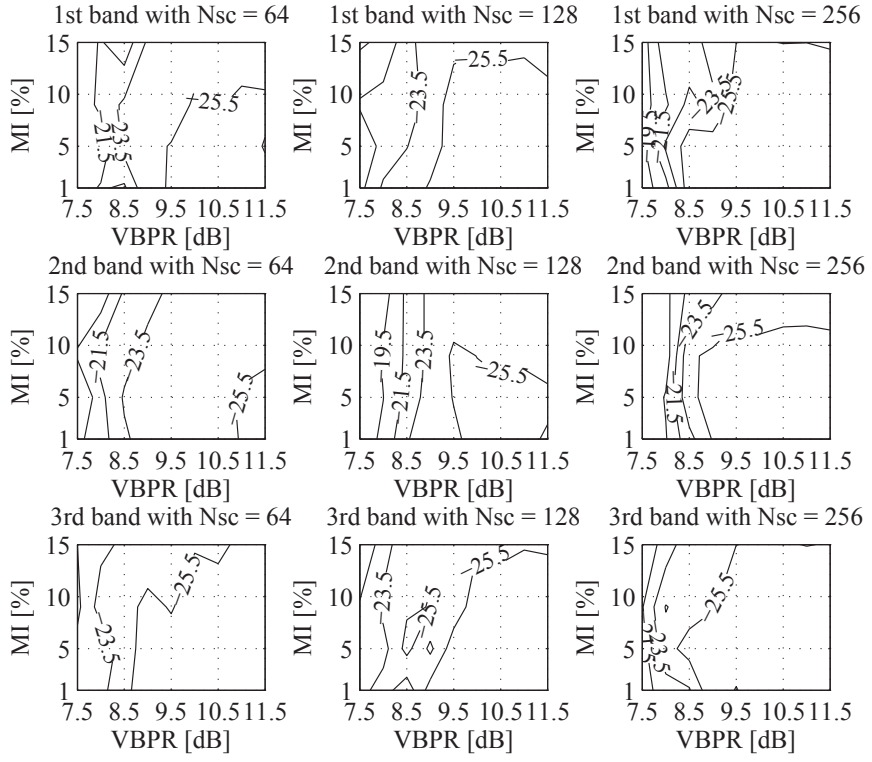

(b)

Figure 3.9: EVMs, using the (a) SG-BS with $M = 32$ and the (b) G-BS with $M = 128$, as a function of the MI and VBPR, for the 3 bands, and with $N_{sc} \in \{64, 128, 256\}$. The corresponding MLL values are shown in Tab. 3.4. $B_d = 200$ MHz and $f_d = 200$ MHz are used for the SG-BS, and $B_d = 0$ MHz and $f_d = 100$ MHz are considered for the G-BS.

between the third-band residual part and the second-band VC. The aforementioned compromises dictate the optimum region. With the SG-BS, the reason for a lower MLL with $N_{sc} = 64$ is the smaller BG when compared with the situations with $N_{sc} = 128$ and $N_{sc} = 256$. A smaller BG induces less filtering to the residual part of the third-band, which originates more crosstalk from the beating between the residual part of the third-band and the second-band VC. With the G-BS, due to its lower selectivity when compared with the SG-BS, the most relevant crosstalk is originated from the beating between the first-band VC and the second-band. This crosstalk is relevant when Eq. 3.11 is not verified, which is the case when $N_{sc} = 64$ and $N_{sc} = 128$. Tab. 3.4 shows that, besides the non-verification of Eq. 3.11 for the situation with $N_{sc} = 128$, the influence of that crosstalk on the MLL is not significant. However, with $N_{sc} = 64$, that crosstalk is relevant as it imposes a 2 dB degradation on the MLL, when compared with the MLL with $N_{sc} = 128$ and $N_{sc} = 256$.

Inspection of Tab. 3.2 and Tab. 3.4 reveals that the use of non-ideal BSs causes a degradation on the MLL between 3 and 5 dB with $N_{sc} = 64$, and between 2 and 3 dB with $N_{sc} = 128$ and $N_{sc} = 256$. Moreover, when comparing the situations considering an ideal BS and non-ideal BSs, the optimum VBPR increases slightly for the same QAM order. This increase is attributed to the intra-band amplitude distortion due to non-ideal filtering. This distortion causes additional performance degradation before SSBI mitigation, degrading also the performance of the SSBI mitigation algorithm. With a small VBPR increase, the SSBI component power decreases slightly and the algorithm is then able to estimate and mitigate correctly the SSBI component.

Fig. 3.10(a) shows the LPE of the MB-OFDM signal with 3 bands, with $M = 32$, $N_{sc} = 128$, MLL = 27 dB, MI = 5%, and VBPR = 7 dB and the selection of each band with the SG-BS with $B_d = 200$ MHz and $f_d = 200$ MHz. The central frequencies of the 3 bands are 1.75, 4.875 and 8 GHz. Fig. 3.10(b) shows the second pair band-VC after band selection, in order to clearly identify the residual parts of the neighbouring pairs. Fig. 3.10(c) shows the EVMs of the subcarriers for each band. A higher subcarrier index corresponds to a subcarrier farther away from the corresponding VC. Fig. 3.10 illustrates that when selecting each band individually, in a MB-OFDM signal with 3 bands, residual parts from the neighbouring bands are present. When selecting the first and second bands, the neighbouring band at higher frequency causes EVM degradation in the subcarriers with index between 48 and 64. The bands are also affected by the non-ideal amplitude response of the BSs, especially in the subcarriers with higher index. The EVM degradation verified for subcarriers with lower indexes (closer to the VC) is mostly attributed to the non-perfect SSBI mitigation when employing a VBPR of 7 dB with $M = 32$.

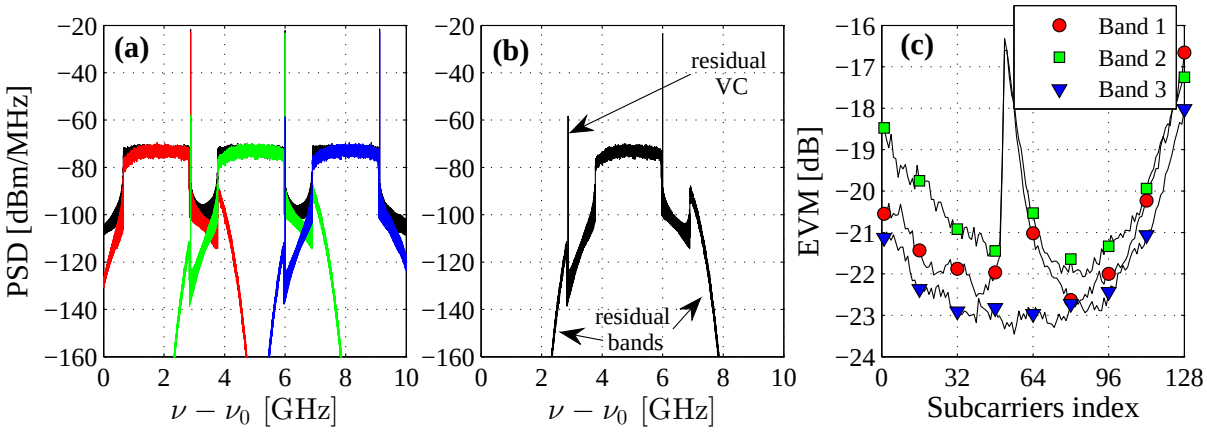

Figure 3.10: (a) LPE of the MB-OFDM signal spectrum with 3 bands (black). Selection of each band using the SG-BS. $M = 32$, $N_{sc} = 128$, MLL = 27 dB, MI = 5%, VBPR = 7 dB, $B_d = 200$ MHz and $f_d = 200$ MHz are considered. (b) Second pair band-VC after band selection, with the residual bands and residual VC identified. (c) EVMs of the subcarriers of each band. Average EVM of each band: band $1 \rightarrow -20.7$ dB, band $2 \rightarrow -20.1$ dB, and band $3 \rightarrow -22.0$ dB. $\nu - \nu_0$ stands for the LPE frequency.

Fig. 3.11(a) shows the LPE of the MB-OFDM signal with 3 bands, with $M = 128$, $N_{sc} = 128$, MLL = 22 dB, MI = 5%, and VBPR = 10 dB and the selection of each band with the G-BS with $B_d = 0$ MHz and $f_d = 100$ MHz. The central frequencies of the 3 bands are 1.75, 4.875 and 8 GHz. Fig. 3.11(b) shows the second pair band-VC after band selection, in order to clearly identify the residual parts of the neighbouring pairs. Fig. 3.11(c) shows the EVMs of the subcarriers for each band. A higher subcarrier index also corresponds to a subcarrier farther away from the corresponding VC. Fig. 3.11 illustrates that, when selecting the bands individually, in a MB-OFDM signal with 3 bands, residual parts from neighbouring bands are present. For the first and second bands, the beating between the corresponding VC with the residual part of the OFDM band at higher frequency affects significantly the EVM of a few subcarriers with higher index (EVM degradation exceeding 6 dB). For the third-band, the same subcarriers are affected by inter-band crosstalk but with a smaller EVM degradation (around 2 dB). This degradation is induced by the beating between the second-band VC and the third band. The EVM degradation verified for subcarriers with lower indexes (closer to the corresponding VC) is attributed to the non-perfect SSBI mitigation when employing a VBPR of 10 dB with $M = 128$, together with the attenuation of the subcarriers due to the non-ideal BS amplitude response.

3.4.2 WDM channel spacing

In the analysis of the channel spacing influence on the performance of the MB-OFDM signal, $N_{sc} = 128$ is considered. With 128 OFDM subcarriers per OFDM symbol, two important conditions are verified simultaneously: 1) $T_p < 1$ ms (necessary and sufficient condition to fully

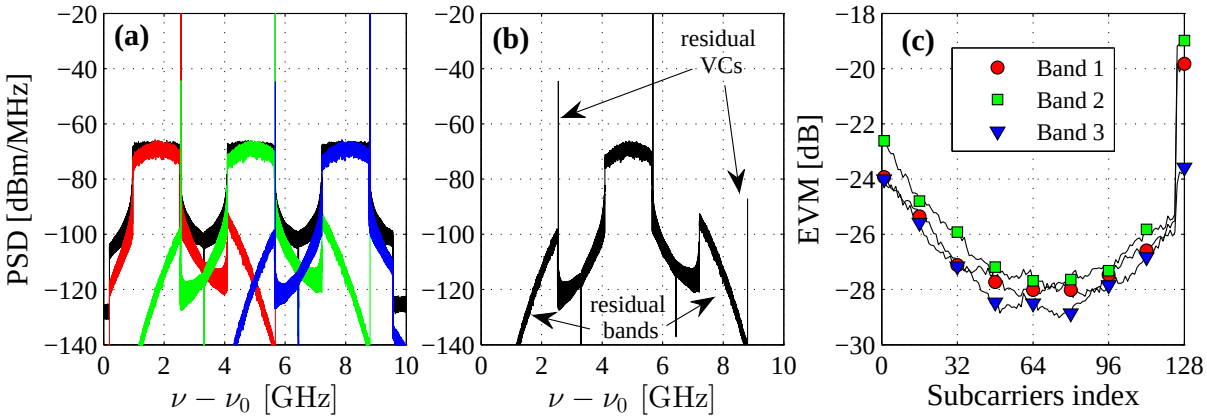

Figure 3.11: (a) LPE of the MB-OFDM signal spectrum with 3 bands (black). Selection of each band using the G-BS. $M = 128$, $N_{sc} = 128$, MLL = 22 dB, MI = 5%, VBPR = 10 dB, $B_d = 0$ MHz and $f_d = 100$ MHz are used. (b) Second pair band-VC after band selection, with the residual bands and VCs identified. (c) EVMs of the subcarriers of each band. Average EVM of each band: band 1 $\rightarrow -26.2$ dB; band 2 $\rightarrow -25.6$ dB; band 3 $\rightarrow -27.0$ dB. $\nu - \nu_0$ stands for the LPE frequency.

compensate the polarization variations in the optical channel); and 2) 128 subcarriers is the minimum N_{sc} that does not present MLL degradation, for all the BSs considered in this work, as verified when comparing Tab. 3.2 and Tab. 3.4. As explained in section 3.2, for channel spacings of 12.5, 25 and 50 GHz, the maximum number of bands that those channels can accommodate are 2, 5 and 10, respectively. To evaluate the MLL for the different channels, a strategy similar to the one considered in section 3.4.1 is adopted. First, the MLL is obtained through MI and VBPR optimization, using an ideal BS for $M = 32$ and $M = 128$. Second, the BS parameters are optimized, with a fixed MI and VBPR close to the optimum values. Third, the MLL is obtained through MI and VBPR optimization, using the non-ideal BSs with the optimized parameters.

Tab. 3.5 shows the MLL and the optimum VBPR, using the ideal BS, with $N_{sc} = 128$, $N_B \in \{2, 5, 10\}$ and $M \in \{32, 128\}$. A MI = 5% is considered as optimum MI. Fig. 3.12 shows the EVMs, using an ideal BS, as a function of the MI and VBPR, for the 3 bands, with $N_B \in \{2, 5, 10\}$, $N_{sc} = 128$, and with $M = 32$ and $M = 128$, for the MLLs of Tab. 3.5. Tab. 3.5 shows that, as N_B increases, the MLL decreases for the same M. In fact, duplicating the number of bands per channel causes a 3 dB MLL degradation. As the average power at the MB-OFDM Tx output is the same for different channel spacings, increasing the number of bands implies less power per band, which originates a lower SNR per band considering that the thermal noise PSD is maintained. Inspection of Tab. 3.5 also reveals a small increase in the optimum VBPR when increasing M. This is attributed to the SSBI algorithm limitations that, for correctly recover and mitigate the SSBI component, requires a higher SNR to operate with higher QAM orders.

The requirement of higher SNR for higher QAM orders is also the reason for the MLL penalty of around 4 dB when increasing M, as shown in Tab. 3.5.

Table 3.5: MLL and optimum VBPR, using the ideal BS, with $N_{sc} = 128$, $N_B \in \{2, 5, 10\}$, and $M \in \{32, 128\}$.

	N_B	MLL [dB]	Opt. VBPR [dB]
Ideal BS $N_{sc} = 128$ $M = 32$	2	31	6.0
	5	27	6.5
	10	24	6.0
	N_B	MLL [dB]	Opt. VBPR [dB]
Ideal BS $N_{sc} = 128$ $M = 128$	2	27	8.0
	5	23	8.0
	10	20	7.5

Tab. 3.6 shows the optimum f_d and B_d ranges for the band with worst performance of each channel and the MLL for the G-BS and SG-BS, with $N_B \in \{2, 5, 10\}$, $N_{sc} = 128$ and MI = 5%. Fig. 3.13 shows the EVMs for the first, penultimate and last bands of each channel, as a function of B_d and f_d for the SG-BS with $M = 32$ and the G-BS with $M = 128$, with channels comprising 2, 5, and 10 bands ($N_B \in \{2, 5, 10\}$), with $N_{sc} = 128$ and MI = 5%. For the SG-BS and G-BS, VBPR = 8 dB and VBPR = 10 dB are considered, respectively. The corresponding MLLs are shown in Tab. 3.6. The results of Tab. 3.6 are for the bands with worst performance. The optimum region is comprised by the optimum point plus the surrounding B_d and f_d values which lead to EVMs not exceeding 1 dB from the optimum point. With $N_B = 2$, the EVM results of both bands are combined to obtain the optimum ranges. With $N_B = 5$ and $N_B = 10$, similarly to the channels with $N_B = 3$ exemplified in section 3.4.1, the bands most affected by inter-band crosstalk are the ones in the middle of each channel. However, besides inter-band crosstalk there is other impairment to take into consideration: the non-ideal HC amplitude response. Channels with $N_B = 5$ and $N_B = 10$ use almost all the HC passband and the bands with higher frequency are the most affected by the HC amplitude response. Thus, the bands most limited by both the inter-band crosstalk and the HC amplitude response are the penultimate bands of the channels with $N_B = 5$ and $N_B = 10$. Hence, in the case of $N_B = 5$ and $N_B = 10$, Tab. 3.6 shows the results for the penultimate band.

Tab. 3.6 shows positive B_d and f_d ranges with the use of SG-BS. The main reasons for these ranges are: 1) to guarantee low filtering to the VC of the band to be selected, and 2) to ensure high rejection to the neighbouring VC with lower frequency, without filtering considerably the OFDM band to be selected. With the G-BS, the reason for the positive f_d range is the same as explained for the SG-BS. For the B_d range, the existence of negative values, which is different from the situation with the SG-BS, is attributed to the need to filter even more the neighbouring

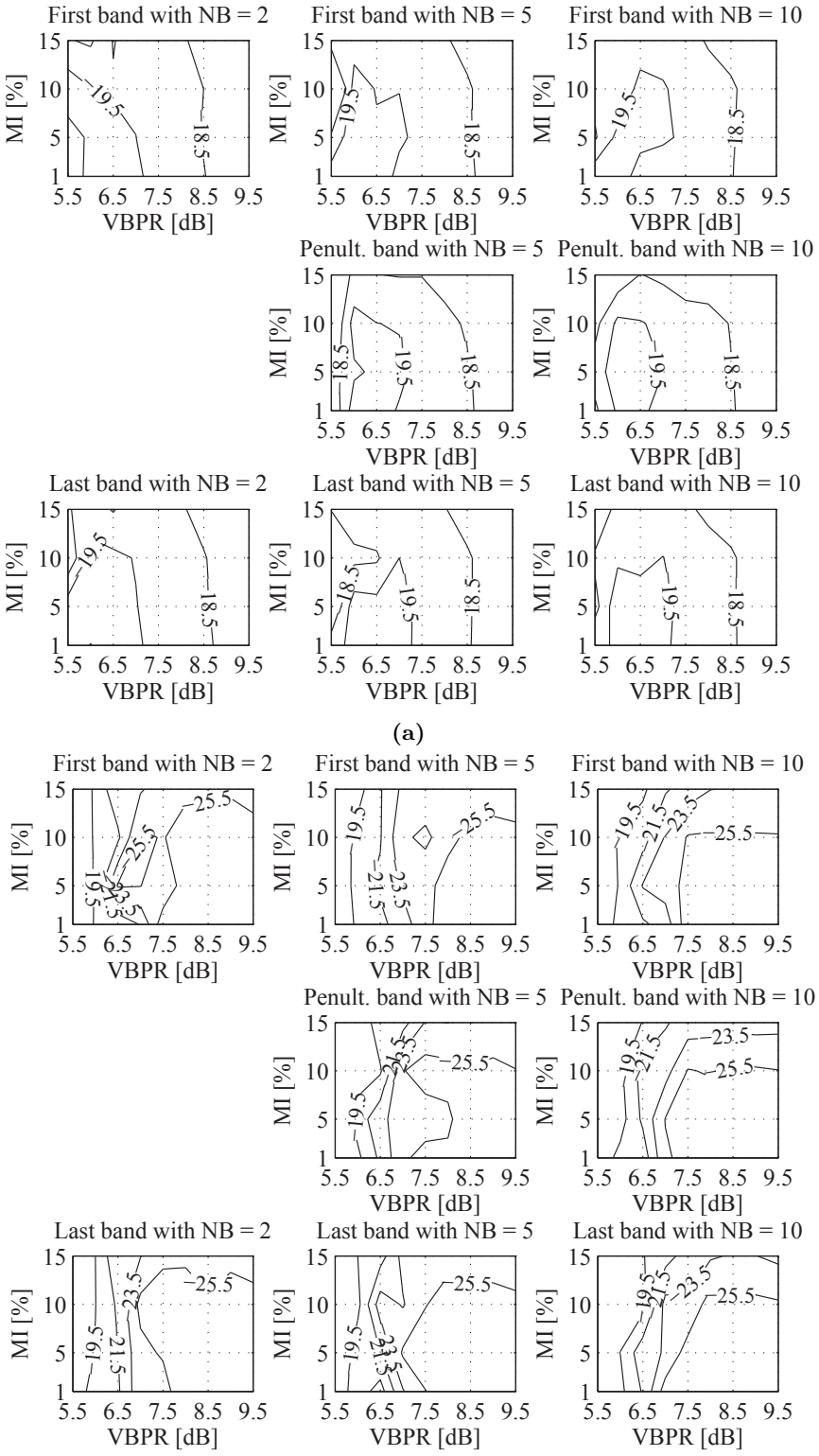

Figure 3.12: EVMs, using an ideal BS, as a function of the MI and VBPR, for the 3 bands, with $N_B \in \{2, 5, 10\}$, $N_{sc} = 128$, and with (a) $M = 32$ and (b) $M = 128$. The corresponding MLL values are shown in Tab. 3.5.

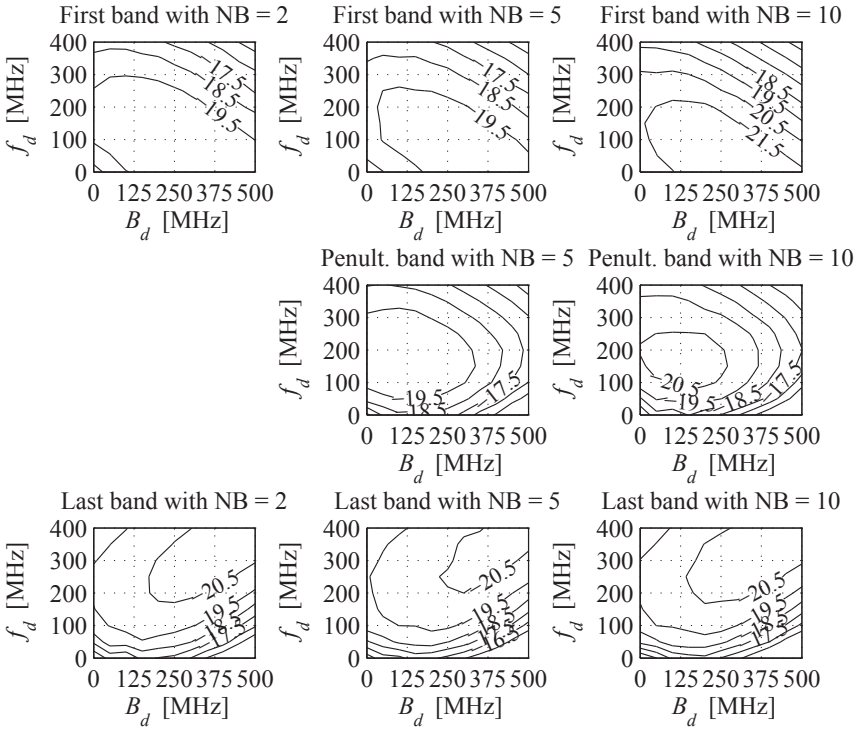

(a)

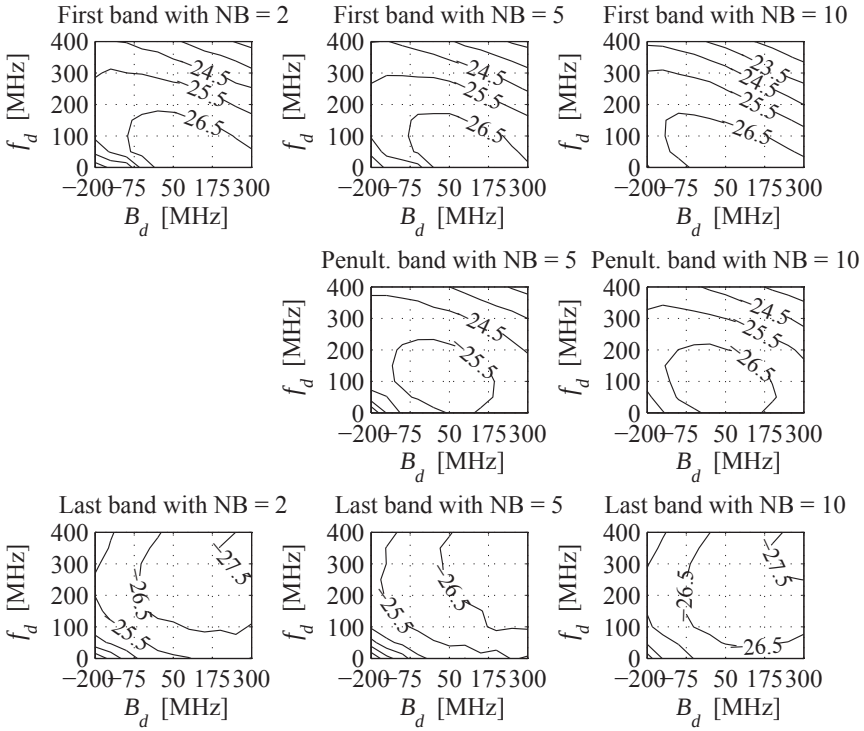

(b)

Figure 3.13: EVMs for the first, penultimate and last bands of each channel, as a function of B_d and f_d for the (a) SG-BS with $M = 32$ and the (b) G-BS with $M = 128$, with channels comprising 2, 5, and 10 bands ($N_B \in \{2, 5, 10\}$), with $N_{sc} = 128$ and MI = 5%. For the SG-BS and G-BS, VBPR = 8 dB and VBPR = 10 dB are considered, respectively. The corresponding MLL values are shown in Tab. 3.6.

Table 3.6: Optimum f_d and B_d ranges for the band with worst performance of each channel and the MLL for the G-BS and SG-BS, with $N_B \in \{2, 5, 10\}$, MI = 5% and $N_{sc} = 128$. For the SG-BS, $M = 32$ and VBPR = 8 dB are considered. For the G-BS, $M = 128$ and VBPR = 10 dB are employed.

	N_B	f_d [MHz]	B_d [MHz]	MLL [dB]
SG-BS	2	$[100, 250]$	$[0, 400]$	29
	5	$[100, 250]$	$[0, 400]$	25
	10	$[150, 300]$	$[0, 300]$	21
	N_B	f_d [MHz]	B_d [MHz]	MLL [dB]
G-BS	2	$[100, 250]$	$[-100, 100]$	23
	5	$[100, 250]$	$[-100, 100]$	19
	10	$[100, 250]$	$[-200, 100]$	15

VC with lower frequency. This reduces the crosstalk level after photodetection originated from the beating between that neighbouring VC and the band to be selected.

Tab. 3.7 shows the MLL and the optimum VBPR for the G-BS and SG-BS, with $N_B \in \{2, 5, 10\}$ and $N_{sc} = 128$. Through inspection of Tab. 3.6, the following values for B_d and f_d can be used, as adopted in section 3.4.1: $B_d = 200$ MHz and $f_d = 200$ MHz for the SG-BS, and $B_d = 0$ MHz and $f_d = 100$ MHz for the G-BS. A MI = 5% is considered as optimum MI. Fig. 3.14 shows the EVMs for the first, penultimate and last bands of each channel, using the SG-BS with $M = 32$ and the G-BS with $M = 128$, as a function of the MI and VBPR, with channels comprising 2, 5, and 10 bands ($N_B \in \{2, 5, 10\}$), and with $N_{sc} = 128$. The corresponding values for the MLL, B_d and f_d of Fig. 3.14, are shown in Tab. 3.7.

Table 3.7: MLL and optimum VBPR for the G-BS and SG-BS, with $N_B \in \{2, 5, 10\}$, MI = 5% and $N_{sc} = 128$.

SG-BS	N_B	MLL [dB]	Opt. VBPR [dB]
$M = 32$	2	29	6.5
$B_d = 200$ MHz	5	25	6.5
$f_d = 200$ MHz	10	21	7.0
G-BS	N_B	MLL [dB]	Opt. VBPR [dB]
$M = 128$	2	23	9.0
$B_d = 0$ MHz	5	19	9.5
$f_d = 100$ MHz	10	16	9.5

Tab. 3.7 shows that the MLL decreases as N_B increases, in the same way as shown in Tab. 3.5 where an ideal BS was employed. When comparing the MLL degradation of Tab. 3.5 and Tab. 3.7, the MLL decrease with the increase of the number of bands is slightly different, which can be attributed to degradation due to non-ideal BS filtering together with the degradation induced by the non-ideal HC amplitude response. A MLL penalty between 2 and 3 dB when using the SG-BS and between 3 and 4 dB with the G-BS, is verified when comparing the MLL results achieved with the ideal BS of Tab. 3.5 and the results achieved with the non-ideal BSs and presented in Tab. 3.7. Tab. 3.7 also shows a penalty between 5 and 6 dB when comparing the results with

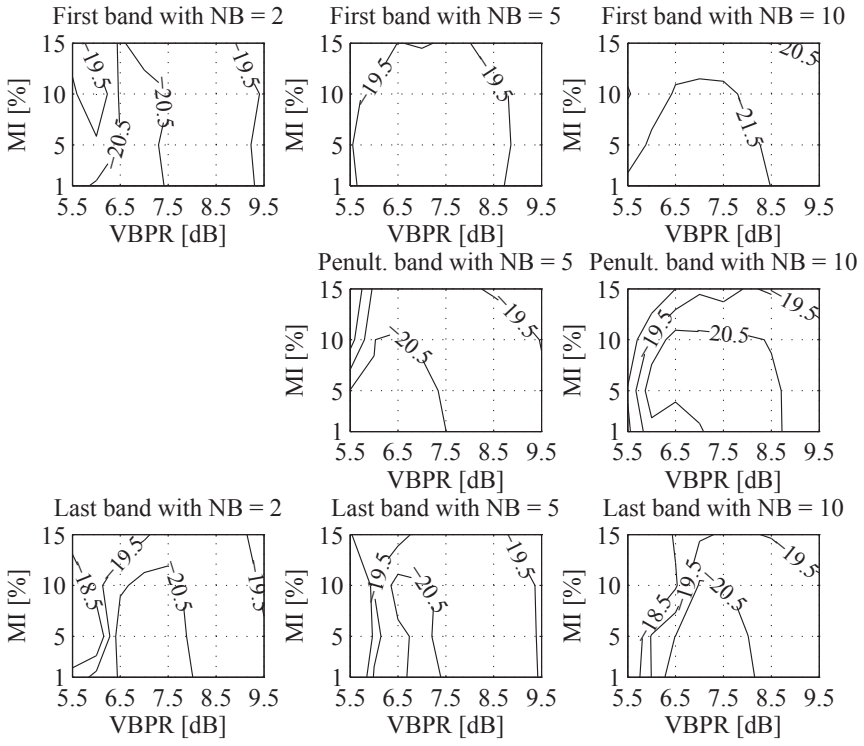

(a)

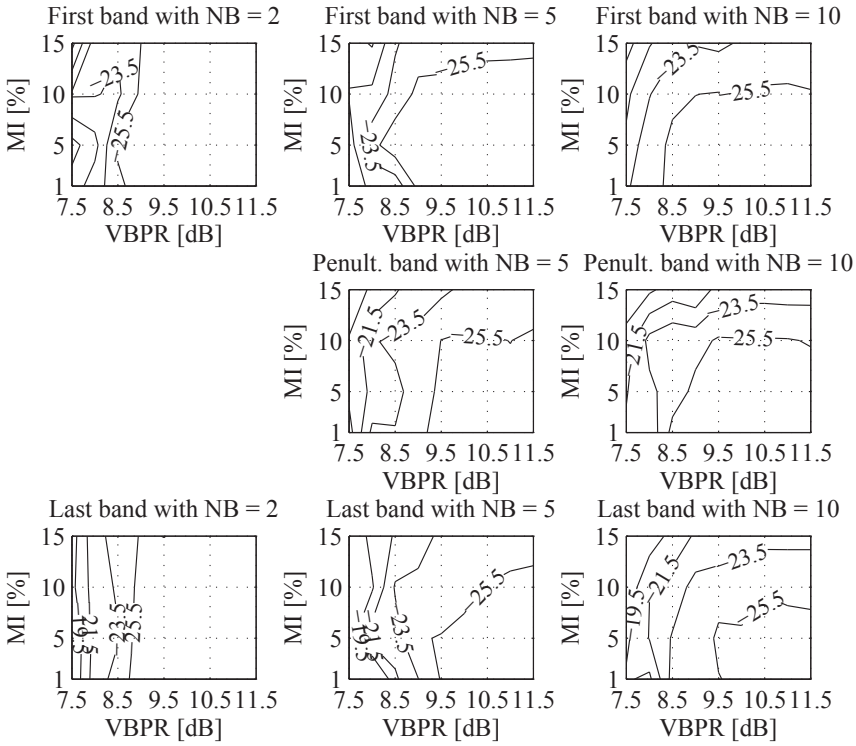

(b)

Figure 3.14: EVMs for the first, penultimate and last bands of each channel, using the (a) SG-BS with $M = 32$ and the (b) G-BS with $M = 128$, as a function of the MI and VBPR, with channels comprising 2, 5, and 10 bands ($N_B \in \{2, 5, 10\}$), and with $N_{sc} = 128$. The corresponding MLL values are shown in Tab. 3.7. $B_d = 200$ MHz and $f_d = 200$ MHz are used for the SG-BS, and $B_d = 0$ MHz and $f_d = 100$ MHz are considered for the G-BS.

the different BSs. This penalty is a direct consequence of the higher SNR requirement for higher QAM orders. Moreover, the optimum VBPR has increased slightly when comparing Tab. 3.5 and Tab. 3.7. The reason for this small increase is the same as explained in section 3.4.1: the intra-band amplitude distortion due to non-ideal filtering degrades the performance of the SSBI mitigation algorithm and increasing slightly the VBPR improves its performance.

3.4.3 WSS successive filtering

In a metro network, the use of WSS-based ROADMs causes passband narrowing from WSS successive filtering. Fig. 3.15 shows the WSS successive filtering effect when a 25 GHz WSS is considered. Fig. 3.15 shows that as the number of concatenated WSSs increases, the passband becomes narrower and with a higher selectivity (as shown previously in Fig. 3.3). To evaluate the impact of WSS successive filtering on the performance of the MB-OFDM system, the initial WSS central frequency has to be defined. The LPE of the initial WSS central frequency, $f_{\mathrm{WSS,ini}}$, is given as follows:

$$f_{\mathrm{WSS,ini}} = \frac{f_{\min} + f_{\max}}{2}. \tag{3.14}$$

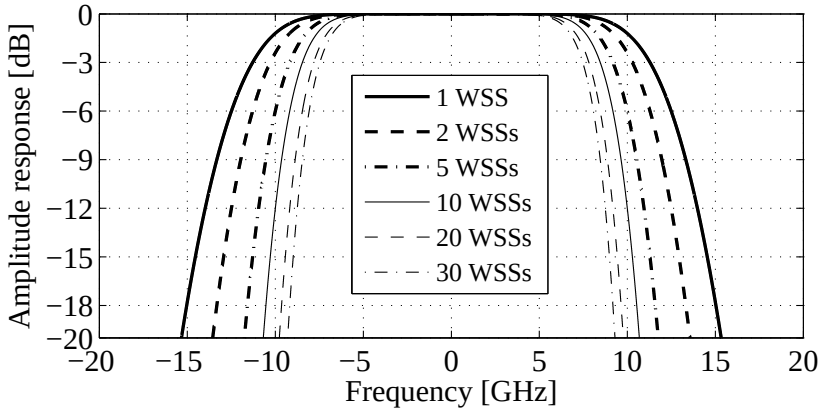

Figure 3.15: WSS successive filtering effect when the 25 GHz WSS is employed.

The optimum WSS central frequency corresponds to the frequency that leads to the maximum number of concatenated WSSs while not exceeding a certain performance penalty in at least one OFDM band of the MB-OFDM signal within the WDM channel. The maximum number of concatenated WSSs is limited mostly by the performance of the OFDM bands on the channel edges, as they suffer the most by the WSS passband narrowing. Therefore, the performance penalty due to WSS concatenation is evaluated by analysing the performance of the bands on the edges of the WDM channel. The LPE of the optimum WSS central frequency, $f_{\mathrm{WSS,opt}}$, is investigated by detuning the initial central frequency of the WSS by a frequency spacing, $f_{\mathrm{WSS},d}$.

The frequency $f_{\mathrm{WSS,opt}}$ is given by:

$$f_{\mathrm{WSS,opt}} = f_{\mathrm{WSS,ini}} + f_{\mathrm{WSS},d}. \tag{3.15}$$

The optimum detuning frequency is the frequency that leads to the maximum number of concatenated WSSs achieved with an EVM degradation of 1 dB, relative to the EVM obtained without WSS concatenation. The maximum number of concatenated WSSs with an EVM degradation of 1 dB is represented by $\mathrm{WSS}_{\mathrm{max}}^{1\,\mathrm{dB}}$. The optimum detuning frequency is also assessed with an EVM degradation of 2 dB, relative to the EVM obtained without WSS concatenation. The maximum number of concatenated WSSs in this case is represented by $\mathrm{WSS}_{\mathrm{max}}^{2\,\mathrm{dB}}$.

Tab. 3.8 shows $f_{\mathrm{WSS},d}$ for $\mathrm{WSS}_{\mathrm{max}}^{1\,\mathrm{dB}}$ and $\mathrm{WSS}_{\mathrm{max}}^{2\,\mathrm{dB}}$, for WDM channels with 12.5, 25 and 50 GHz, which transport 2, 5 and 10 bands, respectively. The MLL values and optimum VBPRs considered in Tab. 3.8 are the same as in Tab. 3.7. Fig. 3.16 shows the EVM as a function of the $f_{\mathrm{WSS},d}$ and the number of concatenated WSSs, using the SG-BS with $M = 32$ and the G-BS with $M = 128$, with the optimized B_d and f_d values, with channels comprising 2, 5, and 10 bands and with the MLL values and optimum VBPRs considered in Tab. 3.7.

Table 3.8: Detuning frequency $f_{\mathrm{WSS},d}$ for $\mathrm{WSS}_{\mathrm{max}}^{1\,\mathrm{dB}}$ and $\mathrm{WSS}_{\mathrm{max}}^{2\,\mathrm{dB}}$, with $N_B \in \{2, 5, 10\}$.

SG-BS	N_B	$f_{\mathrm{WSS},d}$ [MHz]	$\mathrm{WSS}_{\mathrm{max}}^{1\,\mathrm{dB}}$	$f_{\mathrm{WSS},d}$ [MHz]	$\mathrm{WSS}_{\mathrm{max}}^{2\,\mathrm{dB}}$
$M = 32$	2	[-400,750]	>30	[-700,1200]	>30
$B_d = 200$ MHz	5	450	12	450	22
$f_d = 200$ MHz	10	600	7	700	15
G-BS	N_B	$f_{\mathrm{WSS},d}$ [MHz]	$\mathrm{WSS}_{\mathrm{max}}^{1\,\mathrm{dB}}$	$f_{\mathrm{WSS},d}$ [MHz]	$\mathrm{WSS}_{\mathrm{max}}^{2\,\mathrm{dB}}$
$M = 128$	2	[-600,800]	>30	[-900,1300]	>30
$B_d = 0$ MHz	5	0	19	[200,500]	>30
$f_d = 100$ MHz	10	1000	12	600	25

Tab. 3.8 shows that, in some cases, there is an optimum $f_{\mathrm{WSS},d}$ range instead of a single optimum $f_{\mathrm{WSS},d}$. This occurs because the maximum number of concatenated WSSs is more than 30, and a single optimum $f_{\mathrm{WSS},d}$ was not reached yet. Inspection of Tab. 3.8 also reveals that the optimum $f_{\mathrm{WSS},d}$ values are mostly positive. This indicates that the optimum $f_{\mathrm{WSS},d}$ values are mostly limited by the VC of the last band (which has frequency equal to f_{max}), and a positive $f_{\mathrm{WSS},d}$ avoids to filter considerably that VC. Tab. 3.8 also shows that, for both EVM degradations, the maximum number of concatenated WSSs 1) decreases when N_B increases while maintaining M, and 2) increases when M increases while maintaining N_B. These variations are attributed to the different MB-OFDM signal bandwidths, which induce different spectral occupations within each WDM channel. These variations can be justified through the ratio between the MB-OFDM signal bandwidth (the effective bandwidth occupied with information within one WDM channel)

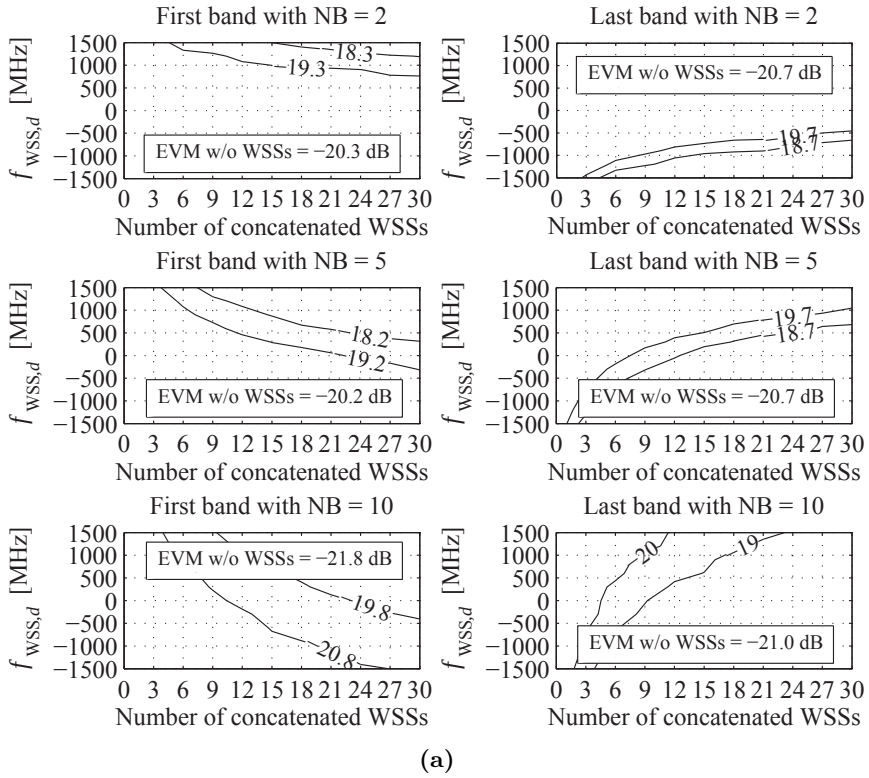

(a)

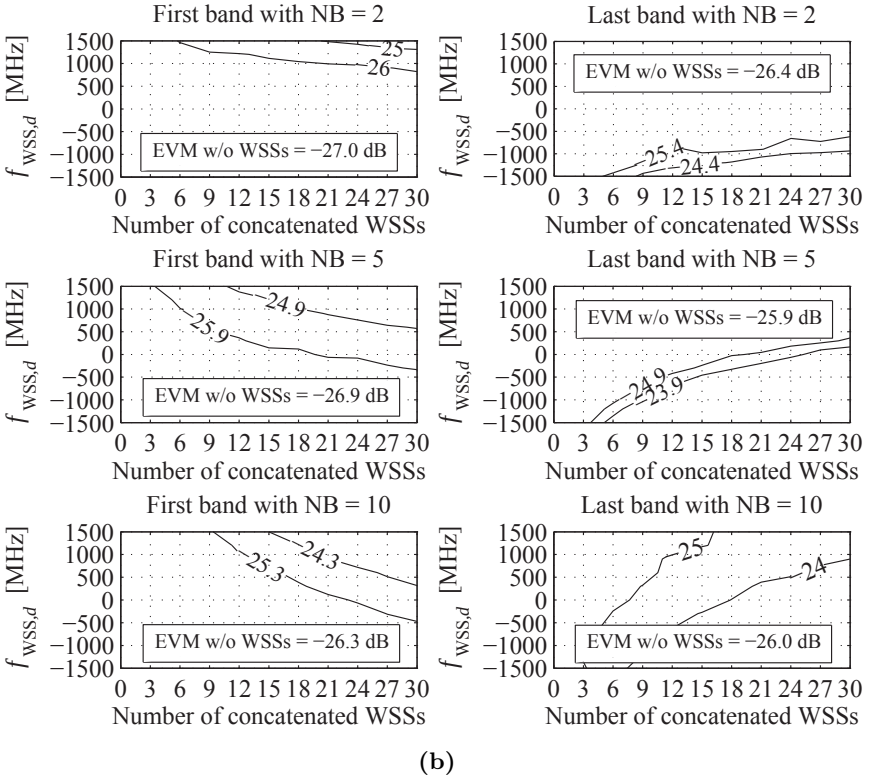

(b)

Figure 3.16: EVMs as a function of the WSS detuning frequency $f_{\mathrm{WSS},d}$ and the number of concatenated WSSs, using the (a) SG-BS with $M = 32$ and the (b) G-BS with $M = 128$, with the optimized B_d and f_d values, with channels comprising 2, 5, and 10 bands ($N_B \in \{2, 5, 10\}$). The MLL values and optimum VBPRs considered in Tab. 3.8 are the same as in Tab. 3.7.

and the −3 dB bandwidth of one WSS (the effective bandwidth of one WDM channel), which can be used as a metric for bandwidth efficiency. This bandwidth efficiency, η_B, in percentage, is given by:

$$\eta_B = \frac{B_{\text{MB-OFDM}}}{B_{-3\,\text{dB,WSS}}} \times 100\% \tag{3.16}$$

where $B_{\text{MB-OFDM}}$ is the MB-OFDM signal bandwidth approximately given by:

$$B_{\text{MB-OFDM}} = f_{\max} - f_{\min} \approx (N_B - 1)\Delta f_b + B_w \tag{3.17}$$

when VBG $\ll B_w$ (see Eq. 3.12).

Tab. 3.9 shows the efficiency η_B as function of M and N_B, with $N_{sc} = 128$, $R_b = 10.89$ Gb/s, and $\Delta f_b = 3.125$ GHz. Inspection of Tab. 3.8 and Tab. 3.9 show that, as η_B increases, the maximum number of WSSs decreases, as there is less margin for WSS passband narrowing. For the cases where $\text{WSS}^{1\,\text{dB}}_{\max}$ and $\text{WSS}^{2\,\text{dB}}_{\max}$ are greater than 30, the margin for WSS passband narrowing is given by the $f_{\text{WSS},d}$ range: a smaller range indicates a smaller margin, and a higher range a higher margin.

Table 3.9: Bandwidth efficiency η_B as function of M and N_B, with $N_{sc} = 128$, $R_b = 10.89$ Gb/s, and $\Delta f_b = 3.125$ GHz.

	N_B	$B_{\text{MB-OFDM}}$ [GHz]	$B_{-3\,\text{dB,WSS}}$ [GHz]	η_B [%]
$M = 32$	2	5.3	11.3	46.9
	5	14.7	22.6	65.0
	10	30.3	45.2	67.0
	N_B	$B_{\text{MB-OFDM}}$ [GHz]	$B_{-3\,\text{dB,WSS}}$ [GHz]	η_B [%]
$M = 128$	2	4.7	11.3	41.6
	5	14.1	22.6	62.4
	10	29.7	45.2	65.7

3.5 Conclusions

A DD-SSB-MB-OFDM system, employing VCs, with 10 Gb/s data rate guaranteed-per-user for low-cost next generation metro networks has been presented and optimized. A study concerning the limits and compromises between the number of OFDM subcarriers and OFDM bands of the MB-OFDM signal has been developed for WDM channel spacings of 12.5, 25 and 50 GHz, where it has been shown that these channels are able to transport MB-OFDM signals comprising 2, 5 and 10 bands, respectively. The main impairments due to non-ideal filtering from the BSs and the WSSs have been presented and discussed.

The EVM has been used as the figure of merit for performance evaluation, and from the EVM,

the MLL for the different WDM channels has been assessed. Using an ideal BS, the obtained MLLs are between 20 dB (128-QAM per subcarrier and channels with 10 bands) and 31 dB (32-QAM per subcarrier and channels with 2 bands). Two BSs with different selectivity have been employed and compared with the ideal BS. A MLL penalty not exceeding 3 dB for the BS with higher selectivity, and not exceeding 4 dB for the BS with lower selectivity has been shown. It has been also shown that, with systems with 2 bands, more than 30 WSSs can be concatenated with a EVM degradation not exceeding 1 dB. With 5 and 10 bands, more than 15 WSSs can be concatenated with a EVM degradation not exceeding 2 dB.

Chapter 4

Nonlinear crosstalk in VC-assisted DD-MB-OFDM metro networks

4.1 Introduction

To cope with the capacity demand increase, three basic requirements should be fulfilled: i) high number of wavelength division multiplexing (WDM) channels; ii) high optical power levels launched into the fibre; and iii) reduced channel spacing. However, orthogonal frequency-division multiplexing (OFDM) and consequently direct-detection (DD)-multi-band (MB)-OFDM, has weak tolerance to fibre nonlinearity, which restricts the maximum optical power levels used [62, 80, 81]. This weak tolerance is due to the high peak-to-average power ratio (PAPR), inherent to the multicarrier nature of OFDM [82], and constrains the design of future MB-OFDM metro networks.

The impact of fibre nonlinearity in coherent detection (CO)-OFDM systems was intensely studied in the past years, where it was shown that four wave mixing (FWM) is the dominant fibre nonlinear effect responsible for signal quality degradation [83, 84]. In DD-OFDM systems, a similar behaviour is expected. However, due to the transmission of a carrier to assist photodetection, additional FWM terms are present, when compared with CO-OFDM systems [84]. To analyse the FWM-induced impairments in DD-OFDM systems, theoretical and numerical work [70, 81, 85] and also experimental results [36] were presented recently. In [81], the FWM effect in DD double sideband (DSB) OFDM optical systems was characterized analytically through closed-form expressions for the FWM variance. The impact of FWM on DD block-wise phase switched OFDM systems was investigated in [85] using a theoretical approach and simulation re-

sults. In [70], the impact of FWM in an ultradense wavelength division multiplexing (UDWDM) single sideband (SSB)-MB-OFDM metro network employing a new virtual carrier (VC)-assisted DD scheme was evaluated numerically with band spacing of 3.125 GHz. In [36], the impact of the FWM on a metro network using this new DD scheme was assessed experimentally for a band spacing of 6 GHz.

Due to the high spectral efficiency provided by the VC-assisted DD scheme with its densely-packed OFDM bands, FWM products resulting from the mixing between the VCs and the OFDM bands cause severe performance degradation [36, 70]. In [36], it was shown that the performance degradation for high power levels is mainly attributed to the FWM products generated from the mixing between two VCs and an OFDM band (VC-VC-band products). This suggests that a fast and accurate theoretical method to assess the performance of VC-assisted WDM-MB-OFDM systems limited by the FWM effect, especially the VC-VC-band FWM products, is of great interest for network designers.

In this chapter, a theoretical method (TM) to evaluate the FWM power in an UDWDM SSB-MB-OFDM system employing a VC-assisted DD scheme is proposed and validated numerically. This method is derived considering that the FWM effect in MB-OFDM systems is dominantly governed by the VC-VC-band products and enables to estimate an upper bound of the power limit (UBPL) due to FWM. The power limit is defined as the average power level per optical channel, corresponding to a penalty of 2 dB due to the fibre nonlinearity on the error vector magnitude (EVM) at the forward error correction (FEC) threshold, when a very high number of optical channels is transmitted in the network. Based on the TM, a simplified theoretical method (STM) with reduced complexity that provides the maximum allowed average power at the fibre input for the worst pair band-VC of the WDM-MB-OFDM signal (the OFDM band most impaired by FWM), is also proposed.

The TM and STM results are validated by numerical simulation (NS) in a ultradense (UD) 450 Gb/s WDM MB-OFDM metro network scenario employing 9 optical channels, 5 OFDM bands per channel, 10 Gb/s per band and a band spacing of 3.125 GHz. The maximum allowed average powers obtained with the TM and STM are compared for standard single mode fibre (SSMF) transmission and the corresponding UBPLs are assessed for different number of fibre spans and channel gaps.

This chapter is structured as follows. In section 4.2, the TM used to obtain the FWM power of the VC-VC-band products in UDWDM VC-assisted DD MB-OFDM metro networks is presented. A STM to obtain the maximum allowed average power at the fibre input for the worst

pair band-VC of the WDM-MB-OFDM signal is also presented. In section 4.3, the TM is validated by comparison with the NS results for different number of fibre spans, channel gaps (CGs) and with 9 WDM channels. The maximum allowed average power estimates of the worst pair band-VC obtained with the TM and STM for SSMF transmission are compared and the UBPLs provided by both methods for different number of fibre spans and CGs are shown. In section 4.4, the main conclusions are summarized.

The work presented along this chapter is also published in [37].

4.2 FWM power of the VC-VC-band products

In this section, the TM used to obtain the FWM power of the VC-VC-band products in UDWDM VC-assisted DD MB-OFDM networks is presented. From the FWM power, the EVM of an OFDM subcarrier due to the FWM effect is estimated. The STM used to obtain the maximum allowed average power at the fibre input for the worst pair band-VC of the WDM-MB-OFDM signal is also presented.

4.2.1 MB-OFDM signal description

In order to derive the TM and STM, the structure of the MB-OFDM signal considered in the analysis has to be identified. Fig. 4.1 illustrates a simplified diagram of the WDM-MB-OFDM signal spectrum, showing the main parameters.

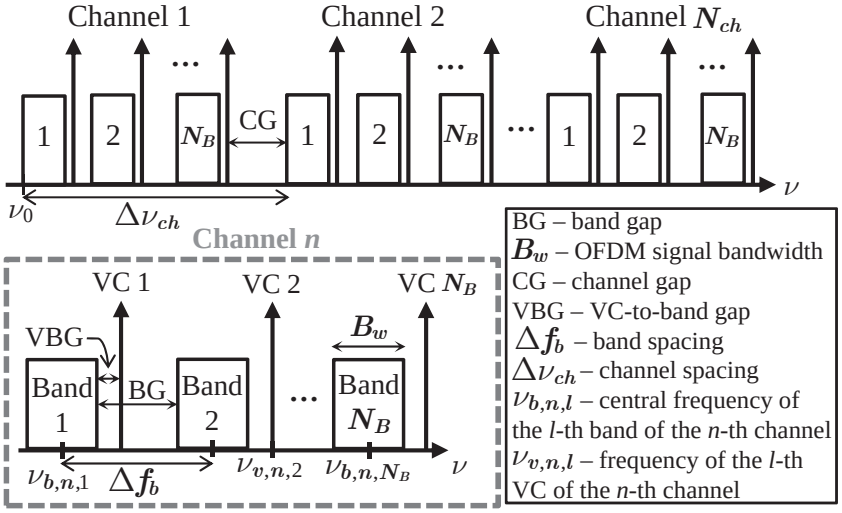

Figure 4.1: Illustration of the WDM-MB-OFDM signal spectrum. ν is the optical frequency and ν_0 is the reference optical frequency.

The MB-OFDM signal is composed by N_{ch} channels, each one carrying N_B bands. The detection of each OFDM band is assisted by a VC and each VC is located at a frequency higher than the corresponding OFDM band. The frequency spacing between the VC and the OFDM band, referred as the virtual carrier-to-band gap (VBG), is an important parameter that controls the amount of signal-signal beat interference (SSBI) that interferes with the OFDM band. If the VBG is less than the OFDM signal bandwidth, the SSBI overlaps with the OFDM band after photodetection, causing performance degradation [9]. The band gap (BG) between different OFDM bands inside the same WDM channel is a parameter which depends mainly on the selectivity of the band selector (BS) used to select the band prior to photodetection. To ensure high spectral efficiency, a high selectivity BS is needed in order to enable a small BG with negligible crosstalk from the adjacent bands. From the BG and the OFDM signal bandwidth B_w, the frequency spacing between the central frequencies of two consecutive bands, that is, the band spacing, is defined as $\Delta f_b = \text{BG} + B_w$. Another parameter which controls the overall spectral efficiency of the metro network is the frequency spacing between adjacent WDM channels, referred in this work as the CG. The CG is defined as:

$$\text{CG} = g \cdot \Delta f_b + \text{BG} - \text{VBG} \tag{4.1}$$

where g is a non-negative integer. Having the CG defined as in Eq. 4.1 avoids the FWM products originated only from the VCs to interfere with the OFDM bands. Non-integer g values could also be used and still avoid interference from the FWM products originated only from the VCs. However, this would lead to negligible FWM-induced performance variation and to uneven spectral occupation. With $g = 0$ (minimum CG), all the bands of all the channels are spaced equally. Another important parameter characteristic of carrier-assisted signals is the ratio between the VC power and the power of the corresponding OFDM band, known as virtual carrier-to-band power ratio (VBPR) [9]. The VBPR is of particular relevance as it controls the power of the SSBI component.

For the sake of simplicity, the following assumptions are made for the structure of the WDM-MB-OFDM signal. (i) All the OFDM bands have the same power and all the VCs also have the same power; thus, the VBPR is the same for all pairs band-VC. (ii) Each OFDM band has the same bandwidth B_w. (iii) The CG is the same between all the WDM channels. (iv) All WDM channels have the same number of OFDM bands. (v) The BGs are kept the same inside each channel, as well as the VBGs. Considering the aforementioned assumptions, the optical frequency of the l-th VC of the n-th channel, $\nu_{v,n,l}$, and the central optical frequency of the l-th

band of the n-th channel, $\nu_{b,n,l}$, can be written as:

$$\nu_{v,n,l} = B_w \cdot l + (l-1)\,\mathrm{BG} + \mathrm{VBG} + (n-1)\,\Delta\nu_{ch} + \nu_0 \tag{4.2}$$

and

$$\nu_{b,n,l} = (l-1)\Delta f_b + B_w/2 + (n-1)\,\Delta\nu_{ch} + \nu_0 \tag{4.3}$$

where $\Delta\nu_{ch} = (g + N_B)\ \Delta f_b$ is the channel spacing and ν_0 is the reference optical frequency that, without loss of generality, is set equal to the frequency of the first subcarrier of the first OFDM band of the first channel.

A further simplification, which has negligible impact on the system performance, can be made on the theoretical formulation by assuming that the BG, VBG and B_w are multiples of the OFDM subcarrier spacing Δf_{sc}. In this way, the following definitions are assumed: 1) $\mathrm{BG} = b \cdot \Delta f_{sc}$, 2) $\mathrm{VBG} = v \cdot \Delta f_{sc}$ and 3) $B_w \simeq N_{sc} \cdot \Delta f_{sc}$, where b and v are positive integers and N_{sc} is the number of OFDM subcarriers per OFDM band. After some simple calculations, Eq. 4.2 and Eq. 4.3 are simplified to:

$$\frac{\nu_{v,n,l} - \nu_0}{\Delta f_{sc}} = N_{sc} \cdot l + (l-1)\,b + v + (n-1)(g + N_B)(N_{sc} + b) \tag{4.4}$$

and

$$\frac{\nu_{b,n,l} - \nu_0}{\Delta f_{sc}} = (N_{sc} + b)\,[(n-1)(g + N_B) + (l-1)] + \frac{N_{sc}}{2}. \tag{4.5}$$

From Eq. 4.5, the frequency of the m-th OFDM subcarrier of the l-th band of the n-th channel can be written as:

$$\frac{\nu_{sc,n,l,m} - \nu_0}{\Delta f_{sc}} = (N_{sc} + b)\,[(n-1)(g + N_B) + (l-1)] + m \tag{4.6}$$

with $m \in \{1, 2, \ldots, N_{sc}\}$ (index 1 stands for the subcarrier with lowest frequency and index N_{sc} corresponds to the subcarrier with highest frequency).

Fig. 4.2 illustrates a WDM-MB-OFDM signal spectrum described in terms of the normalized parameters. In this example, the WDM-MB-OFDM signal has 3 optical channels, each with 3 bands, and two different CGs are considered: CG with $g = 0$ and with $g = 1$. Fig. 4.2 shows that, with the increase of the CG, the frequency spacing between the bands of different channels is higher. This reduces the impact of the FWM effect on the different bands and relaxes the power limit due to the fibre nonlinearity at the expense of decreasing the spectral efficiency.

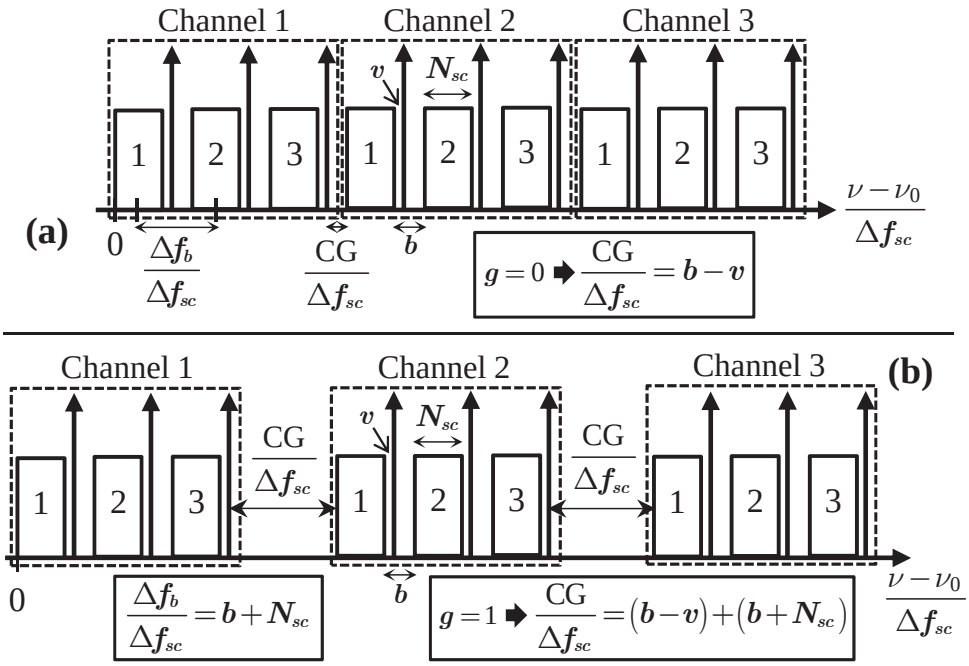

Figure 4.2: Illustration of the WDM-MB-OFDM signal spectrum with 3 optical channels, each with 3 bands, for two different CGs: (a) CG with $g = 0$ and (b) CG with $g = 1$.

4.2.2 Theoretical method for the FWM power

In this section, the TM used to obtain the FWM power of the VC-VC-band products is demonstrated. The VC-VC-band FWM products that contribute to the FWM power are identified and expressions for the FWM power are derived. From the FWM power, the EVM of the OFDM subcarriers due to the FWM effect is estimated.

The FWM effect consists in the generation of a new wave with optical frequency $\nu_n = \nu_i + \nu_j - \nu_k$ resulting from the mixing between three different waves with frequencies ν_i, ν_j and ν_k [86]. When $\nu_i = \nu_j$, the resulting FWM product is called degenerate (DG) and, when $\nu_i \neq \nu_j$, the FWM product is non-degenerate (NDG) [86].

The most important inter-band FWM products in WDM VC-assisted DD MB-OFDM systems are the ones resulting from: i) the mixing between three VCs (VC-VC-VC); ii) the mixing between two VCs and an OFDM subcarrier of a certain band (VC-VC-band); and iii) the mixing between two different subcarriers and a VC (VC-band-band). With the CG defined as in Eq. 4.1, the VC-VC-VC products overlap in frequency with the VCs of each band. Thus, the FWM products which overlap in frequency with the OFDM bands are the VC-VC-band and VC-band-band. These in-band products cause distortion that increases with the fibre nonlinearity strength [36]. In this work, the focus is on the VC-VC-band products, which are considered dominant over the VC-band-band ones. This assumption is valid for systems where the power

of the VC is much higher than the power of the OFDM band, as it is the case of VC-assisted DD MB-OFDM systems employing digital iterative techniques for SSBI mitigation [36]. There are three different types of VC-VC-band FWM products that contribute to the FWM power at the OFDM subcarrier frequency ν_n. i) DG products originated from the mixing between two times a VC with frequency ν_{v,n_1,l_1} (l_1-th VC of the n_1-th channel) and an OFDM subcarrier with frequency $\nu_k = 2 \times \nu_{v,n_1,l_1} - \nu_n$. ii) NDG products originated from two different VCs with frequencies ν_{v,n_1,l_1} and ν_{v,n_2,l_2} (l_2-th VC of the n_2-th channel) and an OFDM subcarrier with frequency $\nu_k = \nu_{v,n_1,l_1} + \nu_{v,n_2,l_2} - \nu_n$ (NDG1-type products). iii) NDG products originated from two different VCs with frequencies ν_{v,n_1,l_1} and ν_{v,n_2,l_2} and an OFDM subcarrier with frequency $\nu_j = \nu_{v,n_2,l_2} - \nu_{v,n_1,l_1} + \nu_n$ (NDG2-type products).

The FWM power depends on the strength of each mixing product, which is regulated by the FWM efficiency [87]. For a multi-span system with N_{sp} fibre spans of length L_f, the FWM efficiency η_{FWM} of a generic mixing product with frequency $\nu_n = \nu_i + \nu_j - \nu_k$ is given by [87,88]:

$$\eta_{\mathrm{FWM}}(\nu_i,\nu_j,\nu_k) = \frac{1}{{N_{sp}}^2}\frac{\alpha^2}{\alpha^2+\Delta\beta^2}\frac{\sin^2(N_{sp}\Delta\beta\frac{L_f}{2})}{\sin^2(\Delta\beta\frac{L_f}{2})} \times \left\{1 + \frac{4\cdot\exp\left(-\alpha L_f\right)}{\left[1-\exp\left(-\alpha L_f\right)\right]^2}\sin^2\left(\Delta\beta\frac{L_f}{2}\right)\right\} \tag{4.7}$$

with $\Delta\beta$ obtained from Eq. F.19. The contribution of the term dependent on $\partial D(\lambda)/\partial\lambda$ in Eq. F.19 can be neglected at wavelengths far from the wavelength corresponding to zero fibre dispersion [88].

The FWM power at a certain frequency depends on the FWM efficiencies of the FWM products falling on that frequency. For the DG-type products, the FWM power at a certain frequency ν_n, $P^{(\mathrm{DG})}_{\mathrm{FWM},n}$, is given by (additional details provided in section F.2.3):

$$P^{(\mathrm{DG})}_{\mathrm{FWM},n} = (D_{\mathrm{DG}})^2\,\zeta \sum_{n=1}^{N_{ch}}\sum_{l=1}^{N_B}\eta_{\mathrm{FWM}}(\nu_j,\nu_j,\nu_k)\Big|\begin{array}{l}\nu_j=\nu_{v,n,l}\\ \nu_k=2\nu_j-\nu_n\end{array} \tag{4.8}$$

where $\zeta = (N_{sp}\gamma L_e P_{\mathrm{VC}})^2 P_{sc}$, D_{DG} is the degeneracy factor for the DG products which equals 1. γ is the fibre nonlinearity coefficient, L_e is the effective length per span, P_{VC} is the VC power and P_{sc} is the OFDM subcarrier power. For the NDG1-type products, the FWM power at a certain frequency ν_n, $P^{(\mathrm{NDG1})}_{\mathrm{FWM},n}$, is given by:

$$P^{(\mathrm{NDG1})}_{\mathrm{FWM},n} = (D_{\mathrm{NDG}})^2\,\zeta \sum_{\substack{n_1=1\\(n_1>n_2)\vee[(n_1=n_2)\wedge(l_1>l_2)]}}^{N_{ch}}\sum_{n_2=1}^{N_{ch}}\sum_{l_1=1}^{N_B}\sum_{l_2=1}^{N_B}\eta_{\mathrm{FWM}}(\nu_i,\nu_j,\nu_k)\Big|\begin{array}{l}\nu_i=\nu_{v,n_1,l_1}\\ \nu_j=\nu_{v,n_2,l_2}\\ \nu_k=\nu_i+\nu_j-\nu_n\end{array} \tag{4.9}$$

where D_{NDG} is the degeneracy factor for the NDG products which equals 2.

For the NDG2-type products, the FWM power at a certain frequency ν_n, $P_{\mathrm{FWM},n}^{(\mathrm{NDG2})}$, is given as follows:

$$P_{\mathrm{FWM},n}^{(\mathrm{NDG2})} = (D_{\mathrm{NDG}})^2\,\zeta \sum_{\substack{n_1=1}}^{N_{ch}} \sum_{n_2=1}^{N_{ch}} \sum_{l_1=1}^{N_B} \sum_{l_2=1}^{N_B} \eta_{\mathrm{FWM}}(\nu_i,\nu_j,\nu_k) \Bigg| \begin{array}{l} \nu_i = \nu_{v,n_1,l_1} \\ \nu_k = \nu_{v,n_2,l_2} \\ \nu_j = \nu_k + \nu_n - \nu_i \end{array} \tag{4.10}$$
$$(l_1 \neq l_2) \vee [(l_1 = l_2) \wedge (n_1 \neq n_2)]$$

Different types of VC-VC-band FWM products have a different impact on the OFDM bands. If the condition $b \leq N_{sc} + 2v - 1$ holds, the DG and NDG1 products interfere partially with an OFDM band. For an OFDM band with central frequency $\nu_{b,n,l}$, the DG and NDG1 products which interfere with the OFDM band are centred at a frequency equal to $\nu_{b,n,l} + (2v - b)\Delta f_{sc}$. The number of OFDM subcarriers affected by these products is $N_{sc} - b + 2v - 1$. If the condition $b > N_{sc} + 2v - 1$ holds, the DG and NDG1 products do not interfere with the OFDM bands. The NDG2 products are centred at the same frequency as the OFDM bands. The most bandwidth-efficient case is when the condition $b \leq N_{sc} + 2v - 1$ holds. This bandwidth-efficient case is hereafter considered. For this case, using Eq. 4.8, Eq. 4.9 and Eq. 4.10, the FWM power generated at the frequency ν_n (where ν_n corresponds to the m-th OFDM subcarrier of the l-th band of the n-th channel) is given by:

$$P_{\mathrm{FWM},n}(\nu_n = \nu_{sc,n,l,m}) = \begin{cases} P_{\mathrm{FWM},n}^{(\mathrm{DG})} + P_{\mathrm{FWM},n}^{(\mathrm{NDG1})} + P_{\mathrm{FWM},n}^{(\mathrm{NDG2})}, & 1 \leq m \leq \Gamma \\ P_{\mathrm{FWM},n}^{(\mathrm{NDG2})}, & \Gamma < m \leq N_{sc} \end{cases} \tag{4.11}$$

with $\Gamma = N_{sc} - b + 2v - 1$.

The EVM of an OFDM subcarrier due to the FWM effect can be approximated by the ratio between the FWM power falling on the frequency of that subcarrier and the power of the OFDM subcarrier [84]. Hence, the average EVM due to the FWM effect, in decibel, of the l-th band of the n-th channel, $EVM_{\mathrm{FWM},n,l}$, can be obtained by averaging the EVM due to the FWM effect of each subcarrier over all the OFDM subcarriers of the l-th band of the n-th channel, as follows:

$$EVM_{\mathrm{FWM},n,l} = 10\log_{10}\left[\frac{1}{N_{sc}} \sum_{m=1}^{N_{sc}} \frac{P_{\mathrm{FWM},n}(\nu_n = \nu_{sc,n,l,m})}{P_{sc}}\right]. \tag{4.12}$$

4.2.3 Maximum allowed average power estimation for the worst pair band-VC

Low-dispersion fibre transmission

For the case of low fibre dispersion, the FWM efficiency is close to one and the summations of the different efficiencies to obtain the FWM power at a given frequency (see Eq. 4.8, Eq. 4.9 and Eq. 4.10) can be replaced, as a good approximation, by the number of FWM products falling at that frequency. With this approximation, a simplified expression for the FWM power that enables estimating the maximum allowed average power of the worst pair band-VC of the WDM-MB-OFDM signal (pair band-VC including the OFDM band most impaired by FWM) is obtained. The estimation provided by the simplified expression is hereafter referred to as the STM for transmission with low-dispersion fibres. As the target of the application scenario considered in this work is to deliver one band to each user, the analysis is focused on the worst case scenario, that is, on the analysis of the band most affected by the FWM power (worst band).

Expressions for the number of VC-VC-band FWM products of types DG, NDG1 and NDG2 (N_{DG}, N_{NDG1} and N_{NDG2}, respectively) falling in the worst OFDM subcarriers (the ones affected by the three FWM products) of the worst band were derived considering a MB-OFDM signal with an arbitrary number of N_B bands and with $g = 0$ (situation with higher spectral efficiency and higher FWM power). These expressions are shown in Tab. 4.1. For channels with even N_B, the worst band is the $[(N_B/2) + 1]$-th band. For channels with an odd N_B number, the worst band is the $[(N_B + 1)/2]$-th band.

Table 4.1: Number of FWM products of the three different types of FWM (N_{DG}, N_{NDG1} and N_{NDG2}) as a function of N_B, for the worst band, with $n \in \mathbb{N}$.

FWM products	N_{DG}	N_{NDG1}	N_{NDG2}
N_B even (2,4,6,...)	$\frac{N_B}{2}$	$\frac{3}{8}{N_B}^2 - \frac{1}{4}N_B$	$\frac{3}{4}{N_B}^2 - N_B$
$N_B = 4n - 1$ (3,7,11,...)	$\frac{N_B + 1}{2}$	$\frac{3}{8}{N_B}^2 - \frac{1}{4}N_B - \frac{5}{8}$	$\frac{3}{4}{N_B}^2 - N_B + \frac{1}{4}$
$N_B = 4n + 1$ (5,9,13,...)	$\frac{N_B - 1}{2}$	$\frac{3}{8}{N_B}^2 - \frac{1}{4}N_B - \frac{1}{8}$	$\frac{3}{4}{N_B}^2 - N_B + \frac{1}{4}$

The expressions of Tab. 4.1 allow obtaining an upper bound of the FWM power for WDM transmission with low dispersion and with the minimum CG ($g = 0$), as this particular WDM signal has the same spectral occupancy of a single-channel signal with $N_{ch} \cdot N_B$ bands. For the low fibre dispersion case, the FWM power interfering with the m-th OFDM subcarrier of the

worst band (l_w-th pair band-VC of the n_w-th channel) can be simplified to the following:

$$P_{\mathrm{FWM},n}(\nu_n = \nu_{sc,n_w,l_w,m}) \approx \begin{cases} \left[(D_{\mathrm{DG}})^2 N_{\mathrm{DG}} + (D_{\mathrm{NDG}})^2 (N_{\mathrm{NDG1}} + N_{\mathrm{NDG2}})\right] \zeta, & 1 \leq m \leq \Gamma \\ (D_{\mathrm{NDG}})^2 N_{\mathrm{NDG2}}\, \zeta, & \Gamma < m \leq N_{sc}. \end{cases} \tag{4.13}$$

Using Eq. 4.13 and assuming that the product $N_{ch} \cdot N_B$ is even, a closed-form expression for the maximum allowed average power of the worst pair band-VC in dBm, $P_{b,w}$, in MB-OFDM systems with low-dispersion fibres, for a given EVM impaired by FWM, EVM_{NL}, can be obtained as follows:

$$\begin{aligned} P_{b,w} =& \frac{EVM_{\mathrm{NL}}}{2} + 30 - 10\log_{10}\left(N_{sp}\gamma L_e\right) + 10\log_{10}\left(\frac{1+vbpr}{vbpr}\right) - \\ & - 5\log_{10}\left\{\left(\frac{3}{8}\frac{\Gamma}{N_{sc}} + \frac{3}{4}\right)(D_{\mathrm{NDG}})^2 N_t^2 + \left[\frac{1}{2}\frac{\Gamma}{N_{sc}} - \left(\frac{1}{4}\frac{\Gamma}{N_{sc}} + 1\right)(D_{\mathrm{NDG}})^2\right] N_t\right\} \end{aligned} \tag{4.14}$$

with $N_t = N_{ch} \cdot N_B$ and $vbpr = 10^{(VBPR_{dB}/10)}$ ($VBPR_{dB}$ is the VBPR in dB). Note that the average power of the VC close to the worst band, $P_{v,w}$, relates to $P_{b,w}$ by: $P_{v,w} = P_{b,w} + 10\log_{10}[vbpr/(1+vbpr)]$. The average power per channel is given by $10\log_{10}(N_B) + P_{b,w}$.

For the sake of illustration, Fig. 4.3 depicts the number of VC-VC-band FWM products of types DG, NDG1 and NDG2 as a function of the normalized frequency $(\nu - \nu_0)/\Delta f_{sc}$, for a single MB-OFDM signal with $N_B = 5$, $N_{sc} = 8$, $b = 10$ and $v = 3$. As a reference, the spectral location of the MB-OFDM signal is shown as well. With $b = 10$ and $v = 3$, $\Gamma = 3$ is obtained, which means that, for each OFDM band, 3 subcarriers are impaired by all the VC-VC-band products and 5 subcarriers ($N_{sc} - \Gamma = 5$) are impaired only by the NDG2-type product. Fig. 4.3 shows that the third and fourth bands are the ones which have the higher number of FWM products interfering with the OFDM bands (24 in total). Due to the higher degeneracy factor of the NDG-type products, the worst-band is the third band.

High-dispersion fibre transmission

The maximum allowed average power of the worst pair band-VC provided by Eq. 4.14 assumes that all VC-VC-band FWM products have maximum FWM efficiency after the transmission along several number of spans, which is not the case for high-dispersion fibre, such as SSMF. For high-dispersion fibre, the FWM efficiencies of the different FWM products have to be taken into account. As the number of WDM channels increases, the number of FWM products to be accounted to obtain an accurate EVM estimation also increases, requiring more computational

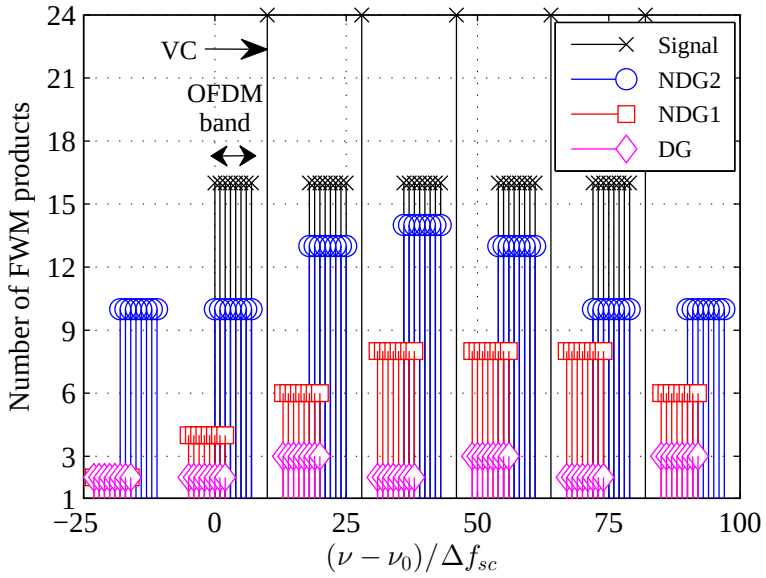

Figure 4.3: Number of VC-VC-band FWM products of types DG (diamonds), NDG1 (squares) and NDG2 (circles) as a function of the normalized frequency $(\nu-\nu_0)/\Delta f_{sc}$, for a MB-OFDM signal with $N_B=5$, $N_{sc}=8$, $b=10$ and $v=3$. The MB-OFDM signal spectral location is also shown, as a reference.

time to perform the estimation. As shown in Tab. 4.1, the total number of VC-VC-band FWM products falling on a specific OFDM subcarrier (in the case of Tab. 4.1 the subcarrier belongs to the worst band) increases proportionally to the square of the total number of OFDM bands of all WDM channels. Following a procedure similar to the low-dispersion fibre case, this subsection presents a closed-form expression for the maximum allowed average power of the worst pair band-VC in MB-OFDM systems employing high-dispersion fibres. This is achieved by reducing the complexity of the expressions for the FWM power presented in section 4.2.2.

As the majority of the FWM products are of the type NDG2 (see Tab. 4.1), the DG and NDG1-type products are neglected and the FWM power is derived considering only the NDG2-type products. In addition, to simplify the analysis, it is considered that N_{ch} is odd.

If only the NDG2-type products are considered and assuming that the variation of the dispersion parameter along the wavelength is negligible, Eq. F.19 can be written as:

$$\Delta\beta \approx \frac{2\pi\lambda^2}{c}\cdot \underbrace{(l'\Delta f_b)}_{\Delta\nu_{ik}=\nu_i-\nu_k}\cdot \underbrace{(p'\Delta f_b-\mathrm{VBG}+m\Delta f_{sc}-B_w)}_{\Delta\nu_{jk}=\nu_j-\nu_k}\cdot D(\lambda) \tag{4.15}$$

where $l'=l+g\lceil l/N_B\rfloor$, $p'=p+g\lceil p/N_B\rfloor$ with $l,p\in[-(N_t-1)/2,(N_t-1)/2]$ and $l,p\in\mathbb{Z}$, $m=\{1,2,\ldots,N_{sc}\}$, and with $\lceil\cdot\rfloor$ representing the operation of rounding to the nearest integer. The values of l' and p' used in Eq. 4.15 are related to the frequency slot where the worst band is located. The worst band corresponds to the case where l' and p' are zero. The bands located in

frequency slots at a lower frequency than the worst band have negative l' and p' and the bands located in frequency slots at a higher frequency than the worst band have positive l' and p'. The higher the frequency gap between a band and the worst band, the higher the values of $|l'|$ and $|p'|$. The rounding operation in l' and p' ensures that $\Delta\nu_{ik}$ and $\Delta\nu_{jk}$ are calculated with frequencies inside frequency slots with OFDM bands instead of frequency slots corresponding to the CGs. For the sake of illustration, Fig. 4.4 shows a WDM-MB-OFDM signal with 3 channels with 3 bands each and CG with $g = 1$ with the values of l' and p' inside the OFDM bands. Fig. 4.4 shows that the values ±2 correspond to the CGs, the value zero to the worst band (the central band with respect to all the channels), and the values ±1, ±3, ±4 and ±5 to the other bands. For the signal illustrated in Fig. 4.4, given that $N_B = 3$, $N_t = 9$, $g = 1$ and $l \in [-4, 4]$, $l' = l + \lceil l/3 \rfloor$ is obtained. This gives $l' = l$ for $l = \{-1, 0, 1\}$, $l' = l + 1$ for $l = \{2, 3, 4\}$ and $l' = l - 1$ for $l = \{-2, -3, -4\}$. The possible values for l' are 0, ±1, ±3, ±4 and ±5, which are exactly the same values attributed to the OFDM bands when $l \in [-4, 4]$. The same procedure can be applied to p' as $p \in [-4, 4]$.

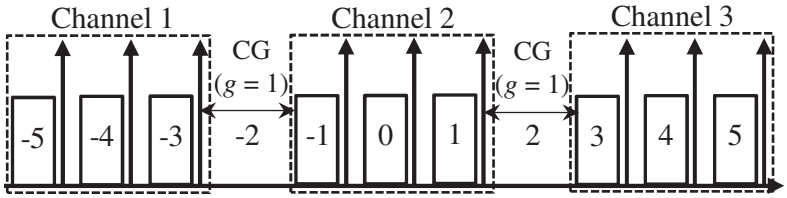

Figure 4.4: WDM-MB-OFDM signal with 3 channels with 3 bands each and CG with $g = 1$, with the values of l' and p' inside the OFDM bands.

In order to further simplify the calculation of the FWM power, the frequency range of $\Delta\nu_{jk}$ is truncated when calculating the different FWM efficiencies in Eq. 4.15, by limiting the minimum and maximum values of p. With this, $p \in [-\Lambda, \Lambda]$ is set, where Λ is a limiting parameter $[0 \leq \Lambda \leq (N_t - 1)/2]$. When the FWM power of the NDG2-type products is evaluated in Eq. 4.10, all the NDG2-type products are accounted for, that is, $\Lambda = (N_t - 1)/2$. With $\Lambda < (N_t - 1)/2$, not all NDG2-type products are accounted for in the FWM power. In this case, from Eq. 4.7 and Eq. 4.15, the products with lower FWM efficiency are being neglected. A good value for Λ is the one that gives less than the total number of NDG2-type products but still enables a good FWM power estimate. Further investigation has shown that a good maximum allowed average power estimate is obtained when $\Lambda \geq 7$, for different number of spans, channel gaps and number of WDM channels. For this reason, hereafter, $\Lambda = 7$ is considered. With $\Lambda = 7$, $\Delta\nu_{jk}$ is limited to 7 bands apart from the worst band (the value of p goes from -7 to 7). For channels with 5 bands each, $\Lambda = 7$ is equivalent to say that the $\Delta\nu_{jk}$ range is limited to 3 channels: the channel with the worst band (n_w) and the two channels which are neighbours to the channel with the

worst band ($n_w - 1$ and $n_w + 1$).

The maximum allowed average power of the worst pair band-VC in dBm, in MB-OFDM systems with high-dispersion fibres, can then be written as:

$$P_{b,w} = \frac{EVM_{\mathrm{NL}}}{2} + 30 - 10\log_{10}\left(N_{sp}\gamma L_e\right) + 10\log_{10}\left(\frac{1+vbpr}{vbpr}\right) - 5\log_{10}\left\{\frac{(D_{\mathrm{NDG}})^2}{N_{sc}}\sum_{m=1}^{N_{sc}}\Upsilon(m)\right\} \tag{4.16}$$

with

$$\Upsilon(m) = \sum_{p=-\Lambda}^{-1}\sum_{\substack{l=-\frac{N_t-1}{2}-p \\ (l\neq 0)}}^{\frac{N_t-1}{2}}\eta_{\mathrm{FWM}}(l,p,m) + \sum_{p=0}^{\Lambda}\sum_{\substack{l=-\frac{N_t-1}{2} \\ (l\neq 0)}}^{\frac{N_t-1}{2}-p}\eta_{\mathrm{FWM}}(l,p,m) \tag{4.17}$$

where $\eta_{\mathrm{FWM}}(l,p,m)$ is given by Eq. 4.7 with $\Delta\beta$ given by Eq. 4.15. The expression $\Upsilon(m)$ gives the sum of the FWM efficiencies of all accounted FWM products at the m-th OFDM subcarrier of the worst band. When evaluating the FWM power in the worst band, the value of $[-(l'+p')]$ identifies the frequency slot in which the VC with frequency ν_k is located. Moreover, when evaluating $\Upsilon(m)$ for $g > 0$ and $p \neq 0$, a condition that depends on the value of $|l'+p'|$ has to hold. This condition is given by:

$$|l'+p'| \neq (g+N_B)n - \frac{(N_B+1)}{2} - r \tag{4.18}$$

with $n = \{1, 2, \ldots, (N_{ch}-1)/2\}$ and $r = \{0, 1, \ldots, g-1\}$. The condition shown in Eq. 4.18 guarantees that the FWM products are evaluated considering that some frequency slots are being used as CGs, that is, slots without transmitting an OFDM band.

4.3 Numerical results and discussion

In this section, the TM validation is performed by comparison with the NS results for different number of fibre spans, CGs and number of WDM channels. A UD band spacing of 3.125 GHz and 10 Gb/s data rate per band are considered. The maximum allowed average power of the worst pair band-VC obtained with the TM and STM are compared considering SSMF transmission. The UBPLs of the VC-assisted MB-OFDM DD metro network provided by both methods are obtained for different number of fibre spans and CGs. The DD-SSB-MB-OFDM metro network employed in this chapter to evaluate the FWM impact on the system performance is similar to

the one presented in section 2.4. The main differences are the following: 1) each node is directly connected to the optical network unit (ONU), that is, optical distribution network (ODN) losses are not considered; 2) to focus the analysis on the performance degradation induced by the FWM effect, optical and electrical noise are neglected; and 3) the performance degradation induced by the reconfigurable optical add-drop multiplexers (ROADMs) cascade is assumed negligible.

The EVM is the figure of merit used to assess the system performance. 300 OFDM information symbols are transmitted and used for EVM evaluation. Although in a deployed system, this number of information symbols can be much higher, there was no advantage of increasing it in the numerical simulations, as it would lead to similar performance results. The EVM in dB of a certain OFDM band, EVM_{dB}, results from the sum of two different contributions: the EVM not impaired by the fibre nonlinearity (EVM_{L}) and the EVM impaired by the fibre nonlinearity (EVM_{NL}). This relation can be written as:

$$EVM_{\mathrm{dB}} = 10\log_{10}\left(10^{\frac{EVM_{\mathrm{L}}}{10}} + 10^{\frac{EVM_{\mathrm{NL}}}{10}}\right) \tag{4.19}$$

where EVM_{L} and EVM_{NL} are expressed in dB. The EVM_{L} includes impairments such as the distortion induced by the imperfect SSB-MB-OFDM signal generators and the imperfect filtering performed by the BS. From [89], the EVM corresponding to an average bit error ratio (BER) of 3.8×10^{-3} (7% FEC [90]) is approximately -18.2 dB for cross 32-quadrature amplitude modulation (QAM) systems. If a maximum of 2 dB for the EVM penalty due to fibre nonlinearity is assumed, $EVM_{\mathrm{L}} = -20.2$ dB is obtained, which gives $EVM_{\mathrm{NL}} \leq -22.5$ dB in order to guarantee that the BER threshold is not surpassed. Thus, the maximum allowed EVM due to fibre nonlinearity, or threshold EVM, is -22.5 dB.

4.3.1 System parameters

The MB-OFDM signal parameters are summarized in Tab. 4.2. Only the FEC overhead is accounted in the overall bit rate of each band. The SSMF parameters used in the simulation are shown in Tab. 2.2. The length of each SSMF span is 40 km, leading to an effective length L_e of 18.3 km.

A modulation index of 5% is employed [9]. As shown in Eq. 4.14 and Eq. 4.16, the maximum allowed average power limited by the FWM effect is affected by the VBPR. However, in this chapter, the VBPR is set to 9 dB rather than being optimized to minimize the FWM power. This VBPR value is selected due to the convergence requirements of the SSBI mitigation algorithm

Table 4.2: MB-OFDM signal parameters.

Overall bit-rate per band, R_b [Gb/s]	10.7
FEC overhead [%]	7
Pre-FEC BER	3.8×10^{-3}
Data bit-rate per band, R_d [Gb/s]	10
Band spacing, Δf_b [GHz]	3.125
Number of subcarriers per OFDM band, N_{sc}	128
QAM mapping order	32
OFDM symbol duration, t_s [ns]	59.8
Cyclic prefix (CP) duration [ns] ($= t_s/N_{sc}$)	0.47
Bandwidth of each OFDM band, B_w [GHz]	2.14
Subcarrier spacing, Δf_{sc} [MHz] ($= 1/t_s$)	16.7
VBG [MHz] ($= 3\Delta f_{sc}$)	50.1
BG [MHz]	985

which operates adequately only for VBPR ≥ 7.5 dB for cross 32-QAM [63]. The BS is optimized in terms of central frequency and bandwidth for each pair band-VC. The BS central frequency is equal to the central frequency of each pair band-VC and the BS -3 dB bandwidth is 400 MHz larger than the bandwidth of the OFDM band. These BS optimization values ensure that crosstalk from neighbouring bands is negligible.

4.3.2 Validation of the theoretical methods

In this section, the TM is validated by comparison with the NS results considering SSMF transmission. The EVMs obtained from the TM are evaluated using Eq. 4.12. After validation, the maximum allowed average powers of the worst pair band-VC obtained with the TM and the STM for high-dispersion fibres (such as the SSMF) are compared. The STM-estimated average powers are assessed using Eq. 4.16. The maximum average power level per optical channel corresponding to the threshold EVM, hereafter defined as the threshold average power (TAP), is also evaluated in this section for an UDWDM network with different number of optical channels and different number of SSMF spans. In this section, the EVMs obtained from the TM result from adding the theoretical FWM EVM estimates (EVM_{NL}) and the EVM of the MB-OFDM system in back-to-back operation obtained through NS ($EVM_{\mathrm{L}} = -32.3$ dB). With $EVM_{\mathrm{L}} = -32.3$ dB, the threshold EVM (-22.5 dB) is reached for $EVM_{\mathrm{NL}} \approx -23.0$ dB.

The validation of the TM and STM is accomplished for a metro network with a maximum of 6 spans, a span length of 40-km, and a maximum CG of 10.31 GHz (CG with $g = 3$). In Appendix G and in [70], it was shown that the efficiency of the nonlinear effects depends on the time-delay between the signals of different bands at the input of the first span. Considering the

results obtained in Appendix G, 16 independent non-synchronized signal runs are generated in the simulation process and the average EVM over all runs is evaluated. For each signal run, random delays between different bands and different channels, and random binary sequences for each band are considered to ensure that the bands are decorrelated inside each channel and between channels. The final EVM is obtained by averaging over the EVMs of the different runs.

Fig. 4.5 shows the EVM obtained from the TM and by NS as a function of the average power at the SSMF input for the third-band. A single MB-OFDM signal with 5 bands is transmitted over 1, 3 and 6 spans. This analysis allows identifying the EVM discrepancies between the TM and NS results in single-channel transmission and to confirm if the VC-band-band FWM products can be neglected, as assumed by the TM derived in section 4.2.2. Fig. 4.5 shows that the TM provides good estimates for the EVM obtained with NS. The EVM difference does not exceed 1 dB for EVMs below the threshold EVM. Two different effects contribute to this discrepancy: i) the non-null uncertainty of the EVM convergence process after performing the average over the independent signal runs; and ii) the neglected contribution of the VC-band-band FWM products. The small EVM discrepancy not exceeding 1 dB suggests the VC-band-band products can be neglected while maintaining acceptable accuracy of the EVM estimation.

Using the STM given by Eq. 4.14, which considers the FWM power estimation given by Eq. 4.13 obtained with a FWM efficiency of one, the TAP of a single channel with 5 bands is 2.9, -1.9 and -4.9 dBm for 1, 3 and 6 spans, respectively. Compared with the TM, these results correspond to a TAP discrepancy of 0, 0.5 and 1.2 dB for 1, 3 and 6 spans, respectively. These discrepancies are due to the FWM efficiency reduction caused by the higher level of accumulated dispersion when the number of spans increases.

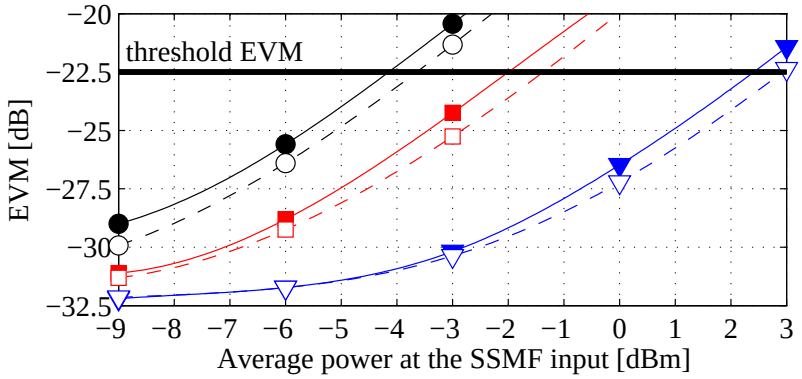

Figure 4.5: EVM of the third-band of a single-channel MB-OFDM signal as a function of the average power at the SSMF input. TM (empty symbols) and NS (filled symbols) results are shown. Transmission along 1 (triangles), 3 (squares) and 6 (circles) spans is considered.

Fig. 4.6 shows the power spectral density (PSD) before and after nonlinear transmission of a

single-channel MB-OFDM signal with 5 bands, for a performance level close to the threshold EVM (single-span transmission and average power at the SSMF input of 3 dBm are considered). Fig. 4.6 shows the FWM products (VC-VC-VC and VC-VC-band) appearing around the signal spectra. Some in-band VC-VC-VC and VC-VC-band FWM products (which cannot be seen in the spectra of Fig. 4.6 but are similar to the ones that can be seen around the signal spectra) overlap in frequency with the VCs and OFDM bands, respectively. These in-band FWM products are responsible for the performance degradation with the increase of the fibre nonlinearity effect. Inset of Fig. 4.6 illustrates the spectra of the three different types of VC-VC-band FWM products identified in section 4.2.2. Each one of these products has a bandwidth equal to the bandwidth of a OFDM band. The higher power level observed in the inset [marked as (b)] results from the superposition of the three VC-VC-band FWM products.

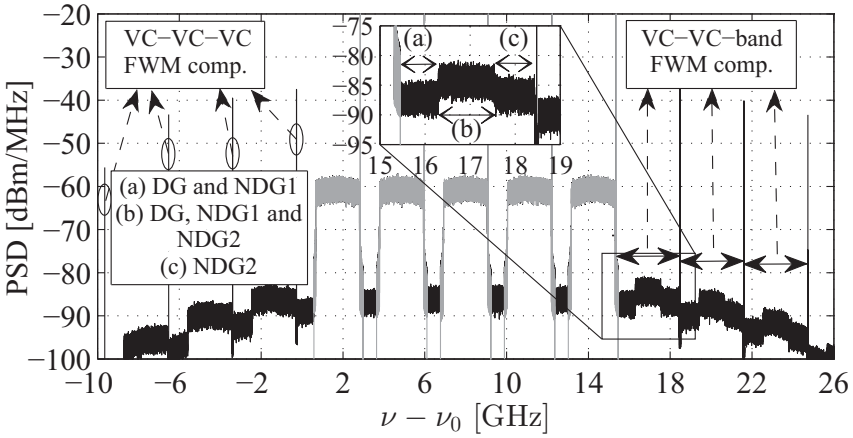

Figure 4.6: Optical spectra before (grey) and after (black) single-channel MB nonlinear transmission along 1 span, with average power at the SSMF input of 3 dBm.

Fig. 4.7 shows the EVM evaluated from the TM and obtained by NS as a function of the average power at the SSMF input per WDM channel. Results of the third-band of the first-channel (edge channel) and of the third-band of the fifth-channel (centre channel) are shown. A WDM MB-OFDM signal with 9 channels ($N_{ch} = 9$) and 5 bands per channel is considered. The transmission is performed along 1, 3 and 6 SSMF spans and two different CGs are considered (see Eq. 4.1): CG with $g = 0$ (minimum CG: CG = BG − VBG = 0.935 GHz) and CG with $g = 3$ (CG $= 3 \cdot \Delta f_b +$ BG − VBG = 10.31 GHz). This analysis aims at evaluating the accuracy of the TM to describe the FWM degradation in multi-channel operation. Four main conclusions can be drawn from inspection of Fig. 4.7. (i) For higher number of spans and higher CGs, that is, for lower FWM efficiency, the EVM estimates obtained from the TM show lower discrepancy when compared with the EVM estimates obtained with NS. (ii) The third-band of the centre channel presents worse performance results than the third-band of the edge channel. This is due to the higher number of VC-VC-band FWM products falling in the bands of the centre channel

when compared with the bands of other channels. When comparing the TAPs obtained for the third-band of the centre channel and the edge channel, the difference does not exceed 1 dB. (iii) When comparing the EVM results obtained from the TM and by NS, the discrepancies for EVMs below the threshold EVM do not exceed 0.9 dB for 1 span, 0.5 dB for 3 spans and 0.3 dB for 6 spans. This means that the error of the method decreases for systems with several spans, which is the case of real networks. (iv) Increasing the CG from 0.935 GHz ($g = 0$) to 10.31 GHz ($g = 3$), which sacrifices spectral efficiency, allows for a TAP increase close to 2 dB for 1 span and 1 dB for 6 spans.

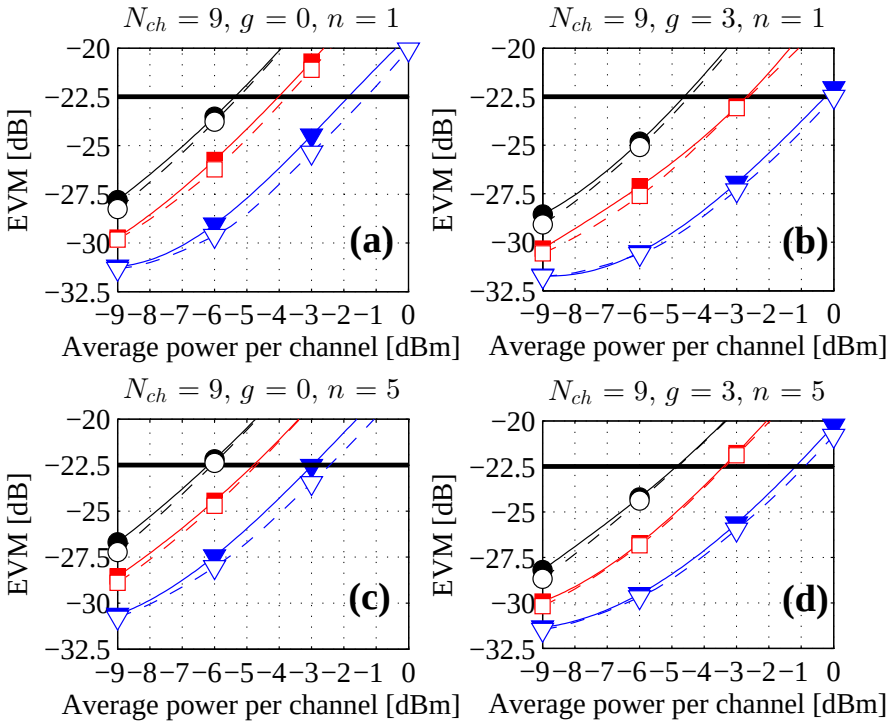

Figure 4.7: EVM evaluated from the TM (empty symbols) and NS (filled symbols) as a function of the average power at the SSMF input per WDM channel, for the third-band of the first-channel ($n = 1$) employing a CG with (a) $g = 0$ and (b) $g = 3$, and for the third-band of the fifth-channel ($n = 5$) with (c) $g = 0$ and (d) $g = 3$. A WDM-MB-OFDM signal with 9 channels ($N_{ch} = 9$) with 5 bands each is transmitted along 1 (triangles), 3 (squares) and 6 (circles) SSMF spans. The black line at EVM = −22.5 dB indicates the threshold EVM.

Fig. 4.8 shows the TAP of the worst pair band-VC as a function of the total number of transmitted WDM channels (5 bands per channel) of a metro network with 1, 3 and 6 spans. The TM, STM and NS results are compared for two different CGs: CG with $g = 0$ and with $g = 3$. Fig. 4.8 shows that good TAP estimates are obtained with the TM. The TAP discrepancy between the TM-estimated and NS-estimated TAPs is around 0.6 dB for one SSMF span, and is negligible for 3 or 6 spans. Fig. 4.8 also shows that the STM results provide a TAP discrepancy not exceeding 1 dB when compared with the TAP evaluated with the TM. About 0.7 dB of the

average power discrepancy is due to the neglected contribution of the DG and NDG1-type products. The remaining average power discrepancy (not exceeding 0.3 dB) is from having $\Lambda = 7$ and not $\Lambda = (N_t - 1)/2$. This small discrepancy with $\Lambda = 7$ indicates that it gives a good approximation of the average power with a higher number of WDM channels and for different number of spans and channel gaps. Inspection of Fig. 4.8 reveals also that, when increasing the number of WDM channels from 13 to 17, the TAP reduction does not exceed 0.1 dB. For this reason, the TAP obtained with the transmission of 17 optical channels is considered a tight estimate of the power limit, which can be considered as the TAP for a network with a very high channel count. Henceforth, the TAP estimate with 17 optical channels is referred to as the UBPL.

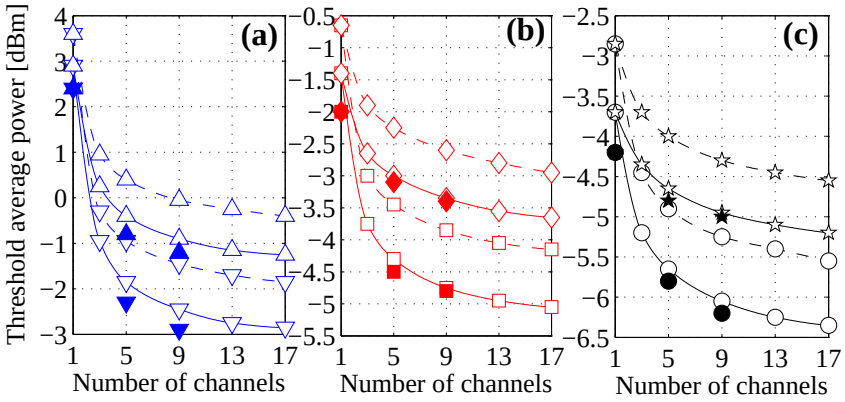

Figure 4.8: Threshold average power of the worst pair band-VC as a function of the number of WDM channels (5 bands per channel). TM (empty symbols with continuous lines), STM (empty symbols with dashed lines), and NS (filled symbols) results are shown for propagation along (a) 1, (b) 3 and (c) 6 SSMF spans and for CGs with $g = 0$ (symbols $\triangledown$, $\square$ and $\bigcirc$) and $g = 3$ (symbols $\triangle$, $\Diamond$ and $\star$).

4.3.3 Upper bound for the power limit

In this section, to extend the analysis of section 4.3.2, the UBPL is evaluated using the TM and STM for up to 10 SSMF spans and for CGs up to 22.81 GHz (CG with $g = 7$). An UDWDM MB-OFDM signal with 17 optical channels, each one with 5 bands (net bit rate of 50 Gb/s per WDM channel) is considered to obtain the UBPL.

Fig. 4.9 shows the UBPL as a function of the CG, for the worst pair band-VC, with transmission along different number of spans and using the TM and the STM. Fig. 4.9 also shows the net spectral efficiency for the considered CGs. The net spectral efficiency is defined as the ratio between the net bit rate per WDM channel and the channel spacing. Two main conclusions can be drawn from the results of Fig. 4.9. (i) Due to the reduction of the FWM efficiency, the UBPL increases for higher CGs. Increasing the CG leads to a higher frequency spacing between

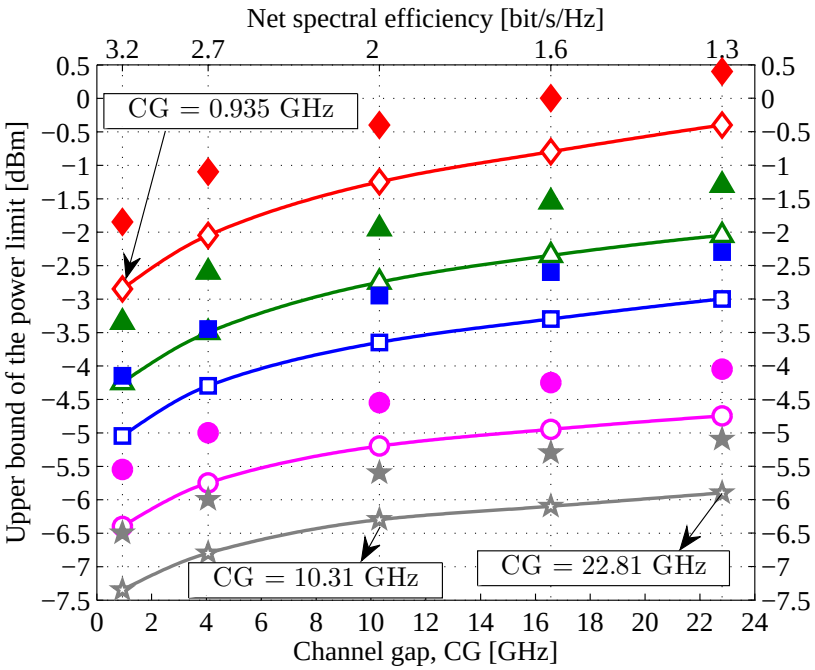

Figure 4.9: Upper bound of the power limit as a function of the CG, for the worst pair band-VC. Results using the TM (empty symbols) and STM (filled symbols) are shown. Transmission along 1 (◊), 2 (△), 3 (□), 6 (○) and 10 (☆) spans is considered. The net spectral efficiency for each considered CG is also shown.

different bands of different channels, as shown in Fig. 4.2. The UBPL improvement obtained when increasing the CG is lower with the increase of the number of spans. As an example, increasing the CG from 0.935 GHz to 22.81 GHz results in an UBPL increase that exceeds 2 dB for 1 span and does not exceed 1.5 dB for 10 spans. (ii) The STM provides UBPLs not exceeding 1 dB from the UBPL obtained with the TM, for all the number of spans and channel gaps considered.

Through a compromise between the UBPL and the net spectral efficiency, a good CG from the fibre nonlinearity viewpoint is when $g = 3$ (CG $\approx$ 10.3 GHz). This CG ensures a high net spectral efficiency ($\geq$ 2 bit/s/Hz). A CG with $g = 3$ enables the transmission along 1 span with a TM-estimated UBPL of -1.3 dBm. With 10 spans, the TM-estimated UBPL decreases to -6.3 dBm (5 dB reduction).

4.4 Conclusions

In this chapter, a TM to evaluate the FWM power in UDWDM VC-assisted MB-OFDM systems using DD has been presented assuming that the VC-VC-band FWM products are dominant over other FWM-induced products. A simplified TM to obtain the FWM power for MB-OFDM

systems with high-dispersion fibre, where only part of the FWM products of the type NDG2 are considered, has been derived to relax the computation complexity of the FWM power evaluation. A closed-form expression for the FWM power in MB-OFDM systems employing low-dispersion fibre has been also proposed. Analytical expressions for the maximum allowed average power of the worst pair band-VC at the fibre input in VC-assisted DD-MB-OFDM systems, for a given EVM impaired by FWM, have also been derived.

The TM and STM validation has been performed considering an application scenario with band spacing of 3.125 GHz and 10 Gb/s data rate per OFDM band. It has been shown that the TM provides good performance estimates of the FWM-induced degradation. The discrepancy between the NS-estimated and TM-estimated TAPs is close to 0.5 dB with 1 SSMF span, and is negligible for 3 or 6 spans. When compared with the NS results, the STM-estimated TAP provides a discrepancy that may achieve 1.5 dB. However, for the scenarios of main interest in which the number of spans is higher than one, the discrepancy does not exceed 1 dB. Using the TM and STM, an UBPL is obtained for an arbitrary number of SSMF spans and CGs. Thus, the proposed methods can be employed as powerful tools to obtain an estimate of the power limit of WDM VC-assisted DD-SSB-MB-OFDM systems limited by the FWM effect.

Chapter 5

Improving the FWM tolerance of VC-assisted DD-MB-OFDM schemes

5.1 Introduction

The study presented in chapter 4 and the work reported in [36] have shown that the system performance of direct-detection (DD)-multi-band (MB)-orthogonal frequency-division multiplexing (OFDM) networks is remarkably impaired by the four wave mixing (FWM) effect due to the existence of several tight-spaced OFDM subcarriers and virtual carriers (VCs) that origin a considerable amount of FWM products. This effect constrains the tolerance of these systems to the fibre nonlinearity, and thus, imposes a maximum optical power launched into the fibre.

Several techniques were proposed in the last years to relax the fibre nonlinearity impact on the performance of OFDM-based systems [47, 62, 91–99]. Most of these techniques focused on relaxing the impact of fibre nonlinearity in OFDM-based systems employing coherent-detection. In the scope of DD-OFDM-based systems, only a few techniques were reported. In [62], the fibre nonlinearity tolerance in a 10 Gb/s single sideband (SSB) DD-OFDM system was increased using a peak-to-average power ratio (PAPR) reduction technique based on symbol precoding. A bit error ratio (BER) improvement of 2 orders of magnitude after the propagation along 75 km of standard single mode fibre (SSMF) was shown. In [98], it was demonstrated that phase-conjugated twin-waves can be used in DD-OFDM systems to increase the tolerance to fibre nonlinear impairments. A BER improvement of 2 orders of magnitude was shown in a 5 Gb/s DD-OFDM system, leading to a 4 dB increased tolerance in the received optical power. Another technique for increasing the fibre nonlinearity tolerance was presented in [99], which

used a PAPR reduction technique based on the transmission of a constant envelope signal in a 10 Gb/s DD-OFDM system. A BER improvement of 3 orders of magnitude after the propagation along 960 km of SSMF was shown. The works reported in [62,98,99] were developed considering single-band transmission.

The impact of the FWM effect on the performance of wavelength division multiplexing (WDM) DD-MB-OFDM systems employing a VC-assisted DD-MB-OFDM scheme was extensively studied in chapter 4. It was shown that FWM is dominant over other fibre nonlinear effects such as self phase modulation (SPM) or cross phase modulation (XPM). In chapter 4, the distribution of the VCs and OFDM bands in the frequency domain was not optimized. By optimizing the distribution of the OFDM bands and VCs in VC-assisted DD MB-OFDM systems, a reduction of the impact of the FWM products on the system performance is expected.

In this chapter, VC-assisted DD MB-OFDM schemes with high tolerance to the FWM effect are proposed. These schemes are selected from a set of alternative MB-OFDM schemes chosen with high potential to increase the tolerance to the FWM effect. The increase of the number of users potentiated by relaxing the impact of the FWM effect on the proposed VC-assisted DD MB-OFDM metro-access network is also assessed.

This chapter is structured as follows. In section 5.2, the limits and compromises when designing new VC-assisted schemes are analysed and discussed. In section 5.3, the performance results of the WDM metro-access network employing the new VC-assisted MB-OFDM schemes are assessed. The power budget (PB) improvements provided by these new schemes are also shown. In section 5.4, the main conclusions are summarized.

The work presented along this chapter is also published in [64].

5.2 VC-assisted DD-MB-OFDM schemes

5.2.1 Design of VC-assisted schemes

In a VC-assisted DD-MB-OFDM scheme, each OFDM band is assisted by one VC for detection at the receiver side and each band is dedicated to a given user of the access network. The VCs can be located near the OFDM subcarrier with lowest or highest frequency. To relax the bandwidth requirements of the receiver front-end, a small virtual carrier-to-band gap (VBG) is required [9]. However, a small VBG leads to significant performance degradation due to

the signal-signal beat interference (SSBI) [9]. SSBI can be efficiently mitigated with an iterative digital signal processing (DSP) algorithm [36], techniques based on Volterra inverse theory [100], linearisation filters [101] or using the Kramers-Kronig scheme [101]. All these techniques require a high virtual carrier-to-band power ratio (VBPR) (≥ 6 dB) to operate adequately.

So far, the design of VC-assisted DD MB-OFDM systems has been accomplished using the VC near the OFDM subcarrier with highest frequency [9,35–37,76,102]. Hereafter, the signal scheme where the VC is located near the OFDM subcarrier with highest frequency for all pairs band-VC is referred to as the baseline scheme. Fig. 5.1 depicts the WDM signal spectrum together with the MB-OFDM signal employing the baseline scheme. For the baseline scheme, the channel bandwidth (CB) is given by $\mathrm{CB} = (N_B - 1)\Delta\nu_m + B_w + \mathrm{VBG}$, and the channel gap (CG) by $\mathrm{CG} = g\Delta\nu_m + \mathrm{BG} - \mathrm{VBG}$, where N_B corresponds to the number of OFDM bands per WDM channel, g is the number of empty frequency slots occupied by the CG, $\Delta\nu_m$ is the width of each frequency slot, B_w corresponds to the OFDM signal bandwidth and BG is the band gap. With $\Delta\nu_{ch} = \mathrm{CB} + \mathrm{CG}$, the channel spacing can be written as $\Delta\nu_{ch} = (N_B + g)\Delta\nu_m$. Moreover, $\Delta\nu_m$ can be expressed as $\Delta\nu_m = B_w + \mathrm{BG}$.

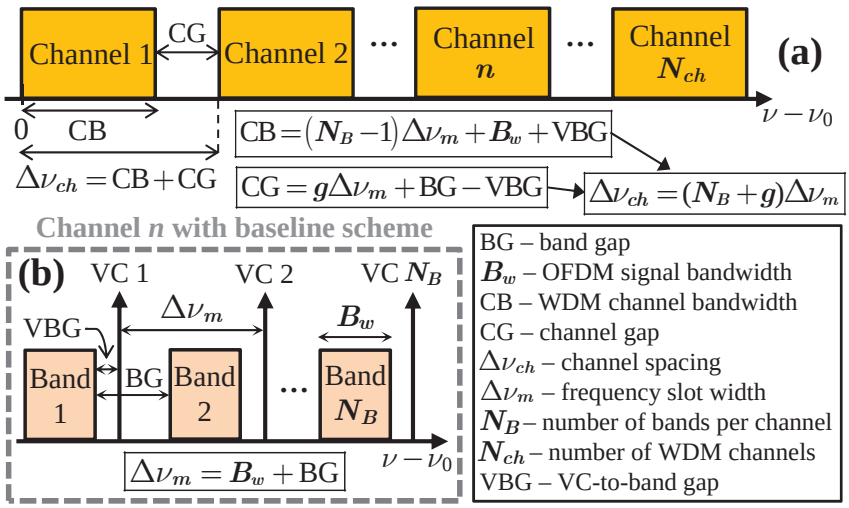

Figure 5.1: (a) WDM signal spectrum. (b) MB-OFDM signal using the baseline scheme.

In VC-assisted DD-MB-OFDM systems, the dominant FWM products result from the mixing between three VCs (VC-VC-VC products) and from the mixing between two VCs and an OFDM band (VC-VC-band products) [37]. By using frequency slots for each OFDM band and corresponding VC (pair band-VC) with the same bandwidth along the WDM channels and by setting the frequency difference between different VCs as a multiple of $\Delta\nu_m$, the VC-VC-VC products do not interfere with the OFDM subcarriers [37]. In this situation, the VC-VC-band products become the dominant FWM-induced impairment.

In this work, the design of the new VC-assisted schemes considers that: (i) all frequency slots have the same width $\Delta\nu_m$, which can be either 3.125 GHz or 6.25 GHz; (ii) the VBPR is the same for all pairs band-VC; (iii) the OFDM bands have the same bandwidth; (iv) each WDM channel comprises N_B OFDM bands and N_B VCs with $N_B = 4$; (v) the relative frequencies of the bands and VCs from different channels are the same; (vi) the filter for band-VC selection is an ideal brick-wall shaped optical filter; and (vii) the capacity delivered to each user by each band is 10 Gb/s (with $\Delta\nu_m = 3.125$ GHz) and 25 Gb/s (with $\Delta\nu_m = 6.25$ GHz).

In [37], it was shown that the performance of VC-assisted ultradense wavelength division multiplexing (UDWDM) DD MB-OFDM systems with high channel count is impaired mainly by the VC-VC-band FWM products. The properties of the new VC-assisted schemes are similar to the ones of [37], that is, the new VC-assisted schemes continue to present densely-packed OFDM bands and VCs, and WDM transmission with high-channel count. For this reason, in this chapter, the performance of the new VC-assisted schemes is evaluated from their tolerance to the VC-VC-band FWM products.

MB-OFDM schemes with VCs close to the OFDM subcarrier with lowest and highest frequency are analysed. A pair band-VC with the VC located near the subcarrier with lowest frequency is referred to as a L-pair, and a pair band-VC with the VC located near the subcarrier with highest frequency is referred to as a H-pair. Using this notation, the baseline scheme shown in Fig. 5.1 with 4 bands per channel can be represented as {H,H,H,H}. MB-OFDM schemes comprising a slot with a H-pair followed by another slot with a L-pair are not allowed unless an empty slot with width $\Delta\nu_m$ is placed in-between. This ensures that the minimum frequency gap between the two VCs of the H-pair and L-pair is $\Delta\nu_m$ (requirement to avoid interference from the VC-VC-VC products). Fig. 5.2 depicts the schemes {L,H,L,H} and {L,H,E,L,H} to exemplify the difference of having or not an empty slot with width $\Delta\nu_m$ between a H-pair and a L-pair. E-slot represents an empty slot with width $\Delta\nu_m$.

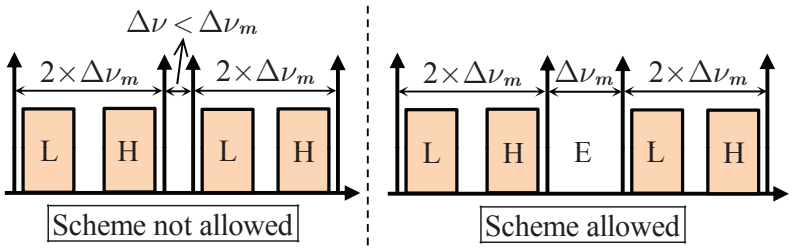

Figure 5.2: Schemes {L,H,L,H} and {L,H,E,L,H}. Slot E represents an empty slot with width $\Delta\nu_m$.

The main goal of these new MB-OFDM schemes is to find the scheme with the highest FWM tolerance while maintaining the same spectral efficiency. The spectral efficiency depends on

the channel spacing $\Delta\nu_{ch}$, which in turn depends on the CB and the CG. By varying the CB and CG while maintaining the same number of transmitted bands per WDM channel, different spectral efficiencies are obtained. In the new VC-assisted schemes, MB-OFDM schemes with three different CB classes are considered: minimum CB, medium CB and maximum CB. In the minimum CB class, the slots within each channel are all occupied with pairs band-VC. In the medium CB class, one slot is empty in-between the slots occupied with pairs band-VC, which means that the CB occupies $N_B + 1$ slots. In the maximum CB class, two slots are empty (contiguous or not) in-between the occupied slots, which means that the CB occupies $N_B + 2$ slots. Parameter δ indicates the number of slots inside the WDM channel that are not occupied with OFDM bands ($\delta = 0$ for minimum CB, $\delta = 1$ for medium CB, and $\delta = 2$ for maximum CB). The channel spacing of the new VC-assisted MB-OFDM schemes can then be written as $\Delta\nu_{ch} = (N_B + g + \delta)\Delta\nu_m$. Note that, as N_B, g and δ are integer numbers, the channel spacing is multiple of $\Delta\nu_m$. Hence, the spectral efficiency of the WDM MB-OFDM signal, η_s, is given by

$$\eta_s = \frac{N_B R_d}{\Delta\nu_{ch}} = \frac{N_B}{N_B + g + \delta}\frac{R_d}{\Delta\nu_m} \tag{5.1}$$

where R_d is the data rate of each OFDM band and the ratio $R_d/\Delta\nu_m$ is the spectral efficiency of each OFDM band.

Tab. 5.1 shows the spectral efficiencies for the VC-assisted MB-OFDM schemes considering different CBs and CGs, with $N_B = 4$, for the two different scenarios considered in this work: $\Delta\nu_m = 3.125$ GHz with $R_d = 10$ Gb/s, and $\Delta\nu_m = 6.25$ GHz with $R_d = 25$ Gb/s. These architectures correspond to WDM channels with a data-rate capacity of 40 Gb/s and 100 Gb/s. Only the cases with spectral efficiencies greater or equal to half of the maximum spectral efficiency are shown in Tab. 5.1. The maximum spectral efficiency (3.2 bit/s/Hz for $\Delta\nu_m = 3.125$ GHz and 4 bit/s/Hz for $\Delta\nu_m = 6.25$ GHz) are achieved with $g = \delta = 0$ and with the baseline scheme. In schemes other than the baseline, $g = 0$ should be avoided as it could lead to a frequency gap of less than $\Delta\nu_m$ between the last VC of channel n and the first VC of channel $n + 1$. Tab. 5.1 shows that, to maintain the spectral efficiency for different schemes, a compromise between δ and g is needed.

When the frequencies of the VCs are maintained, changing the VBG influences the frequency location of the OFDM bands and thus, is expected to influence the frequency location and efficiency of the VC-VC-band products. A wide range of VBGs can be chosen for each pair band-VC. However, some pairs are restricted to small VBGs (VBG $\ll B_w$). These pairs are the ones that have bands surrounded by two VCs separated by $\Delta\nu_m$ (one is the VC of interest and the

Table 5.1: Spectral efficiencies [bit/s/Hz] for the VC-assisted MB-OFDM schemes considering different CBs and CGs, with $N_B = 4$, for two different scenarios: $\Delta\nu_m = 3.125$ GHz with $R_d = 10$ Gb/s, and $\Delta\nu_m = 6.25$ GHz with $R_d = 25$ Gb/s.

$R_d = 10$ Gb/s $\Delta\nu_m = 3.125$ GHz	Baseline ($\delta = 0$)	Min. CB ($\delta = 0$)	Med. CB ($\delta = 1$)	Max. CB ($\delta = 2$)
CG with $g = 0$	3.20	n/a	n/a	n/a
CG with $g = 1$	2.56	2.56	2.13	1.83
CG with $g = 2$	2.13	2.13	1.83	1.60
CG with $g = 3$	1.83	1.83	1.60	< 1.60
CG with $g = 4$	1.60	1.60	< 1.60	< 1.60
$R_d = 25$ Gb/s $\Delta\nu_m = 6.25$ GHz	Baseline ($\delta = 0$)	Min. CB ($\delta = 0$)	Med. CB ($\delta = 1$)	Max. CB ($\delta = 2$)
CG with $g = 0$	4.00	n/a	n/a	n/a
CG with $g = 1$	3.20	3.20	2.67	2.29
CG with $g = 2$	2.67	2.67	2.29	2.00
CG with $g = 3$	2.29	2.29	2.00	< 2.00
CG with $g = 4$	2.00	2.00	< 2.00	< 2.00

other is an unwanted VC from a neighbouring pair which causes crosstalk after photodetection if not sufficiently filtered by the optical filter): L-pair followed by a L-pair, and the H-pair preceded by a H-pair. Let us consider the case with two consecutive L-pairs. This case is illustrated in Fig. 5.3, where it is assumed non-ideal filtering for illustrative purposes. The two consecutive L-pairs are shown before and after filtering, when the VBG of first L-pair is increased in a way that the first band is near the VC of the second pair. If the VBG of the first L-pair is increased in a way that the first band is near the VC of the second pair, the following occurs: 1) when selecting the first pair, to avoid filtering considerably the first band, the second VC is not sufficiently filtered; 2) when selecting the second pair, to avoid filtering considerably the second VC, the first band is not sufficiently filtered. Both cases origin crosstalk after photodetection which will considerably affect the performance.

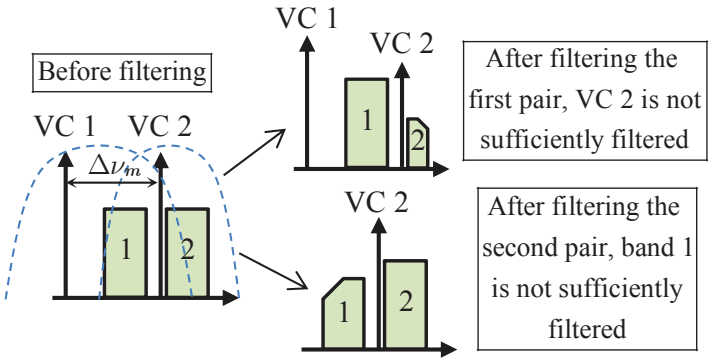

Figure 5.3: Two L-pairs before and after filtering, with the first band near the VC of the second pair. Non-ideal filtering is assumed for illustrative purposes.

5.2.2 New VC-assisted schemes

In this section, a set of possible VC-assisted MB-OFDM schemes with minimum, medium and maximum CB are shown. For each CB class, a scheme is chosen to illustrate the number of VC-VC-VC and VC-VC-band products and the FWM power. Each one of the VC-VC-band products interfering with the OFDM subcarriers, weighted by the corresponding FWM efficiency, will contribute to the FWM power that affects the performance of the OFDM bands.

From the three different types of VC-VC-band FWM products only the non-degenerate (NDG)-type products are shown in this section. Additionally, the normalized FWM power is also shown. The normalized FWM power at a given frequency consists on the sum of the FWM efficiencies from the NDG1-type and NDG2-type products at that frequency [obtained from Eq. 4.9 and Eq. 4.10, respectively] multiplied by 4 (square of the degeneracy factor of the NDG products) [37]. The normalized FWM power is assessed in this section considering slots with $\Delta\nu_m = 3.125$ GHz. A network with reach of 360 km separated evenly by 9 SSMF spans (each with 40-km length) is considered. The SSMF parameters at the wavelength of 1550 nm are shown in Tab. 2.2.

To analyse the impact of changing the VBG on the FWM power in the new VC-assisted schemes which employ $\Delta\nu_m = 3.125$ GHz, two different VBGs are considered: VBG1 $= 2 \cdot \Delta f_{sc} = B_w/64$ (small VBG) and VBG2 $= 32 \cdot \Delta f_{sc} = B_w/4$ (large VBG), where Δf_{sc} is the OFDM subcarrier spacing. With these VBGs, two different configurations are considered. (i) Minimum VBG configuration: all pairs of all schemes have a VBG equal to VBG1. (ii) Relaxed VBG configuration: VBG1 is employed only for L-pairs followed by a L-pair and H-pairs preceded by a H-pair; the other pairs employ VBG2. The baseline scheme considers only the minimum VBG configuration, to stay in accordance with what was presented in chapter 4. To avoid increasing substantially the bandwidth of each pair (bandwidth of the OFDM band plus the VBG), and thus, the OFDM receiver bandwidth, VBG2 was limited to 25% of the OFDM band width.

Minimum CB

Let us consider that all slots inside the WDM channel are occupied with pairs band-VC. With 4 bands per channel, 5 schemes remain (from a total of 16 different schemes) after excluding the ones having a H-pair followed by a L-pair. One is the baseline scheme ({H,H,H,H}) and four are new schemes: {L,L,L,L}, {L,L,L,H}, {L,L,H,H} and {L,H,H,H}. Fig. 5.4 illustrates these new schemes.

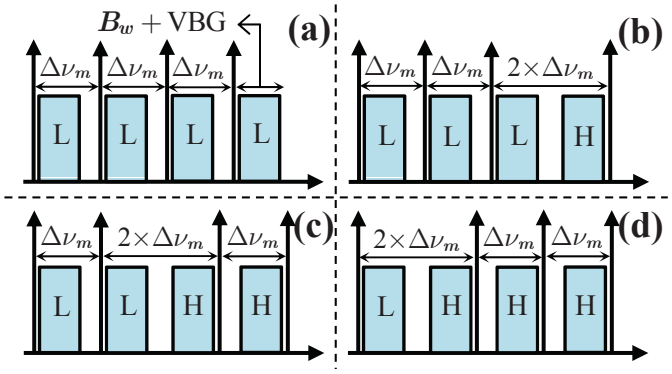

Figure 5.4: Examples of schemes with minimum CB: (a) {L,L,L,L}, (b) {L,L,L,H}, (c) {L,L,H,H}, and (d) {L,H,H,H}.

Fig. 5.5(a) and Fig. 5.5(b) show the number of VC-VC-VC products and VC-VC-band products NDG1 and NDG2 around the third channel for the scheme {L,L,H,H}, with the minimum and relaxed VBG configurations, respectively. Transmission of 5 channels with a CG with $g = 4$ is considered in both configurations to achieve a spectral efficiency of 1.6 bit/s/Hz. For the relaxed VBG configuration, the first and fourth bands employ VBG1 and the second and third bands employ VBG2. Through analysis of Fig. 5.5(a) and Fig. 5.5(b), three main conclusions are drawn. (i) Changing the VBG influences significantly the distribution of the VC-VC-band products inside the OFDM bands. (ii) The VC-VC-VC products do not interfere with the OFDM bands for both configurations and are not influenced by the VBG variation. (iii) For the scheme {L,L,H,H}, the number of NDG2-type products is greater than the number of NDG1-type products. This conclusion holds also for the other schemes with minimum CB under analysis.

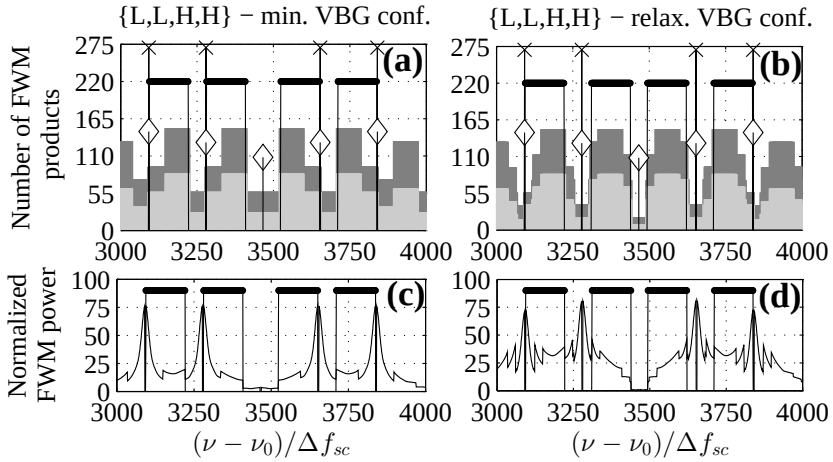

Figure 5.5: Number of VC-VC-VC products (◊) and VC-VC-band products NDG1 (light grey) and NDG2 (dark grey) around the third channel for the scheme {L,L,H,H} with the (a) minimum and (b) relaxed VBG configurations. Transmission of 5 channels with $g = 4$ is considered in both configurations. The spectral location of the subcarriers (dots) and VCs (×) is also shown as a reference (it is not related with the number of FWM products or the normalized FWM power). Normalized FWM power with the (c) minimum and (d) relaxed VBG configurations, together with the spectral location of the subcarriers.

Fig. 5.5(c) and Fig. 5.5(d) show the normalized FWM power for the scheme {L,L,H,H}, with

the minimum and relaxed VBG configurations, respectively. Comparing between the number of FWM products and the normalized FWM power for both configurations reveals that a higher number of VC-VC-band products does not mean necessarily that a higher FWM power is observed. Moreover, it shows that FWM products with the highest power are the ones closer to the VCs. In addition, comparison between Fig. 5.5(c) and Fig. 5.5(d) reveals that the VBG increase experienced by the second and third pairs allows to reduce significantly the FWM power falling on the OFDM bands of those pairs.

Medium CB

For channels with 4 bands, and excluding the ones having a H-pair followed by a L-pair, 25 different schemes with medium CB can be designed. These schemes are obtained considering all different combinations of L, H and E, with exception of the combinations in which the E-slot is located in the edges of the channel. Schemes with the E-slot in the first or last slots are not considered as they would only increase the CG. Fig. 5.6 depicts 4 different examples of schemes with medium CB: {L,E,L,H,H}, {L,H,E,L,H}, {L,L,E,H,H}, and {L,L,H,E,H}.

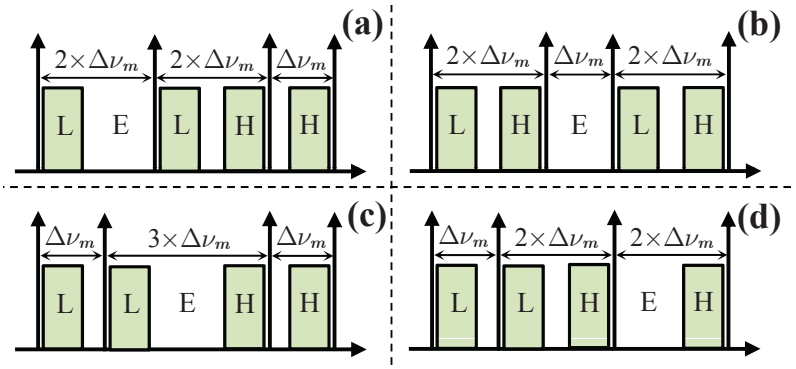

Figure 5.6: Examples of schemes with medium CB: (a) {L,E,L,H,H}, (b) {L,H,E,L,H}, (c) {L,L,E,H,H}, and (d) {L,L,H,E,H}.

Fig. 5.7(a) and Fig. 5.7(b) show the number of VC-VC-VC products and VC-VC-band products NDG1 and NDG2 around the third channel for the scheme {L,H,E,L,H}, with the minimum and relaxed VBG configurations, respectively. Transmission of 5 channels with a CG with $g = 3$ is considered in both configurations. For the relaxed VBG configuration, all bands employ VBG2. Comparison between Fig. 5.7(a) and Fig. 5.7(b) show that the increase of the VBG redistribute the VC-VC-band products in a way that more products are interfering with the subcarriers closer to the VCs and that almost all subcarriers are impaired by the same number of products. Furthermore, the number of NDG2-type products continues to be higher than the number of NDG1-type products.

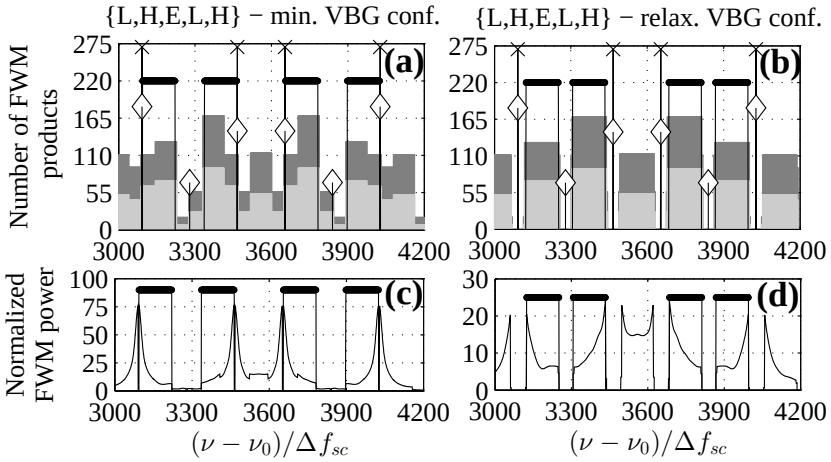

Figure 5.7: Number of VC-VC-VC products (◊) and VC-VC-band products NDG1 (light grey) and NDG2 (dark grey) around the third channel for the scheme {L,H,E,L,H} with the (a) minimum and (b) relaxed VBG configurations. Transmission of 5 channels with $g = 3$ is considered in both configurations. The spectral location of the subcarriers (dots) and VCs (×) is also shown as a reference (it is not related with the number of FWM products or the normalized FWM power). Normalized FWM power with the (c) minimum and (d) relaxed VBG configurations, together with the spectral location of the subcarriers.

Fig. 5.7(c) and Fig. 5.7(d) show the normalized FWM power for the scheme {L,H,E,L,H}, with the minimum and relaxed VBG configurations, respectively. Fig. 5.7(c) and Fig. 5.7(d) show that the VBG increase allowed to reduce significantly the FWM power affecting the OFDM subcarriers closer to the VCs for all pairs, and that subcarriers farther away from the corresponding VCs are impaired by lower FWM power than the subcarriers closer to the corresponding VCs. Further investigation has shown that these conclusions hold also for the other possible schemes with medium CB. The FWM power reduction is directly related to the reduction of the FWM efficiency. For instance, let us consider a NDG2-type product with high FWM efficiency. From the FWM efficiency definition [37], a product with high FWM efficiency is a product where $\Delta\nu_{ik} = \nu_i - \nu_k$ and $\Delta\nu_{jk} = \nu_j - \nu_k$ or both are small. Fig. 5.8 depicts an example of a NDG2-type product with small $\Delta\nu_{ik}$ and $\Delta\nu_{jk}$ ($\Delta\nu_{ik} = \Delta\nu_m = 3.125$ GHz and $\Delta\nu_{jk} =$ VBG). The FWM efficiency of the product falling in frequency ν_n is close to its maximum for small VBGs (on the order of tens of MHz). In this way, it is beneficial to increase the VBG to reduce the FWM efficiency, and thus, the power of the products falling on the subcarriers closer to the VCs.

Maximum CB

For channels with 4 bands, and excluding the ones having a H-pair followed by a L-pair, 61 different schemes with maximum CB can be designed. These schemes are obtained by considering all different combinations of L, H and E, with the exception of the combinations in which the

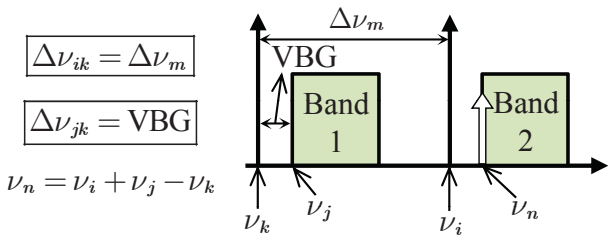

Figure 5.8: Example of a NDG2-type product with small $\Delta\nu_{ik}$ and $\Delta\nu_{jk}$. The FWM product (white arrow) falls in frequency ν_n.

E-slot is located in the edges of the channel. Fig. 5.9 depicts 4 different examples of schemes with maximum CB: {L,E,L,H,E,H}, {L,H,E,E,L,H}, {L,E,L,E,L,H}, and {L,H,E,L,E,H}.

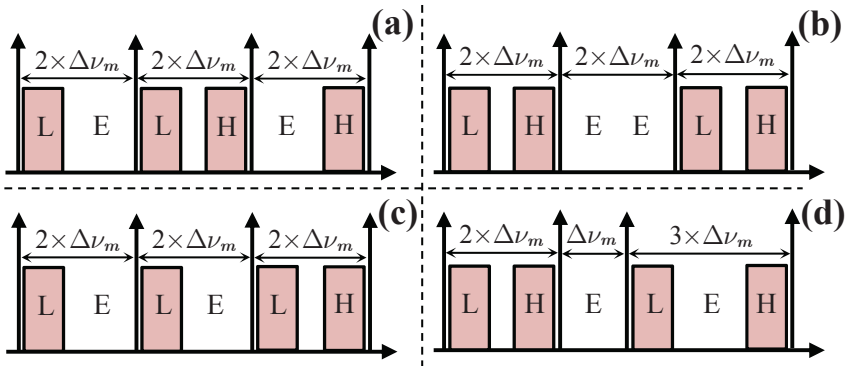

Figure 5.9: Examples of schemes with maximum CB: (a) {L,E,L,H,E,H}, (b) {L,H,E,E,L,H}, (c) {L,E,L,E,L,H}, and (d) {L,H,E,L,E,H}.

Fig. 5.10(a) and Fig. 5.10(b) show the number of VC-VC-VC products and VC-VC-band products NDG1 and NDG2 around the third channel for the scheme {L,E,L,H,E,H}, with the minimum and relaxed VBG configurations, respectively. Transmission of 5 channels with a CG with $g = 2$ is considered in both configurations. For the relaxed VBG configuration, all bands employ VBG2. Fig. 5.10 shows that, for both configurations, the number of NDG2-type products continues to be higher than the number of NDG1-type products. It also shows that changing the VBG does not influence the number of products interfering with the OFDM subcarriers, which is a different behaviour from what is shown in Fig. 5.5 and Fig. 5.7. Inspection of Fig. 5.10(a) and Fig. 5.10(b) also reveal that the VC-VC-VC products only fall on top of the VCs. The minimum frequency gap of consecutive VCs considering the whole WDM signal dictates the minimum frequency gap of the VC-VC-VC products. For this scheme, the CG coincides with the minimum frequency gap of consecutive VCs inside each channel (both are equal to $2 \cdot \Delta\nu_m$), and the minimum frequency gap of consecutive VCs considering the whole WDM signal is also equal to $2 \cdot \Delta\nu_m$. For instance, with a CG equal to $\Delta\nu_m$, the minimum frequency gap of the VC-VC-VC products would instead be $\Delta\nu_m$, even though the frequency gap between consecutive VCs inside each channel is $2 \cdot \Delta\nu_m$.

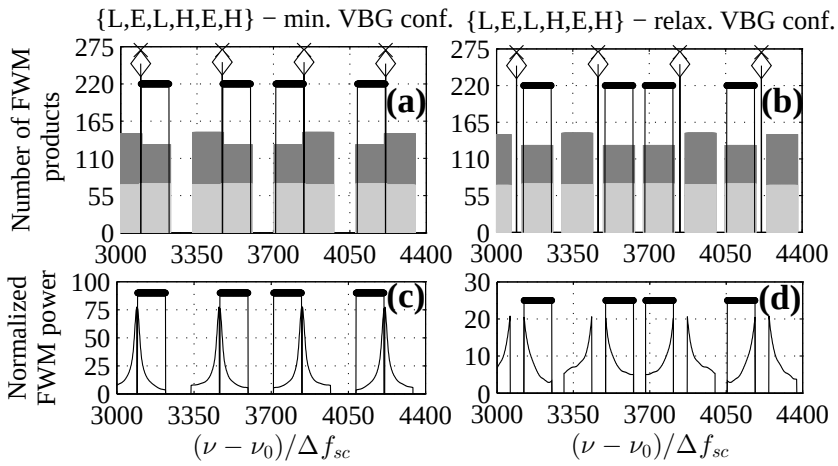

Figure 5.10: Number of VC-VC-VC products (◊) and VC-VC-band products NDG1 (light grey) and NDG2 (dark grey) around the third channel for the scheme {L,E,L,H,E,H} with the (a) minimum and (b) relaxed VBG configurations. Transmission of 5 channels with $g = 2$ is considered in both configurations. The spectral location of the subcarriers (dots) and VCs (×) is also shown as a reference (it is not related with the number of FWM products or the normalized FWM power). Normalized FWM power with the (c) minimum and (d) relaxed VBG configurations, together with the spectral location of the subcarriers.

Fig. 5.10(c) and Fig. 5.10(d) show the normalized FWM power for the scheme {L,E,L,H,E,H}, with the minimum and relaxed VBG configurations, respectively. Fig. 5.10(c) and Fig. 5.10(d) show that, in a similar way to what is shown for schemes with minimum and medium CBs, the increase of the VBG enables a remarkable reduction in the FWM power of the subcarriers closer to the VCs, and that subcarriers farther away from the corresponding VCs are impaired by lower FWM power when compared with the subcarriers closer to the corresponding VCs.

5.3 WDM metro-access network employing new VC-assisted DD schemes

The metro-access network employed in this chapter is similar to the one presented in section 2.4. To focus the analysis on the tolerance to FWM of the VC-assisted schemes, noiseless optical and electrical amplifiers, ideal brick-wall shaped filters and negligible impact of the reconfigurable optical add-drop multiplexer (ROADM) cascade are considered. In this section, the performance results of the WDM metro-access network employing the new VC-assisted DD schemes are assessed. The PB improvements provided by these new schemes are also shown.

Each OFDM band of each channel transports a bit rate of 10.7 Gb/s [10 Gb/s data rate plus 7% forward error correction (FEC) overhead] when $\Delta\nu_m = 3.125$ GHz, and a 26.75 Gb/s bit rate (25 Gb/s data rate plus 7% FEC overhead) when $\Delta\nu_m = 6.25$ GHz. This FEC overhead enables an almost error-free output BER with an input BER of $4 \cdot 10^{-3}$ [90]. Cross 32-quadrature amplitude

modulation (QAM) mapping is employed in all the $N_{sc} = 128$ subcarriers of each OFDM band. In [63], it was shown that, to ensure adequate SSBI removal, the VBPR must be 7.5 dB or higher for 32-QAM transmission, when an iterative SSBI mitigation algorithm is employed. In this work, for each pair band-VC, the VBPR is set to 9 dB. With 32-QAM mapping and 128 subcarriers per band, an OFDM signal bandwidth of 2.14 GHz and a subcarrier spacing, $\Delta f_{sc} = B_w/N_{sc}$, of 16.72 MHz, when $\Delta\nu_m = 3.125$ GHz, is obtained. For slots with $\Delta\nu_m = 6.25$ GHz, $B_w = 5.35$ GHz and $\Delta f_{sc} = 41.80$ MHz are obtained. With $\Delta\nu_m = 6.25$ GHz, VBG2 cannot be the same as defined for 3.125 GHz-width slots, as it will cause frequency overlapping between different bands. For this reason, VBG2 should be reduced and is set to half of the value used when $\Delta\nu_m = 3.125$ GHz: $16 \cdot \Delta f_{sc} = B_w/8$. Tab. 5.2 shows the values of VBG1 and VBG2 for the two different frequency slot widths considered: $\Delta\nu_m = 3.125$ GHz and $\Delta\nu_m = 6.25$ GHz.

Table 5.2: VBG1 and VBG2 for different frequency slot widths.

	VBG1 (small VBG)	VBG2 (large VBG)
$\Delta\nu_m = 3.125$ GHz	$2 \cdot \Delta f_{sc}$	$32 \cdot \Delta f_{sc}$
$\Delta\nu_m = 6.25$ GHz	$2 \cdot \Delta f_{sc}$	$16 \cdot \Delta f_{sc}$

With these subcarrier spacings and VBGs, the minimum bandwidth required for the OFDM receiver (bandwidth of the OFDM band plus the VBG) does not exceed 2.18 GHz for a pair employing VBG1, and reaches 2.68 GHz for a pair employing VBG2 (bandwidth increase of 23%), when $\Delta\nu_m = 3.125$ GHz. For slots with $\Delta\nu_m = 6.25$ GHz, the minimum bandwidth does not exceed 5.43 GHz for a pair employing VBG1, and reaches 6.02 GHz for a pair employing VBG2 (bandwidth increase of 11%).

5.3.1 VC-assisted schemes with best FWM tolerance

The performance degradation induced by the FWM effect on each OFDM band can be evaluated from the FWM power falling on the OFDM subcarriers of that band. The FWM power at a given frequency is obtained from the FWM efficiency of the VC-VC-band products that fall at that frequency. From the FWM power, the error vector magnitude (EVM) due to FWM is obtained [37]. In this work, the impact of the FWM effect on the performance is assessed using the theoretical method (TM) presented in chapter 4. In chapter 4, the TM was validated by comparison with numerical simulation of the scalar generalized nonlinear Schrödinger equation. The main advantage of the TM is that it provides fast and accurate threshold average power (TAP) estimates of any band, for any number of SSMF spans and for a high number of WDM channels. In this section, TAP estimates for the pair band-VC which includes the band most

impaired by FWM (or worst band) are presented. Two different scenarios are considered: transmission of 25 WDM channels with 4 bands each (100 transmitted bands), with i) each band delivering 10 Gb/s in a 3.125 GHz-width slot, and ii) with each band delivering 25 Gb/s in a 6.25 GHz-width slot. Transmission along N_{sp} SSMF spans is considered with $N_{sp} \in \{3, 6, 9\}$ [$N_{sp} - 1$ spans along the metro ring and 1 span at the optical distribution network (ODN)]. Two different lengths for each SSMF metro span, L_{sp}, are employed: 40-km and 80-km. With this, a metro-access network with accumulated capacity of 1 Tb/s with 3.125 GHz-width slots or 2.5 Tb/s with 6.25 GHz-width slots is analysed, considering a network with reach between 120 km and 720 km. For the sake of simplicity, it is assumed that the same WDM signal travels along the $N_{sp} - 1$ spans of the metro ring and along the ODN span. This is a pessimistic approach as in fact only a small subset of the total number of the WDM channels travels along the ODN, and thus, the FWM effect suffered by the small subset of WDM channels in the ODN span is lower than the FWM effect suffered by the complete number of WDM channels. 25 WDM channels ($N_{ch} = 25$), with 4 bands each, is a good representation of a very high channel count transmission as, for 3, 6 and 9 spans, the TAP difference when increasing from 25 to 50 channels, does not exceed 0.2 dB regardless of the VC-assisted scheme under analysis. Hereafter, the TAP of the worst pair band-VC among all WDM channels is referred to as the upper bound of the power limit (UBPL).

In order to assess which schemes show the best FWM tolerance, the UBPLs of all possible combinations for the schemes with minimum, medium and maximum CB were obtained. The spectral efficiency was maintained in 1.6 bit/s/Hz for 3.125 GHz-width slots and 2 bit/s/Hz for 6.25 GHz-width slots, and the relaxed VBG configuration was used for all schemes except the baseline. The schemes showing the best tolerance to FWM (or highest UBPL) for the three different CBs are: i) for the minimum CB class, scheme {L,L,H,H}, hereafter referred as scheme A; ii) for the medium CB class, scheme {L,H,E,L,H}, hereafter referred as scheme B; and iii) for the maximum CB class, schemes {L,E,L,H,E,H} and {L,H,E,E,L,H}, hereafter referred as schemes C1 and C2, respectively. Fig. 5.11 illustrates the MB-OFDM schemes showing the best tolerance to FWM for the different CB classes under analysis, together with the baseline scheme. Note that schemes A, B and C1 were the ones analysed in detail in section 5.2.2. For the maximum CB class, two different schemes were chosen as they present discrepancies not exceeding 0.2 dB from the optimal UBPL in the analysed number of spans and SSMF span lengths.

Fig. 5.12 shows the UBPLs of the different schemes (5 schemes with minimum CB, 25 schemes with medium CB and 61 schemes with maximum CB) for the system parameters under analysis.

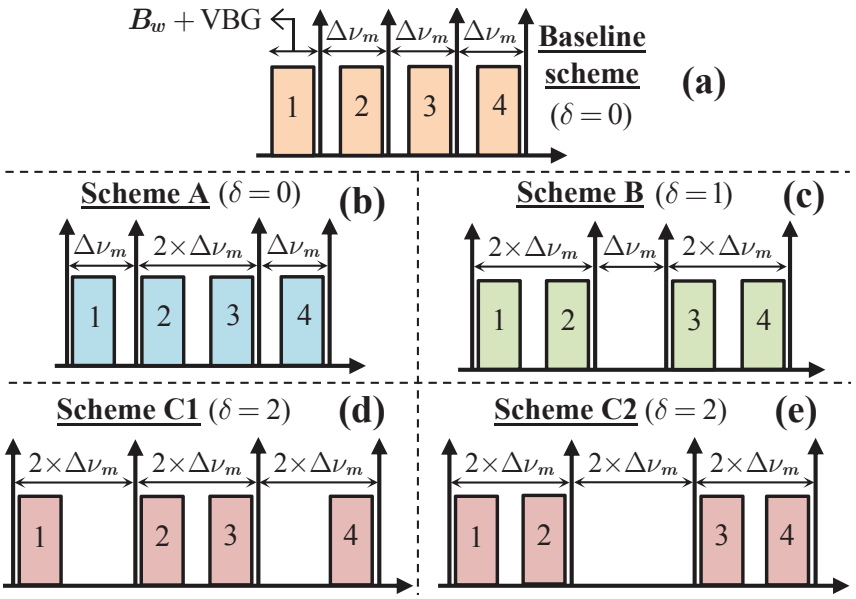

Figure 5.11: The (a) baseline scheme, and four proposed VC-assisted MB-OFDM schemes showing the best tolerance for a given δ: (b) scheme A ($\delta = 0$), (c) scheme B ($\delta = 1$), (d) scheme C1 ($\delta = 2$) and (e) scheme C2 ($\delta = 2$).

Schemes with higher UBPL present higher tolerance to FWM. The schemes are indexed according to their tolerance to FWM: a higher index corresponds to a higher FWM tolerance. The scheme with lowest index in Fig. 5.12(a) is the baseline scheme employing the minimum VBG configuration. The schemes with highest index in Fig. 5.12(a) and Fig. 5.12(b) are schemes A and B, respectively. The schemes with indexes 60 and 61 in Fig. 5.12(c) are schemes C1 and C2, respectively. Similar conclusions in terms of the optimal schemes can be drawn when spans with 80-km length are considered.

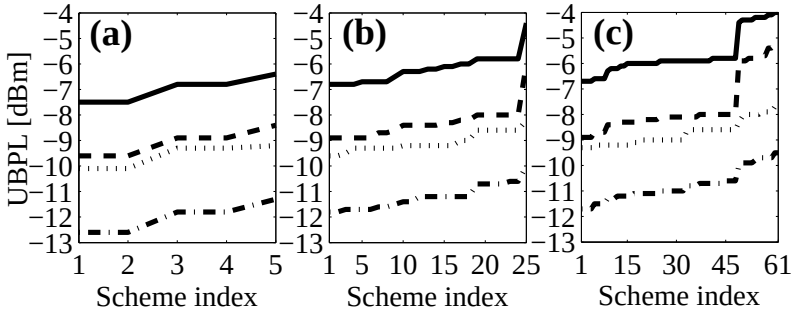

Figure 5.12: UBPLs of the different schemes for the (a) minimum, (b) medium and (c) maximum CB classes, considering slots with $\Delta\nu_m = 3.125$ GHz and transmission along 3 (dotted line) and 9 (dash-dot line) spans, and considering slots with $\Delta\nu_m = 6.25$ GHz and transmission along 3 (solid line) and 9 (dashed line) spans. The length of each span is 40 km.

Tab. 5.3 presents the UBPLs for the baseline scheme and schemes A, B, C1 and C2 using the minimum and relaxed VBG configurations, as a function of the spectral efficiency, with $\Delta\nu_m = 3.125$ GHz, $L_{sp} = 40$ km and $N_{sp} = 9$. In each scheme, the spectral efficiency is

modified by changing the CG. Tab. 5.3 shows that decreasing the spectral efficiency enables higher UBPLs. This is attributed to the reduction of the FWM efficiency caused by increasing the frequency gap of the different channels. The baseline scheme shows the lowest UBPLs as it is the case impaired by FWM products with higher efficiency. Inspection of Tab. 5.3 also reveals that, when comparing the results with the same scheme, the highest UBPLs are obtained when the relaxed VBG configuration is employed. This conclusion holds for all the number of spans, SSMF span lengths and frequency slot-widths considered in this work. The relaxed VBG configuration allows to reduce the FWM efficiency of the VC-VC-band products (especially the ones falling in the subcarriers closest to the VCs) when compared with the minimum VBG configuration, and consequently, to improve the overall performance. Tab. 5.4 summarizes the best schemes as a function of the spectral efficiency, for $\Delta\nu_m = 3.125$ GHz and $\Delta\nu_m = 6.25$ GHz.

Table 5.3: UBPLs, in dBm, for the baseline scheme and schemes A, B, C1 and C2, using the minimum and relaxed VBG configurations, with $\Delta\nu_m = 3.125$ GHz, $L_{sp} = 40$ km and $N_{sp} = 9$.

	1.60 b/s/Hz	1.83 b/s/Hz	2.13 b/s/Hz	2.56 b/s/Hz	3.20 b/s/Hz
Baseline (minimum)	-12.6	-12.8	-13.1	-13.5	-14.3
Sch. A (minimum)	-11.8	-12.1	-12.5	-13.1	
Sch. A (relaxed)	-11.3	-11.5	-12.0	-12.6	
Sch. B (minimum)	-11.5	-11.8	-12.2		
Sch. B (relaxed)	-10.1	-10.4	-11.0		
Sch. C1 (minimum)	-11.2	-11.6			
Sch. C2 (minimum)	-11.3	-11.8			
Sch. C1 (relaxed)	-9.5	-10.2			
Sch. C2 (relaxed)	-9.5	-10.3			

Table 5.4: Schemes showing the best FWM tolerance as a function of the spectral efficiency, for two different frequency slot-widths.

η_s for $\Delta\nu_m = 3.125$ GHz	η_s for $\Delta\nu_m = 6.25$ GHz	Schemes showing the best FWM tolerance (best schemes)
2.56 b/s/Hz	3.20 b/s/Hz	Scheme A (relaxed)
2.13 b/s/Hz	2.67 b/s/Hz	Scheme B (relaxed)
1.83 b/s/Hz	2.29 b/s/Hz	Schemes C1 and C2 (relaxed)
1.60 b/s/Hz	2.00 b/s/Hz	Schemes C1 and C2 (relaxed)

The impact of changing the VBG configuration on the performance of the OFDM subcarriers can be seen in Fig. 5.13. Fig. 5.13 shows the EVM of the OFDM subcarriers of the worst band, due to the FWM effect. The baseline scheme and schemes A, B and C1 using the minimum and relaxed VBG configurations, with the corresponding UBPLs obtained with a spectral efficiency of 1.6 bit/s/Hz and with $\Delta\nu_m = 3.125$ GHz, are considered. The EVMs of scheme C2 are not shown as they are similar to the EVMs of scheme C1. The worst band is the first band of the $[(N_{ch} + 1)/2]$-th WDM channel when employing scheme A and the second band of the

same channel when employing the other schemes. The lowest subcarrier index corresponds to the OFDM subcarrier closest to the VC. Fig. 5.13 shows that the subcarriers closer to the VC present the worst EVM, for all curves. This occurs due to the higher FWM efficiency of the products falling on these subcarriers.

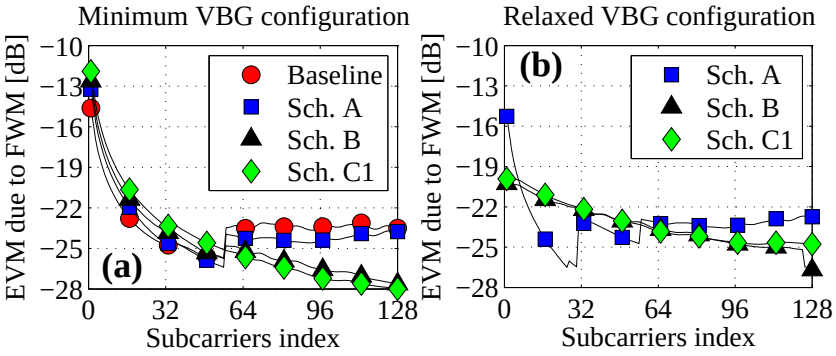

Figure 5.13: EVM due to FWM of the subcarriers of the worst band, for the UBPLs obtained with $\eta_s = 1.6$ bit/s/Hz and $\Delta\nu_m = 3.125$ GHz, for: (a) the baseline scheme and schemes A, B and C1 using the minimum VBG configuration and (b) schemes A, B and C1 using the relaxed VBG configuration. Transmission along 9 spans with 40-km each is employed.

Inspection of Fig. 5.13(a) reveals that the EVMs of the subcarriers with higher indexes are slightly worse for the baseline scheme and scheme A than for schemes B and C1 (EVM difference close to 5 dB). This difference is attributed to the higher FWM power interfering with those subcarriers, as shown in Fig. 5.5(c) (first band, scheme A), Fig. 5.7(c) (second band, scheme B) and Fig. 5.10(c) (second band, scheme C1). To better understand this effect, Fig. 5.14 shows an example of a NDG1-type product falling on the subcarrier of band 1 with higher frequency (represented as ν_n) when employing schemes A and B. Fig. 5.14 shows that $\Delta\nu_{jk}$ is substantially larger with scheme B than with scheme A. For this reason, the FWM products falling on frequency ν_n are more efficient for scheme A, and thus, present higher EVM.

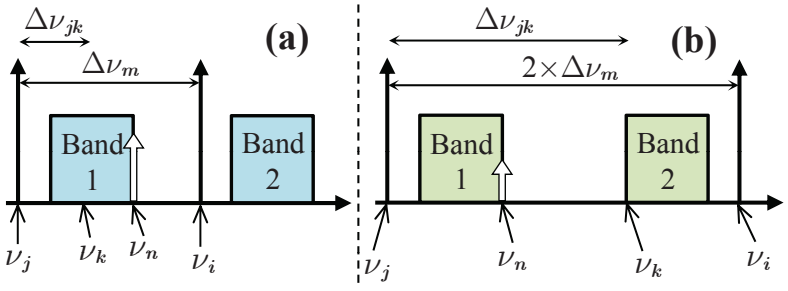

Figure 5.14: Example of NDG1-type products falling in the subcarrier of band 1 farther away from the corresponding VC when employing (a) scheme A and (b) scheme B. The FWM products (white arrows) fall in frequency ν_n for both examples.

Fig. 5.13(b) shows that when employing the relaxed VBG configuration, a substantial improvement in the EVM of the subcarriers closer to the VCs is experienced for schemes B and C1, when compared with the same scheme but with the minimum VBG configuration (EVM reduction that

can reach 8 dB). This is a direct consequence of increasing $\Delta\nu_{ik}$ and/or $\Delta\nu_{jk}$, at the expense of a small increase of the bandwidth of each pair band-VC, and consequently, of the OFDM receiver. For scheme A, the pairs with the worst band (first and fourth pairs) employ VBG1, and thus, continue to show a strong peak in the EVM of the subcarriers closer to the VC. As the EVM results are directly related to the FWM power, this peak can be seen in the normalized FWM power results shown in Fig. 5.5(d) for the first and fourth bands (worst bands). Additionally, the EVM variation not exceeding 4 dB that can be observed in Fig. 5.13(b) for subcarriers of scheme A with index between 25 and 50 is attributed to the FWM power variations seen in the first and fourth bands of Fig. 5.5(d). Note that, in Fig. 5.13(b), the results with scheme B show a small EVM reduction not exceeding 2 dB in the last few subcarriers with highest index. This is attributed to a considerable reduction of the FWM power in these subcarriers.

5.3.2 Power budget improvements

The PB is defined as the difference, in decibel, between the UBPLs and the receiver sensitivity. Assuming that the receiver sensitivity is the same for all schemes, the PB improvements can be obtained directly from the difference between the UBPLs of two different schemes while maintaining the same spectral efficiency. In this section, the PB improvement for a given spectral efficiency is obtained as the difference between the UBPL evaluated with the baseline scheme employing the minimum VBG configuration and the UBPL of the best schemes shown in Tab. 5.4. For instance, the PB improvement obtained with scheme B, with the relaxed VBG configuration and a spectral efficiency of 2.13 bit/s/Hz, is 2.1 dB (see the UBPLs of baseline and scheme B shown in Tab. 5.3).

Fig. 5.15 shows the PB improvement of schemes A, B, C1 and C2 for different spectral efficiencies, with 3.125-GHz width slots and with a data bit-rate of 40 Gb/s per WDM channel. Fig. 5.15 shows that the best schemes provide a higher PB improvement with increasing number of spans, regardless of the analysed span length. This is attributed to a stronger reduction of the FWM efficiency in the best schemes due to the higher phase mismatching, when increasing the number of spans. Fig. 5.15 also shows that the PB improvements increase for schemes with higher δ (that is, higher number of empty slots inside each WDM channel) and lower spectral efficiency for the same δ. This is a direct consequence of the increase of the minimum frequency gap between different VCs, which causes a reduction of the FWM efficiency of the VC-VC-band products at a given frequency. For instance, scheme B has a frequency gap between the second and third VCs of $\Delta\nu_m$, whereas in schemes C1 and C2, the gap is $2 \cdot \Delta\nu_m$. The highest PB

improvement is obtained with scheme C2 employing 9 spans with 40-km length and having a spectral efficiency of 1.6 bit/s/Hz. This PB improvement achieves 3 dB, enabling to double the number of users served by the metro-access network or to extend the ODN coverage by 12 km if a fibre loss coefficient of 0.25 dB/km is considered.

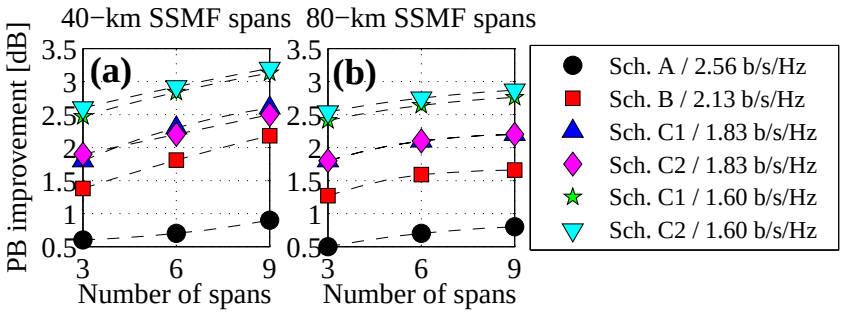

Figure 5.15: PB improvement of schemes A, B, C1 and C2 for different spectral efficiencies, after transmission along 3, 6 and 9 SSMF spans, with (a) 40-km and (b) 80-km length each. The data bit-rate per channel is 40 Gb/s.

Fig. 5.16 shows the PB improvement of schemes A, B, C1 and C2 for different spectral efficiencies, with 6.25-GHz width slots and with a data bit-rate of 100 Gb/s per WDM channel. Fig. 5.16 shows that increasing the number of spans enables a higher PB improvement only when spans with 40-km length are considered. This is a similar behaviour to what was shown for 40 Gb/s per WDM channel. The case with 80-km spans is the situation analysed with lowest FWM efficiency for the same number of spans or with the highest phase mismatching (highest L_{sp} and highest $\Delta\nu_m$). In this situation, Fig. 5.16 shows that the PB improvement tends to stabilize or even decrease for increasing number of spans. This is attributed to the phase matching of the FWM contributions of all spans that occurs at specific OFDM subcarriers. In the case of 6.25-GHz width slots with 80-km spans, and for the best schemes, the phase matching leads to the appearance of FWM power resonances. These resonances increase the FWM power averaged among all the subcarriers of each OFDM band, which translates into a UBPL decrease that limits the increase of the PB improvement with increasing number of spans. With 6.25-GHz width slots and 40-km spans, as well as with 3.125-GHz width slots, the influence of the FWM power resonances on the average FWM power is negligible. This occurs because the major contribution to the PB improvement comes from the EVM of the subcarriers closer to the VCs. Fig. 5.16 also shows that the PB improvement increases for schemes with higher δ or lower spectral efficiency for the same δ. This is also attributed to the higher frequency gap between the VCs with higher δ, which results in a decrease of the efficiency of the VC-VC-band FWM products. The highest PB improvement is obtained with scheme C2 after transmission along 9 spans with 40-km length and with a spectral efficiency of 2 bit/s/Hz. This PB improvement

reaches 4.4 dB, enabling to double the number of users served by the metro-access network and simultaneously extend the ODN coverage by 5 km for a fibre loss coefficient of 0.25 dB/km.

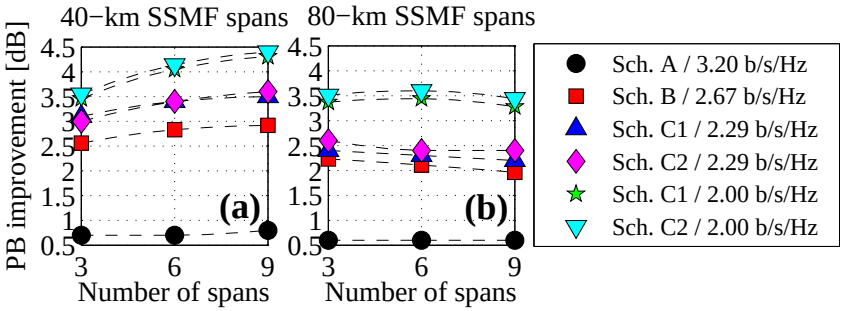

Figure 5.16: PB improvement of schemes A, B, C1 and C2 for different spectral efficiencies, after transmission along 3, 6 and 9 SSMF spans, with (a) 40-km and (b) 80-km length each. The data bit-rate per channel is 100 Gb/s.

Fig. 5.17 shows the spectral occupancy of the WDM MB-OFDM signal employing scheme C2 in each channel, which enables the highest PB improvement when compared with the baseline scheme with the same spectral efficiency.

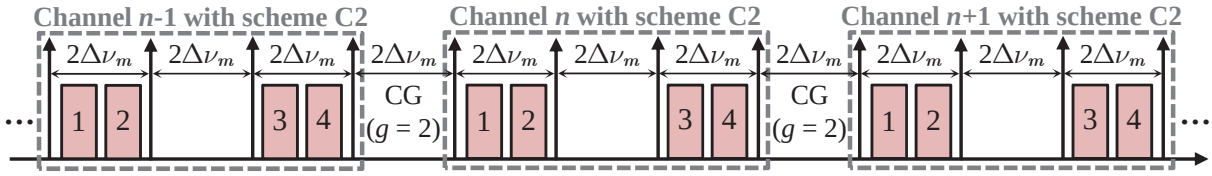

Figure 5.17: Spectral occupancy of the WDM-MB-OFDM signal that enables the highest PB improvement when compared with the baseline scheme with the same spectral efficiency.

5.4 Conclusions

The tolerance to the FWM effect of VC-assisted DD SSB-MB-OFDM schemes has been investigated in a UDWDM metro-access network scenario, and schemes with improved tolerance to FWM have been proposed. Schemes showing the best tolerance to FWM, among all the analysed schemes within each CB class, have been identified for specific spectral efficiencies. This study has been performed considering channel grids of 3.125 GHz and 6.25 GHz for each OFDM band, which deliver a dedicated capacity of 10 Gb/s and 25 Gb/s to each user, respectively.

For a channel grid of 3.125 GHz, it has been shown that an adequate design of the VC-assisted scheme enables a PB improvement that achieves 3 dB. This improvement allows to double the number of users of the metro-access network or to extend the ODN reach by about 12 km. With a 6.25 GHz channel grid, the PB improvement surpasses 4 dB, enabling to double the number of users and simultaneously extend the ODN coverage by about 5 km.

Chapter 6

Experimental assessment of VC-assisted DD-MB-OFDM schemes

6.1 Introduction

Works reported in [35, 36] have demonstrated experimentally the virtual carrier (VC)-assisted direct-detection (DD)-multi-band (MB)-orthogonal frequency-division multiplexing (OFDM) transmission using the baseline scheme, as a solution which provides high spectral efficiency, granularity at the band level and relaxed receiver bandwidth requirements. In [35], a VC-assisted DD-MB-OFDM passive optical network (PON) with a dedicated band capacity per user of 10 Gb/s employing an ultradense band spacing of 6.25 GHz was proposed and experimentally validated for application in next-generation access networks. In [36], a 100 Gb/s VC-assisted 9-band DD-MB-OFDM metro network with ultradense band spacing of 6 GHz was experimentally demonstrated. In this chapter, the experimental assessment of two different VC-assisted DD-MB-OFDM schemes is performed and compared using wavelength division multiplexing (WDM) transmission. Particularly, the performance of a VC-assisted MB-OFDM scheme designed to present high tolerance to the four wave mixing (FWM) effect (identified in chapter 5 as the scheme C2) is measured and compared with the performance obtained with the baseline scheme, while maintaining the spectral efficiency.

This chapter is structured as follows. In section 6.2, the two MB-OFDM schemes under analysis (the baseline scheme and the scheme C2) are presented. In section 6.3, the experimental setup for both schemes is explained and the laboratory equipment and components are listed and briefly discussed. In section 6.4, the maximum allowed average powers using the theoretical

method (TM) for the two schemes are compared. The performance is assessed experimentally for both schemes and compared as a function of the total average power launched into each standard single mode fibre (SSMF) span, for single-channel and multi-channel transmission and for single-span and multi-span propagation. In section 6.5, the main conclusions are summarized.

6.2 VC-assisted DD-MB-OFDM schemes

For experimental demonstration, two VC-assisted DD-MB-OFDM schemes are employed: the baseline scheme and the scheme C2. Four pairs band-VC are transmitted per WDM channel, each one carrying a data rate, R_d, of 10 Gb/s. Each OFDM subcarrier is modulated using squared 16-quadrature amplitude modulation (QAM) and a total of 128 subcarriers are transmitted in each OFDM band. The overall bit rate per band is 10.7 Gb/s [includes a 7% overhead due to forward error correction (FEC) and neglects the small overheads due to the cyclic prefix (CP) and training symbols (TSs)], which results in a bandwidth per band of 2.675 GHz, and in a subcarrier spacing, Δf_{sc}, of 20.90 MHz. The transmission of four WDM channels is also considered, which translates into a total of 16 pairs band-VC and aggregate data rate of 160 Gb/s. The frequency slot width $\Delta\nu_m$ is 6.25 GHz; thus, the spectral efficiency in each slot for both schemes, given by $R_d/\Delta\nu_m$, is 1.6 bit/s/Hz. For the scheme C2, $g = 1$ and $\delta = 1$ are employed. This ensures a spectral efficiency of the WDM-MB-OFDM signal employing the scheme C2 greater than 1 bit/s/Hz (in this case, equal to 1.07 bit/s/Hz), which translates into a gap between consecutive VCs of $1.5\Delta\nu_m$ (9.375 GHz) instead of $2\Delta\nu_m$ as considered in chapter 5 [see Fig. 5.11(e)]. For the baseline scheme, in order to have the same spectral efficiency of the scheme C2, $g = 2$ and $\delta = 0$ are considered.

Fig. 6.1 illustrates the spectral disposition of both schemes. For the baseline scheme, a virtual carrier-to-band gap (VBG) equal to 11 subcarrier spacings (VBG $= 11 \cdot \Delta f_{sc}$) is employed; the reason for this VBG will be explained afterwards in section 6.3. For the scheme C2, there is a higher margin to increase the VBGs, as the frequency gap between consecutive VCs is higher. Mathematically, the following relation is verified for the first two and the last two pairs band-VC inside each channel: $1.5\Delta\nu_m = 2 \cdot \text{VBG} + 2 \cdot B_w + \text{BG}$. Since $\Delta\nu_m \approx 300 \cdot \Delta f_{sc}$ and $B_w = 128 \cdot \Delta f_{sc}$, the VBG has to be smaller than 96 subcarrier spacings ($96 \cdot \Delta f_{sc}$) to avoid a null band gap (BG). It was considered that the VBGs for the scheme C2 are equal to 32 subcarrier spacings ($32 \cdot \Delta f_{sc}$) which is equivalent to 25% of the OFDM signal bandwidth. This VBG results from a compromise between: i) relaxing the FWM efficiency of the subcarriers closer to the VCs, and ii) maintaining a reduced bandwidth for the OFDM receiver ($\approx B_w + \text{VBG}$).

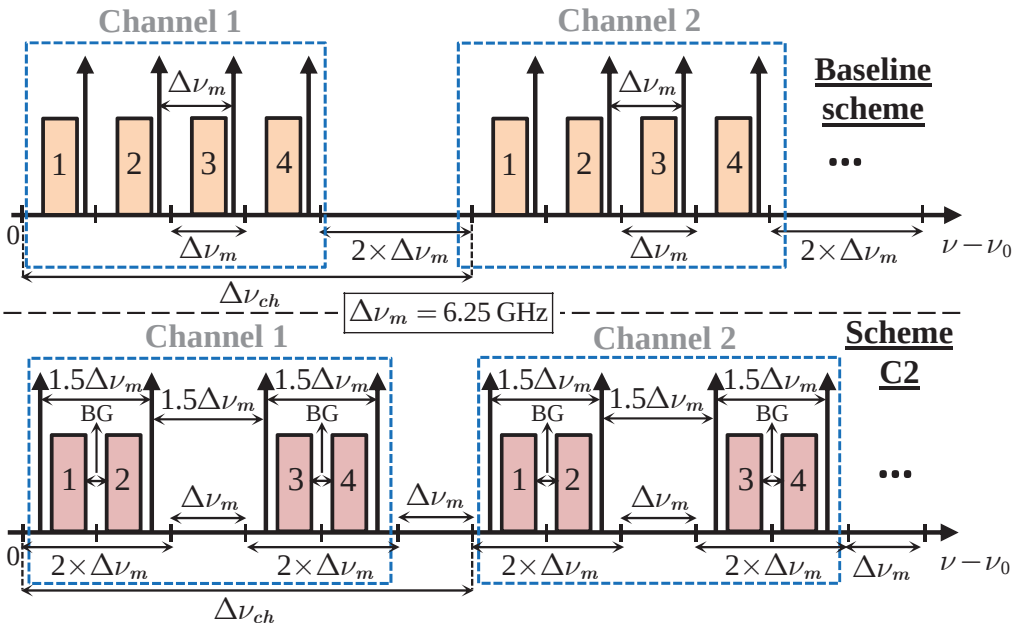

Figure 6.1: Spectra of the baseline scheme and the scheme C2 considered for experimental demonstration (only two channels are shown).

6.3 Experimental setup

Fig. 6.2 shows the experimental setup employed for both VC-assisted DD-MB-OFDM schemes. When the switches inside the MORFEUS insertion block (MIB) are in position (1), the scheme C2 is employed. When the switches are in position (2), the baseline scheme is employed.

In the experimental setup, each employed erbium doped fibre amplifier (EDFA) provides constant average power at its output. Considering the limitations of the available laboratory equipment and components, the experimental setup employed for both schemes considers the transmission of the same data information in all pairs band-VC.

Let us suppose that the switches are in position (1), that is, the scheme C2 is employed. At the MIB, four lasers are combined to form an optical comb comprised by four carriers. The optical comb is employed to generate the 4 WDM channels. To each laser (each with a linewidth lower than 5 MHz), an average power of 13 dBm is attributed. For both schemes, the frequency gap between consecutive continuous wave (CW) signals generated by the lasers is equal to the channel spacing $\Delta\nu_{ch}$, which is 37.5 GHz (0.3 nm). The optical comb is applied to a Mach-Zehnder modulator (MZM) (identified as MZM 1). MZM 1 is biased at the minimum transmission point to modulate additional carriers and neglect the CW signals. A sinusoidal waveform is generated by RF2 with frequency of 9.375 GHz (RF1 is off for the scheme C2). Before electrical amplification, the sinusoidal waveform is attenuated to ensure that the intermodulation products

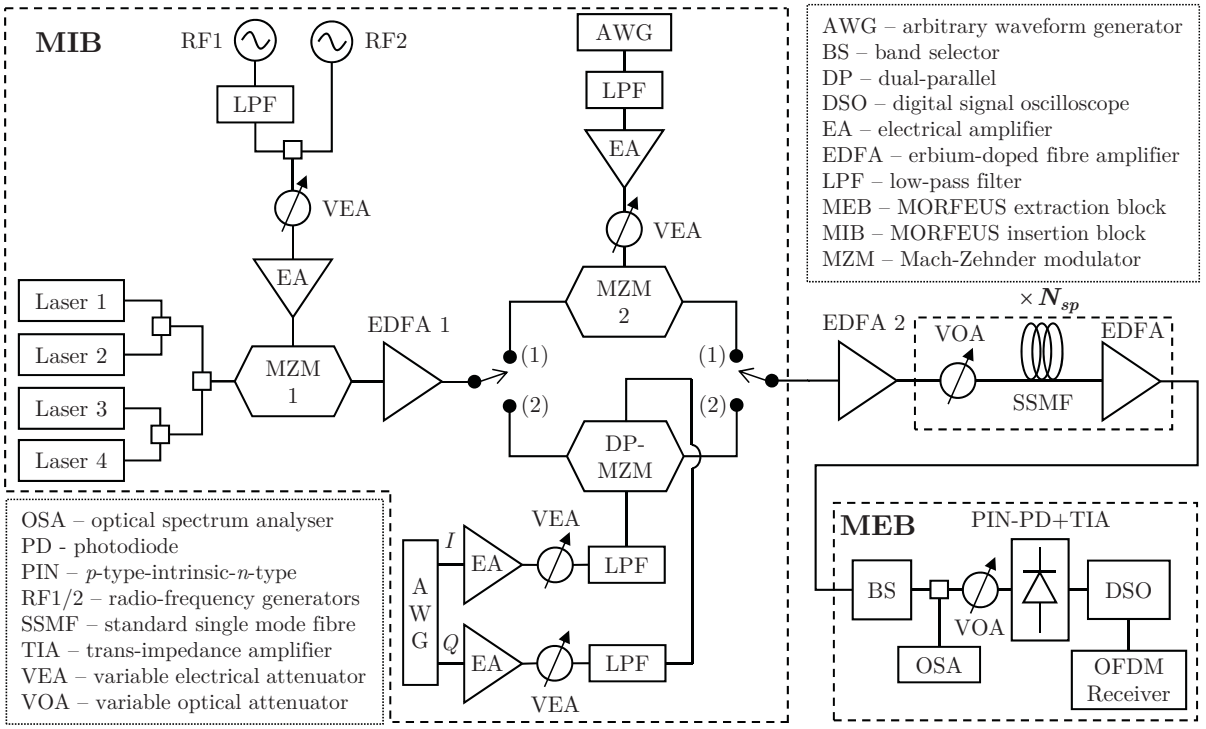

Figure 6.2: Block diagram of the experimental setup for both VC-assisted DD-MB-OFDM schemes.

induced by the electrical amplifier (EA) that follows have reduced average power. The sinusoidal waveform is then amplified by the EA (Mini-Circuits ZVA-183W-S+) and applied to MZM 1 which generates two carriers separated by 9.375 GHz from the laser frequency. This results in a total of 8 carriers separated by 18.75 GHz (0.15 nm) at the MZM 1 output. This optical signal is then amplified by an EDFA (identified as EDFA 1), which compensates the losses induced by MZM 1. The signal at the EDFA 1 output is then fed to MZM 2, which modulates the carriers at the EDFA 1 output with pairs band-VC. First, a pair band-VC is generated by the arbitrary waveform generator (AWG) (Tektronix 7122B, operating at 24 Gsamples/s) with the VC at a higher frequency than the OFDM band (H-pair). The VC frequency is equal to 4.6875 GHz (corresponds to the maximum frequency of the generated pair band-VC by the AWG). The VC frequency sets the separation between consecutive VCs (consecutive VCs will be separated by twice this frequency). The corresponding pair is low-pass filtered (Mini-Circuits VLF-3800+) to reduce the power of a few unwanted carriers generated by the AWG at higher frequencies than the VC, and amplified (Mini-Circuits ZVA-183W-S+). The double sideband (DSB) signal at the EA output has the form of a L-pair followed by a H-pair, with the VCs separated by 9.375 GHz (the same as, for instance, the first two pairs of channel 1 of the scheme C2 shown in Fig. 6.1). This DSB signal composed by two pairs band-VC is fed to MZM 2, which generates 16 pairs band-VC at the MIB output (scheme C2 with 4 pairs band-VC for each one of the 4 WDM channels).

If the switches are in position (2), the baseline scheme is employed. For the baseline scheme, RF1 and RF2 are both on and RF1 generates a sinusoidal waveform with frequency equal to 3.125 GHz. The signal at the RF1 output is filtered (Mini-Circuits VLF-3800+) to suppress the generated intermodulation product at 6.25 GHz and the signals of both RF1 and RF2 are combined (Mini-Circuits ZFRSC-183-S+) to form a radio frequency (RF) signal with two carriers: one at 3.125 GHz and another at 9.375 GHz. This RF signal is amplified (Mini-Circuits ZVA-183W-S+) and fed to MZM 1. At the MZM 1 output, the 4 WDM channels are composed by 4 carriers each. In each channel, consecutive carriers are separated by 6.25 GHz (one for each pair band-VC). This array of 16 carriers is amplified by EDFA 1 and fed to the dual-parallel (DP)-MZM. The DP-MZM works as a IQ-MZM. The I and Q components of the pair band-VC generated in the two channels of the AWG (Tektronix 7122B, operating at 9.375 Gsamples/s per AWG channel) are amplified (5865-107 Picosecond drivers), low-pass filtered (Mini-Circuits VLF-1500+) to suppress the unwanted components at each EA output, and fed to the two RF inputs of the DP-MZM. The complex signal of the OFDM band is generated in baseband (maximum frequency equal to $B_w/2$) and the VC is placed at a higher frequency than the OFDM band. The VC frequency is the maximum frequency of the pair band-VC and is equal to $B_w/2 + \text{VBG}$. The pair band-VC modulates each optical carrier, resulting in 16 pairs band-VC at the MIB output (the baseline scheme with 4 pairs band-VC for each one of the 4 WDM channels).

Fig. 6.3 shows the optical spectra at the MZM 1 input, and at the EDFA 1 output for the scheme C2 and the baseline scheme. Fig. 6.3(a) shows that the CW signals of the optical comb for WDM generation have approximately the same average power. Fig. 6.3(b) shows that each one of the main carriers that will modulate a L-pair followed by a H-pair in the scheme C2

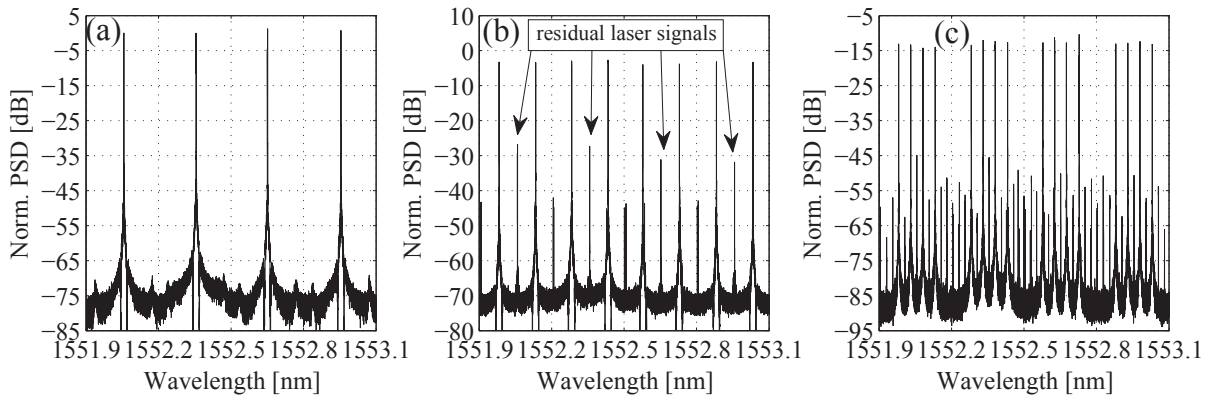

Figure 6.3: (a) Optical spectra at the MZM 1 input (carriers separated by 37.5 GHz). Optical spectra at the EDFA 1 output for (b) the scheme C2 (carriers separated by 18.75 GHz), and (c) the baseline scheme (carriers separated by 6.25 GHz).

also have approximately the same average power. The power unbalance does not exceed 1.5 dB. Fig. 6.3(b) also shows that the CW signals surrounding the main carriers were not totally suppressed, leaving residual laser signals in-between the main carriers [see Fig. 6.3(b)]. This means that MZM 1 is not polarized exactly at the minimum transmission point. This translates into an average power difference between the residual laser signals and the main carriers of around 25 dB. Fig. 6.3(c) shows that each one the main carriers that will modulate a H-pair in the baseline scheme also have approximately the same average power. The power unbalance does not exceed 3 dB. Fig. 6.3(c) also shows that the average power difference between the main carriers and the residual laser signals together with the intermodulation products generated by the EA at the MZM 1 input exceeds 30 dB.

The WDM-MB-OFDM signal at the MIB output generated for both schemes is amplified by EDFA 2 to compensate the power losses induced by the DP-MZM in the case of the baseline scheme, and by MZM 2 in the case of the scheme C2. Fig. 6.4 shows the optical spectra at the EDFA 2 output for both schemes. Fig. 6.4(a) shows that, for the baseline scheme, the power is evenly distributed by the four WDM channels, and a similar average power per pair band-VC is obtained. Fig. 6.4(a) also shows the appearance of additional carriers inside the channels other than the VCs. These carriers have two different origins. i) The residual carriers located at the centre of the OFDM bands [it can be seen in Fig. 6.4(a) for the last two channels] result from the non-perfect suppression of the carriers shown in Fig. 6.3(c). To accommodate the non-perfect suppression of these carriers performed by the DP-MZM, an additional subcarrier is transmitted and the subcarrier in the frequency corresponding to the centre of the OFDM band is not accounted for performance evaluation (129 transmitted subcarriers, with 128 accounted for performance evaluation). ii) The residual carrier originated from the non-ideal I-Q signal

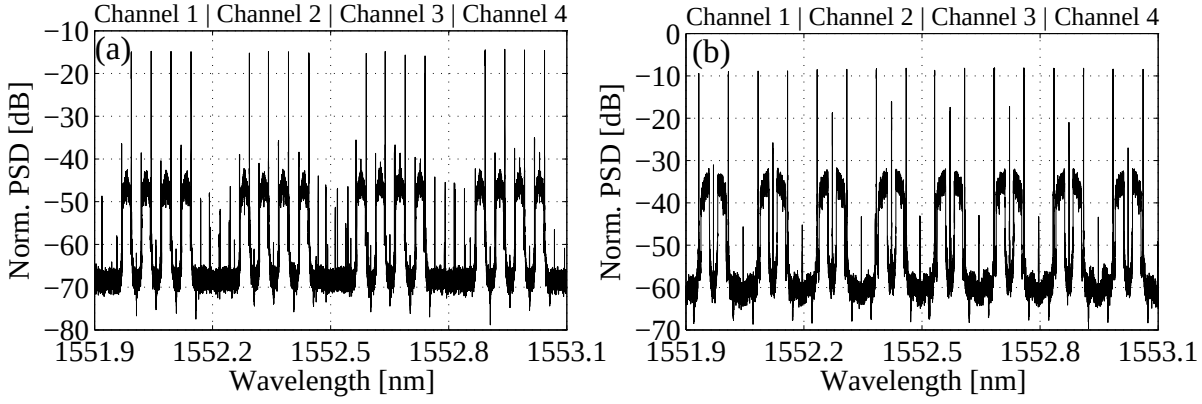

Figure 6.4: Optical spectra at the EDFA 2 output (a) for the baseline scheme and (b) for the scheme C2.

generation performed by the DP-MZM, which appears near the left-hand side of each OFDM band (separated by VBG from the OFDM band). Both these residual carriers present an average power difference when compared with the VC that exceeds 20 dB. Additionally, Fig. 6.4(a) shows the detrimental effect of the AWG on the subcarriers, where the subcarriers at the centre of each OFDM band have higher average power ($\approx$ 3 dB) than the subcarriers at the edges of the OFDM band. Fig. 6.4(b) shows that, for the scheme C2, the power is also evenly distributed by the four WDM channels, and a similar average power per pair band-VC is also obtained. Fig. 6.4(b) also shows the appearance of strong carriers located in the middle of the first two or the last two pairs of each channel. These carriers are a consequence of the non-perfect minimum transmission point obtained with MZM 2, and have lower average power when compared with the VCs. However, the average power difference could be as low as 10 dB for the second and third channels. Additionally, Fig. 6.4(b) shows the detrimental effect of the AWG on the subcarriers, which induces a considerable power reduction on the subcarriers as they become closer to the VC.

After the optical amplification performed by EDFA 2, the optical signal passes through a sequence of N_{sp} loss-compensated SSMF spans to emulate the metro network transmission. The variable optical attenuator (VOA) sets the average optical power at the input of each SSMF span. The length per span is 50 km and two different values for the number of spans are considered in this analysis: $N_{sp} = 1$ (single-span transmission) and $N_{sp} = 3$ (multi-span transmission). After SSMF transmission, the optical signal enters the MORFEUS extraction block (MEB). At the MEB, the desired pair band-VC is selected by a band selector (BS) which is a Gaussian-shape optical filter with -3 dB bandwidth of approximately 4 GHz (Yenista XTM-50 Ultrafine). The bandwidth of each pair band-VC, which is equal to $B_w + \text{VBG}$, is smaller than the -3 dB bandwidth of the BS, since $B_w + \text{VBG}$ does not surpass 3.35 GHz (corresponds to the case where the VBG is equal to 32 subcarrier spacings: each pair of the scheme C2). The optical spectrum at different points of the setup is acquired by the optical spectrum analyser (OSA), with frequency resolution of 20 MHz. After band selection, the average power of the selected pair is adjusted by a VOA to ensure that the average power before photodetection does not exceed -2 dBm. The selected pair is then photodetected by a p-type-intrinsic-n-type (PIN)-photodiode (PD) which incorporates a trans-impedance amplifier (TIA) for electrical amplification. The OFDM band is digitized by an 8-bit real-time digital storage oscilloscope (DSO) (Agilent DSO81204A) operating at 40 Gsamples/s, and the digitized OFDM signal is demodulated at the OFDM receiver (Rx) using off-line digital signal processing (DSP) with MATLAB®. The OFDM Rx includes the operations shown previously in chapter 2 (see Fig. 2.8). These operations include time

synchronization, fast-Fourier transform, equalization, and signal-signal beat interference (SSBI) mitigation. After demodulation, the performance is evaluated over 1.28×10^5 16-QAM symbols (10 sequences of 100 OFDM symbols with random binary data in each one of the 128 OFDM subcarriers).

Although a high bandwidth PIN-PD is used (bandwidth of 20 GHz), the required bandwidth is similar to the bandwidth of the OFDM band, given that a VBG not exceeding 25% of the OFDM signal bandwidth is employed. For the scheme C2, the employed VBGs are equal to 32 subcarrier spacings ($32 \cdot \Delta f_{sc}$) which is equal to 25% of the OFDM signal bandwidth. For the baseline scheme, a VBG equal to 11 subcarrier spacings (VBG $= 11 \cdot \Delta f_{sc}$) is employed. This VBG is of particular importance for the third pair band-VC of each channel. It ensures the overlapping in frequency of the residual laser signal (located between the second and third VCs of each channel) and the residual carrier due to the non-ideal I-Q signal generation performed by the DP-MZM, which appears near the left-hand side of each OFDM band (separated by VBG from the OFDM band). The overlapping of these residual carriers minimizes their impact on the performance of the third band of each channel. Fig. 6.5 illustrates the spectrum of the third pair of a given channel with the baseline scheme, with the employed VBG and with a lower VBG. Mathematically, the following relation has to be ensured for the third pair band-VC of each channel: $\Delta\nu_m/2 = B_w + 2 \cdot \text{VBG}$. Since $\Delta\nu_m \approx 300 \cdot \Delta f_{sc}$ and $B_w = 128 \cdot \Delta f_{sc}$, a VBG equal to 11 subcarrier spacings meets the aforementioned relation. Since the employed VBGs do not surpass 25% of the bandwidth of the OFDM band (668.75 MHz), the maximum required receiver bandwidth does not surpass 3.35 GHz.

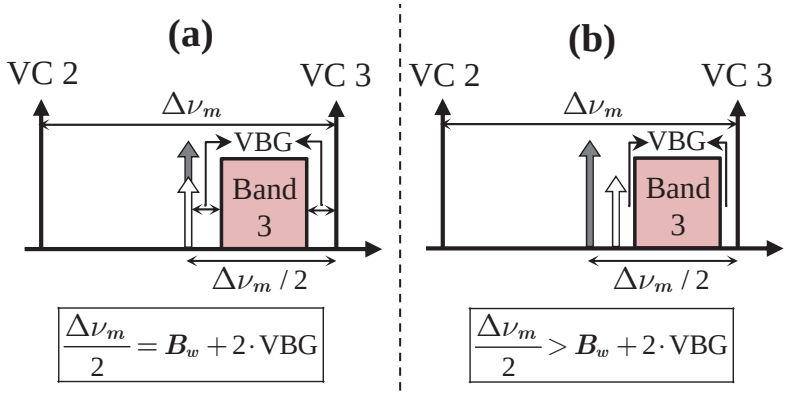

Figure 6.5: Spectrum of the third pair of a given channel with the baseline scheme, with the (a) employed VBG and (b) with a lower VBG. The white arrow stands for the residual carrier originated from the non-ideal I-Q signal generation performed by the DP-MZM, and the grey arrow stands for the residual laser signal.

Fig. 6.6 shows a photo of the laboratory equipment and main components of the experimental setup.

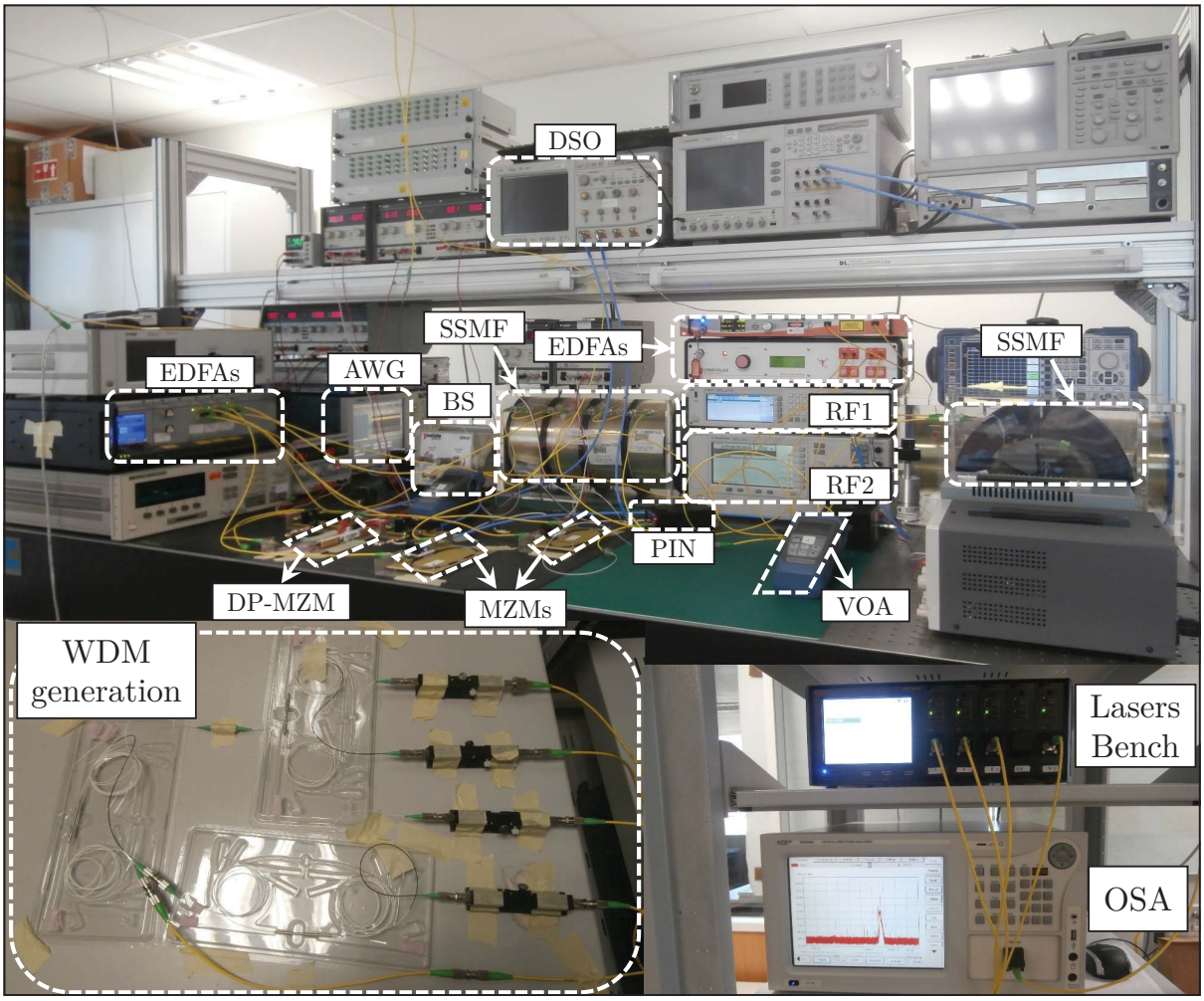

Figure 6.6: Photo of the laboratory equipment and main components of the experimental setup.

6.4 Performance evaluation

In this section, the performance evaluation results for both schemes given by the TM and from the experimental setup are presented and explained. The theoretical results shown in chapter 5 for the baseline scheme and the scheme C2 cannot be used in this chapter as the schemes used in the experimental assessment employ a different set of system parameters (for instance, the number of spans, the span length, and the number of WDM channels are different).

The performance is assessed experimentally by considering the following steps: 1) the error vector magnitude (EVM) of each subcarrier is evaluated; 2) the bit error ratio (BER) of each subcarrier is obtained directly from the EVM per subcarrier using Eq. D.2; 3) the average BER is computed from the BER per subcarrier; and 4) the average EVM is obtained from the average BER using Eq. D.3. This procedure is employed instead of calculating the average EVM directly from the EVM per subcarrier to ensure that the average EVM is more sensitive to the errors of

the subcarriers with the worst performance.

The virtual carrier-to-band power ratio (VBPR) and the modulation index (MI) were optimized experimentally in optical back-to-back operation. As a result of this optimization, VBPR = 8 dB and MI = 13% are employed in the experiments. These values are in agreement with what was experimentally shown in [36].

6.4.1 Theoretical estimation

The theoretical estimation of the maximum allowed average power per pair band-VC is assessed from the EVM results in optical back-to-back (corresponds to the EVM not impaired by the fibre nonlinearity - EVM_{L} - and is obtained experimentally without transmission along the SSMF) and from the EVM estimates for the FWM power (corresponds to the EVM impaired by the fibre nonlinearity - EVM_{NL} - and is obtained theoretically from the TM). The EVM results in optical back-to-back are assessed experimentally by replacing the SSMF spans by VOAs with similar power losses, for an average power per pair band-VC where optical noise is not dominant. The maximum allowed average power per pair band-VC is reached when the EVM in optical back-to-back plus the EVM due to the FWM effect provided by the TM reaches the threshold EVM. With 16-QAM, the threshold EVM, which is the EVM that corresponds to an average BER of 3.8×10^{-3}, is approximately -15.2 dB (see Appendix D). Experimental results in optical back-to-back operation have shown that the variation of the obtained EVMs for all OFDM bands of all WDM channels is reduced (does not exceed 1 dB). To assess the EVMs in optical back-to-back, the third band of the third channel has been chosen. Tab. 6.1 shows the EVMs of the third band of the third channel in optical back-to-back operation, for both schemes, with single-span ($N_{sp} = 1$) and multi-span ($N_{sp} = 3$) propagation, and for single-channel ($N_{ch} = 1$) and multi-channel ($N_{ch} = 4$) transmission. Tab. 6.1 shows that the EVMs of the scheme C2 are lower than the ones of the baseline scheme, for all the situations considered. This difference is attributed to the AWG frequency limitations. Since a lower sampling frequency is employed with the baseline scheme, higher power attenuation as the frequency increases is experienced. Tab. 6.1 also shows a small EVM degradation from single-channel to multi-channel and from single-span to multi-span. Since the EDFAs provide constant average power at their output, increasing the number of channels means that the total average power has to be distributed among the different channels, which translates into a EVM degradation. Increasing the number of spans means that the number of optical amplifiers also increases, resulting in an increase of the accumulated optical noise induced by the EDFAs.

Table 6.1: EVMs obtained experimentally in optical back-to-back (in dB), for the baseline scheme and the scheme C2.

	Single-channel	Multi-channel
Baseline scheme (single-span)	-17.5	-16.7
Baseline scheme (multi-span)	-17.2	-16.3
Scheme C2 (single-span)	-19.0	-17.6
Scheme C2 (multi-span)	-17.7	-16.8

Tab. 6.2 shows the maximum allowed average power per pair band-VC using the theoretical estimation for both schemes, with single-span and multi-span propagation, and for single-channel and multi-channel transmission. Tab. 6.2 shows that the scheme C2 provides higher maximum allowed average powers per pair band-VC when compared with the baseline scheme, which exceeds 2 dB for single-span and single-channel transmission, and 1.5 dB for the remaining cases considered. The improvement of the maximum allowed average powers per pair band-VC provided by the scheme C2 are lower than the ones shown in section 5.3.2. This is attributed to the lower spectral efficiency of the employed schemes for experimental assessment, which results in a lower reduction of the FWM efficiency when changing from the baseline scheme to the scheme C2.

Table 6.2: Maximum allowed average power per pair band-VC (in dBm), using the theoretical estimation for the baseline scheme and the scheme C2.

	Single-channel	Multi-channel
Baseline scheme (single-span)	0.1	-2.6
Baseline scheme (multi-span)	-3.3	-5.7
Scheme C2 (single-span)	2.4	-0.9
Scheme C2 (multi-span)	-1.7	-3.7

Fig. 6.7(a) and Fig. 6.7(b) show the number of VC-VC-VC products and VC-VC-band products of types non-degenerate (NDG)1 and NDG2 close to the third channel, for the baseline scheme and the scheme C2, respectively. Fig. 6.7(c) and Fig. 6.7(d) show the normalized FWM power (already defined in section 5.2.2) for the baseline scheme and the scheme C2, respectively. Fig. 6.7 shows that, for the baseline scheme, only the NDG2-type products interfere with the OFDM bands, whereas for the scheme C2, the interfering products are of both types (NDG1 and NDG2). Fig. 6.7(c) and Fig. 6.7(d) also shows that employing the scheme C2 instead of the baseline scheme enables reducing the FWM power interfering with the OFDM bands (reduction of approximately 50% for the subcarriers closer to the VCs).

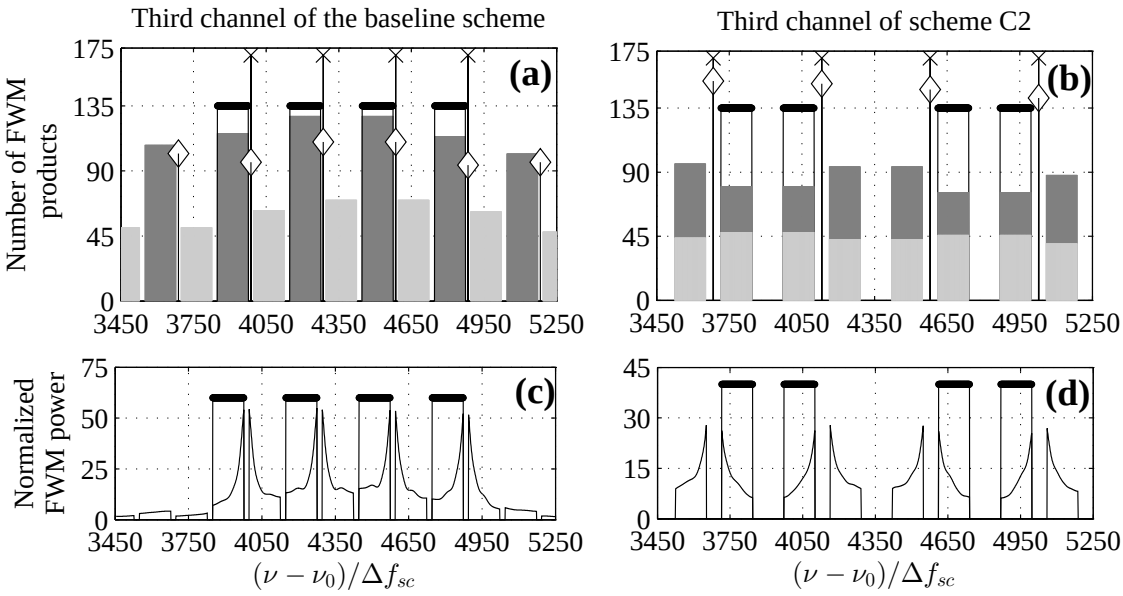

Figure 6.7: Number of VC-VC-VC products (◊) and VC-VC-band products NDG1 (light grey) and NDG2 (dark grey) around the third channel for (a) the baseline scheme and (b) the scheme C2. The spectral location of the subcarriers (dots) and VCs (×) is also shown as a reference (it is not related with the number of FWM products or the normalized FWM power). Normalized FWM power for (c) the baseline scheme and (d) the scheme C2, together with the spectral location of the subcarriers. Transmission along 3 spans is considered.

6.4.2 Experimental results

The maximum allowed average powers are assessed experimentally by obtaining the EVM as a function of the total average power launched into each SSMF span, P_t. P_t relates with the average power per pair band-VC, P_p, in the following way: $P_t\,[\text{dBm}] = P_p\,[\text{dBm}] + 10\log_{10}(N_{ch} \cdot N_B)$. This relation considers that the total average power is evenly divided by all pairs band-VC.

Fig. 6.8 shows the EVM as a function of the average power per pair band-VC for the baseline scheme and the scheme C2, considering single-span and multi-span propagation, and single-channel transmission. Fig. 6.9 shows the EVM as a function of the average power per pair band-VC for the baseline scheme and the scheme C2, considering single-span and multi-span propagation, and multi-channel transmission. Fig. 6.8 and Fig. 6.9 show that the optimum average power (which gives the lower EVM) is approximately -2 dBm for single-channel transmission and -7 dBm for multi-channel transmission. The EVM results as a function of the average power can be divided in three different regions: 1) linear transmission region (average powers below the optimum average power), 2) weakly-nonlinear transmission region (average powers around the optimum average power), and 3) strong-nonlinear transmission region (average powers above the optimum average power). For the linear transmission region, optical noise is the dominant effect. For the strong-nonlinear transmission region, fibre nonlinearity is the

dominant impairment. For the weakly-nonlinear transmission region, neither the optical noise nor the fibre nonlinearity are dominant. Fig. 6.8 and Fig. 6.9 also show that single-span transmission provides better results than multi-span transmission. For average powers in the linear transmission region, this is attributed to the accumulated optical noise from the EDFAs, which is higher for increasing number of spans. For average powers in the strong-nonlinear transmission region, it is attributed to the FWM impact on the performance, which is also higher for increasing number of spans. The average power in the strong-nonlinear transmission region with EVM equal to the threshold EVM is the maximum allowed average power. This average power is identified from the results of Fig. 6.8 and Fig. 6.9. Tab. 6.3 shows the maximum allowed average power per pair band-VC obtained experimentally. Tab. 6.3 shows that the baseline scheme provides higher average powers for single-span transmission when compared with the scheme C2 (difference of 0.4 dB). In addition, with multi-span transmission, both schemes provide similar average powers. Compared with the theoretical estimation results of section 6.4.1, the experimental results have a different behaviour. This is mainly attributed to the existence, in the scheme C2, of unwanted carriers (UCs) that limit the performance when FWM is dominant (average powers in the strong-nonlinear transmission region). These UCs are a consequence of the non-perfect minimum transmission point obtained with MZM 2 and can be seen in Fig. 6.4(b) (see, for instance, the carrier located between the third and fourth bands of the second channel or the carrier located between the first and second bands of the third channel). These carriers have lower average power than the VCs but they still present a power high enough to produce additional FWM products that degrade the performance of the OFDM bands (a power difference

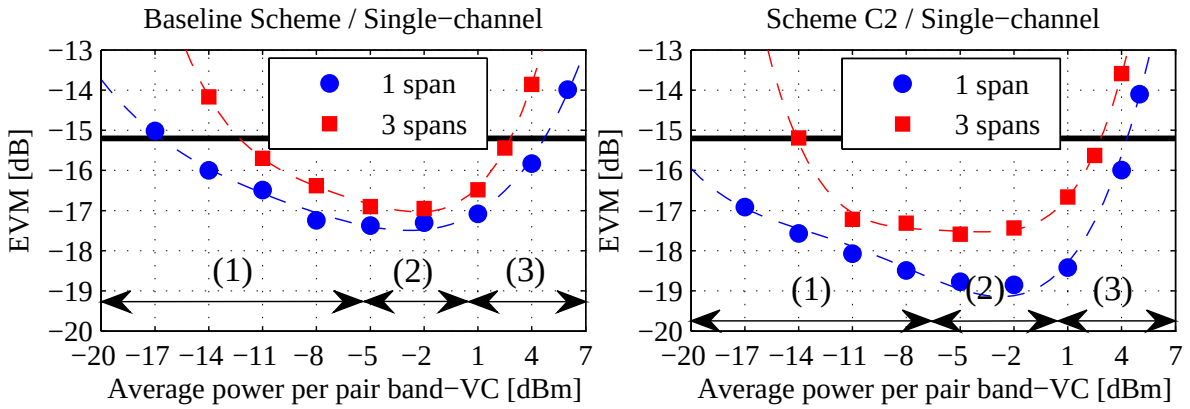

Figure 6.8: EVM as a function of the average power per pair band-VC for the baseline scheme and the scheme C2, for single-channel transmission, and for transmission along 1 (○) and 3 (□) spans. The black line at EVM = −15.2 dB indicates the threshold EVM, which gives the maximum allowed average power per pair band-VC. The dashed curves correspond to fourth-degree polynomials that are the best fit (in a least-squares sense) for the data. Region (1): linear transmission; region (2): weakly-nonlinear transmission; region (3): strong-nonlinear transmission.

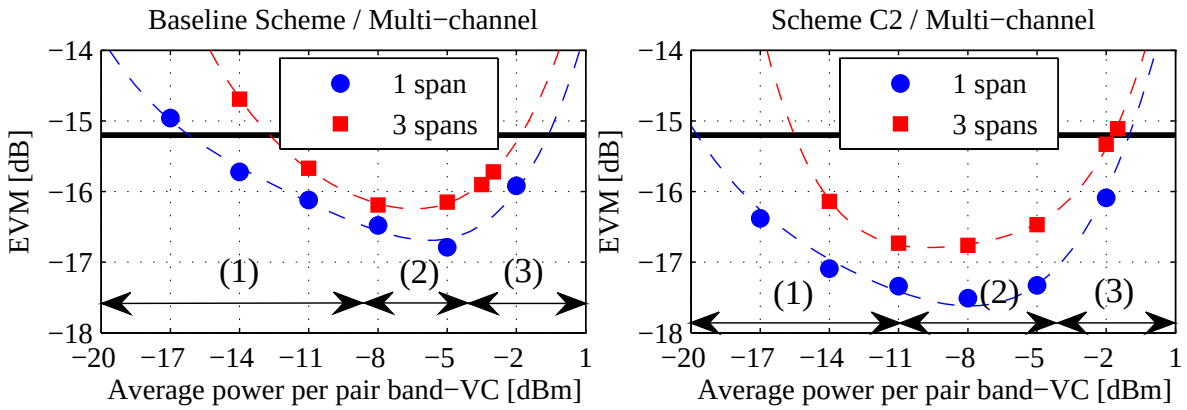

Figure 6.9: EVM as a function of the average power per pair band-VC for the baseline scheme and the scheme C2, for multi-channel transmission (4 channels), and for transmission along 1 (○) and 3 (□) spans. The black line at EVM = −15.2 dB indicates the threshold EVM, which gives the maximum allowed average power per pair band-VC. The dashed curves correspond to fourth-degree polynomials that are the best fit (in a least-squares sense) for the data. Region (1): linear transmission; region (2): weakly-nonlinear transmission; region (3): strong-nonlinear transmission.

from the VCs of only 10 dB can be seen in the second and third channels). The FWM products originated from the UCs are similar to the NDG2 products generated in the baseline scheme and shown in Fig. 5.8, with the difference that one UC is seen as a VC. For this reason, they are referred as UC-VC-band products. To understand this effect, Fig. 6.10 shows the generation of two UC-VC-band products in the scheme C2. The unwanted UC-VC-band products have a fixed $\Delta\nu_{ik}$ (equal to $0.75\cdot\Delta\nu_m$) and a variable $\Delta\nu_{jk}$. With VBG $= 32\cdot\Delta f_{sc}$, they interfere with the 96 subcarriers with higher index, that is, the ones farther away from the corresponding VCs: 1) for $\Delta\nu_{jk} = B_w/4 + \text{VBG}$, the generated FWM product with frequency ν_n interferes with the subcarrier with index equal to N_{sc}; 2) for $\Delta\nu_{jk} = B_w + \text{VBG}$, the generated FWM product with frequency ν_n interferes with the subcarrier with index equal to $N_{sc}/4$. The first has the highest FWM efficiency since it has the lowest $\Delta\nu_{jk}$; the second has the lowest FWM efficiency since it has the highest $\Delta\nu_{jk}$. With the baseline scheme, UCs are also generated by the non-ideal DP-MZM conversion process but are not strong enough to limit the performance since a power difference from the VCs equal or greater than 20 dB is obtained [see Fig. 6.4(a)]. Tab. 6.3 also shows that the maximum allowed average powers obtained experimentally are considerably higher than the ones obtained with the theoretical estimation (see Tab. 6.2). This difference can be attributed to the transmission of the same information in the different OFDM bands, which may improve the maximum allowed average powers.

Fig. 6.11 shows the EVM per OFDM subcarrier for average powers per pair band-VC in the linear, weakly-nonlinear and strong-nonlinear transmission regions, for the third band of the third channel of the baseline scheme and the second band of the third channel of the scheme

Table 6.3: Maximum allowed average power per pair band-VC (in dBm), obtained experimentally for the baseline scheme and the scheme C2.

	Single-channel	Multi-channel
Baseline scheme (single-span)	4.7	-0.6
Baseline scheme (multi-span)	2.8	-1.8
Scheme C2 (single-span)	4.3	-1.0
Scheme C2 (multi-span)	2.8	-1.7

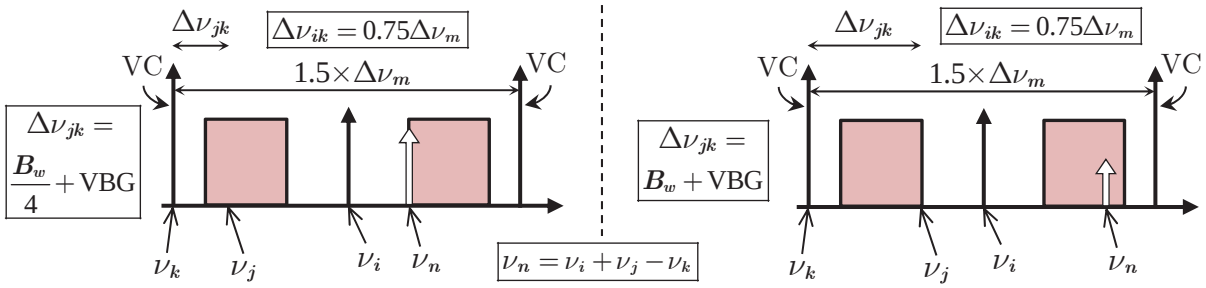

Figure 6.10: Generation of UC-VC-band FWM products in the scheme C2 (white arrow with frequency ν_n), where the UC (with frequency ν_i) is generated as a consequence of the non-perfect minimum transmission point of MZM 2. Two different values for $\Delta\nu_{jk}$ are considered: $\Delta\nu_{jk} = B_w/4 + \text{VBG}$ and $\Delta\nu_{jk} = B_w + \text{VBG}$.

C2, considering transmission with 1 and 4 channels and along 1 and 3 spans. From the TM results, these bands are among the most affected by the FWM impairments. It is stressed that lower indexes correspond to subcarriers closer to the VC. Fig. 6.11 shows that, for the baseline scheme, the subcarriers with higher EVMs are the ones closer and farther away from the VC and the subcarriers with the best EVMs are located in the centre of the OFDM band. This can be verified for the average powers in the three different transmission regions and is mostly attributed to the frequency limitations of the AWG. For the scheme C2 and for average powers in the linear and weakly-nonlinear transmission regions, Fig. 6.11 shows that the performance of the subcarriers degrades as the index decreases, that is, the EVM increases for subcarriers closer to the VC. Given that, in the scheme C2, the VCs of the H-pairs have a higher frequency than the OFDM band, the subcarriers closer to the VC and the VC itself are the frequencies suffering more from the AWG limitations. Fig. 6.11 also shows that, for the scheme C2 and for average powers in the strong-nonlinear transmission region, especially for single-channel transmission (the case where the average power per pair band-VC is the highest), the subcarriers farther away from the VC start to degrade as the subcarrier index increases. This is attributed to the FWM products generated by the UCs, which affect mostly the subcarriers farther away from the corresponding VC (see Fig. 6.10). For these subcarriers, as the index increases, $\Delta\nu_{jk}$ decreases and $\Delta\nu_{ik}$ remains the same. This results in a higher FWM efficiency, which leads to a higher EVM degradation (in agreement to what is shown in Fig. 6.11).

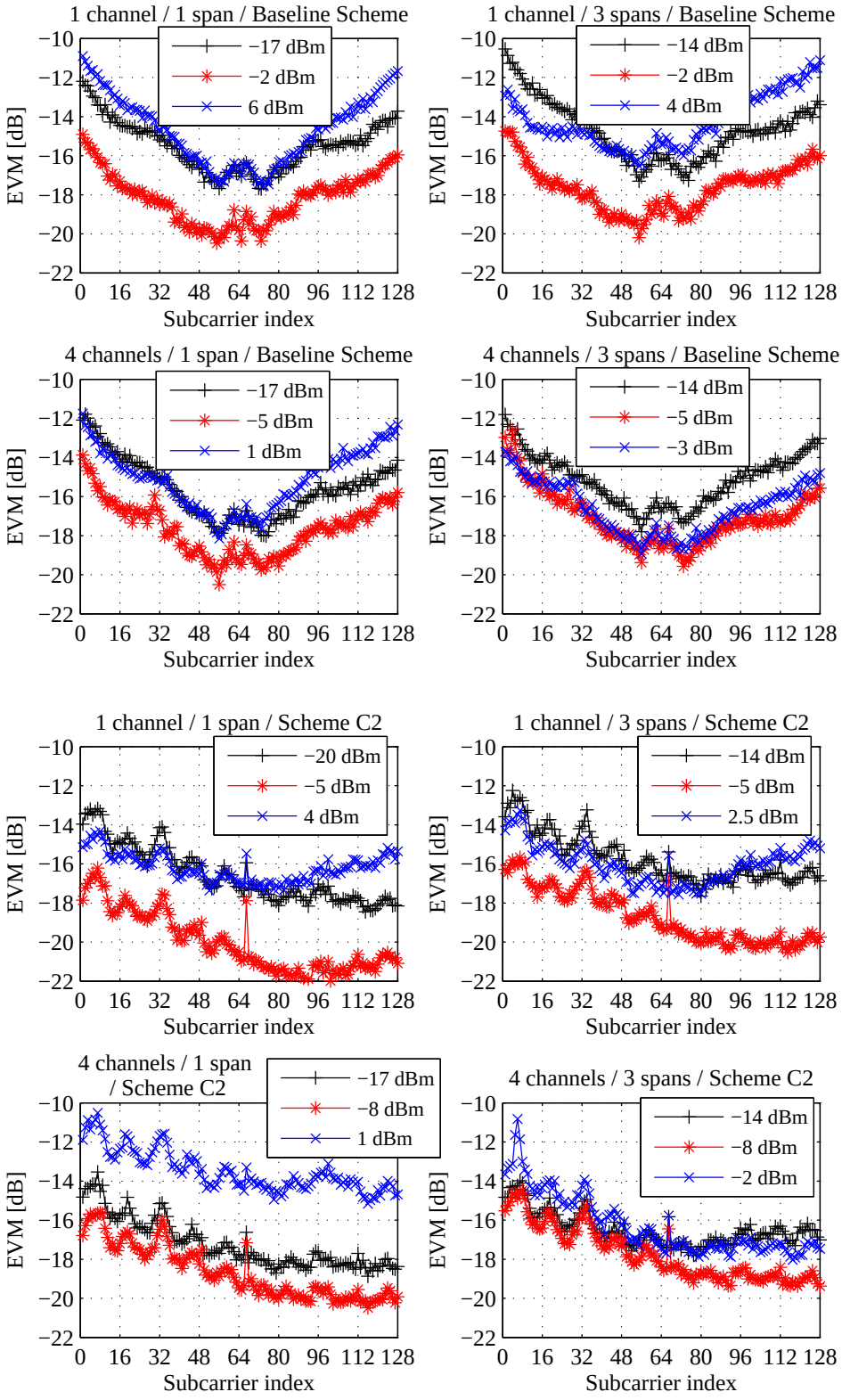

Figure 6.11: EVM per OFDM subcarrier for different average powers per pair band-VC, for the third band of the third channel of the baseline scheme and the second band of the third channel of the scheme C2, considering transmission with 1 and 4 channels and along 1 and 3 spans. The EVM per subcarrier for average powers in the three different transmission regions is shown in each sub-figure: linear (+), weakly-nonlinear (∗) and strong-nonlinear (×).

Fig. 6.12 shows the spectrum of the third band of the third channel for the baseline scheme and the spectrum of the second band of the third channel for the scheme C2, after band selection (at the BS output), for average powers per pair band-VC in the linear, weakly-nonlinear and strong-nonlinear transmission regions, considering transmission with 1 and 4 channels and along 1 and 3 spans. Fig. 6.12 shows that the selected pair band-VC is adequately filtered by the band selector, since the neighbouring pairs have a considerably lower average power when compared with the selected pair. To avoid significant crosstalk after photodetection, the BS must induce at least a power attenuation to the neighbouring pairs of 20 dB (as referred in chapter 3), which has been verified in all cases considered. With the increase of the average power, new FWM components appear surrounding the selected OFDM band and VC. Although these components are out-of-band, the ones close to and at a higher frequency than the selected VC can induce performance degradation as they lead to in-band distortion after photodetection. Fig. 6.12 also shows that, even though the average powers per pair band-VC at the input of each SSMF span can differ by more than 20 dB, the normalized power spectral density (PSD) does not show this significant difference. This is attributed to the mode of operation of the EDFAs, which provide constant power at their output.

Fig. 6.13 shows the spectrum at the MEB input, of all WDM channels for the baseline scheme, with transmission after 1 span with an average power per band-VC of -8 dBm (weakly-nonlinear transmission region) and 1 dBm (strong-nonlinear transmission region). Fig. 6.13 shows the appearance of out-of-band VC-VC-band products next to each VC for the average power in the strong-nonlinear transmission region. These products are of type NDG1, as shown in Fig. 6.7(a). Additionally, Fig. 6.13 shows a similar normalized PSD per pair band-VC, when increasing the average power per pair band-VC. This is also attributed to the mode of operation of the EDFAs.

Fig. 6.14 shows the spectrum of all WDM channels for the scheme C2, with transmission after 1 span with an average power per band-VC of -8 dBm (weakly-nonlinear transmission region) and 1 dBm (strong-nonlinear transmission region). Fig. 6.14 shows the appearance of out-of-band VC-VC-band products surrounding the VCs, which are originated from both types NDG1 and NDG2, as it is shown in Fig. 6.7(b). Fig. 6.14 also shows that, by changing the average power per pair band-VC, a different power distribution between the UCs is observed. This is mainly attributed to the appearance of UC-VC-VC products falling on the frequency of the UCs. Additionally, it is shown that, by increasing the average power, the average power difference between some UCs and VCs reduces. Besides generating non-negligible UC-VC-band products, a strong UC requires also careful BS adjustment to avoid the beating after photodetection of the UC with the selected band.

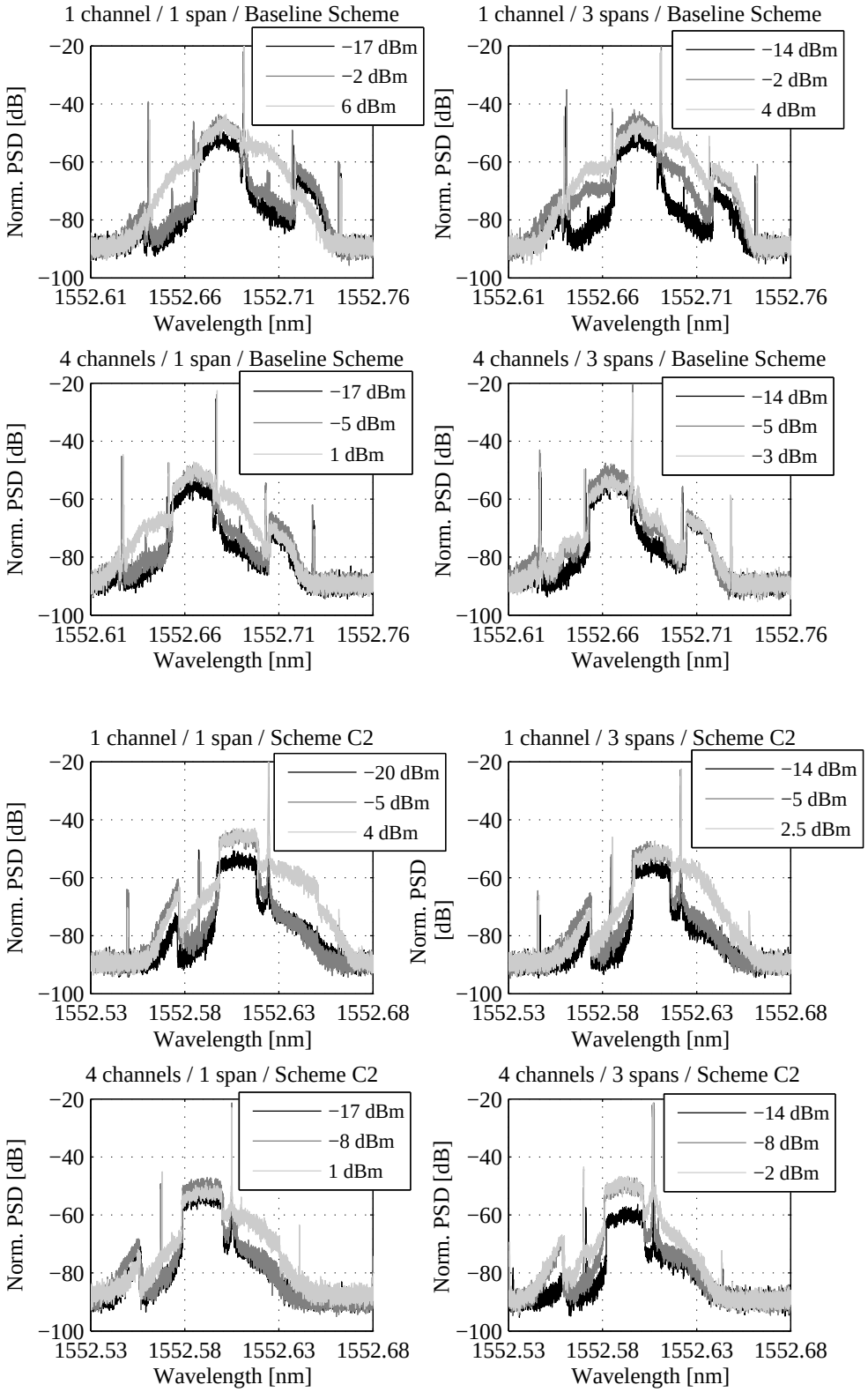

Figure 6.12: Spectrum of the third band of the third channel for the baseline scheme and spectrum of the second band of the third channel for the scheme C2, after band selection (at the BS output), for different average powers per pair band-VC, considering transmission with 1 and 4 channels and along 1 and 3 spans. The spectrum for average powers in the three different transmission regions is shown in each sub-figure: linear (black), weakly-nonlinear (dark grey) and strong-nonlinear (light grey).

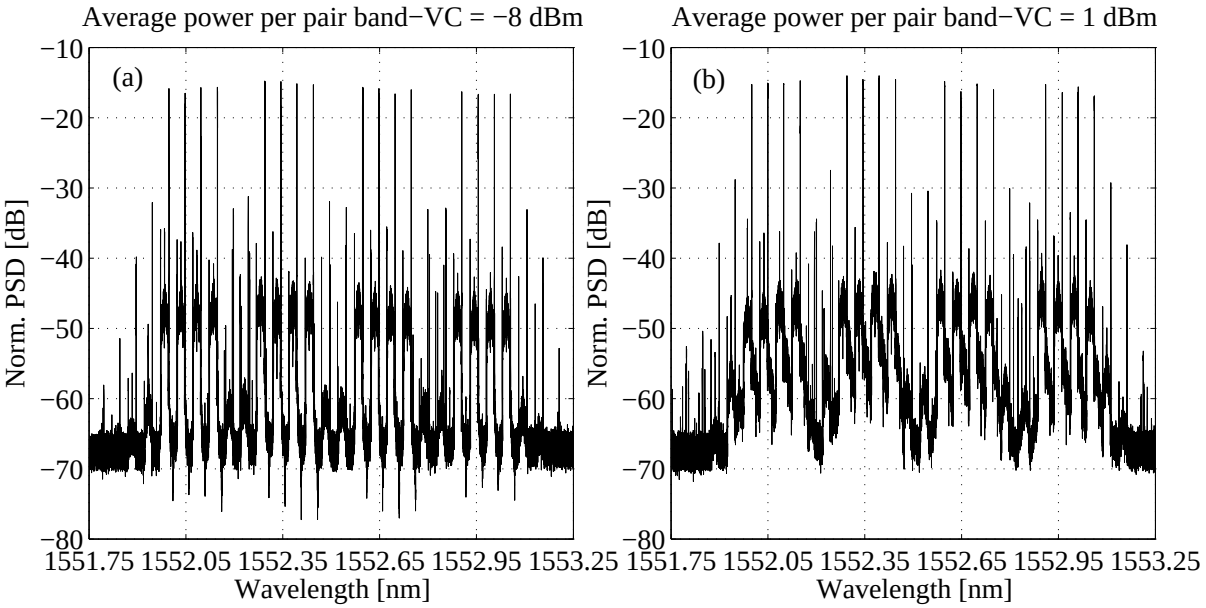

Figure 6.13: WDM signal spectrum at the MEB input with the baseline scheme, with transmission after 1 span with an average power per band-VC of (a) -8 dBm (weakly-nonlinear transmission region) and (b) 1 dBm (strong-nonlinear transmission region).

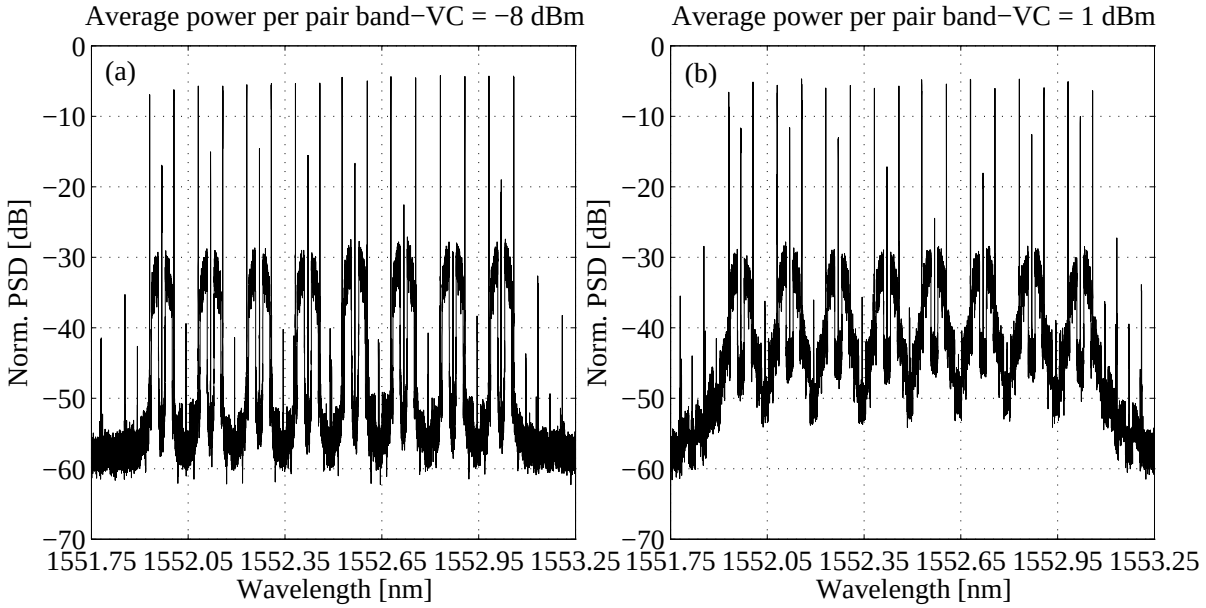

Figure 6.14: WDM signal spectrum at the MEB input with the scheme C2, with transmission after 1 span with an average power per band-VC of (a) -8 dBm (weakly-nonlinear transmission region) and (b) 1 dBm (strong-nonlinear transmission region).

6.5 Conclusions

In this chapter, the experimental evaluation of two different VC-assisted DD-MB-OFDM schemes (the baseline scheme and the scheme C2) has been performed and compared for single-channel and multi-channel transmission. Scheme C2 has been identified in the previous chapter as the

scheme showing the best FWM tolerance. The spectral efficiency has been maintained the same for both schemes and propagation along 1 and 3 SSMF spans, with 50-km length each, has been considered.

Theoretical estimation results of the two schemes have shown that the scheme C2 provides maximum allowed average powers per pair band-VC exceeding 1.5 dB when compared with the average powers of the baseline scheme. However, experimental results have shown that the scheme C2 does not provide improvement of the maximum allowed average powers when compared with the baseline scheme results. This has been attributed to the existence, in the scheme C2, of strong UCs that limit the performance when FWM is dominant (the region where the maximum allowed average powers are evaluated). These UCs are a consequence of the non-perfect minimum transmission point of the MZM responsible for modulating the pairs band-VC. The UCs in the scheme C2 can have an average power sufficient to generate UC-VC-band FWM products (the UC is seen as one VC) that degrade considerably the performance of the OFDM bands for high average powers. Given that the UCs of the baseline scheme are not strong enough to cause significant performance degradation, to effectively compare the baseline scheme with the scheme C2, a different experimental signal generation for the scheme C2, which avoids the generation of strong UCs, is required.

Chapter 7

Conclusions and future work

7.1 Conclusions

In this thesis, the impact of the nonlinear crosstalk induced by the Kerr effect on the transmission of multi-band (MB)-orthogonal frequency-division multiplexing (OFDM) signals along metro-access networks has been investigated. As a result of this investigation, MB-OFDM schemes showing enhanced tolerance to this optical fibre-induced nonlinear effect have been proposed. The degradation induced by the fibre nonlinearity has been characterized considering direct-detection (DD)-OFDM transmission in order to keep the system complexity and cost as low as possible, as required by metro-access networks. In the following paragraphs, the main outcomes of each chapter are presented.

In chapter 2, the main parameters which characterize the OFDM signal have been explained and it has been shown that the overall bit rate depends considerably on the system overheads [due to forward error correction (FEC), training symbols (TSs) and cyclic prefix (CP)] and on the number of OFDM subcarriers. The analysis of virtual carrier (VC)-assisted MB-OFDM signals has shown that the frequency allocation of a MB-OFDM signal depends on a set of parameters and the most relevant are the virtual carrier-to-band gap (VBG) and band gap (BG). Regarding the power distribution inside each MB-OFDM signal, the virtual carrier-to-band power ratio (VBPR) has been defined (similar to the well-known carrier-to-signal power ratio). It has been concluded that single sideband (SSB) transmission is preferable when compared with double sideband (DSB) transmission. Considering the generation of SSB-MB-OFDM signals, the dual-parallel (DP)-Mach-Zehnder modulator (MZM) together with the Hilbert transform (HT) have been employed to avoid the use of an optical filter with high selectivity after electrical-to-optical

conversion. Given that the considered SSB-MB-OFDM generation is not an ideal process, the modulation index has been defined to control the impact of the nonlinearity induced by the DP-MZM (caused by electrical-to-optical conversion) on the system performance. Considering the operations involving OFDM signal demodulation, it has been shown that signal-signal beat interference (SSBI) poses an important limitation to the performance of the received OFDM signal, and requires mitigation. Regarding the integrated metro-access network, the elements that compose that network have been described and it has been decided that only the downstream direction will be considered in the analysis performed in the following chapters. This decision is based on the assumption that the upstream transmission employs a signal structure similar to the one employed in the downstream transmission.

In chapter 3, a DD SSB MB-OFDM system, employing VCs, with 10 Gb/s data rate guaranteed-per-user for low-cost next generation metro networks has been presented and its performance has been analysed in back-to-back operation. A study concerning the limits and compromises between the number of OFDM subcarriers and OFDM bands of the MB-OFDM signal has been developed for wavelength division multiplexing (WDM) channels with bandwidths of 12.5, 25 and 50 GHz, where it has been shown that these channels are able to transport MB-OFDM signals comprising 2, 5 and 10 bands, respectively. The main impairments due to non-ideal filtering from the band selectors (BSs) and the wavelength selective switches (WSSs) have been presented and discussed. The error vector magnitude (EVM) has been used as figure of merit for performance evaluation, and from the EVM, the maximum link loss (MLL) for the different WDM channels has been assessed. Using an ideal BS, the obtained MLLs are between 20 dB [128-quadrature amplitude modulation (QAM) per subcarrier and channels with 10 bands] and 31 dB (32-QAM per subcarrier and channels with 2 bands). Two BSs with different selectivity have been employed and compared with the ideal BS. A MLL penalty not exceeding 3 dB for the BS with higher selectivity, and not exceeding 4 dB for the BS with lower selectivity has been shown. It has been also shown that, with systems with 2 bands, more than 30 WSSs can be concatenated with a EVM degradation not exceeding 1 dB. With 5 and 10 bands, more than 15 WSSs can be concatenated with a EVM degradation not exceeding 2 dB.

In chapter 4, a theoretical method (TM) to evaluate the four wave mixing (FWM) power in ultradense wavelength division multiplexing (UDWDM) VC-assisted MB-OFDM systems using DD has been presented assuming that the VC-VC-band FWM products are dominant over other FWM-induced products. A simplified TM to obtain the FWM power for MB-OFDM systems with high-dispersion fibre, where only part of the FWM products of the type non-degenerate (NDG)2 are considered, has been derived to relax the computation complexity of the

FWM power evaluation. A closed-form expression for the FWM power in MB-OFDM systems employing low-dispersion fibre has been also proposed. Analytical expressions for the maximum allowed average power of the worst pair band-VC at the fibre input in VC-assisted DD-MB-OFDM systems, for a given EVM impaired by FWM, have also been derived. The TM and simplified theoretical method (STM) validation has been performed considering an application scenario with band spacing of 3.125 GHz and 10 Gb/s data rate per OFDM band. It has been shown that the TM provides good performance estimates of the FWM-induced degradation. The discrepancy between the numerical simulation (NS)-estimated and TM-estimated threshold average powers (TAPs) is close to 0.5 dB with 1 standard single mode fibre (SSMF) span, and is negligible for 3 or 6 spans. When compared with the NS results, the STM-estimated TAP provides a discrepancy that may achieve 1.5 dB. However, for the scenarios of main interest in which the number of spans is higher than one, the discrepancy does not exceed 1 dB. Using the TM and STM, the upper bound of the power limit (UBPL) has been obtained for an arbitrary number of SSMF spans and channel gaps (CGs).

In chapter 5, the tolerance to the FWM effect of VC-assisted DD SSB-MB-OFDM schemes has been investigated in a UDWDM metro-access network scenario, and schemes with improved tolerance to FWM have been proposed. Schemes showing the best tolerance to FWM, among all the analysed schemes within each channel bandwidth (CB) class, have been identified for specific spectral efficiencies. This study has been performed considering channel grids of 3.125 GHz and 6.25 GHz for each OFDM band, which deliver a dedicated capacity of 10 Gb/s and 25 Gb/s to each user, respectively. For a channel grid of 3.125 GHz, it has been shown that an adequate design of the VC-assisted scheme enables a power budget (PB) improvement that achieves 3 dB. This improvement allows to double the number of users of the metro-access network or to extend the optical distribution network (ODN) reach by about 12 km. With a 6.25 GHz channel grid, the PB improvement surpasses 4 dB, enabling to double the number of users and simultaneously extend the ODN coverage by about 5 km.

In chapter 6, the experimental evaluation of two different VC-assisted DD-MB-OFDM schemes (the baseline scheme and the scheme C2) has been performed and compared for single-channel and multi-channel transmission. The scheme C2 has been identified in the previous chapter as the scheme showing the best FWM tolerance. The spectral efficiency has been maintained the same for both schemes and propagation along 1 and 3 SSMF spans, with 50-km length each, has been considered. Theoretical estimation results of the two schemes have shown that the scheme C2 provides maximum allowed average powers per pair band-VC exceeding 1.5 dB when compared with the average powers of the baseline scheme. However, experimental results have shown

that the scheme C2 does not provide improvement of the maximum allowed average powers when compared with the baseline scheme results. This has been attributed to the existence, in the scheme C2, of strong unwanted carriers (UCs) that limit the performance when FWM is dominant (the region where the maximum allowed average powers are evaluated). These UCs are a consequence of the non-perfect minimum transmission point of the MZM responsible for modulating the pairs band-VC. The UCs in the scheme C2 can have an average power sufficient to generate UC-VC-band FWM products (the UC is seen as one VC) that degrade considerably the performance of the OFDM bands for high average powers. Given that the UCs of the baseline scheme are not strong enough to cause significant performance degradation, to effectively compare the baseline scheme with the scheme C2, a different experimental signal generation for the scheme C2, which avoids the generation of strong UCs, is required.

7.2 Future work

As a result of the work developed in this thesis, the following topics are suggested as future work:

- Identification of the performance improvement achieved by using adaptive modulation in the OFDM subcarriers instead of having fixed modulation for all the subcarriers.
- Upgrade of the digital signal processing (DSP)-based SSBI mitigation algorithm to operate in the digital domain. This avoids having digital-to-analogue conversion in the SSBI estimation process.
- Development of a DSP-based algorithm which conjugates peak-to-average power ratio (PAPR) reduction at the transmitter (for instance, using the raised-cosine symbol precoding technique presented in [62]) and SSBI mitigation at the receiver. A PAPR reduction technique should provide additional tolerance to the FWM effect experienced with VC-assisted DD-MB-OFDM transmission.
- Experimental assessment of scheme C2 with a different signal generation method to avoid the detrimental effect of the UCs on its performance.

Appendix A

List of publications

A.1 Papers in international journals

- P. Cruz, T. Alves, and A. Cartaxo, "Virtual carrier-assisted DD-MB-OFDM schemes for UDWDM metro-access networks with improved tolerance to four-wave mixing," *IEEE/OSA Journal of Lightwave Technology*, vol. 35, no. 20, pp. 4468 - 4478, October, 2017.
  `http://ieeexplore.ieee.org/document/8016318/`

- P. Cruz, T. Alves, and A. Cartaxo, "Theoretical analysis of the four-wave mixing effect in virtual carrier-assisted DD MB-OFDM ultra-dense WDM metropolitan networks," *IEEE/OSA Journal of Lightwave Technology*, vol. 34, no. 23, pp. 5401 - 5411, December, 2016.
  `http://ieeexplore.ieee.org/document/7583738/`

A.2 Book chapter

- P. Cruz, T. Alves, and A. Cartaxo, "Performance evaluation of optical noise-impaired multi-band OFDM systems through analytical modeling," Chapter in *Photoptics 2014 - Proceedings of the 2nd International Conference on Photonics, Optics and Laser Technology - Revised Selected Papers*, Eds. Paulo Ribeiro and Maria Raposo, Springer Proceedings in Physics, vol. 177, Springer International Publishing, Switzerland, 2016.
  `https://link.springer.com/chapter/10.1007/978-3-319-27321-1_8`

A.3 Communications in international conferences

- P. Cruz, T. Alves, and A. Cartaxo, "Loss budget of ultra-dense 10 Gb/s per-user guaranteed direct-detection MB-OFDM metro-access networks," in *Proc. International Conference on Transparent Optical Networks (ICTON)*, Budapest, Hungary, July 2015, Paper Tu.B1.4.
  `http://ieeexplore.ieee.org/document/7193420/`

- P. Cruz, T. Alves, and A. Cartaxo, "Impact of inter-band crosstalk due to nonlinear fibre transmission on the performance of direct-detection single-sideband MB-OFDM metro networks," in *Proc. International Conference on Transparent Optical Networks (ICTON)*, Budapest, Hungary, July 2015, Paper Tu.B1.3.
  `http://ieeexplore.ieee.org/document/7193419/`

- P. Cruz, J. Rosário, T. Alves, and A. Cartaxo, "Exhaustive Gaussian approach for performance evaluation of direct-detection OFDM systems employing square and cross QAM," in *Proc. International Telecommunications Symposium (ITS)*, São Paulo, Brazil, August 2014.
  `http://ieeexplore.ieee.org/document/6947998/`

- P. Cruz, T. Alves, and A. Cartaxo, "Analytical modelling for performance evaluation of distortion-impaired direct-detection single-sideband optical OFDM systems employing virtual-carriers," in *Proc. International Conference on Transparent Optical Networks (ICTON)*, Graz, Austria, July 2014, Paper We.A1.6.
  `http://ieeexplore.ieee.org/document/6876501/`

- P. Cruz, T. Alves, and A. Cartaxo, "Analytical modeling for performance evaluation of ASE noise-impaired direct-detection single-sideband multi-band optical OFDM systems," in *Proc. International Conference on Photonics, Optics and Laser Technology (PHOTOPTICS)*, pp. 134-141, Lisbon, Portugal, January 2014.
  `http://www.scitepress.org/DigitalLibrary/Link.aspx?doi=10.5220/0004881301340141`

Appendix B

Analytical modelling of VC-assisted OFDM systems

B.1 Introduction

Analytical models of the performance of orthogonal frequency-division multiplexing (OFDM)-based systems are of great interest to network designers as they provide fast performance estimates without requiring extensive numerical simulations.

In section B.2, an analytical model for performance evaluation of amplified spontaneous emission (ASE) noise-impaired direct-detection (DD) single sideband (SSB) multi-band (MB)-OFDM systems is proposed, using the bit error ratio (BER) as figure of merit. This model does not account for the distortion effects caused by the Mach-Zehnder modulator (MZM) (which performs electrical-to-optical conversion) and the p-type-intrinsic-n-type (PIN)-photodiode (PD) (which performs optical-to-electrical conversion).

In section B.3, an analytical model for performance evaluation of distortion-impaired DD SSB OFDM systems with one pair band-virtual carrier (VC) is presented using the error vector magnitude (EVM) as figure of merit. This model accounts for the MZM distortion effects as it considers a third-order approximation for the MZM, which is biased at the quadrature point.

The performance results obtained with these models can be seen as benchmarks for the performance of VC-assisted MB-OFDM systems. For both models, operation in optical back-to-back is considered.

The work presented along this appendix is also published in [65–67].

B.2 Noise-impaired VC-assisted MB-OFDM systems

B.2.1 System model

The model considered to describe the noise-impaired VC-assisted MB-OFDM system in optical back-to-back (without fibre transmission) is presented in Fig. B.1. This model considers the following simplifications when compared with the integrated metro-access network presented in section 2.4: 1) a single MB-OFDM transmitter (Tx), generating one MB-OFDM signal, is employed; 2) the SSB generation is performed by a chirpless MZM plus an SSB filter; 3) only the ASE noise introduced by the erbium doped fibre amplifiers (EDFAs) is considered (modelled by an ASE noise loader); 3) it is assumed that the ASE noise is dominant over trans-impedance amplifier (TIA)-induced noise; 4) the optical distribution network (ODN) losses are not accounted; and 5) signal-signal beat interference (SSBI) mitigation is not performed at the OFDM receiver (Rx), as the virtual carrier-to-band gap (VBG) is assumed sufficiently large to accommodate the SSBI impairment.

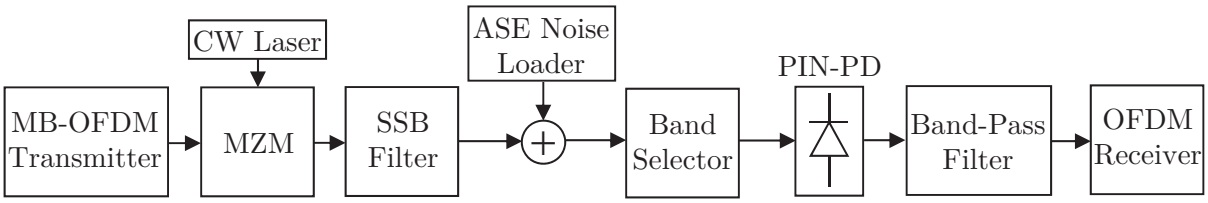

Figure B.1: MB-OFDM system model in optical back-to-back.

The radio frequency (RF) MB-OFDM signal generated at the MB-OFDM transmitter is composed by N_B OFDM signals (or bands) and N_B RF carriers [or VCs], as depicted in Fig. B.2.

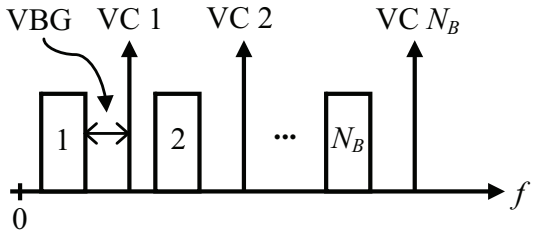

Figure B.2: Simplified scheme of a MB-OFDM signal, with N_B bands and N_B VCs. VBG - virtual-carrier-to-band gap.

The optical signal is generated by a continuous wave (CW) laser and the MB-OFDM signal modulates that optical signal using a chirpless MZM, biased at the quadrature point. The optical signal at the MZM output is then filtered by a SSB filter, creating a SSB signal. This allows overcoming the chromatic dispersion-induced power fading impairment caused by the square-law

photodetection of a double-sided optical signal transmitted along a dispersive medium. After SSB filtering, an ASE noise loader adds optical noise to the MB-OFDM signal. After ASE noise addition, the pair band-VC to be dropped at the receiver is selected by an optical filter referred as band selector (BS). The selected signal is photodetected by a PIN-PD, which converts the optical signal to an electrical signal. A band-pass filter (BPF) is used to recover the OFDM signal after photodetection and to remove the out-of-band noise. Finally, the OFDM receiver digitally-converts and demodulates the electrical signal.

B.2.2 Analytical modelling

In this section, the analytical modelling of the signal and noise power along the MB-OFDM system is performed. The main objective is to obtain analytical expressions for the optical signal-to-noise ratio (OSNR) and the electrical signal-to-noise ratio (ESNR) at the BPF output. With these expressions, fast BER estimates can be obtained to provide insight on the performance of SSB MB-OFDM systems employing direct-detection.

The output electrical field of a chirpless MZM, $e_{MZM}(t)$, can be expressed as:

$$e_{MZM}(t) = E_i \cos\left\{\frac{\pi}{2V_\pi}\left[-V_b + v(t)\right]\right\}\exp\left(j2\pi\nu_0 t\right) \tag{B.1}$$

where E_i is the optical field of the CW laser, V_b is the MZM bias voltage, V_π is the MZM switching voltage, and ν_0 is the reference optical frequency.

Making use of the first-order approximation given by Taylor series, with respect to $v(t)$, around zero to linearise the MZM output field, the following approximation for $e_{MZM}(t)$ is obtained:

$$e_{MZM}(t) \approx E_i \left[\cos\left(\frac{\pi}{2V_\pi}V_b\right) + \sin\left(\frac{\pi}{2V_\pi}V_b\right)\frac{\pi}{2V_\pi}v(t)\right]\exp\left(j2\pi\nu_0 t\right). \tag{B.2}$$

Considering that the MZM is biased at quadrature point ($V_b = V_\pi/2$), the linearised output field, $e_{MZM,l}(t)$, can be written as:

$$e_{MZM,l}(t) = E_i \left[\frac{\sqrt{2}}{2} + \frac{\sqrt{2}}{4}\frac{\pi}{V_\pi}v(t)\right]\exp\left(j2\pi\nu_0 t\right). \tag{B.3}$$

Using Eq. 2.23, Eq. 2.24 and Eq. 2.25, the mean power at the linearised MZM output, $p_{MZM,l}$,

can be expressed as:

$$p_{MZM,l} = \left\langle |e_{MZM,l}|^2 \right\rangle = \underbrace{\frac{E_i^2}{2}}_{p_o} + \underbrace{\frac{1}{8}\frac{\pi^2}{V_\pi^2} E_i^2 \frac{p_{RF}}{1+A_v^2}}_{p_b} + \underbrace{\frac{1}{8}\frac{\pi^2}{V_\pi^2} E_i^2 \frac{p_{RF}}{1+A_v^2} A_v^2}_{p_v} \tag{B.4}$$

where p_o is the mean power of the optical carrier, p_b is the mean power of all the OFDM bands ($p_b = N_B \cdot p_{b,n}$), and p_v is the mean power of all the VCs ($p_v = N_B \cdot p_{v,n}$).

Two important power ratios can be determined from Eq. B.4. One is the virtual carrier-to-band power ratio (VBPR) (already defined in Eq. 2.26 for a single pair band-VC):

$$\text{VBPR} = \frac{p_v}{p_b} = A_v^2 \tag{B.5}$$

and the other is the optical carrier-to-band power ratio (OBPR):

$$\text{OBPR} = \frac{p_o}{p_b} = \frac{4V_\pi^2}{\pi^2}\left(\frac{1+\text{VBPR}}{V_{RMS,req}^2}\right). \tag{B.6}$$

OSNR derivation

After electrical-to-optical conversion, SSB filtering is performed and the lower sidebands and VCs are removed.

Let us focus our attention on a specific band n of the MB-OFDM signal. An up-converted OFDM signal $s_{b,n}(t)$ can be written as:

$$s_{b,n}(t) = s_{I,n}(t)\cos(2\pi f_{b,n}t) - s_{Q,n}(t)\sin(2\pi f_{b,n}t) \tag{B.7}$$

where $s_{I,n}(t)$ is the low-pass filtered in-phase (I) component of the OFDM signal of band n, $s_{Q,n}(t)$ is the low-pass filtered quadrature (Q) component of the OFDM signal of band n, and $f_{b,n}$ is the n-th band up-converter frequency. Together with the up-converted OFDM signal $s_{b,n}(t)$, is a VC, $s_{v,n}(t)$, given by:

$$s_{v,n}(t) = \sqrt{2}\cos[2\pi f_{v,n}t + \varphi_v] = \sqrt{2}\cos[\phi_v(t)] \tag{B.8}$$

where $f_{v,n}$ is the n-th VC frequency, φ_v is the VC initial phase and $\phi_v(t) = 2\pi f_{v,n}t + \varphi_v$. After ideal SSB filtering, the lower sideband and lower VC are removed. The resulting signals,

$s_{b,n,SSB}(t)$ and $s_{v,n,SSB}(t)$, are given as follows:

$$\begin{cases} s_{b,n,SSB}(t) = \dfrac{1}{2}\underbrace{[s_{I,n}(t) + j s_{Q,n}(t)]}_{s_n(t)} \exp\left(j2\pi f_{b,n} t\right) = \dfrac{1}{2} s_n(t) \exp\left(j2\pi f_{b,n} t\right) \\ s_{v,n,SSB}(t) = \dfrac{\sqrt{2}}{2} \exp\left\{j[2\pi f_{v,n} t + \varphi_v]\right\} = \dfrac{\sqrt{2}}{2} \exp\left[j\phi_v(t)\right] \end{cases} \tag{B.9}$$

where $s_n(t)$ is the complex baseband OFDM signal of band n. Considering all the N_B bands of the MB-OFDM signal, the mean power at the SSB filter output, p_{SSB}, can be expressed as:

$$p_{SSB} = p_o + \frac{p_v}{2} + \frac{p_b}{2}. \tag{B.10}$$

Afterwards, an ASE noise loader is added to the signal at the SSB filter output. Hence, it is important to define the OSNR after noise loading (NL). Considering a ASE noise, characterized by zero-mean additive white Gaussian noise (AWGN) process, that is present in the parallel ($\|$) and perpendicular ($\perp$) polarization directions, and assuming the signal field at the SSB filter output polarized in the parallel direction, the low-pass equivalent (LPE) of the field after NL, $\mathbf{e}_{NL}(t)$, can be expressed as:

$$\mathbf{e}_{NL}(t) = \Big[e_{SSB,\|}(t) + n_{I,\|}(t) + j n_{Q,\|}(t)\Big]\,\mathbf{u}_{\|} + \Big[n_{I,\perp}(t) + j n_{Q,\perp}(t)\Big]\mathbf{u}_{\perp} \tag{B.11}$$

where $e_{SSB,\|}(t)$ is the OFDM signal field at the SSB filter output in the $\|$ polarization defined by $\mathbf{u}_{\|}$, $n_{I,\|}(t)$ and $n_{Q,\|}(t)$ are the I and Q noise components in the $\|$ polarization, respectively, and $n_{I,\|}(t)$ and $n_{Q,\|}(t)$ are the I and Q noise components in the $\perp$ polarization defined by $\mathbf{u}_{\perp}$, respectively. Assuming that each one of the four noise components has a constant power spectral density (PSD) given by S_{ASE}, the optical noise mean power in a bandwidth B_N after NL, $p_{n,NL}$, can be expressed as:

$$p_{n,NL} = 4\, S_{ASE} B_N. \tag{B.12}$$

Usually, B_N corresponds to a reference bandwidth of 0.1 nm, which is approximately 12.5 GHz.

The OSNR is defined as the ratio between the signal power after NL, $p_{s,NL}$ (which is equal to the signal power at the SSB filter output, p_{SSB}), and the noise mean power, $p_{n,NL}$, in the reference bandwidth B_N, after NL. Using Eq. B.10 and Eq. B.12, the OSNR is then expressed as:

$$\text{OSNR} = \frac{p_{s,NL}}{p_{n,NL}} = \frac{p_{SSB}}{p_{n,NL}} = \left(p_o + \frac{p_v}{2} + \frac{p_b}{2}\right) \frac{1}{4\, S_{ASE} B_N}. \tag{B.13}$$

ESNR derivation

After ASE noise loading, the BS is used to select the OFDM band and VC that will be photodetected (dropped). The LPE of the BS considered here is an ideal filter, with transfer function $H_{BS,n}(f)$ and impulse response $h_{BS,n}(t)$, that only selects the n-th OFDM signal and the n-th VC. The transfer function $H_{BS,n}(f)$ can be written as:

$$H_{BS,n}(f) = \text{rect}\left(\frac{f - f_{BS,n}}{B_{BS}}\right) \tag{B.14}$$

where B_{BS} is the BS bandwidth and $f_{BS,n}$ is the BS centre frequency given by:

$$f_{BS,n} = \frac{f_{\text{max,BS}} + f_{\text{min,BS}}}{2} = \frac{1}{2}\left[f_{v,n} + \left(f_{b,n} - \frac{B_w}{2}\right)\right] \tag{B.15}$$

where $f_{\text{max,BS}}$ and $f_{\text{min,BS}}$ are the maximum and minimum frequencies of the BS passband, respectively, and B_w is the OFDM signal bandwidth.

The LPE of the signal at the BS output, $\mathbf{e}_{BS,n}(t)$, can be expressed as:

$$\mathbf{e}_{BS,n}(t) = \mathbf{e}_{NL}(t) \circledast h_{BS,n}(t) = \left[e_{BS,n,\parallel}(t) + n'_{I,\parallel}(t) + jn'_{Q,\parallel}(t)\right]\mathbf{u}_{\parallel} + \left[n'_{I,\perp}(t) + jn'_{Q,\perp}(t)\right]\mathbf{u}_{\perp} \tag{B.16}$$

where $\circledast$ denotes the convolution operation, $e_{BS,n,\parallel}(t)$ is the field, at the BS output, of the n-th OFDM signal and n-th VC in the $\parallel$ polarization, $n'_{I,\parallel}(t)$ and $n'_{Q,\parallel}(t)$ are the filtered I and Q noise components in the $\parallel$ polarization, respectively, and $n'_{I,\parallel}(t)$ and $n'_{Q,\parallel}(t)$ are the filtered I and Q noise components in the $\perp$ polarization, respectively. Considering the formulation for $v(t)$ shown in Eq. 2.22, and taking into account that, after SSB filtering, $s_{v,n}(t)$ and $s_{b,n}(t)$ become $s_{v,n,SSB}(t)$ and $s_{b,n,SSB}(t)$, respectively, the field $e_{BS,n,parallel}(t)$ is given by:

$$\begin{aligned} e_{BS,n,\parallel}(t) =& \frac{\sqrt{2}}{4}\frac{\pi}{V_\pi}E_i\left[\frac{V_{RMS,req}}{V_{RMS,s_e}V_{RMS,s_{b,n}}}s_{b,n,SSB}(t) + \frac{V_{RMS,req}}{V_{RMS,s_e}V_{RMS,s_{v,n}}}A_v s_{v,n,SSB}(t)\right] \times \\ & \times \exp\left(j2\pi\nu_0 t\right). \end{aligned} \tag{B.17}$$

The mean power of the field $e_{BS,n,\parallel}(t)$, $p_{BS,n}$, is given as follows:

$$p_{BS,n} = \frac{1}{N_B}\left(\frac{p_v + p_b}{2}\right) = \frac{p_{v,n} + p_{b,n}}{2}. \tag{B.18}$$

After band selection, the signal is photodetected. The PIN-PD is modelled by a square modulus function with responsivity of 1 $\mathrm{A}\cdot\mathrm{W}^{-1}$. The photocurrent at the PIN-PD output, $i_{PIN}(t)$, can be written as:

$$i_{PIN}(t) = |\mathbf{e}_{BS,n}(t)|^2 = \left|e_{BS,n,\parallel}(t) + n'_{I,\parallel}(t) + jn'_{Q,\parallel}(t)\right|^2 + \left|n'_{I,\perp}(t) + jn'_{Q,\perp}(t)\right|^2. \tag{B.19}$$

After some calculations, the PIN-PD output current can be separated in two different groups: the signal-dependent photocurrent and the noise-dependent photocurrent. The signal dependent photocurrent, denoted as $i_{s,PIN}(t)$, is given by:

$$\begin{aligned} i_{s,PIN}(t) = &\left|e_{BS,n,\parallel}(t)\right|^2 = \frac{1}{8}\frac{\pi^2}{V_\pi^2}E_i^2 \times \\ &\times \left[\frac{1}{4}\left(\frac{V_{RMS,req}}{V_{RMS,s_{b,n}}V_{RMS,s_e}}\right)^2 |s_n(t)|^2 + \frac{1}{2}\left(\frac{V_{RMS,req}}{V_{RMS,s_{v,n}}V_{RMS,s_e}}A_v\right)^2 + \right. \\ &\left. + \frac{\sqrt{2}}{2}\frac{V_{RMS,req}^2}{V_{RMS,s_{b,n}}V_{RMS,s_{v,n}}V_{RMS,s_e}^2}A_v\,\Re\{s_n(t)\exp[-j(2\pi f_{r,n}t+\varphi_v)]\}\right] \end{aligned} \tag{B.20}$$

with $f_{r,n} = f_{v,n} - f_{b,n}$. The first term of $i_{s,PIN}(t)$ is the SSBI, the second term is the direct-current (DC) component, and the third term is the received OFDM signal. The noise-dependent photocurrent, denoted as $i_{n,PIN}(t)$, where the noise-noise beat terms were neglected, can be expressed as:

$$i_{n,PIN}(t) = e_{BS,n,\parallel}(t)\left[n'_{I,\parallel}(t) - jn'_{Q,\parallel}(t)\right] + \left\{e_{BS,n,\parallel}(t)\right\}^*\left[n'_{I,\parallel}(t) + jn'_{Q,\parallel}(t)\right]. \tag{B.21}$$

In order to obtain the noise power at the PIN-PD output, $p_{n,PIN}$, the auto-correlation function of $i_{n,PIN}(t)$ must be evaluated. Using Eq. B.17 and Eq. B.9 and taking into account that $V_{RMS,s_n} = \sqrt{2}V_{RMS,s_{b,n}}$, $e_{BS,n,\parallel}(t)$ can be rewritten as follows:

$$\begin{aligned} e_{BS,n,\parallel}(t) &= \frac{\sqrt{2}}{4}\frac{\pi}{V_\pi}E_i\frac{\sqrt{2}}{2}\frac{V_{RMS,req}}{V_{RMS,s_e}}\left[\tilde{s}_n(t)\exp\left(-j2\pi f_{r,n}t\right) + A_v\right]\exp\left(j2\pi\nu_0 t\right)\exp\left[j\phi_v(t)\right] = \\ &= S(t)\exp\left[j\phi_v(t)\right] \end{aligned} \tag{B.22}$$

where $\tilde{s}_n(t) = s_n(t)/V_{RMS,s_n}$. Using Eq. B.22, $i_{n,PIN}(t)$ can be rewritten as:

$$i_{n,PIN}(t) = S(t)\exp\left[j\phi_v(t)\right]n^*(t) + S^*(t)\exp\left[-j\phi_v(t)\right]n(t) \tag{B.23}$$

with $n(t) = n'_{I,\parallel}(t) + jn'_{Q,\parallel}(t)$. Using Eq. B.23, the auto-correlation function of $i_{n,PIN}(t)$,

$R_{n,PIN}(\tau)$, is given by:

$$\begin{aligned} R_{n,PIN}(\tau) &= \mathbb{E}[i_{n,PIN}(t)\, i_{n,PIN}(t+\tau)] = \\ &= \mathbb{E}\{S(t)S(t+\tau)\exp\{j\,[\phi_v(t)+\phi_v(t+\tau)]\}\, n^*(t)\, n^*(t+\tau)\}+ \\ &+ \mathbb{E}\{S(t)S^*(t+\tau)\exp\{j\,[\phi_v(t)-\phi_v(t+\tau)]\}\, n^*(t)\, n(t+\tau)\}+ \\ &+ \mathbb{E}\{S^*(t)S(t+\tau)\exp\{-j\,[\phi_v(t)-\phi_v(t+\tau)]\}\, n(t)\, n^*(t+\tau)\}+ \\ &+ \mathbb{E}\{S^*(t)S^*(t+\tau)\exp\{-j\,[\phi_v(t)+\phi_v(t+\tau)]\}\, n(t)\, n(t+\tau)\} \end{aligned} \tag{B.24}$$

where $\mathbb{E}\{\cdot\}$ corresponds to the expected value. Taking into account that the expected value of the terms depending on φ_v are zero, $R_{n,PIN}(\tau)$ can be simplified as:

$$\begin{aligned} R_{n,PIN}(\tau) = \mathbb{E}\{S(t)S^*(t+\tau)\}\exp(-j2\pi f_{v,n}\tau)\,\mathbb{E}\{n^*(t)\, n(t+\tau)\}+ \\ + \mathbb{E}\{S^*(t)S(t+\tau)\}\exp(j2\pi f_{v,n}\tau)\,\mathbb{E}\{n(t)\, n^*(t+\tau)\}. \end{aligned} \tag{B.25}$$

After performing some calculations, in which the Fourier transform definition and the Wiener-Khintchine theorem were employed, $R_{n,PIN}(\tau)$ becomes:

$$\begin{aligned} R_{n,PIN}(\tau) = \mathbb{E}\{S(t)S^*(t+\tau)\}\int_{-\infty}^{\infty}[S_I(f)+S_Q(f)]\exp[j2\pi(f-f_{v,n})\tau]\,|H_{BS,n}(f)|^2\,\mathrm{d}f+ \\ + \mathbb{E}\{S^*(t)S(t+\tau)\}\int_{-\infty}^{\infty}[S_I(f)+S_Q(f)]\exp[j2\pi(f+f_{v,n})\tau]\,|H_{BS,n}(-f)|^2\,\mathrm{d}f \end{aligned} \tag{B.26}$$

where $S_I(f)$ and $S_Q(f)$ correspond to the noise PSD of the I and Q components, respectively. The noise power at the PIN-PD output, $p_{n,PIN}$, is obtained from $R_{n,PIN}(\tau)$ by imposing $\tau = 0$. Hence, the noise power at the PIN-PD output, $p_{n,PIN}$, can be written as:

$$\begin{aligned} p_{n,PIN} &= \underbrace{\mathbb{E}\{|S(t)|^2\}}_{p_{BS,n}}\left\{\int_{-\infty}^{+\infty}\underbrace{[S_I(f)+S_Q(f)]}_{2S_{ASE}}|H_{BS,n}(f)|^2\,\mathrm{d}f+\int_{-\infty}^{+\infty}\underbrace{[S_I(f)+S_Q(f)]}_{2S_{ASE}}|H_{BS,n}(-f)|^2\,\mathrm{d}f\right\}= \\ &= \underbrace{2\,p_{BS,n}S_{ASE}}_{S_{n,PIN}(f)}\left\{\int_{-\infty}^{+\infty}|H_{BS,n}(f)|^2\,\mathrm{d}f+\int_{-\infty}^{+\infty}|H_{BS,n}(-f)|^2\,\mathrm{d}f\right\} = 4\,p_{BS,n}\,S_{ASE}B_{BS}. \end{aligned} \tag{B.27}$$

After photodetection, a BPF is used to remove the SSBI and the DC component from the photodetected signal. The BPF transfer function, $H_{BPF}(f)$, is given by:

$$H_{BPF}(f) = \mathrm{rect}\left(\frac{f+f_{r,n}}{B_E}\right)+\mathrm{rect}\left(\frac{f-f_{r,n}}{B_E}\right) \tag{B.28}$$

where B_E is the BPF bandwidth, which is equal to the OFDM signal bandwidth B_w. Using Eq. B.20, the signal at the BPF output, $i_{s,BPF}(t)$, is given by:

$$i_{s,BPF}(t) = \frac{1}{8}\frac{\pi^2}{V_\pi^2}E_i^2\frac{\sqrt{2}}{2}\frac{V_{RMS,req}^2}{V_{RMS,s_{b,n}}\,V_{RMS,s_{v,n}}\,V_{RMS,s_e}^2}A_v\,\Re\{s_n(t)\exp[-j(2\pi f_{r,n}t+\varphi_v)]\}. \quad \text{(B.29)}$$

The mean power of $i_{s,BPF}(t)$, $p_{s,BPF}$, is obtained using the expected value, and can be written as:

$$p_{s,BPF} = \mathbb{E}\{|i_{s,BPF}(t)|^2\} = \frac{p_{v,n}\,p_{b,n}}{2}. \quad \text{(B.30)}$$

The noise mean power at the BPF output, $p_{n,BPF}$, depends on the noise PSD at the PIN-PD output, $S_{n,PIN}(f)$ (see Eq. B.27), and is given by:

$$p_{n,BPF} = \int_{-\infty}^{+\infty} S_{n,PIN}(f)\,|H_{BPF}(f)|^2\,\mathrm{d}f = 4\,p_{BS,n}\,S_{ASE}B_E. \quad \text{(B.31)}$$

The ESNR is defined as the ratio between the signal mean power, $p_{s,BPF}$, and the noise mean power, $p_{n,BPF}$, at the BPF output. Using Eq. B.30 and Eq. B.31, the ESNR is then given by:

$$\mathrm{ESNR} = \frac{p_{s,BPF}}{p_{n,BPF}} = \frac{p_{v,n}\,p_{b,n}}{4\,(p_{v,n}+\,p_{b,n})\;S_{ASE}B_E}. \quad \text{(B.32)}$$

ESNR as function of the OSNR for the MZM at the quadrature point

The figure of merit used in this study to assess the system performance is the BER. With AWGN dominance, the BER can be estimated as a function of the ESNR with the following expression [38] (see Appendix D):

$$\mathrm{BER} = \left(1-\frac{1}{\sqrt{M}}\right)\frac{2}{\log_2(M)}\mathrm{erfc}\left(\sqrt{\frac{3\,\mathrm{ESNR}}{2(M-1)}}\right) \quad \text{(B.33)}$$

where erfc$(\cdot)$ is the complementary error function, and M is the number of distinct symbols of the quadrature amplitude modulation (QAM) format. Knowing that $p_o/p_{b,n} = N_B \times \mathrm{OBPR}$, $p_v/p_{b,n} = N_B \times \mathrm{VBPR}$, $p_b/p_{b,n} = N_B$, and using Eq. B.32 and Eq. B.13, the ESNR can be expressed as:

$$\mathrm{ESNR} = \frac{1}{N_B}\frac{2}{(2\times\mathrm{OBPR}+\mathrm{VBPR}+1)}\frac{\mathrm{VBPR}}{(\mathrm{VBPR}+1)}\frac{B_N}{B_E}\mathrm{OSNR}. \quad \text{(B.34)}$$

Some important conclusions can be derived from Eq. B.34. When the OBPR and VBPR are maintained, the ESNR of one band is inversely proportional to the number of bands. This

means that transmitting more than one band will require an OSNR increase proportional to the number of bands to achieve the same performance. A VBPR increase will also lead to a higher required OSNR, to achieve the same performance obtained with low VBPR. A VBPR increase also results in an OBPR increase, as the OBPR depends on the VBPR. When increasing the VBPR, the power attributed to the OFDM band decreases and the power assigned to the VC increases, meaning lower ESNR.

ESNR as function of the OSNR for the MZM at the minimum point

So far, the analysis considers the transmission of the optical carrier generated by the CW laser at the MZM output, as the MZM is biased at quadrature point. However, the ESNR as function of the OSNR can also be derived when the MZM is biased at the minimum point ($V_b = V_\pi$). Instead of performing all the derivations, the previous developed expressions can be used. With the MZM biased at minimum point, the optical carrier is not transmitted at the MZM output ($p_o = 0$) and the mean power at the SSB filter output can be expressed as:

$$p_{SSB} = \frac{p_b}{2} + \frac{p_v}{2} \tag{B.35}$$

which results in the following expression for the OSNR:

$$\text{OSNR} = \frac{p_{SSB}}{4\,S_{ASE} B_N} = \left(\frac{p_b}{2} + \frac{p_v}{2}\right) \frac{1}{4\,S_{ASE} B_N}. \tag{B.36}$$

Rearranging Eq. B.32 and Eq. B.36 enables expressing the ESNR as a function of the OSNR as follows:

$$\text{ESNR} = \frac{2}{N_B} \frac{\text{VBPR}}{(\text{VBPR}+1)^2} \frac{B_N}{B_E} \text{OSNR}. \tag{B.37}$$

When comparing Eq. B.34 and Eq. B.37, the optical carrier removal enables higher ESNRs for the same OSNR, which translates into lower required OSNR values for the same ESNR. An important conclusion can be drawn from the expression Eq. B.37. The ESNR no longer depends on the OBPR. This results in a constant OSNR for the same performance, when N_B and VBPR are kept fixed, which does not occur using Eq. B.34. Although expressions Eq. B.34 and Eq. B.37 do not consider the MZM and PIN-PD distortion effects, they provide insight on the performance of VC-assisted MB-OFDM systems and allow to estimate the best possible performance that can be achieved.

B.2.3 Validation of the developed expressions

The effectiveness of the proposed analytical model for MB-OFDM systems is assessed by comparison with numerical results. The OSNR that leads to a BER of 10^{-3} (OSNR_{req}) and the BER itself are used as figures of merit. To assess the analytical model (AM) accuracy, the BER obtained with the AM is compared with the BER retrieved from numerical simulation (NS) using the exhaustive Gaussian approach (EGA) [69, 103]. In the analysis, the MZM is at quadrature point [ESNR as a function of the OSNR given by Eq. B.34], each OFDM symbol has 128 subcarriers, each OFDM band has a bit rate of 5 Gb/s and $B_w = 2.5$ GHz, the maximum total bit rate (assuming a maximum of 4 bands) is 20 Gb/s, and the following parameters are fixed: $M = 4$, $V_\pi = 5$ V, $B_E = B_w = 2.5$ GHz, $B_N = 12.5$ GHz, $f_{b,n} \in [2.25, 8.25, 14.25, 20.25]$ GHz and $f_{v,n} \in [6, 12, 18, 24]$ GHz with $n \in [1, 2, 3, 4]$.

The linearised MZM given by Eq. B.3 is used in the numerical results. A particular study, in which a real MZM is considered in the simulation, is also performed and explicitly mentioned. The target of that study is to assess the validity range of the AM in presence of MZM distortion. With the real MZM, is important to set the VC frequencies as multiple of $f_{v,1}$ (in this section, $f_{v,1} = 6$ GHz is set), to guarantee that the inter-modulation products of the VCs do not interfere with the OFDM bands.

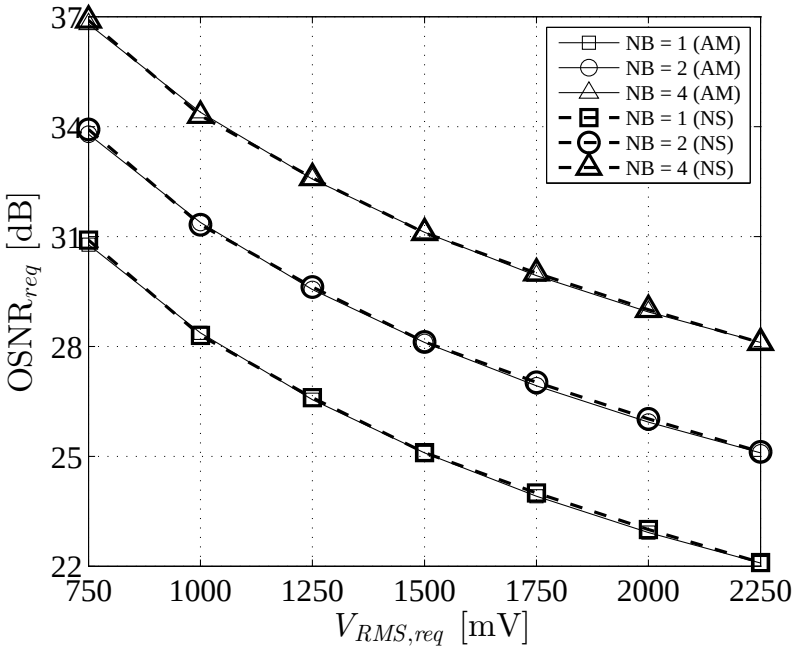

Figure B.3: OSNR_{req} as function of $V_{RMS,req}$ for $N_B = [1, 2, 4]$, with AM (solid lines) and NS (dashed lines), with a fixed VBPR of 15 dB.

The number of bands affects significantly the performance of the MB-OFDM system, as it was

concluded through analysis of Eq. B.34. Fig. B.3 shows the OSNR_{req} as function of $V_{RMS,req}$ for $N_B = [1, 2, 4]$, obtained with the AM and with NS. A VBPR of 15 dB is considered. Fig. B.3 shows that the AM results have excellent agreement with the ones obtained with NS. Fig. B.3 also demonstrates that when N_B doubles, the OSNR_{req} increases 3 dB. Fig. B.3 shows also that increasing $V_{RMS,req}$ leads to a OSNR_{req} decrease, which is valid for this system because it does not exhibit MZM distortion.

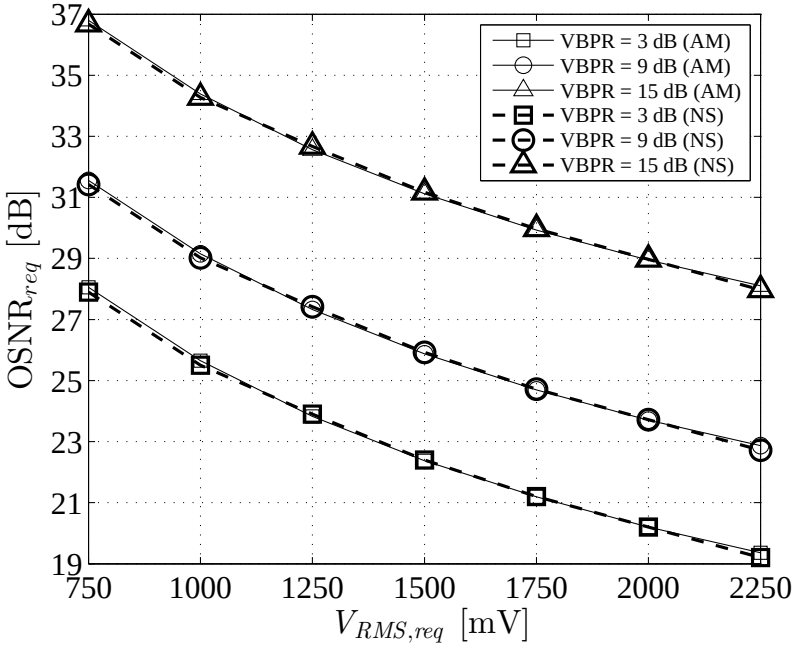

Figure B.4: OSNR_{req} as function of $V_{RMS,req}$ for VBPR $= [3, 9, 15]$ dB, with AM (solid lines) and NS (dashed lines), and with $N_B = 4$.

Another parameter besides N_B that influence significantly the performance results is the VBPR. Fig. B.4 shows the OSNR_{req} as function of $V_{RMS,req}$ for VBPR $= [3, 9, 15]$ dB, obtained with the AM and with NS. The MB-OFDM system has four bands ($N_B = 4$). Fig. B.4 shows an excellent agreement between the AM results and the NS results. Fig. B.4 also shows that increasing VBPR leads to an increase of the OSNR_{req}. This increase is higher for higher VBPRs.

In the results of Fig. B.3 and Fig. B.4, the VBG is selected in order to avoid the SSBI overlapping with the received OFDM band. However, it is important to verify the resilience of the AM when PIN-PD distortion interferes with the information-bearing signal, as a smaller VBG means more spectral efficiency. Fig. B.5 shows the BER as function of the VBG width in GHz, for VBPR $= [3, 9, 15]$ dB and $V_{RMS,req} = 1500$ mV. The OSNR is 22.4 dB for VBPR = 3 dB, 25.9 dB for VBPR = 9 dB and 31.1 dB for VBPR = 15 dB. With these OSNR levels and as the AM does not take into account the PIN-PD distortion, the BER obtained using the AM is 10^{-3} for all VBG widths. Therefore, Fig. B.5 only shows the NS results. Fig. B.5 shows that the SSBI

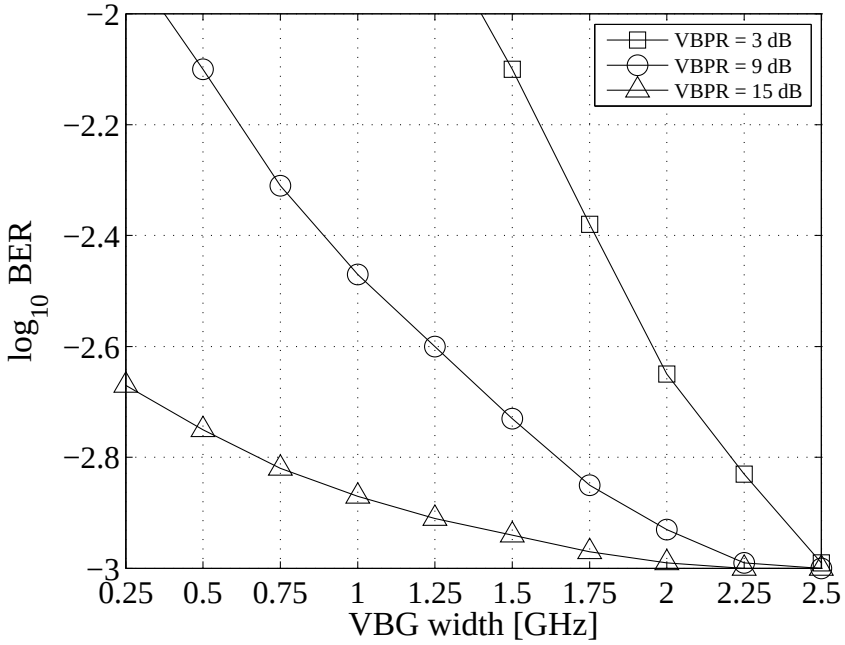

Figure B.5: BER as function of the VBG width, for VBPR = $[3, 9, 15]$ dB and $V_{RMS,req}$ = 1500 mV, with NS. With the AM, the BER is 10^{-3} for all VBG widths.

caused by the PIN-PD affects the performance when the VBG width is lower than the bandwidth of the OFDM signal, as the SSBI spectrum overlaps with the OFDM signal spectrum. Fig. B.5 shows also that the BER degrades more substantially for lower VBPRs. This is because lower VBPR levels leads to more SSBI power.

The results shown in Fig. B.3, Fig. B.4 and Fig. B.5 present the effects of ASE noise and PIN-PD distortion on the performance. However, the effects of MZM distortion were not considered in the simulation results. To illustrate the impact of MZM nonlinearity on the required OSNR and assess the AM validity range, a real MZM described by Eq. B.1 is also considered in the simulation.

Fig. B.6 shows the OSNR_{req} as function of $V_{RMS,req}$, for VBPR = $[3, 9, 15]$ dB, and for the first band which is the most affected by MZM distortion. The MB-OFDM system has four bands ($N_B = 4$), and a VBG width of 2.5 GHz is employed. Fig. B.6 shows that the MZM distortion causes significant performance degradation when the required root-mean-square (RMS) voltage increases. For required RMS voltages around 400 mV, the minimum OSNR_{req} is obtained. From the simulation results, the minimum OSNR_{req} for VBPR = 3 dB is 38 dB, for VBPR = 9 dB is 40 dB, and for VBPR = 15 dB is 45 dB. The error committed by the AM in the minimum OSNR_{req} is approximately 4 dB for VBPR = 3 dB and for VBPR = [9,15] dB is approximately 3 dB. The analytical modelling in this section assumes noise-impaired MB-

OFDM systems. Hence distortion-impaired systems are not well described by this model. This occurs for $V_{RMS,req}$ voltages higher than approximately 200 mV when $V_\pi = 5$V. Taking into account the modulation index definition of Eq. 2.31, this corresponds to modulation indexes (in percentage) higher than 4%.

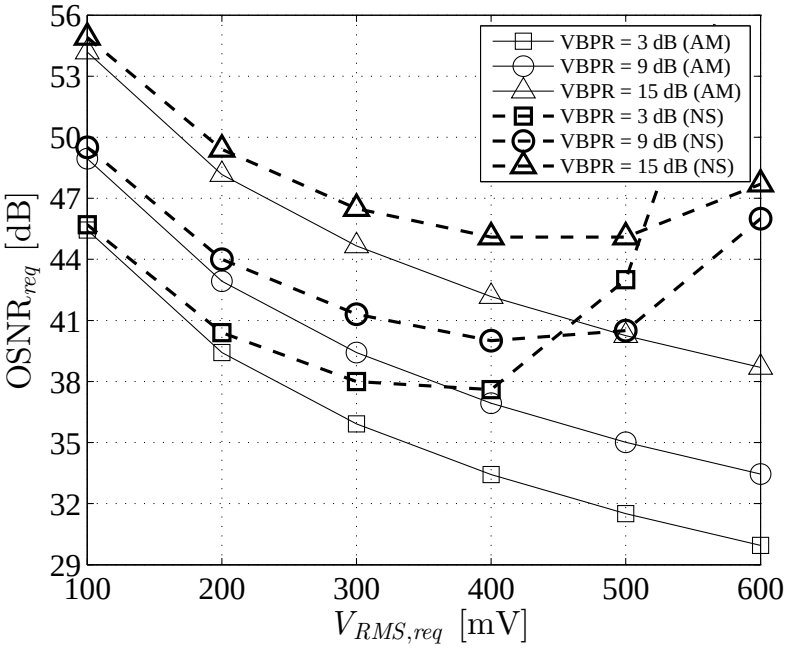

Figure B.6: OSNR$_{req}$ as function of the $V_{RMS,req}$, for VBPR $= [3, 9, 15]$ dB. A MB-OFDM system with 4 bands ($N_B = 4$) is considered. A real MZM is considered in the NS results.

B.3 Distortion-impaired VC-assisted OFDM systems

B.3.1 System model

The system model considered to analyse the performance of distortion-impaired VC-assisted OFDM systems in optical back-to-back operation is similar to the one illustrated in Fig. B.1 with the following simplifications: 1) a single OFDM Tx is considered at the MZM input, that is, a single pair band-VC is transmitted; and 2) the ASE noise impairment is neglected to focus the attention on the distortion-based impairments. The VBG is suitably chosen in order to avoid the SSBI originated by the PIN-PD square-law, that is, the VBG is equal to the OFDM signal bandwidth. However, a particular study, in which different VBGs are considered in the simulation, is performed to assess the validity of the proposed model in the presence of SSBI.

B.3.2 Signal and distortion components at the photodiode output

The key idea is to obtain analytical expressions for the electrical signal and distortion powers in order to calculate the EVM as figure of merit for performance characterisation. From Eq. 2.22, the RF signal with one pair band-VC ($n = 1$) at the MZM input, $v(t)$, is given by:

$$v(t) = \left[\frac{s_{b,1}(t)}{V_{RMS,s_{b,1}}} + A_v \frac{s_{v,1}(t)}{V_{RMS,s_{v,1}}} \right] \frac{V_{RMS,req}}{\sqrt{1 + A_v^2}}. \tag{B.38}$$

For practical purposes, $v(t)$ can be divided into two different components as follows:

$$v(t) = v_+(t) \exp[j(2\pi f_{v,1} t + \varphi_v)] + v_-(t) \exp[-j(2\pi f_{v,1} t + \varphi_v)] \tag{B.39}$$

with $v_-(t) = [v_+(t)]^*$ ($[.]^*$ denotes the complex conjugate). Using Eq. B.7 and Eq. B.8, assuming $\varphi_v = 0$, and taking into account that $V_{RMS,s_{b,1}} = V_{RMS,s_1}/\sqrt{2}$, $v_+(t)$ can be written as:

$$v_+(t) = \frac{V_{RMS,req}}{\sqrt{2(1 + A_v^2)}} \left[A_v + \frac{s_1(t)}{V_{RMS,s_1}} \exp(-j2\pi f_{r,1} t) \right] \tag{B.40}$$

where V_{RMS,s_1} is the RMS voltage of the complex baseband OFDM signal of band 1. The signal $v(t)$ is then fed to the MZM. The optical signal at the MZM output as a function of $v(t)$ is expressed by Eq. B.1. Assuming that the MZM cosine function can be approximated by a Taylor series third-order expansion, the LPE of $e_{MZM}(t)$ after a Taylor series third-order expansion, $e_{MZM,d}(t)$, with respect to $v(t)$ around zero is given by:

$$\begin{aligned} e_{MZM,d}(t) = E_i \Bigg[& \cos\left(\frac{\pi}{2V_\pi} V_b\right) + \sin\left(\frac{\pi}{2V_\pi} V_b\right) \frac{\pi}{2V_\pi} v(t) - \\ & - \frac{1}{2} \cos\left(\frac{\pi}{2V_\pi} V_b\right) \left(\frac{\pi}{2V_\pi}\right)^2 v^2(t) - \frac{1}{6} \sin\left(\frac{\pi}{2V_\pi} V_b\right) \left(\frac{\pi}{2V_\pi}\right)^3 v^3(t) \Bigg]. \end{aligned} \tag{B.41}$$

With the MZM at quadrature point ($V_b = V_\pi/2$), the third-order approximation of the optical signal at the MZM output can be expressed as:

$$\begin{aligned} e_{MZM,d}(t) &= C_0 + C_1 v(t) + C_2 v^2(t) + C_3 v^3(t) = \\ &= \underbrace{\left(\frac{\sqrt{2}E_i}{2}\right)}_{C_0} + \underbrace{\left[\frac{\sqrt{2}E_i}{2} C_\pi\right]}_{C_1} v(t) + \underbrace{\left[-\frac{\sqrt{2}E_i}{4} C_\pi^2\right]}_{C_2} v^2(t) + \underbrace{\left[-\frac{\sqrt{2}E_i}{12} C_\pi^3\right]}_{C_3} v^3(t) \end{aligned} \tag{B.42}$$

with $C_\pi = \pi/(2V_\pi)$. After electrical-to-optical conversion, SSB filtering is performed, and the lower sideband components are removed. The LPE of the optical signal at the SSB filter output,

$e_{SSB,d}(t)$, is given by:

$$e_{SSB,d}(t) = C_0 + C_1 v_+(t)\exp(j\omega_v t) + C_2 v_+^2(t)\exp(j2\omega_v t) + 2C_2 v_+(t)v_-(t) + \\ + C_3 v_+^3(t)\exp(j3\omega_v t) + 3C_3 v_+^2(t)v_-(t)\exp(j\omega_v t) \tag{B.43}$$

with $\omega_v = 2\pi f_{v,1}$. The first term is the optical carrier, the second term is the OFDM signal, the third and fourth terms are MZM second-order distortion components, and the fifth and sixth terms are MZM third-order distortion components. After SSB filtering, the BS is used to select the pair band-VC. After replacing $v_+(t)$ in Eq. B.43 by Eq. B.40 and taking into account that $v_-(t) = [v_+(t)]^*$, the LPE of the optical signal at the BS output, $e_{BS,d}(t)$, can be written as:

$$e_{BS,d}(t) = D_1[\tilde{s}_1(t)]^*\exp(j\omega_r t) + D_2|\tilde{s}_1(t)|^2 + D_3|\tilde{s}_1(t)|^2\exp(j\omega_v t) + D_4\exp(j\omega_v t) + \\ + D_5\tilde{s}_1(t)\exp(j\omega_b t) \tag{B.44}$$

with $\tilde{s}_1(t) = s_1(t)/V_{RMS,s_1}$, $\omega_r = 2\pi f_{r,1}$, $\omega_b = 2\pi f_{b,1}$, and

$$\begin{cases} D_1 = 2C_2 A_v K_d^2 \\ D_2 = 2C_2 K_d^2 = D_1/A_v \\ D_3 = 6C_3 A_v K_d^2 \\ D_4 = C_1 A_v K_d + 3C_3 A_v^3 K_d^3 = C_1 A_v K_d + A_v^2 D_3/2 \\ D_5 = C_1 K_d + 6C_3 A_v^2 K_d^3 = C_1 K_d + A_v D_3 \end{cases} \tag{B.45}$$

with $K_d = V_{RMS,req}/\sqrt{2(1+A_v^2)}$.

Afterwards, photodetection is performed by an ideal square-law PIN-PD with responsivity of $1\ \mathrm{A}\cdot\mathrm{W}^{-1}$. The photocurrent at the PIN-PD output, $i_{PIN,d}(t)$, can be expressed as: $i_{PIN,d}(t) = e_{BS,d}(t)[e_{BS,d}(t)]^*$. From all the terms obtained at the PIN-PD output, the most relevant terms when the SSBI is neglected are the following:

$$i_{PIN,d}(t) \approx \overbrace{2D_1D_4\Re\{\tilde{s}_1(t)\exp(j\omega_b t)\} + 2D_2D_5\Re\left\{|\tilde{s}_1(t)|^2\tilde{s}_1(t)\exp(j\omega_b t)\right\}}^{\text{distortion components}} + \\ + \underbrace{2D_4D_5\Re\{[\tilde{s}_1(t)]^*\exp(j\omega_r t)\}}_{\text{OFDM signal component}} \tag{B.46}$$

with $\Re\{\cdot\}$ denoting the real part. The first term is the beating between a 2nd-order MZM distortion term and the VC, the second term is the beating between a 2nd-order MZM distortion term and the OFDM signal, and the third term is the OFDM signal.

Fig. B.7(a) and Fig. B.7(b) illustrate the spectra at the SSB filter output using the MZM

model given by Eq. B.1 and the approximation given by Eq. B.43, respectively. Fig. B.7(c) and Fig. B.7(d) show the spectra at the PIN-PD output using the MZM model given by Eq. B.1 and the approximation given by Eq. B.46, respectively. The system parameters are an example just to observe the spectra differences between the two models. The spectra at the SSB filter output is similar for both cases and show the signal term centred at $f_{b,1} = 2.75$ GHz and the VC located at $f_{v,1} = 6.5$ GHz. The distortion components at the SSB filter output are centred at $f_{r,1} = 3.75$ GHz, and have a spectrum shape similar to the signal spectrum.

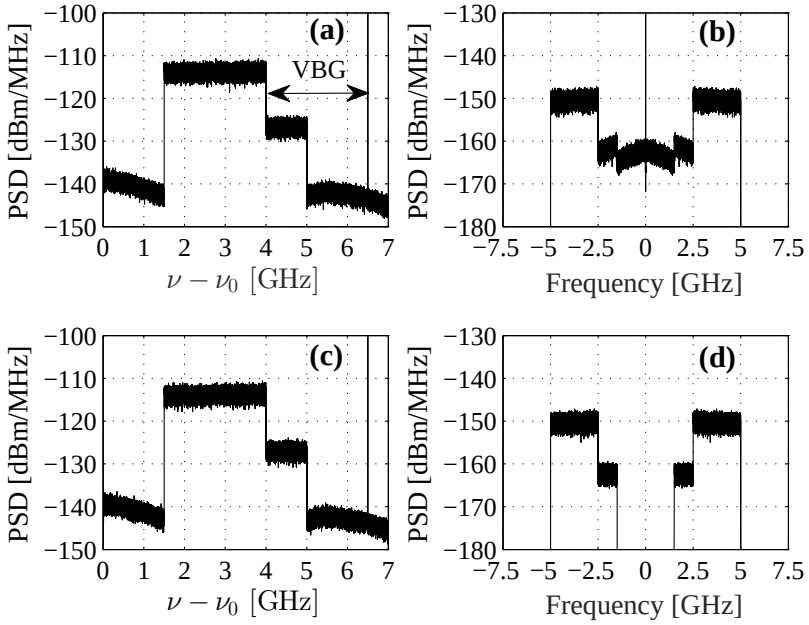

Figure B.7: Spectra at the SSB filter output using (a) the MZM model from Eq. B.1 and (c) the approximation given by Eq. B.43. Spectra at the PIN-PD output obtained using (b) the MZM model given by Eq. B.1 and (d) the approximation given by Eq. B.46. Parameters: $B_w = 2.5$ GHz, VBG $= B_w$, $f_{v,1} = 6.5$ GHz, $f_{b,1} = 2.75$ GHz, VBPR $= 12$ dB and MI $= (V_{RMS,req}/V_\pi) = 20\%$.

B.3.3 EVM due to distortion

The EVM due to distortion, EVM_D, is given by the signal-to-distortion ratio (the ratio between the distortion power P_D and the signal power P_S) and is assessed at the OFDM receiver (after photodetection). In order to obtain the signal and distortion powers for a certain OFDM subcarrier, $\tilde{s}_1(t)$ is expressed as $\tilde{s}_1(t) = \sum_{n_{sc}=1}^{N_{sc}} c_n \exp(j2\pi n_{sc}\Delta f_{sc} t)$, where n_{sc} is the subcarrier index, N_{sc} is the number of OFDM subcarriers, c_n is the normalized subcarrier complex amplitude and Δf_{sc} is the subcarrier spacing. After some calculations, the signal power of a certain OFDM subcarrier can be expressed as:

$$P_S = 2D_4^2 D_5^2 P_{sc} \tag{B.47}$$

where P_{sc} is the power of each OFDM subcarrier (assumed the same for all subcarriers). In a similar way, the distortion power can be written as:

$$P_D = \left(2D_1^2 D_4^2 + 8D_1 D_2 D_4 D_5\right) P_{sc}. \tag{B.48}$$

Hence, EVM_D can be expressed as:

$$EVM_D = \frac{P_D}{P_S} = \frac{2D_1^2 D_4^2 + 8D_1 D_2 D_4 D_5}{2D_4^2 D_5^2}. \tag{B.49}$$

After a few calculations, the EVM of a subcarrier impaired by distortion becomes:

$$EVM_D = \frac{D_1^2}{D_5^2}\left(1 + \frac{4}{VBPR}\right). \tag{B.50}$$

For high VBPRs, the second term in Eq. B.50 can be neglected. This leads to the following EVM due to distortion:

$$EVM_D \approx \frac{D_1^2}{D_5^2}. \tag{B.51}$$

By defining B_i as the bandwidth of the OFDM signal that suffers from distortion interference, and assuming that the subcarriers not affected by distortion have null EVM, the average EVM of the OFDM band due to distortion, $\langle EVM_D \rangle$, can be obtained as follows:

$$\langle EVM_D \rangle = \alpha_i \cdot EVM_D \tag{B.52}$$

with

$$\alpha_i = \frac{B_i}{B_w} = 1 - \frac{|f_{v,1} - 2f_{b,1}|}{B_w} = 1 - \frac{|f_{r,1} - f_{b,1}|}{B_w}. \tag{B.53}$$

For example, if $\alpha_i = 0.6$, it means that 60% of the distortion band interferes in frequency with the signal band (α_i can be modified by changing $f_{b,1}$). Fig. B.7 shows the case where $\alpha_i[\%] = 60\%$. The worst case occurs when $f_{r,1} = f_{b,1}$, which corresponds to the case where all the subcarriers are impaired by distortion.

B.3.4 Assessment of developed expressions

The effectiveness of the AM for the distortion-impaired MB-OFDM system with one pair band-VC is assessed by comparing its EVM estimates with the ones obtained from NS. For performance evaluation, the following parameters are considered: $N_{sc} = 128$, 4-QAM subcarrier mapping, and OFDM band bit rate of 5 Gb/s. Thus, the OFDM signal bandwidth, B_w, is 2.5 GHz.

To evaluate the MB-OFDM system performance, the EVMs obtained through NS using the MZM given by Eq. B.1 are compared with the EVMs obtained by the analytical expressions given by Eq. B.50 and Eq. B.52 (approximation 1), and by Eq. B.51 and Eq. B.52 (approximation 2). With AWGN dominance, an EVM of approximately -9.8 dB corresponds to a bit error ratio of 10^{-3} (see Tab. D.1). Therefore, it is assumed that an EVM value is acceptable when it is below -9.8 dB.

Fig. B.8(a), Fig. B.8(b) and Fig. B.8(c) show the AM and NS EVM results as a function of α_i and the VBPR with VBG = B_w and MI = 20%. The results of Fig. B.8 illustrate that, with the VBPR increase, the agreement between the AM and NS EVM results improves. A discrepancy not exceeding 1 dB is achieved for a VBPR of 12 dB.

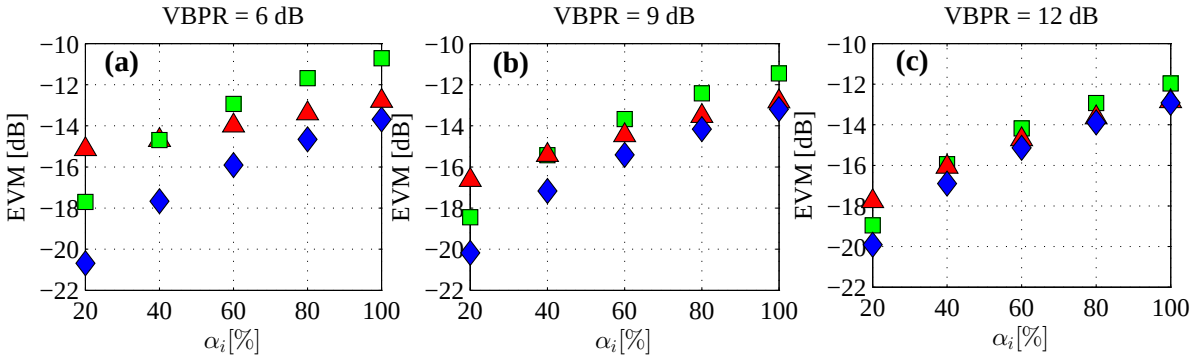

Figure B.8: EVM results obtained with the MZM model from Eq. B.1 (triangles), from approximation 1 (squares) and from approximation 2 (diamonds) as a function of α_i with VBG = B_w, VBPR equal to (a) 6, (b) 9 and (c) 12 dB and MI = 20%.

Fig. B.9(a), Fig. B.9(b) and Fig. B.9(c) show the AM and NS EVM results as a function of α_i and MI for VBG = B_w and VBPR = 12 dB. The results of Fig. B.9 show that, with the variation of the modulation index, the discrepancy between the AM and NS EVM results is similar and does not exceed 1 dB.

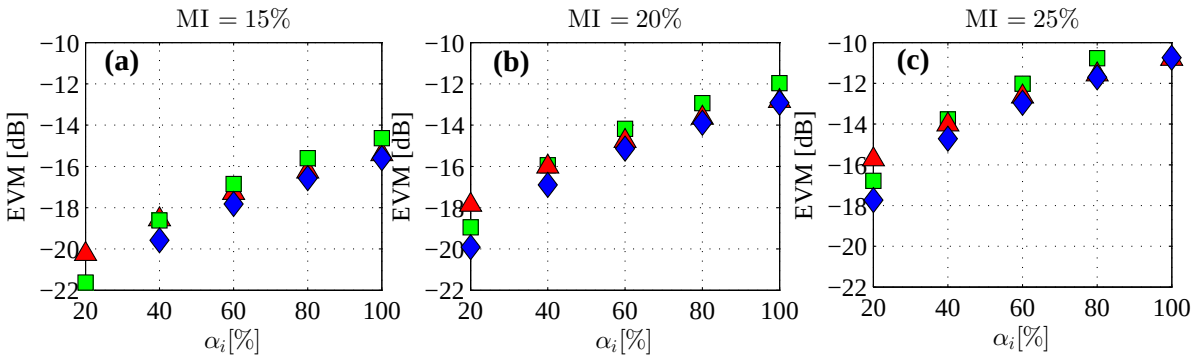

Figure B.9: EVM results obtained with the MZM model from Eq. B.1 (triangles), from approximation 1 (squares) and from approximation 2 (diamonds) as a function of α_i with VBG = B_w, VBPR = 12 dB and (a) MI = 15%, (b) MI = 20% and (c) MI = 25%.

So far, VBG was set equal to B_w to avoid SSBI. However, it is important to analyse the accuracy of the AM (which neglects SSBI) when SSBI is present. The presence of SSBI occurs when VBGs are smaller than B_w, which is of great interest as it means higher spectral efficiency. Fig. B.10(a), Fig. B.10(b) and Fig. B.10(c) illustrate the EVM results obtained with the AM, where SSBI is not accounted for, and with NS, for two different situations: i) SSBI does not interfere with the OFDM band (VBG = B_w) and ii) SSBI interference occurs (VBG < B_w), as a function of α_i, with VBPR = 12 dB and MI = 20%. The results of Fig. B.10 show that, when VBPR = 12 dB and MI = 20%, a discrepancy not exceeding 1 dB between the AM and NS results is verified for VBGs higher than $B_w/2$.

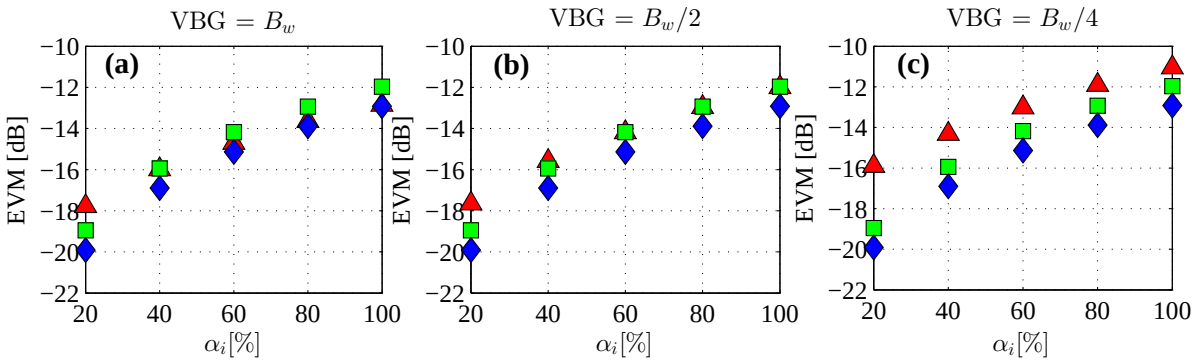

Figure B.10: EVM results obtained with the MZM model from Eq. B.1 (triangles), from approximation 1 (squares) and from approximation 2 (diamonds) as a function of α_i with VBPR = 12 dB, MI = 20% and VBG equal to (a) B_w, (b) $B_w/2$ and (c) $B_w/4$.

B.4 Conclusions

An AM for performance evaluation of ASE noise-impaired DD SSB MB-OFDM systems has been proposed. The AM effectiveness has been verified through comparison with NS using the EGA to evaluate the BER. Excellent agreement in the BER results when MZM and PIN-PD distortion do not interfere with the MB-OFDM signal has been shown. When PIN-PD distortion is affecting the MB-OFDM signal, the AM provides more accurate estimates for high VBPRs. When MZM distortion is interfering with the MB-OFDM signal, the AM presents, for modulation indexes lower than 4%, a deviation in the required OSNR not exceeding 1 dB.

Another AM for performance evaluation, with emphasis on the distortion impairments of DD SSB optical MB-OFDM systems using VCs, has been presented. The effectiveness of this AM has been verified through comparison of its EVM estimates with the ones obtained using NS. Discrepancies between the EVM estimates of the AM and NS not exceeding 1 dB have been shown for a VBPR of 12 dB and for VBGs exceeding half of the signal bandwidth.

Appendix C

Algorithm for signal-signal beat interference mitigation

C.1 Introduction

To ensure that multi-band (MB)-orthogonal frequency-division multiplexing (OFDM) systems employing virtual carrier (VC)-assisted direct-detection (DD) have high spectral efficiency, the frequency gap between the OFDM signal and its corresponding VC should be small or negligible. This is possible only if the signal-signal beat interference (SSBI) has reduced impact on the signal performance. In this appendix, a digital signal processing (DSP)-based iterative algorithm for SSBI mitigation with application in VC-assisted DD-MB-OFDM optical systems is presented and explained. The performance improvement due to the SSBI mitigation is assessed in the presence of optical noise and distortion due to the optical modulator.

C.2 System description

The MB-OFDM system employed to evaluate the SSBI impact on the system performance is illustrated in Fig. C.1. It consists in a MB-OFDM transmitter with $N_B = 1$ (see Fig. 2.5) connected to an OFDM signal demodulator (see Fig. 2.6) with an amplified spontaneous emission (ASE) noise loader in-between.

Each band within the MB-OFDM signal transports an OFDM signal with information data rate of 10 Gb/s. With forward error correction (FEC) overhead of 7%, the total bit rate transmitted

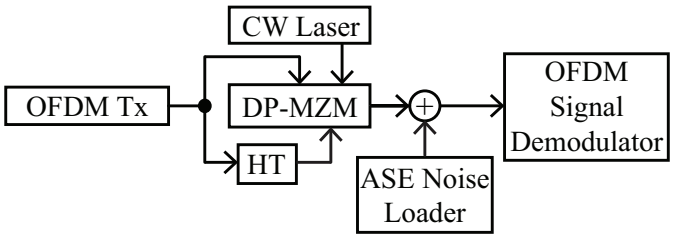

Figure C.1: Block diagram of the simplified MB-OFDM system used to evaluate the SSBI impact on the system performance.

per band, R_b, is 10.7 Gb/s. Each band comprises 128 subcarriers per OFDM symbol and all subcarriers are modulated using three different quadrature amplitude modulation (QAM) constellations: 4-QAM, 16-QAM or cross 32-QAM [89]. For 4-QAM, the OFDM band has a bandwidth, B_w, of 5.35 GHz, for 16-QAM the bandwidth is 2.675 GHz and for 32-QAM is 2.14 GHz. The bandwidth of each band is obtained from $B_w = R_b/\log_2(M)$, with $M = \{4, 16, 32\}$. 300 OFDM information symbols are used for performance assessment, which corresponds to a total of 3.84×10^4 QAM symbols. The error vector magnitude (EVM) is used as figure of merit and the EVM corresponding to a bit error ratio (BER) of 10^{-3} for 4, 16 and 32-QAM is used as reference of the performance limit (see Tab. D.1). The modulation index is set to 5% (low distortion case) and 25% (high distortion case). The ASE noise loader adds optical noise to the OFDM signal in order to set the optical signal-to-noise ratio (OSNR) in a reference bandwidth of 0.1 nm, to the desired value (the OSNR is the ratio between the signal power and the noise power). At the OFDM signal demodulator, photodetection is performed by the p-type-intrinsic-n-type (PIN)-photodiode (PD). Due to the PIN-PD square-law, SSBI is generated at the PIN-PD output. To mitigate the SSBI after photodetection and before demodulation, a DSP-based iterative algorithm is employed. This algorithm allows for a reduced virtual carrier-to-band gap (VBG) and, consequently, enables a reduced receiver bandwidth and high spectral efficiency. A detailed block diagram for the OFDM receiver (Rx) will be given afterwards in this appendix, together with the explanation of the SSBI mitigation algorithm.

C.3 Impact of the SSBI in DD-OFDM systems

In section 2.3.3, the SSBI components were identified after photodetecting one pair band-VC. In MB-OFDM systems assisted by VCs, the SSBI is an important impairment to take into consideration and the virtual carrier-to-band power ratio (VBPR) plays an important role in the SSBI influence on the system performance. The VBPR is set in the electrical domain, inside each OFDM transmitter (Tx) and needs to be carefully chosen as it controls the power of the

SSBI component and if the system is mainly impaired by noise or distortion. In conventional OFDM systems, where the frequency gap between the carrier and the OFDM band (for VC-assisted MB-OFDM systems is the VBG) has a similar width to the OFDM bandwidth, the optimum VBPR is around 0 dB [29] (a VBPR of 0 dB means that the VC power is equal to the OFDM band power). However, this solution is not appropriate as the frequency gap induces considerable spectral efficiency reduction. As the main goal is to have the highest possible spectral efficiency, the best case scenario is to have a very small VBG. As the VBG reduces, the SSBI interferes more and more with the OFDM band. A small VBG is possible by increasing the VBPR, as this improves the relation between the SSBI power and the desired signal. Still, a VBPR increase leads also to the increase of power wasted in the VC and to lower noise tolerance.

Fig. C.2 shows the EVM as a function of the VBG, for an OFDM band with bandwidth of 5.35 GHz, and for low VBPR (2.5 dB) and high VBPR (10 dB), with and without optical noise. When optical noise is accounted, the OSNR is 16 dB. Fig. C.2 shows that by increasing the VBG width, the SSBI component will gradually fall out of the OFDM band, resulting in a EVM decrease (performance improvement). For VBGs greater than or equal to the OFDM signal bandwidth (5.35 GHz), the best performance is achieved as the SSBI no longer interferes with the OFDM band.

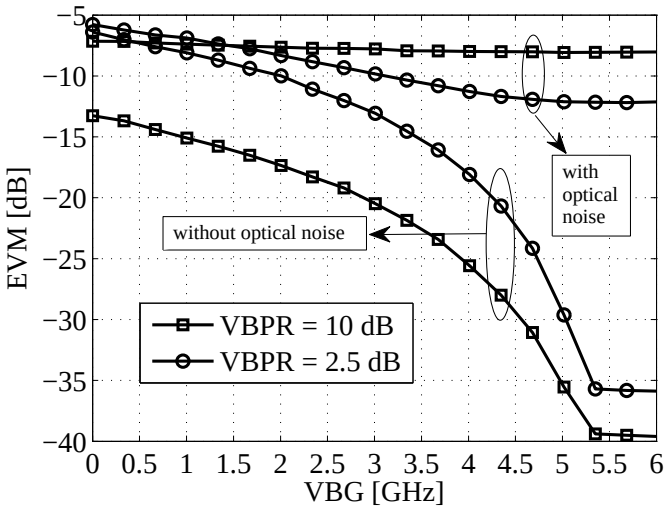

Figure C.2: Tradeoff between the VBG, VBPR and SSBI-induced distortion, without optical noise and with a OSNR of 16 dB. 4-QAM modulation for each OFDM subcarrier and a modulation index of 5% are considered.

Fig. C.2 also shows that, when optical noise is not taken into account, the EVM is lower for the same VBG if the VBPR is increased (higher VBPR means less SSBI influence on the performance). In a real situation with optical noise, increasing the VBPR is not acceptable as it decreases the power of the detected OFDM signal. For a fixed OSNR, decreasing the power of

the OFDM signal would lead to performance degradation. Thus, Fig. C.2 shows a worst performance (higher EVM) when the VBPR increases, when optical noise is accounted. The use of a SSBI mitigation technique would allow the decrease of both the OSNR and VBPR, and would also allow the overlapping between the SSBI and the OFDM signal without severely affecting the performance. The usage of such technique would enable an improvement of the spectral efficiency at the expense of a small increase on the system complexity at the receiver side.

C.4 SSBI mitigation algorithm

In this section, the DSP algorithm used for SSBI mitigation is explained in detail for application in VC-assisted OFDM systems and the performance improvement due to the SSBI mitigation is evaluated using numerical simulation. The SSBI mitigation algorithm used in this work is based on the technique presented in [68].

SSBI mitigation is employed in the electrical domain by an iterative procedure which reconstructs the SSBI terms from the hard decision decoding of the corrupted QAM symbols, and subtracts them from the photodetected signal. The SSBI mitigation algorithm is separated in two different modes: the training mode and the data mode. In the training mode, the SSBI mitigation algorithm uses only the training symbols (TSs) of the OFDM frame to estimate some parameters required by the algorithm to converge. Afterwards, in the data mode, the data information of each OFDM frame is processed in the OFDM receiver and the SSBI is mitigated. In order to achieve an adequate performance, the algorithm needs to perform a few iterations to achieve suitable mitigation of the SSBI. The SSBI mitigation algorithm may introduce some latency issues due to the time needed to perform the necessary iterations. However, by performing the most time-spending iterations in the training mode (where some latency is acceptable), the latency issues can be minimized. In this work, the SSBI mitigation algorithm processes the received signal with all the training symbols and not in a symbol-by-symbol manner.

Fig. C.3 shows the block diagram of the OFDM receiver with the algorithm operating in the training mode. This mode is divided in two different types of iterations: 1) the training iterations used to estimate the SSBI (I_e, with index e), and 2) the amplitude iterations used to adjust the amplitude of the reconstructed SSBI term before each training iteration (I_a, with index a). The signal from the direct-current (DC) block output is digitized by the analogue-to-digital converter (ADC) and the resulting signal is stored in memory. A sequence of operations to demodulate the OFDM signal are performed: cyclic prefix (CP) removal, fast Fourier transform (FFT),

sample selection and equalization. The equalized symbols are stored and the resulting EVM is computed. The selected samples after FFT, which correspond to the OFDM subcarriers, are the following, for a pair band-VC with the VC at a lower frequency than the OFDM band: $[v+1, v+2, \ldots, N_{sc}+v]$, where v is the number of samples corresponding to the VBG. For a pair band-VC with the VC at a higher frequency than the OFDM band, the selected samples after FFT are the following:

$$[2 \cdot N_{sc} \cdot s_{ADC} - N_{sc} + 1 - v, 2 \cdot N_{sc} \cdot s_{ADC} - N_{sc} + 2 - v, \ldots, 2 \cdot N_{sc} \cdot s_{ADC} - v]$$

where s_{ADC} is the ADC oversampling factor (equal to 4 as referred in section 2.3.3). Note that the FFT is performed over $2 \cdot N_{sc} \cdot s_{ADC}$ samples (the factor 2 is due to the zero-padding), and that, after sample selection, only N_{sc} samples remain.

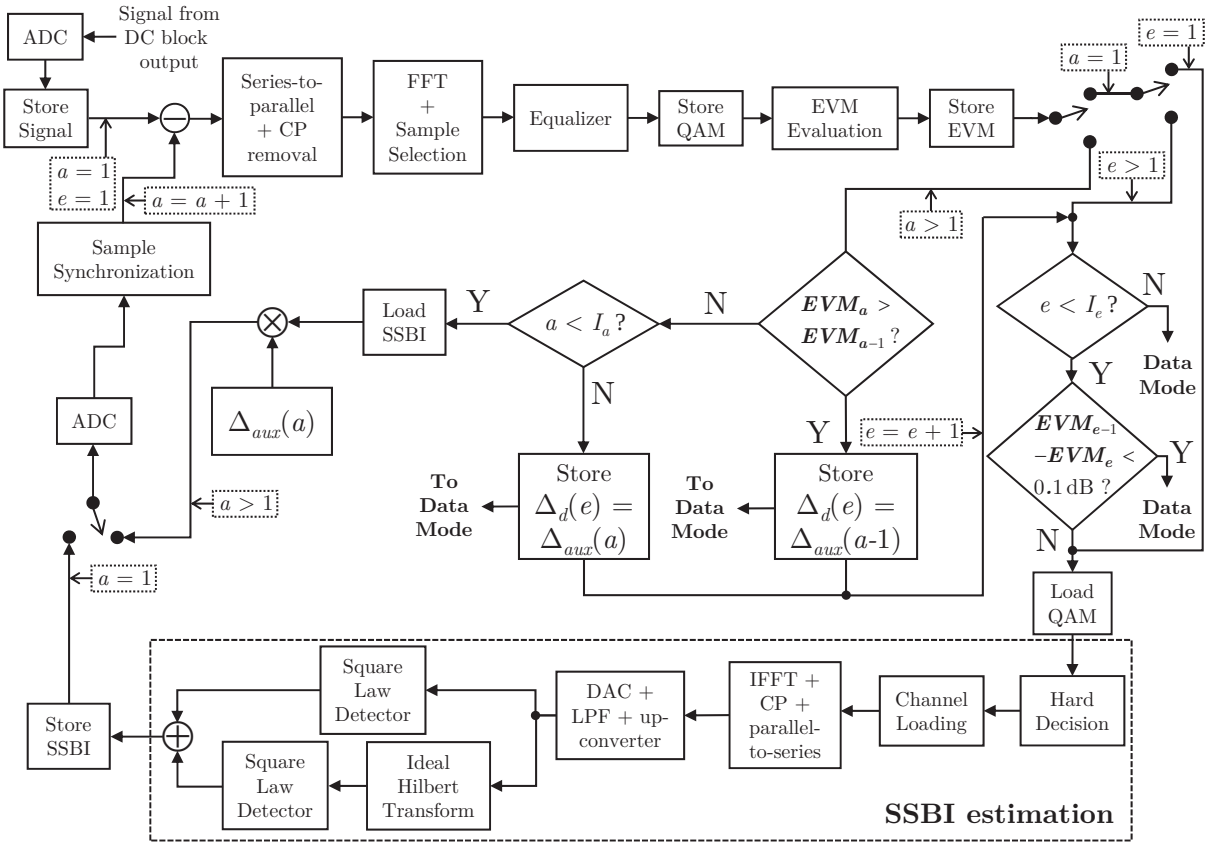

Figure C.3: Block diagram of the OFDM receiver with the SSBI mitigation algorithm operating in the training mode.

At the first amplitude iteration ($a = 1$) in the first training iteration ($e = 1$), OFDM signal estimation is carried out using the previously stored QAM symbols. The following operations are performed: hard decision, channel loading, inverse fast Fourier transform (IFFT), CP insertion, digital-to-analogue conversion, low-pass filtering and up-conversion. At the hard decision

block, the SSBI-impaired symbols are divided by the decision regions of the respective QAM constellation and their I and Q components are changed to the I and Q components of the ideal QAM symbol inside the respective decision region. As the symbols before hard decision where affected by SSBI, the hard-decided symbols may contain errors. Afterwards, the channel loading introduces the channel impairments into the hard-decided symbols. The channel loading transfer function for subcarrier k, $H_{ch}(k)$, is given by:

$$H_{ch}(k) = \frac{1}{\sqrt{2A_v V_{RMS,s_{b,n}} V_{RMS,s_e} H_{eq}(k)}} \tag{C.1}$$

where $H_{eq}(k)$ is the equalizer transfer function for subcarrier k, obtained by dividing the ideal QAM symbols by the received QAM symbols (inverse transfer function of the transmission channel). After up-conversion, the reconstructed OFDM signal is applied to two different branches, one with a square-law detector and another with an ideal Hilbert transformer and a square-law detector. After adding the signals of the two branches, an estimation of the SSBI is obtained [see the terms in (c) of Eq. 2.34]. Afterwards, the SSBI is stored in memory and analogue-to-digital conversion is performed. The digitized signal is synchronized with the stored signal at the output of the main ADC. After sample synchronization, the estimated SSBI is subtracted to the received OFDM signal and index a is incremented. With $a > 1$ and after calculating the EVM of the new digitized signal with SSBI mitigation, SSBI estimation is skipped and the previously stored SSBI is loaded from memory and multiplied by an amplitude coefficient Δ_{aux}. This coefficient is given by:

$$\Delta_{aux}(a) = (a-1)\Delta_i \tag{C.2}$$

where Δ_i is an increment factor (in this work, $\Delta_i = 0.25$ dB is used). The goal of the amplitude iterations is to find the best amplitude coefficient, that multiplied with the estimated SSBI, enables good SSBI mitigation. When the current EVM is higher than the previous (condition $EVM_a > EVM_{a-1}$ is true), the best EVM is stored (corresponds to EVM_{a-1}). If the amplitude iterations reach the value I_a, no more amplitude iterations are performed and the amplitude coefficient is stored. The stored amplitude coefficient, referred as Δ_d, is then used in SSBI iteration of the data mode with index e.

After storing the Δ_d coefficient, index e is incremented. Given that the previously estimated SSBI was subtracted to the signal, the hard decision is expected to produce less errors and the next training iteration is expected to provide a better EVM than the one obtained in the previous training iteration. This procedure is repeated until the value I_e is reached or the best EVM of the current and the previous training iterations (EVM_e and EVM_{e-1}, respectively)

are similar ($EVM_{e-1} - EVM_e < 0.1$ dB), that is, no further improvement is achieved.

Fig. C.4 shows the block diagram of the OFDM receiver with the SSBI mitigation algorithm operating in the data mode. The data mode is similar to the training mode with the exception of not requiring amplitude iterations, given that the best amplitude coefficients (Δ_d coefficient for each iteration e) are already known from the training mode. When the algorithm reaches the last SSBI iteration (index e equal to I_e), it stops, the almost SSBI-free QAM symbols are demapped and the binary output data is recovered.

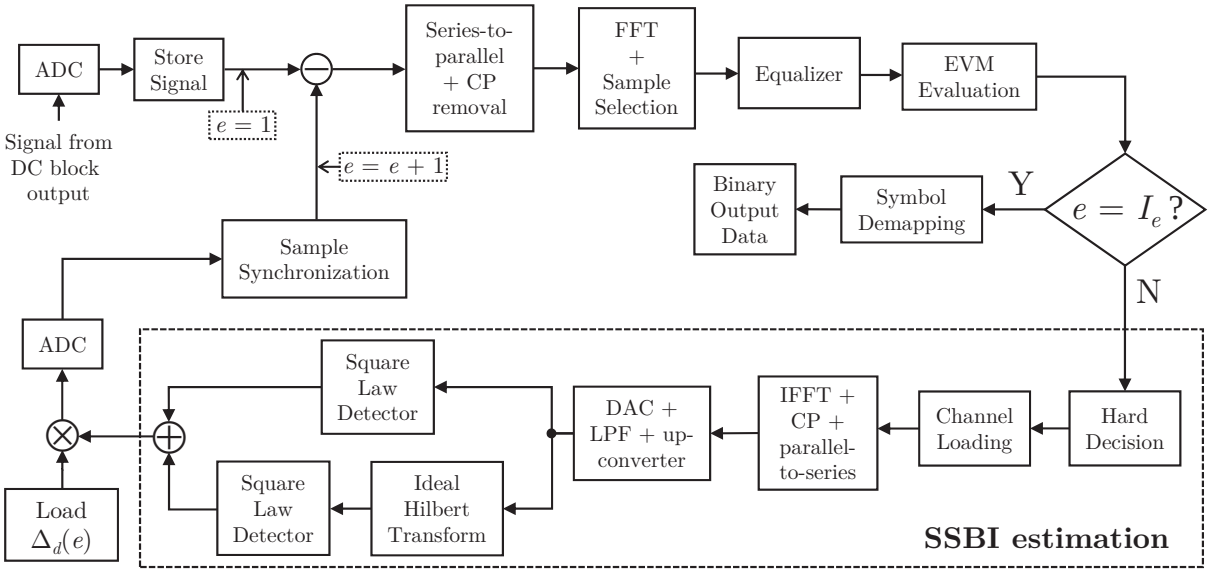

Figure C.4: Block diagram of the OFDM receiver with the SSBI mitigation algorithm operating in the data mode.

C.5 SSBI mitigation results

In this section, the SSBI mitigation algorithm is validated by comparing the results after SSBI mitigation with the results without mitigation. Fig. C.5 shows the EVM as a function of the VBG, for an OFDM band with 5.35 GHz bandwidth, for low VBPR (2.5 dB) and a high VBPR (10 dB), without optical noise, and with and without SSBI mitigation. Results considering a low VBPR and a high VBPR are analysed in order to assess the SSBI mitigation with different SSBI power levels. Fig. C.5 shows a EVM improvement of more than 20 dB for the lowest VBG and for the VBPRs considered. The EVM difference between the lowest and highest VBG cases do not exceed 7 dB and is always lower than -29 dB (EVM with negligible error in the symbols). The two insets show, as a reference, the 4-QAM constellations with and without SSBI removal for a very low VBG (highest spectral efficiency). The QAM symbols in the ideal positions take values $\pm 1 \pm j$ in the complex plane.

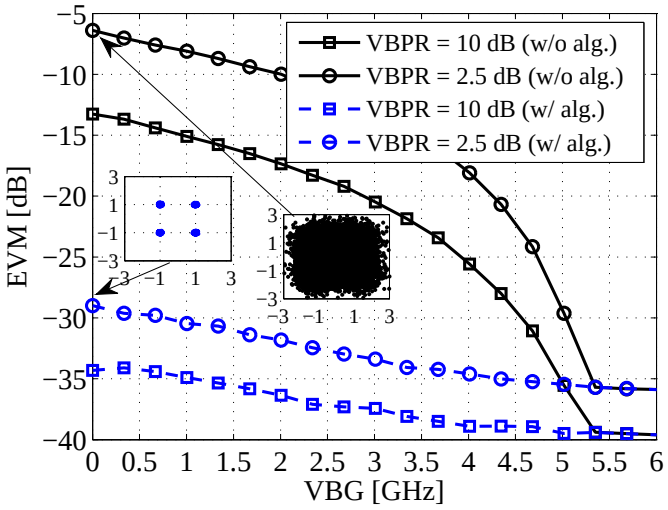

Figure C.5: Tradeoff between the VBG, VBPR and SSBI-induced distortion after the photodetector, with and without the SSBI mitigation algorithm, without optical noise. 4-QAM modulation for each OFDM subcarrier and a modulation index of 5% are considered.

Fig. C.6 shows the EVM as a function of the VBG, for an OFDM band with 5.35 GHz bandwidth, for low VBPR (2.5 dB) and high VBPR (10 dB), with optical noise, and with and without SSBI mitigation. Fig. C.6 shows a lower EVM improvement when compared with that one achieved without optical noise, which is attributed to the optical noise threshold dictated by the OSNR of 16 dB. Notice that, for VBGs lower than 1.5 GHz and without SSBI mitigation, the VBPR increase results in a lower EVM. For a VBPR of 2.5 dB, the SSBI is adequately mitigated since it is dominant over the ASE noise. For a VBPR of 10 dB, the SSBI is not adequately mitigated as the ASE noise is dominant over the SSBI.

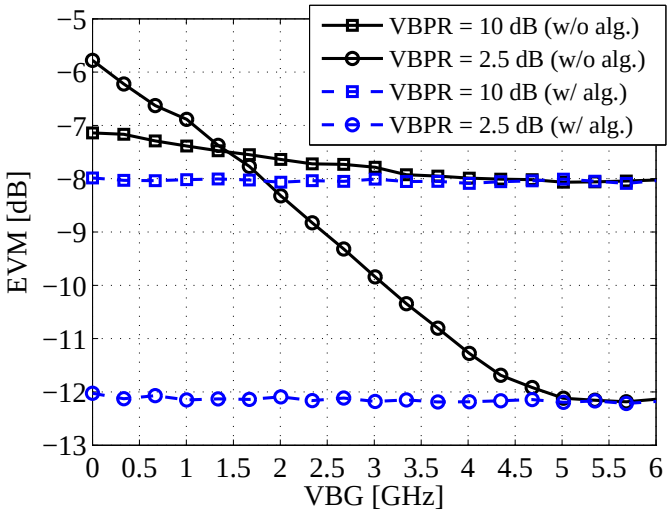

Figure C.6: Tradeoff between the VBG, VBPR and SSBI-induced distortion after the photodetector, with and without the SSBI mitigation algorithm, with optical noise with OSNR of 16 dB. 4-QAM modulation for each OFDM subcarrier and a modulation index of 5% are considered.

Fig. C.7(a) and Fig. C.7(c) depict the optical spectra of a pair band-VC before photodetection, for VBG = $B_w/4$ and VBG = B_w, respectively. Fig. C.7(b) and Fig. C.7(d) depict the electrical spectra after photodetection, for VBG = $B_w/4$ and VBG = B_w, respectively. Fig. C.7(b) also illustrates the spectrum of the digitized signal after SSBI mitigation, for VBG = $B_w/4$. 4-QAM, VBPR = 2.5 dB and modulation index of 5% are considered. Fig. C.7(a) and Fig. C.7(c) show that, before photodetection, decreasing the VBG allows a decrease in the spectral occupancy of the pair band-VC, which results in a higher spectral efficiency. In the same way, Fig. C.7(b) and Fig. C.7(d) show that, after photodetection, decreasing the VBG enables reducing the spectral occupancy of the received signal and, thus, the ADC bandwidth. Fig. C.7 also shows the drawback of decreasing the VBG: the SSBI interferes with the OFDM signal. If the SSBI is not removed, the only way to avoid the SSBI is to impose VBG = B_w [the case shown in Fig. C.7(d)]. Comparing both spectra of Fig. C.7(b), it can be seen that the SSBI has been adequately removed (a more than 20 dB difference in the power levels for low frequencies - for instance 1 GHz - is verified).

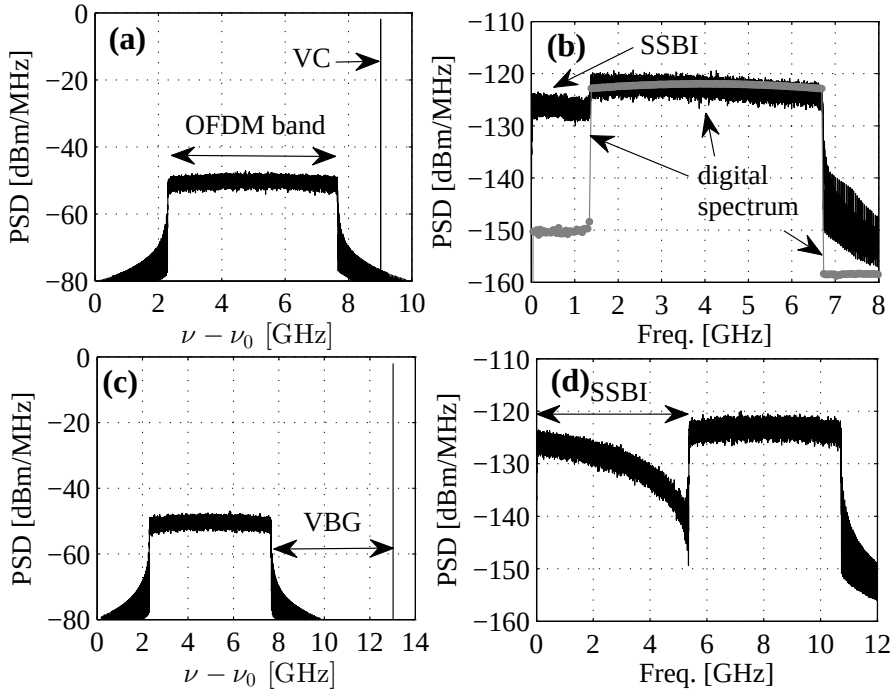

Figure C.7: Optical spectra of the OFDM band and VC before photodetection [(a) and (c)] and the electrical spectra after photodetection [(b) and (d)], for VBG = $B_w/4$ [(a) and (b)] and VBG = B_w [(c) and (d)]. Also shown in (b) is the spectrum of the digitized signal (in grey) after SSBI mitigation, for VBG = $B_w/4$.

In the following analysis, a VBG equal to the subcarrier spacing for 4-QAM (41.8 MHz), and twice the subcarrier spacing for 16-QAM (41.8 MHz) and 32-QAM (33.4 MHz) are considered. The major reasons to consider VBGs multiple of the subcarrier spacing are: 1) to avoid the VC

to overlap with the sinc shape function of the OFDM subcarrier spectrum, which has minimums for multiples of the subcarrier spacing; and 2) to perform correctly the sample selection operation after FFT without resorting to down-conversion and/or resampling.

Fig. C.8 shows the EVM as a function of the training and SSBI iterations in four different situations: (a) without optical noise and with modulation index of 5%, (b) without optical noise and with modulation index of 25%, (c) with OSNR of 16 dB and modulation index of 5% and (d) with OSNR of 16 dB and modulation index of 25%. A fixed VBPR of 2 dB is employed. Fig. C.8 shows that the best EVM degrades considerably with the increase of the modulation index. This is attributed to the increase of the DP-MZM nonlinearity. Fig. C.8 also shows that to remove the SSBI, up to 6 amplitude iterations (white circles) are required per training iteration (lines with circles) in the training mode and up to 5 SSBI iterations (squares) are required in the data mode, for the different cases considered. The black circles indicate the amplitude iteration of each training iteration with the best EVM to employ in the data mode.

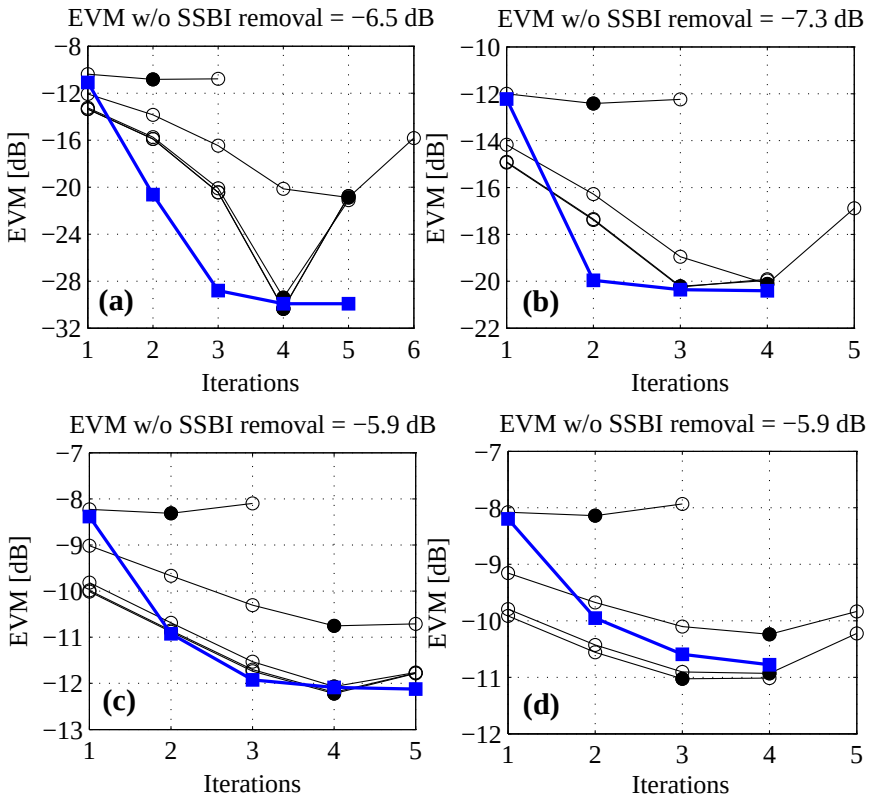

Figure C.8: EVMs as a function of the amplitude/training (circles) and SSBI (squares) iterations: (a) without optical noise and with modulation index of 5%, (b) without optical noise and with modulation index of 25%, (c) with OSNR of 16 dB and modulation index of 5% and (d) with OSNR of 16 dB and modulation index of 25%. The black circles indicate the amplitude iteration with the best EVM in each training iteration. A fixed VBPR of 2 dB is employed.

Fig. C.9 shows the EVM as a function of the VBPR for 4, 16 and 32-QAM transmission and for modulation indexes of 5% and 25%, with and without SSBI mitigation. Without SSBI mitiga-

tion, for 4, 16, and 32-QAM, the OSNR is 16, 19 and 22 dB, respectively. With SSBI mitigation, for 4, 16, and 32-QAM, the OSNR is 22, 29 and 34 dB, respectively. These OSNR values ensure a BER close to 10^{-3}, for the optimum VBPRs. Without SSBI mitigation, the optimum VBPRs are 11, 16 and 19 dB for 4, 16 and 32-QAM, respectively. With SSBI mitigation, the optimum VBPRs decrease to 2.5, 5.5 and 6.5 dB for 4, 16 and 32-QAM, respectively. The SSBI mitigation allows increasing the signal power, resulting in a VBPR reduction and in a lower OSNR required to achieve a given performance. When the SSBI mitigation algorithm is employed and assuming fixed modulation index, the optimum VBPRs are obtained as a compromise between algorithm convergence and optical noise. For VBPRs lower than the optimum value, the algorithm may not converge adequately as the SSBI is considerably stronger. For high VBPRs, the SSBI influence is reduced and the EVM degrades due to the optical noise. Without SSBI mitigation, the optimum VBPRs are obtained as a compromise between SSBI distortion (for low VBPRs) and optical noise (for high VBPRs).

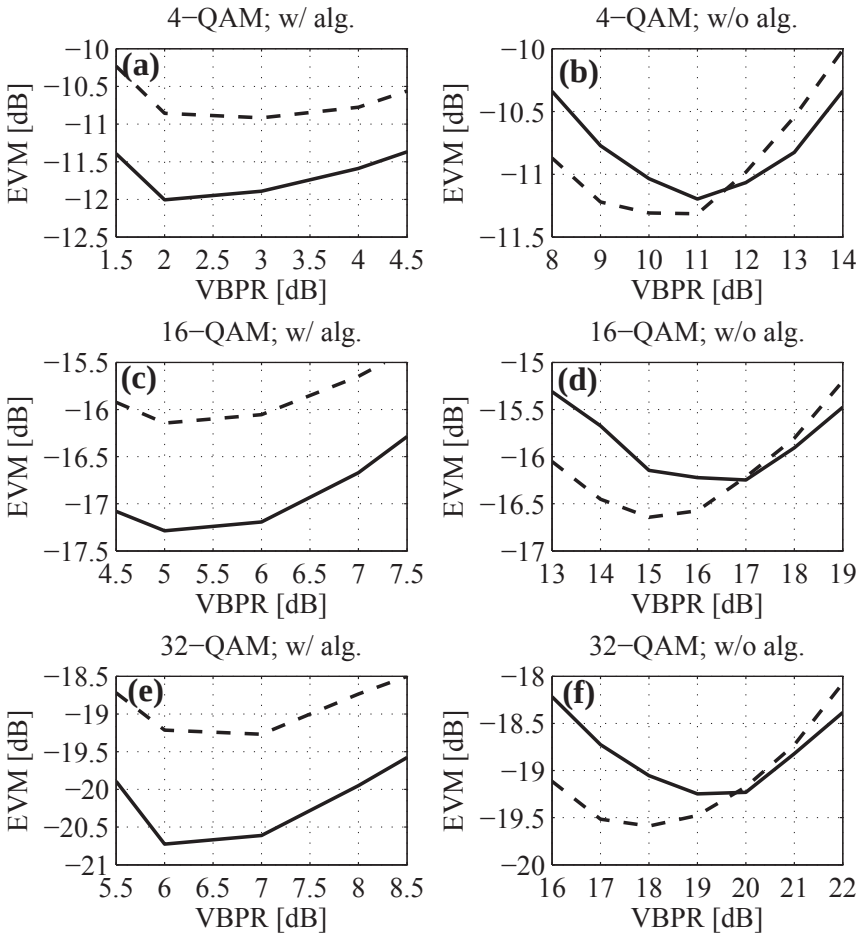

Figure C.9: EVM as a function of the VBPR for 4-QAM [(a) and (b)], 16-QAM [(c) and (d)] and 32-QAM [(e) and (f)] and for modulation indexes of 5% (continuous lines) and 25% (dashed lines), with SSBI mitigation [(a), (c) and (e)] and without SSBI mitigation [(b), (d) and (f)]. With SSBI mitigation and for 4, 16, and 32-QAM, the OSNR is 16, 19 and 22 dB, respectively. Without SSBI mitigation and for 4, 16, and 32-QAM, the OSNR is 22, 29 and 34 dB, respectively.

C.6 Conclusions

A DSP-based iterative algorithm for SSBI mitigation has been presented for VC-assisted DD-OFDM systems. The performance improvement due to the SSBI mitigation has been assessed mainly in the presence of optical noise and distortion due to the optical modulator. Results have shown that the SSBI is accurately removed with a maximum of 5 SSBI iterations, in the case with highest interference. For single-band transmission, optimum VBPRs of 2.5 dB, 5.5 dB and 6.5 dB have been obtained for 4, 16 and 32-QAM, respectively. This translates into a VBPR reduction, relative to the case without SSBI mitigation, of 8.5 dB for 4-QAM systems, 10.5 dB for 16-QAM and 12.5 dB for 32-QAM systems.

Appendix D

Error vector magnitude as metric for performance evaluation

D.1 Error vector magnitude definition

The error vector magnitude (EVM) is a common figure of merit that quantifies the quality of the digital transmission. Its value expresses the difference of amplitude and phase between the value of the actual received constellation symbol and the expected value of the demodulated symbol. Fig. D.1 illustrates the concept of the EVM calculation. The black circle represents the ideal symbol, and the white circle the measured symbol (the real symbol value obtained at the receiver after noise and distortion). The error vector is the distance between the two circles. The average EVM over N_{sym} orthogonal frequency-division multiplexing (OFDM) symbols, where each OFDM symbol has N_{sc} subcarriers, is given in dB by:

$$EVM_{\mathrm{dB}} = 10\log_{10}\left\{\frac{\sum_{n=0}^{N_{sym}-1}\sum_{m=0}^{N_{sc}-1}[(I_{m,n}-\widetilde{I}_{m,n})^2+(Q_{m,n}-\widetilde{Q}_{m,n})^2]}{\sum_{n=0}^{N_{sym}-1}\sum_{m=0}^{N_{sc}-1}(I_{m,n}^2+Q_{m,n}^2)}\right\} \tag{D.1}$$

where N_{sym} stands for the number of OFDM symbols that contribute to the EVM evaluation, N_{sc} is the number of subcarriers within one OFDM symbol, $I_{m,n}$ and $Q_{m,n}$ correspond to the I and Q components of the m-th quadrature amplitude modulation (QAM) symbol of the n-th ideal OFDM symbol, respectively, and $\widetilde{I}_{m,n}$ and $\widetilde{Q}_{m,n}$ represent the I and Q components of the received m-th QAM symbol of the n-th OFDM symbol, respectively. The average EVM of a certain subcarrier is obtained by setting a fixed index m.

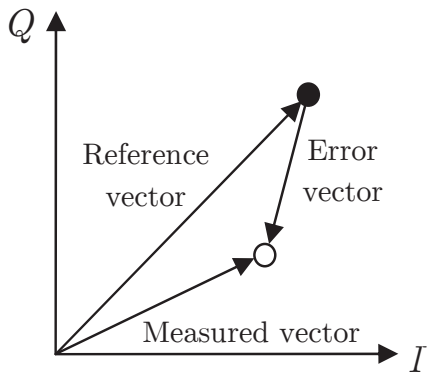

Figure D.1: EVM concept.

D.2 Bit error ratio evaluated from the error vector magnitude

With additive white Gaussian noise (AWGN) dominance, the bit error ratio (BER) can be obtained directly from the EVM when considering square M-QAM constellations [104] ($M = 2^{2p}$, where p is a positive integer number). In this case, the BER as a function of the EVM is given by [104]:

$$\mathrm{BER} = \left(1 - \frac{1}{\sqrt{M}}\right) \frac{2}{\log_2(M)} \mathrm{erfc}\left(\sqrt{\frac{3}{2 \cdot (M-1) \cdot \mathrm{EVM}}}\right) \tag{D.2}$$

where $\mathrm{erfc}(\cdot)$ is the complementary error function, and the EVM is given in linear units. Equivalently, the EVM as a function of the BER using Eq. D.2 can be written as:

$$\mathrm{EVM} = \frac{3}{2 \cdot (M-1)} \left[\mathrm{erfc}^{-1}\left(\frac{\mathrm{BER}}{\left(1 - \frac{1}{\sqrt{M}}\right) \frac{2}{\log_2(M)}}\right)\right]^{-2} \tag{D.3}$$

where $\mathrm{erfc}^{-1}(\cdot)$ is the inverse complementary error function. Taking into account that the electrical signal-to-noise ratio (ESNR) can be obtained directly from the EVM as $\mathrm{ESNR} = (\mathrm{EVM})^{-1}$, Eq. D.2 can be rewritten as:

$$\mathrm{BER} = \left(1 - \frac{1}{\sqrt{M}}\right) \frac{2}{\log_2(M)} \mathrm{erfc}\left(\sqrt{\frac{3 \cdot \mathrm{ESNR}}{2 \cdot (M-1)}}\right). \tag{D.4}$$

For $M \neq 2^{2p}$ (for instance, $M \in \{32, 128\}$), results have shown that this approximation is also reasonable. Nevertheless, an accurate expression to evaluate the BER from the EVM for cross 32-QAM constellations has been derived. This expression is given by [89]:

$$\mathrm{BER} = \frac{91}{240} \mathrm{erfc}\left(\sqrt{\frac{5}{100 \cdot \mathrm{EVM}}}\right). \tag{D.5}$$

Fig. D.2 shows the BER as a function of the EVM for different QAM orders. For 32-QAM, Eq. D.5 was employed instead of Eq. D.2. Tab. D.1 shows the EVM, for different QAM orders, that corresponds to a BER of 3.8×10^{-3} ($\log_{10}\mathrm{BER} = -2.42$) and to a BER of 10^{-3} ($\log_{10}\mathrm{BER} = -3.00$). The former is the 7%-forward error correction (FEC) threshold and the latter is a commonly used BER threshold in optical networks.

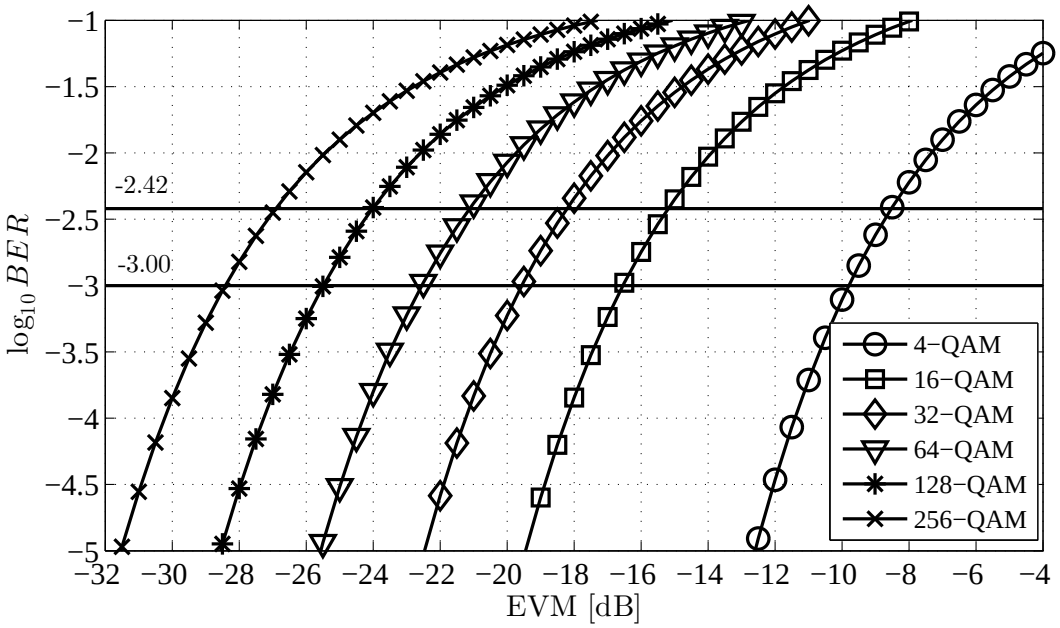

Figure D.2: $\log_{10}\mathrm{BER}$ as a function of the EVM in dB, for different QAM orders. Additional lines at $\log_{10}\mathrm{BER} = -2.42$ and $\log_{10}\mathrm{BER} = -3.00$ are also shown.

Table D.1: EVM, for different QAM orders, that corresponds to a BER of 3.8×10^{-3} ($\log_{10} BER = -2.42$) and to a BER of 10^{-3} ($\log_{10} BER = -3.00$).

QAM orders	EVM [dB] $\Leftrightarrow$ BER of 3.8×10^{-3}	EVM [dB] $\Leftrightarrow$ BER of 10^{-3}
4	-8.6	-9.8
16	-15.2	-16.6
32	-18.2	-19.5
64	-21.1	-22.5
128	-24.1	-25.5
256	-27.0	-28.5

Appendix E

EGA for BER estimation of high-order QAM constellations

E.1 Introduction

The bit error ratio (BER) is commonly employed in previous works as figure of merit to evaluate the performance of direct-detection (DD)-orthogonal frequency-division multiplexing (OFDM) systems [105, 106]. For BER assessment, the most common techniques are Monte Carlo simulation with direct error counting (DEC), the analytical Gaussian approach (AGA), the exhaustive Gaussian approach (EGA), and the error vector magnitude (EVM) [105]. The BER is easily obtained with DEC by counting the received erroneous bits. DEC is a good solution in terms of accuracy. However, the number of transmitted OFDM symbols required and the computation time to achieve BER values lower than 10^{-6} is unacceptable (to achieve a BER of 10^{-6} when 100 errors occur on the subcarrier with worst performance, several hours are required and is necessary to transmit more than one million of OFDM symbols). The BER obtained from the AGA and the EVM overcomes the computation time drawback, providing fast BER estimates. Nevertheless, inaccurate BER estimates can be obtained as the distortion is implicitly assumed as Gaussian-distributed.

In [107], an EGA method has been proposed for BER evaluation. In this method, the mean and standard deviation of each OFDM subcarrier corrupted by noise are obtained by simulation. In [103], the EGA has been extended to experimental DD-OFDM setups. With EGA, fast and accurate BER estimates can be obtained for each subcarrier, considering the noise and distortion effects. EGA estimation considers a Gaussian distribution for the I and Q components of each

OFDM subcarrier to correctly identify the statistical distribution of the distortion [103]. Two different types of symbol mapping were considered for BER evaluation in [103, 107]: binary phase shift keying (BPSK) and quadrature phase shift keying (QPSK).

In this appendix, the EGA method is generalized to evaluate, through numerical simulation, the BER for M-ary quadrature amplitude modulation (QAM) formats with $M \in \{16, 32, 64, 128, 256\}$. To evaluate the EGA accuracy, the BER estimates are compared with the ones obtained with the DEC method. For square QAM constellations with $M = 16$, $M = 64$ and $M = 256$, perfect Gray coding is considered. For cross QAM constellations with $M = 32$ and $M = 128$, Smith-style Gray coding is used [89]. The reason for considering cross QAM constellations for $M = 32$ and $M = 128$ instead of rectangular QAM constellations is related with its better performance results when compared with rectangular QAM. The challenge that cross QAM imposes to the EGA implementation when compared with rectangular QAM is that decision regions are more complex to define.

The work presented along this appendix is also published in [69].

E.2 Exhaustive Gaussian approach

The EGA is a method for performance evaluation that provides fast and accurate BER estimates independently of the BER levels. The EGA assumes that the received in-phase (I) and quadrature (Q) components of each OFDM subcarrier are well described by a Gaussian distribution, as confirmed in [107]. Therefore, the BER of the received I or Q component of a subcarrier belonging to a specific OFDM symbol is evaluated from the subcarrier mean and standard deviation values. In the EGA context, these values are computed from a set of different signal runs impaired by noise and/or distortion.

To illustrate the EGA generalization to high order QAM formats, let us focus the attention on 16-QAM constellations. For other M-QAM constellations, the procedure is similar. The Gray-mapped 16-QAM constellation used to evaluate the BER estimates with the EGA and DEC methods is shown in Fig. E.1. Variables l and c index the position (row and column, respectively) of a QAM symbol on the M-QAM constellation.

The key idea for EGA computation is explained as follows. A certain subcarrier, which has suffered from noise and/or distortion, is received with a mean value and a standard deviation from its I and Q components. First, given a certain transmitted subcarrier, the number of

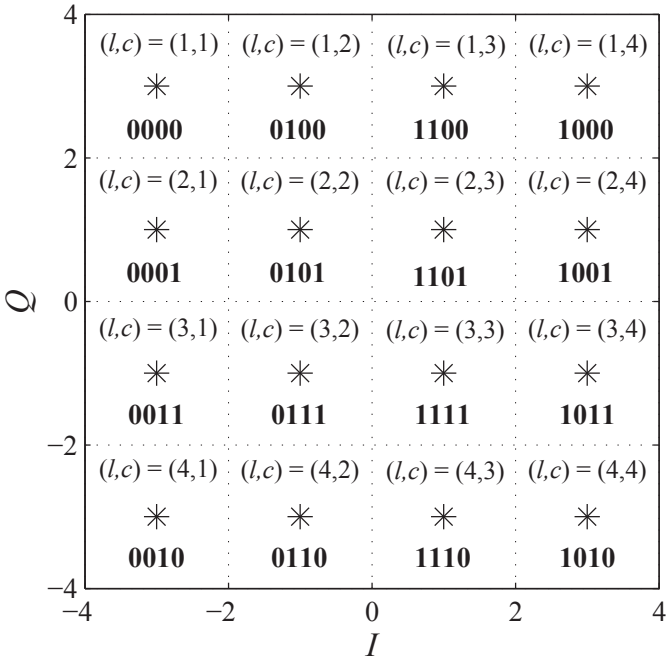

Figure E.1: Square QAM constellation with $M = 16$. The Gray-mapped bits of each QAM symbol represented by a star are highlighted in bold.

different bits between that one and a received subcarrier, for all the possibilities, is obtained. Second, the probability of the I and Q components of a received subcarrier (following a Gaussian distribution) to be in all decision regions, is assessed. Finally, by multiplying both the number of different bits and probabilities for all decision regions, the BER for that certain subcarrier is obtained. Mathematically, the BER of the k-th OFDM subcarrier of the i-th OFDM symbol, $BER^{(i)}[k]$, calculated with the EGA method is given by:

$$BER^{(i)}[k] = \frac{1}{\log_2 M} \sum_{l=1}^{N_l} \sum_{c=1}^{N_c} \left(N^{(i)}_{E,(l,c)}[k] \times P^{(i)}_{I,(l,c)}[k] \times P^{(i)}_{Q,(l,c)}[k] \right) \tag{E.1}$$

where N_l and N_c are the number of rows and columns of QAM symbols in the constellation, respectively, $N^{(i)}_{E,(l,c)}[k]$ is the number of erroneous bits of the k-th OFDM subcarrier of the i-th OFDM symbol when falling in the (l, c) decision region, and $P^{(i)}_{I,(l,c)}[k]$ and $P^{(i)}_{Q,(l,c)}[k]$ denote the probabilities of the I and Q components of the received k-th OFDM subcarrier of the i-th OFDM symbol to fall in the (l, c) decision region, respectively. It is assumed that the I and Q components are uncorrelated and that Gray coding is used. Each probability (I or Q) is obtained through the Q_F function, which is given by:

$$Q_F(z) = \frac{1}{\sqrt{\pi}} \int_{z/\sqrt{2}}^{\infty} \exp(-x^2)\, \mathrm{d}x = \frac{1}{2} \mathrm{erfc}\left(\frac{z}{\sqrt{2}} \right). \tag{E.2}$$

The mean $m^{(i)}_{(I,Q)}[k]$ and standard deviation $\sigma^{(i)}_{(I,Q)}[k]$ of the received k-th OFDM subcarrier of

the i-th OFDM symbol is given by:

$$\begin{cases} m_{(I,Q)}^{(i)}[k] = \dfrac{1}{N_r}\displaystyle\sum_{n=1}^{N_r} y_{(I,Q),n}^{(i)}[k] \\ \sigma_{(I,Q)}^{(i)}[k] = \left[\dfrac{1}{N_r}\displaystyle\sum_{n=1}^{N_r}\left(y_{(I,Q),n}^{(i)}[k] - m_{(I,Q)}[k]\right)^2\right]^{\frac{1}{2}} \end{cases} \tag{E.3}$$

where N_r is the number of signal runs, $y_{(I,Q),n}^{(i)}[k]$ is the amplitude of the I or Q component of the received k-th OFDM subcarrier of the i-th OFDM symbol in the n-th signal run, and $m_{(I,Q)}[k]$ is the mean of the I or Q component of the k-th OFDM subcarrier of the received OFDM symbols.

For the constellation of Fig. E.1, $P_{I,(l,c)}^{(i)}[k]$ is given by:

$$P_{I,(l,c)}^{(i)}[k] = \begin{cases} Q_F\left[\dfrac{2+m_I^{(i)}[k]}{\sigma_I^{(i)}[k]}\right], c=1 \\ Q_F\left[+\dfrac{m_I^{(i)}[k]}{\sigma_I^{(i)}[k]}\right] - Q_F\left[\dfrac{2+m_I^{(i)}[k]}{\sigma_I^{(i)}[k]}\right], c=2 \\ Q_F\left[-\dfrac{m_I^{(i)}[k]}{\sigma_I^{(i)}[k]}\right] - Q_F\left[\dfrac{2-m_I^{(i)}[k]}{\sigma_I^{(i)}[k]}\right], c=3 \\ Q_F\left[\dfrac{2-m_I^{(i)}[k]}{\sigma_I^{(i)}[k]}\right], c=4 \end{cases} \tag{E.4}$$

for all values of $l \in \{1,2,3,4\}$, and $P_{Q,(l,c)}^{(i)}[k]$ is written as:

$$P_{Q,(l,c)}^{(i)}[k] = \begin{cases} Q_F\left[\dfrac{2-m_Q^{(i)}[k]}{\sigma_Q^{(i)}[k]}\right], l=1 \\ Q_F\left[-\dfrac{m_Q^{(i)}[k]}{\sigma_Q^{(i)}[k]}\right] - Q_F\left[\dfrac{2-m_Q^{(i)}[k]}{\sigma_Q^{(i)}[k]}\right], l=2 \\ Q_F\left[+\dfrac{m_Q^{(i)}[k]}{\sigma_Q^{(i)}[k]}\right] - Q_F\left[\dfrac{2+m_Q^{(i)}[k]}{\sigma_Q^{(i)}[k]}\right], l=3 \\ Q_F\left[\dfrac{2+m_Q^{(i)}[k]}{\sigma_Q^{(i)}[k]}\right], l=4 \end{cases} \tag{E.5}$$

for all values of $c \in \{1,2,3,4\}$. The BER of each subcarrier, $BER[k]$, is then obtained as follows:

$$BER[k] = \frac{1}{N_s}\sum_{i=1}^{N_s} BER^{(i)}[k] \tag{E.6}$$

where N_s corresponds to the number of OFDM symbols per signal run. The BER obtained from EGA, while considering a Gaussian distribution for the noise, allows describing correctly the statistical distribution of the distortion through the average over different occurrences of symbols of each subcarrier performed by Eq. E.6. This is achieved by not assuming that the distortion

on all the subcarriers is Gaussian-distributed, as the EVM and AGA methods consider. This means that the degradation induced by distortion, for instance due to the electrical-to-optical conversion or due to non-ideal optical filtering, is correctly accounted by Eq. E.6. The overall BER is then evaluated averaging the BER over all N_{sc} information subcarriers, as follows:

$$BER = \frac{1}{N_{sc}} \sum_{k=1}^{N_{sc}} BER[k]. \tag{E.7}$$

E.3 System setup

To analyse and validate the EGA proposed for high-order QAM formats, the BER estimates from the DEC and EGA methods are compared using the DD-OFDM system in optical back-to-back operation illustrated in Fig. E.2.

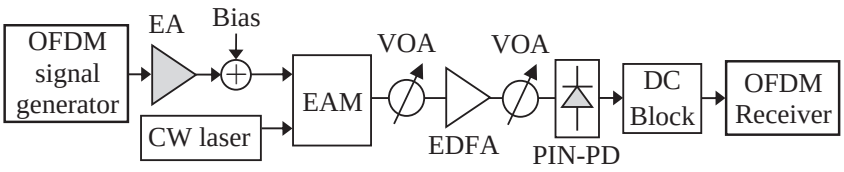

Figure E.2: DD-OFDM system in optical back-to-back. CW: continuous wave, EA: electrical amplifier, EAM: electro-absorption modulator, EDFA: erbium-doped fibre amplifier, PIN-PD: p-type-intrinsic-n-type photodiode, VOA: variable optical attenuator.

The OFDM signal at the output of the OFDM signal generator is amplified by an electrical amplifier (EA) and biased. The OFDM signal has 128 OFDM subcarriers, all carrying information, and its spectrum (approximately rectangular) is centred at 5 GHz with a bit rate R_d of 10 Gb/s. The bandwidth B_w of the OFDM signal is variable and decreases while increasing M: $B_w = R_d / \log_2 M$. The chirpless electro-absorption modulator (EAM) is fed by a continuous wave (CW) laser with output power of 5 mW (7 dBm) and performs the electrical-to-optical conversion of the OFDM band to an optical centre frequency of 193.1 THz. The EAM output power characteristic as a function of the bias voltage is shown in Fig. E.3. Fig. E.3 shows that a good compromise between linear behaviour and EAM power loss is around 0.7 V. This results in an average power at the EAM output of 1 mW (0 dBm) for OFDM signals with root-mean-square (RMS) voltages much smaller than 0.7 V, meaning that the EAM introduces approximately 7 dB insertion loss. After electrical-to-optical conversion, a variable optical attenuator (VOA) and an erbium doped fibre amplifier (EDFA) are used to adjust the optical signal-to-noise ratio (OSNR) that is defined in a reference optical bandwidth of 0.1 nm ($\approx$ 12.5 GHz). The second VOA sets a fixed power of 0 dBm at the p-type-intrinsic-n-type (PIN)-photodiode (PD) input. An ideal

square-law PIN-PD with responsivity of 1 $\mathrm{A \cdot W^{-1}}$ performs optical-to-electrical conversion, and the BER is evaluated at the OFDM receiver.

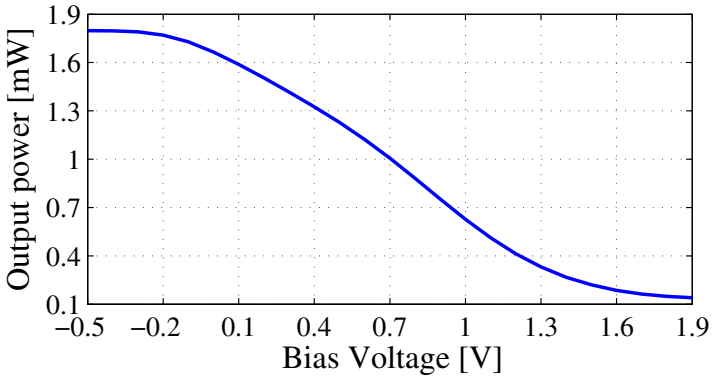

Figure E.3: EAM output power for a CW laser input power of 5 mW.

E.4 EGA validation

In order to assess the EGA accuracy under different transmission situations, different levels of optical noise generated by the EDFA and distortion induced by the EAM and PIN-PD are considered. One of the key parameters of the EGA is the number of runs needed to achieve good BER estimates and particularly good estimates of mean and standard deviation for the different transmitted symbols. In the DEC method, different runs of symbols are transmitted (each run with 250 different OFDM symbols) and for each set of system parameters, the BER is estimated when 100 errors occur on the subcarrier with worst performance [103]. This indicates that, as the BER levels decrease, a higher number of runs is necessary to calculate the BER. The BER of each subcarrier obtained through the EGA considers the BER evaluation of the received subcarriers of 250 OFDM symbols over 200 signal runs. In all situations considered, it was confirmed that this number of runs is enough to obtain stabilized BER estimates.

Fig. E.4 presents the BER estimates of EGA and DEC as a function of the OSNR, with $M \in \{16, 32, 64, 128, 256\}$ and with different RMS voltages at the EAM input. Fig. E.4 shows an excellent agreement between the BER estimated by both methods, independently of the OSNR levels. The different behaviour of the curves for different values of M is related to noise and distortion effects. With $M = 16$ and $M = 32$, optical noise is the dominant effect affecting the performance. With $M = 64$, $M = 128$ and $M = 256$, the BER starts to stabilize for OSNR values higher than 40 dB. This means that the system is impaired mainly by distortion effects. Fig. E.4 also shows that, to achieve the same BER level for higher-order constellations, the OSNR has to increase. This is attributed to the smaller decision regions as M increases.

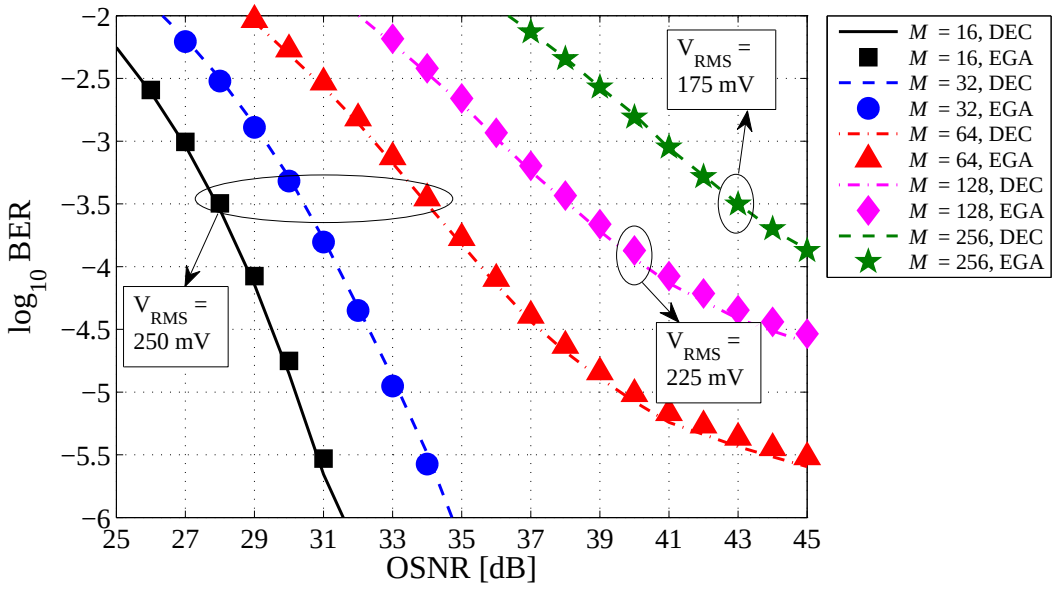

Figure E.4: BER estimates of the EGA and DEC methods as a function of the OSNR, with $M \in \{16, 32, 64, 128, 256\}$ and with different RMS voltages at the EAM input.

Fig. E.5 shows the BER estimates with EGA for 32-QAM constellations, as a function of the signal runs for different OSNRs. Fig. E.5 shows that 100 signal runs are enough to obtain an accurate BER estimate for different BER levels, as the BER difference from 100 runs to 200 runs is negligible.

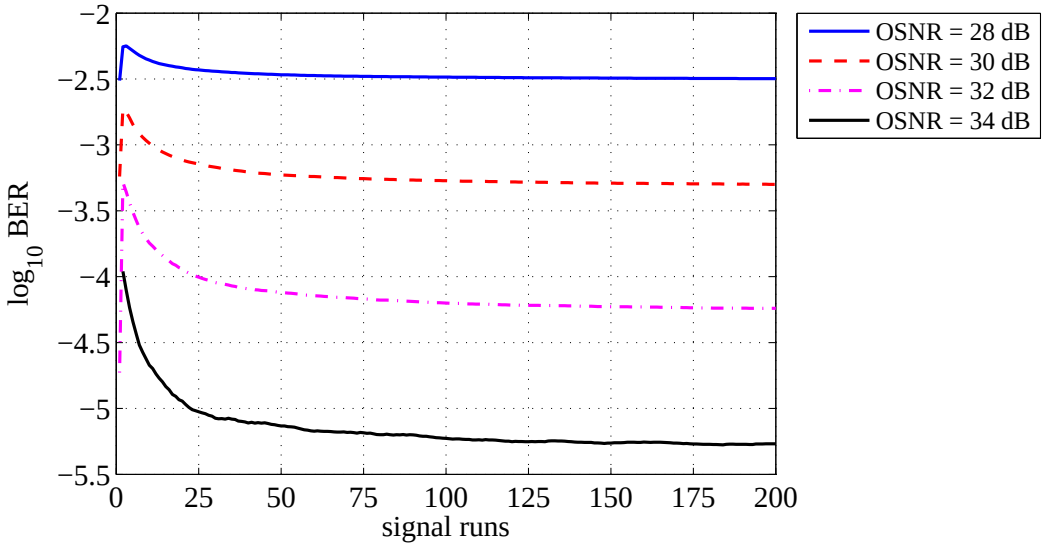

Figure E.5: BER estimates with EGA as a function of the number of signal runs for 32-QAM constellations, considering different OSNR values and a RMS voltage at the EAM input of 250 mV.

Besides varying the OSNR for a fixed RMS voltage, it is also important to verify the EGA accuracy for a fixed OSNR while varying the RMS voltage, as in this case, the optimum RMS voltage that achieves the minimum BER level can be obtained. Fig. E.6 presents the BER

estimates with both methods (EGA and DEC) as a function of the RMS voltage of the signal at the EAM input, for different OSNRs with $M = \{16, 32, 64, 128, 256\}$.

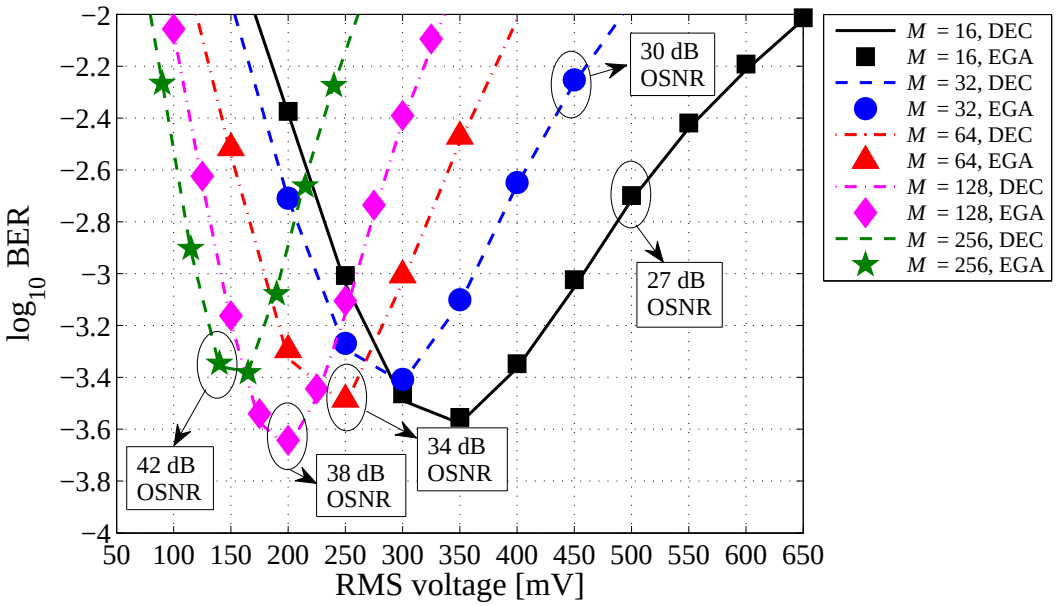

Figure E.6: BER estimates with both methods (EGA and DEC) as a function of the RMS voltage of the signal at the EAM input, with OSNR $= \{27, 30, 34, 38, 42\}$ dB for $M = \{16, 32, 64, 128, 256\}$, respectively.

Fig. E.6 shows an excellent agreement between the estimates obtained with the EGA and DEC, for different RMS voltages of the OFDM signal applied to the EAM input. For RMS voltages higher than the one corresponding to the minimum BER (optimum RMS voltage), the performance is dominantly impaired by distortion from the EAM nonlinear characteristic (depicted in Fig. E.3). For RMS voltages lower than the optimum RMS voltage, the performance is dominantly impaired by optical noise. The results of Fig. E.6 show that the EGA provides accurate BER estimates in the presence of nonlinearities, such as the ones originated from the EAM. In order to obtain similar BER levels for different values of M, different OSNR values were considered. Additionally, a decrease in the optimum RMS voltage as M increases is verified. This is related to the higher influence of distortion as M increases.

Other important metric to evaluate the EGA is the computation time, as it enables to identify how faster EGA is compared with the BER estimates obtained with DEC. Fig. E.7 presents the computation time, in seconds, of the BER estimates obtained with the DEC and EGA, as a function of $-\log_{10}$BER, with $M \in \{16, 32, 64, 128, 256\}$. A 3.5 GHz Intel Core i7-4770K PC with 32 GB of RAM was used in the computation of both methods.

Fig. E.7 shows that the computation time of the DEC method increases substantially with the BER decrease whereas, with EGA, almost the same computation time is obtained for all the

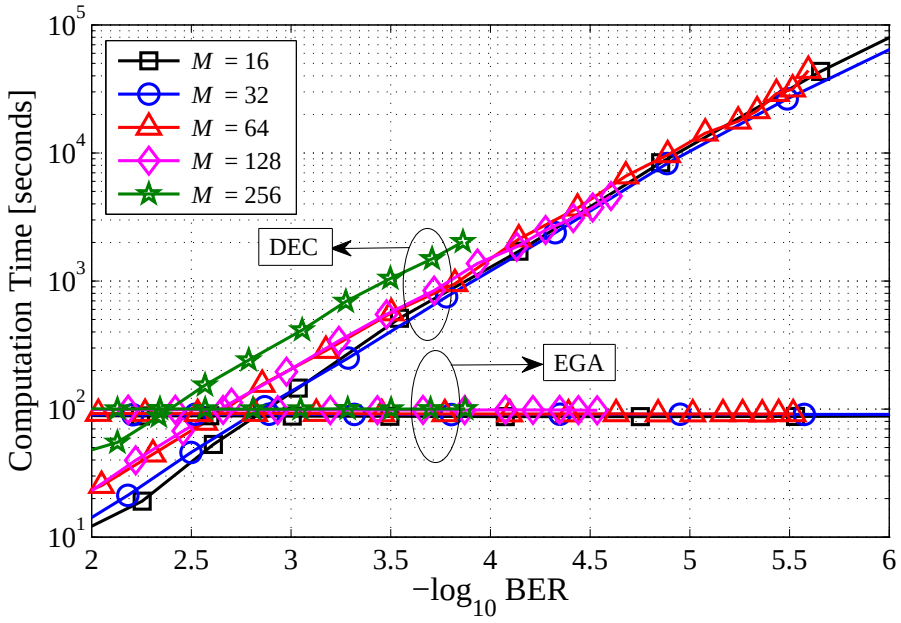

Figure E.7: Computation time, in seconds, of the BER estimates obtained with the DEC and EGA methods, as a function of $-\log_{10}$BER, for $M \in \{16, 32, 64, 128, 256\}$.

BER levels and QAM constellations considered. Fig. E.7 shows also that the DEC method is more time spending than EGA for BER levels lower than about 10^{-3} and that EGA requires, in comparison with DEC, three orders of magnitude less in computation time for BER levels around 10^{-6}. With the DEC method and for the same BER level, the computation time increases slightly as the M increases. This occurs because, with the increase of the M, a higher computation time is required for demapping the QAM symbols into bits.

E.5 Conclusions

The generalization of the EGA for DD-OFDM systems employing square and cross QAM constellations has been presented. Excellent agreement has been shown between the BER estimated by the DEC and EGA. This was confirmed for a system dominantly impaired by noise or by distortion. The computation time of both methods has been compared. For BER levels lower than 10^{-3}, the DEC method is more time spending than EGA. For BER $\approx 10^{-6}$, DEC requires a computation time of 10^5 seconds and EGA requires only 10^2 seconds (computation time improved three orders of magnitude).

Appendix F

Single-mode fibre transmission impairments

In this appendix, the standard single mode fibre (SSMF)-induced impairments with linear transmission are introduced, and their expected impact on the performance of multi-band (MB)-orthogonal frequency-division multiplexing (OFDM) signals is discussed. In addition, the most important nonlinear effects experienced with SSMF transmission are presented.

F.1 Linear transmission

Transmission along the SSMF is linear (that is, the nonlinear effects are negligible) for reduced average power levels. In this case, the SSMF can be modelled by the following transfer function [108]:

$$H_{\mathrm{SMF}}(z,\nu) = \exp\left(-\frac{\alpha}{2}z\right)\exp\left[-j\beta(\nu)z\right] \tag{F.1}$$

where z is the propagation distance along the transmission link, ν is the optical frequency, α is the attenuation coefficient (expressed in $\mathrm{Np}\cdot\mathrm{m}^{-1}$) and $\beta(\nu)$ is the propagation constant at frequency ν. The first term dependent on α accounts for the attenuation effect and the second term dependent on β accounts for the dispersion effect.

F.1.1 Fibre attenuation

Optical fibre attenuation plays an important role in the deployment of any optical network since it determines the maximum length of each SSMF span before requiring amplification. A pure

silica-glass fibre presents an attenuation not exceeding 1 dB/km for wavelengths between 800 and 1800 nm [109]. The two bands around 1300 and 1550 nm correspond to the windows currently used in fibre communication systems (known as the second and third windows, respectively). The lower the attenuation, the greater will be the maximum length and the lower will be the network cost [109]. If P_{in} is the power launched into a SSMF span with length L_f, the power at the SSMF span output, P_{out}, is given by:

$$P_{out} = P_{in} \cdot \exp(-\alpha L_f). \tag{F.2}$$

The attenuation coefficient is normally expressed in $\mathrm{dB} \cdot \mathrm{km}^{-1}$ instead of $\mathrm{Np} \cdot \mathrm{m}^{-1}$. When designing optical systems for long distance applications, the third window is preferred, as it offers the minimum attenuation. For wavelengths around 1550 nm, the attenuation coefficient is around 0.2 $\mathrm{dB} \cdot \mathrm{km}^{-1}$ [108]. The total attenuation of fibre cables used in optical communication systems is slightly larger than 0.2 $\mathrm{dB} \cdot \mathrm{km}^{-1}$ because of splice and connector losses [108].

F.1.2 Group velocity dispersion

Optical fibre transmission can be also impaired by a phenomenon known as group velocity dispersion (GVD), in which different components of the signal travel at different velocities. This can be a limiting factor for transmission systems supporting longer distances and higher bit rates [109]. The propagation constant can be approximated by a Taylor series expansion up to the third term around a reference optical frequency ν_0 as follows [108]:

$$\beta(\nu) \approx \beta_0 + \beta_1 (\nu - \nu_0) + \frac{\beta_2}{2} (\nu - \nu_0)^2 + \frac{\beta_3}{6} (\nu - \nu_0)^3 \tag{F.3}$$

where β_0 is the propagation constant at ν_0, β_1 is the propagation delay (inverse of the group velocity v_g), β_2 is the first-order GVD coefficient and β_3 is the second-order GVD coefficient. The terms up to the third-order provide a good approximation as long as the optical signals have bandwidth much less than ν_0 (which is usually the case). Only the terms dependent on the GVD coefficients (β_2 and β_3) induce signal distortion.

With GVD, different spectral components reach the fibre output at different time instants. Thus, the optical signal at the fibre output is broadened in time. The GVD-induced time-broadening is expressed by the GVD parameter which is written as [108]:

$$D(\nu_0) = -\frac{{\nu_0}^2}{2\pi c}\beta_2 = -\frac{2\pi c}{{\lambda_0}^2}\beta_2 \tag{F.4}$$

where c is the speed of light in vacuum and λ_0 is the optical wavelength at ν_0 [$\lambda_0 = (2\pi c)/\nu_0$]. The GVD parameter is usually expressed in ps·nm^{-1}·km^{-1} and, for SSMF transmission with $\lambda_0 = 1550$ nm, the value of D is around 17 ps·nm^{-1}·km^{-1}.

For wavelengths close to the zero-dispersion wavelength (around 1300 nm), β_2, and consequently D, vanish. However, second-order GVD is still present. The parameter which describes the influence of the second-order GVD coefficient is the dispersion slope, S, which is given as follows:

$$S(\lambda_0) = \left(\frac{2\pi c}{{\lambda_0}^2}\right)^2 \beta_3 - \left(\frac{2}{\lambda_0}\right) D(\lambda_0). \tag{F.5}$$

For deployed single mode fibres (SMFs), the dispersion slope S is approximately equal to 0.09 ps·nm^{-2}·km^{-1} [110].

In direct-detection (DD)-OFDM-based systems, the GVD-induced time-broadening affects the subcarriers of each OFDM band. This effect is usually compensated by the cyclic prefix (CP), which must be dimensioned to account for the GVD-induced time-broadening. With a correctly dimensioned CP (see Eq. 2.10), the equalizer at the corresponding OFDM receiver compensates for the delay difference.

In addition to the GVD-induced time-broadening, there is the GVD-induced power fading [74] which can also affect significantly the performance of OFDM signals after DD. This impairment may affect the power magnitude of the spectral components of an OFDM signal and, contrarily to the GVD-induced time-broadening, cannot be compensated at the receiver side. Let us assume, for simplicity, that a pair band-virtual carrier (VC) is modulated by an ideal optical modulator and photodetected. The optical modulator generates a double sideband (DSB) signal, and due to GVD, the frequencies of the sidebands may be delayed relative to each other. This results in incoherent combination in the photodetection process (which is insensitive to the phase of the different sidebands). This leads to power reduction at certain frequencies when compared with the power in back-to-back operation. To illustrate the GVD-induced power fading, Fig. F.1 shows the spectra of the DSB signal at the ideal optical modulator output, which is biased at minimum point, and the spectra after photodetection considering back-to-back operation and lossless SSMF transmission (to focus the attention on the dispersion-induced effects). Fig. F.1(b) shows that, for the subcarriers around 1.5 GHz, the power fading surpasses 20 dB when compared with the respective power in back-to-back. This results in total loss of information in the subcarriers around 1.5 GHz.

One way to avoid the power fading impairment is to transmit single sideband (SSB) signals

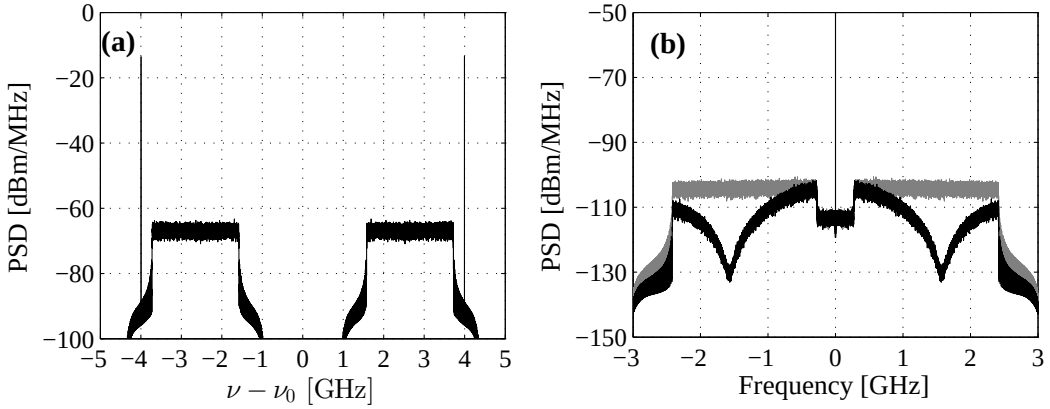

Figure F.1: (a) Spectrum of the DSB signal at the ideal optical modulator output, which is biased at minimum point. (b) Spectra after photodetection, in back-to-back operation (grey) and with lossless SSMF transmission along 9 spans with 40-km length each (black). The VC is centred at 4 GHz, the signal bandwidth is 2.178 GHz and the virtual carrier-to-band gap (VBG) is equal to 12.5% of the signal bandwidth. $\nu - \nu_0$ stands for the low-pass equivalent (LPE) frequency.

instead of DSB signals. The simplest way to generate a SSB signal from a DSB signal is by optically filtering one of the sidebands. A more complex way is using the Hilbert transform (HT) to generate a SSB MB-OFDM signal at the optical modulator output, which was considered in chapter 3. To illustrate the power fading mitigation when transmitting SSB signals, Fig. F.2 shows the spectra of the SSB signal in which the lower sideband was removed, and the spectra after photodetection, with lossless SSMF transmission. Fig. F.2(b) shows that, after photodetection, all subcarriers have similar power which is a result of SSB transmission. SSB transmission avoids the GVD-induced power fading by ensuring that destructive interference between the two sidebands does not occur.

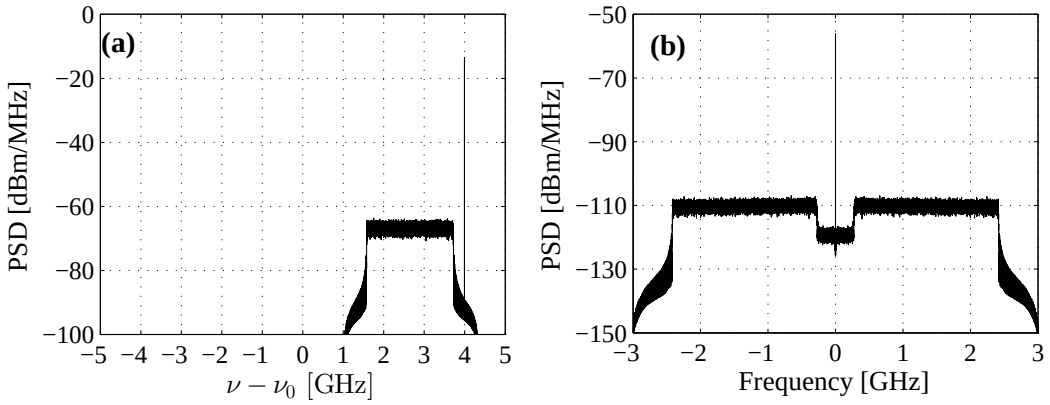

Figure F.2: (a) Spectrum of the SSB signal in which the lower sideband was removed. (b) Spectrum after photodetection with lossless SSMF transmission along 9 spans with 40-km length each. The VC is centred at 4 GHz, the signal bandwidth is 2.178 GHz and the VBG is equal to 12.5% of the signal bandwidth. $\nu - \nu_0$ stands for the LPE frequency.

F.1.3 Polarization mode dispersion

Another pulse broadening mechanism in SMFs besides GVD is known as polarization mode dispersion (PMD) [108, 109]. In reality, SMF is not truly single mode as it can support two polarization modes [108]. Fibre transmission in ideal conditions, that is, considering perfect cylindrical symmetry and no mechanical stress, is independent of the polarization, as the two modes are expected to not couple with each other given that they are polarized orthogonally. However, in real fibres, cylindrical asymmetry occurs due to random variations in the core shape along the fibre length, leading to an exchange of the random power between the two polarization modes. Hence, real transmission is polarization-dependent. As different polarizations propagate at different velocities, a delay between the polarizations is experienced at the receiver side [108, 111]. This effect is called PMD. The PMD-induced signal-broadening in the time domain, $\Delta\tau$, can be estimated as follows:

$$\Delta\tau = D_{\text{PMD}}\sqrt{L_f} \tag{F.6}$$

where D_{PMD} is the PMD parameter. For today manufactured fibres, values of D_{PMD} are in the range of 0.05 ps/$\sqrt{\text{km}}$ [111]. Because of the dependence on the square root of the fibre length, PMD-induced broadening is small when compared with the GVD-induced broadening [110]. In metro and access networks, negligible impairments from the PMD effect are expected, as the total SSMF length does not surpass a few hundreds of kilometres, that is, a small $\Delta\tau$ is expected. The small $\Delta\tau$ can be compensated by assessing the optical channel stability through the use of training symbols (TSs).

F.2 Nonlinear transmission

The basic principles of optical transmission can be explained assuming that SMF is linear, as silica (material which SMF is made) is a weakly nonlinear medium. However, the response of any dielectric to light when exposed to strong electromagnetic fields is nonlinear [108]. As a result, the induced polarization is not linear in the electric field and is dependent on the susceptibilities with orders higher than one. The dominant contribution to the polarization is the linear susceptibility $\chi^{(1)}$. The second-order nonlinear susceptibility $\chi^{(2)}$ is negligible if an inversion symmetry at the molecular level is verified. Given that silica is a symmetric molecule, silica-made optical fibres do not present second-order nonlinear effects [108]. The third-order nonlinear susceptibility $\chi^{(3)}$ is responsible for the most common nonlinear effects in optical fibres,

such as nonlinear refraction. All terms of order greater than three do not contribute significantly to the nonlinear polarization and, for this motive, can be neglected [108].

The nonlinear effects originated by the third-order susceptibility play an important role in optical fibre transmission. Due to the small field cross section, even if the total power carried by the fibre is relatively low, high field intensities are observed. Moreover, the efficiency of the nonlinear effects is enhanced due to the deployment of long fibre lengths, enabled by the low attenuation coefficient of optical fibres [109].

The fibre nonlinear effects can be divided in two different categories: elastic (related to the real part of $\chi^{(3)}$) and inelastic (related to the imaginary part of $\chi^{(3)}$) [108].

In the elastic effects, there is no energy transfer between the optical field and the dielectric medium [108]. These effects induce an intensity-dependent variation in the fibre refractive index, known as Kerr effect. The optical Kerr effect is an example of nonlinear refraction and consists in a self-induced effect in which the phase velocity of an optical wave depends on its own intensity. In silica fibres, the nonlinear refraction index is on the order of $10^{-20}\,\mathrm{m^2\,W^{-1}}$. The most relevant elastic effects are self phase modulation (SPM), cross phase modulation (XPM) and four wave mixing (FWM).

In the inelastic effects, a part of the optical field energy is transferred to the dielectric medium [108]. This effect is known as stimulated inelastic scattering and the most important inelastic effects are stimulated Raman scattering (SRS) and stimulated Brillouin scattering (SBS). SRS and SBS can be neglected if average powers per channel do not exceed 7 mW, assuming SSMF transmission [50]. This average power threshold is dictated by the SBS effect. In a multi-channel system, interaction between different optical channels does not increase the strength of the SBS effect. This means that if the power of each channel is below the SBS threshold, SBS will not occur [50]. Moreover, the SBS threshold does not change with the increase of the number of fibre spans [50]. In this work, the inelastic effects are not addressed as average powers per channel after the propagation along a few fibre spans are not expected to exceed 7 mW.

F.2.1 Nonlinear Schrödinger equation

The nonlinear Schrödinger equation (NLSE) is usually employed to evaluate the fibre nonlinear effects. It models the evolution of the linearly polarized optical field in the fibre along space and

time. When the scattering effects are negligible, the NLSE can be written as [108]:

$$\frac{\partial A(z,T)}{\partial z} = -\underbrace{\frac{\alpha}{2}A(z,T)}_{\text{attenuation}} - \underbrace{j\frac{\beta_2}{2}\frac{\partial^2 A(z,T)}{\partial T^2}}_{\text{dispersion}} + \underbrace{\frac{\beta_3}{6}\frac{\partial^3 A(z,T)}{\partial T^3}}_{\text{dispersion slope}} + \underbrace{j\gamma|A(z,T)|^2 A(z,T)}_{\text{nonlinearities}} \tag{F.7}$$

where $A(z,T)$ is the slowly varying envelope of the optical field, which depends on the propagation distance z and the time T measured in a retarded frame of reference moving at the group velocity v_g ($T = t - z/v_g = t - \beta_1 z$), and γ is the fibre nonlinearity coefficient. $A(z,T)$ is normalized such that $|A(z,T)|^2$ represents the instantaneous optical power [108].

The parameter γ combines the nonlinear refractive index coefficient, n_{NL} (which is related to $\chi^{(3)}$), and the effective core area of the fibre, A_e, in a single coefficient, and is given by:

$$\gamma = \frac{2\pi}{\lambda}\frac{n_{\text{NL}}}{A_e}. \tag{F.8}$$

Eq. F.8 shows that one way to minimize the influence of the nonlinear Kerr effects is by increasing A_e. In a large effective-area fibre, A_e is increased intentionally to reduce the impact of fibre nonlinearity [108]. For the SSMF, which has an effective core area of $8 \times 10^{-11}\,\text{m}^2$ and a nonlinear refractive index coefficient of $2.5 \times 10^{-20}\,\text{m}^2\,\text{W}^{-1}$, the parameter γ is approximately $1.3\,\text{W}^{-1}\text{km}^{-1}$ for a wavelength near 1550 nm. Because n_{NL} is very low, the propagation constant accounting the fibre nonlinearity effects is affected by a small variation. Nevertheless, due to very long interaction lengths provided by optical fibres, the effects caused by the nonlinear refractive index coefficient become significant [109].

Due to the fibre attenuation, the nonlinear interaction decreases as the propagation distance increases. This indicates that the majority of the nonlinear interaction occurs at the beginning of a fibre span. To denote this effect, it is useful to introduce the effective length of the fibre, which accounts for the distance over which the nonlinear effects interact along the fibre. The effective length of the fibre with length L_f is given by [108, 109]:

$$L_e = \frac{1 - \exp(-\alpha L_f)}{\alpha}. \tag{F.9}$$

For small fibres, $L_e \approx L_f$. For long fibres, the exponential term in Eq. F.9 tends to zero and the effective length can be approximated by the inverse of the optical fibre loss coefficient. For SSMF spans with $\alpha = 0.2\ \text{dB} \cdot \text{km}^{-1}$, the effective length is approximately 21.7 km.

The NLSE is a nonlinear partial differential equation that usually is not solved analytically [108, 109]. Therefore, a numerical approach is necessary to understand the nonlinear effects in optical

fibres. The most used numerical approach for the purpose of solving the NLSE is the split-step Fourier method (SSFM) [108]. It is useful to rearrange the NLSE in the following form:

$$\frac{\partial A(z,T)}{\partial z} = (\hat{D} + \hat{N})A(z,T) \tag{F.10}$$

with

$$\hat{D} = -\frac{\alpha}{2} - j\frac{\beta_2}{2}\frac{\partial^2}{\partial T^2} + \frac{\beta_3}{6}\frac{\partial^3}{\partial T^3} \tag{F.11}$$

and

$$\hat{N} = j\gamma|A(z,T)|^2 \tag{F.12}$$

where $\hat{D}$ is the operator that accounts for the dispersion and attenuation effects and $\hat{N}$ accounts for the fibre nonlinearity effects, such as SPM, XPM and FWM. Usually, GVD and the nonlinear effects act together along the fibre link. The SSFM consists in an approximate solution which assumes that, while propagating the slowly varying envelope over a small distance h, GVD and the nonlinear effects act independently [108]. Hence, the smaller the distance h, the better the SSFM accuracy. Propagation from z to $z + h$ is performed in two steps: 1) only nonlinearity is accounted ($\hat{D} = 0$); 2) only GVD is accounted ($\hat{N} = 0$). The slowly varying envelope at $z + h$ can then be expressed by [108]:

$$A(z + h, T) \approx \exp(h\hat{D}) \exp(h\hat{N})A(z,T). \tag{F.13}$$

In this work, the SSFM is used to solve Eq. F.10 numerically and segments with length of 100 meters are employed [81]. This means that if a fibre span has a length of 40 km, the SSFM considers 400 segments with 100 meters each.

F.2.2 Self-phase modulation and cross-phase modulation

When the nonlinear effects are non-negligible and single-channel transmission is considered, a self-induced phase shift on the optical field occurs during fibre propagation (does not involve other waves). This effect is called SPM. SPM does not change the signal shape but introduces a nonlinear phase which depends on the field itself. The maximum SPM-induced nonlinear phase shift occurs for $z = L_f$ and is given by [112]:

$$\phi_{\text{SPM}} = \gamma P_{in} L_e \tag{F.14}$$

where P_{in} is assumed to be constant. Combined with GVD, SPM leads to amplitude distortions and could lead to additional spectral broadening [108, 109].

If more than one optical channel is transmitted simultaneously in the fibre using wavelength division multiplexing (WDM), XPM occurs, which can be seen as a generalization of SPM. In WDM systems, the XPM-induced nonlinear phase shift for a specific channel depends not only on the power of that channel but also on the power of the other channels. The phase shift for the m-th channel of a WDM system with N_{ch} channels can be written as [112]:

$$\phi_{\mathrm{XPM}}(m) = \gamma P_m L_e + 2\gamma L_e \sum_{\substack{n=1 \\ n \neq m}}^{N_{ch}} P_n \tag{F.15}$$

where P_m and P_n are the average powers of the m-th and n-th WDM channels, respectively. The first term is related to SPM and the second term to XPM. Eq. F.15 reveals that XPM is twice as effective as SPM for the same power [110]. Eq. F.15 also shows that the total phase shift depends on the power of all WDM channels. Combined with positive GVD, the XPM-induced phase shift reduces due to the strong phase mismatch between the different channels and due to strong walk-off. The time difference related to the propagation distance of two different signals (which is caused by their different group velocities) is determined by the walk-off parameter $d_{n,m}$, which is defined as [50]:

$$d_{n,m} = \beta_1(\lambda_n) - \beta_1(\lambda_m) = \frac{1}{v_g(\lambda_n)} - \frac{1}{v_g(\lambda_m)} \tag{F.16}$$

where $v_g(\lambda_n)$ and $v_g(\lambda_m)$ are the group velocities at wavelengths λ_n and λ_m, respectively. For instance, let us assume SSMF propagation of two different signals and assume also that the red signal (higher wavelength) was injected into the fibre before the blue signal (lower wavelength). As the group velocity decreases when the wavelength increases, the blue signal moves faster [50]. As the SSMF distance increases, the red and blue signals start to overlap in time. It is assumed that the red and blue signals are different channels of a WDM system and, when they overlap in time, XPM occurs, leading to inter-channel crosstalk [50]. After a certain SSMF length known as walk-off length, the blue signal walks through the red signal completely. As XPM only occurs when signals overlap in time, the interaction between both signals ceases to occur after the walk-off length.

F.2.3 Four-wave mixing

FWM is another nonlinear phenomenon originated from the third-order susceptibility $\chi^{(3)}$. If three optical fields with frequencies ν_i, ν_j and ν_k co-propagate simultaneously in the optical fibre, $\chi^{(3)}$ generates another field with frequency ν_n that is related to ν_i, ν_j and ν_k in the following way: $\nu_n = \nu_i \pm \nu_j \pm \nu_k$ [86]. In practice, most of these combinations are not a problem because the phase-matching condition is hard to satisfy. Combinations that are often troublesome have the form $\nu_n = \nu_i + \nu_j - \nu_k$, which can be nearly phase-matched. The phase mismatch is given by $\Delta\beta = \beta(\nu_k) + \beta(\nu_n) - \beta(\nu_i) - \beta(\nu_j)$ and phase-matching is achieved when $\Delta\beta = 0$ (case with maximum FWM efficiency). FWM can cause severe signal degradation in WDM systems because the FWM products at the newly generated frequencies can overlap in frequency with existing WDM channels.

The power of the FWM product generated at the optical frequency ν_n is a function of the powers of the optical signals at the other optical frequencies responsible for the generation of the FWM product at frequency ν_n [87]. The average power of the FWM product at ν_n, $P_{\mathrm{FWM},n}$, is given by [112]:

$$P_{\mathrm{FWM},n} = (D_g \gamma L_e)^2 \cdot \exp(-\alpha L_f) \cdot P_{\mathrm{FWM},i} \cdot P_{\mathrm{FWM},j} \cdot P_{\mathrm{FWM},k} \cdot \eta_{\mathrm{FWM}} \tag{F.17}$$

where D_g is the degeneracy factor [equal to 1 for degenerate FWM ($\nu_i = \nu_j$) and 2 for non-degenerate FWM ($\nu_i \neq \nu_j$)], $P_{\mathrm{FWM},i}$, $P_{\mathrm{FWM},j}$ and $P_{\mathrm{FWM},k}$ are the average powers of the optical signals at frequencies ν_i, ν_j and ν_k, respectively, and η_{FWM} is the FWM efficiency that regulates the strength of the generated mixing product. If signal losses are compensated by an optical amplifier, the exponent in Eq. F.17 becomes unity. The FWM efficiency of a mixing product with frequency $\nu_n = \nu_i + \nu_j - \nu_k$ after the propagation along a fibre span with length L_f is given by [87, 88]:

$$\eta_{\mathrm{FWM}} = \frac{\alpha^2}{\alpha^2 + (\Delta\beta)^2} \left\{ 1 + \frac{4 \cdot \exp(-\alpha L_f) \cdot \sin^2\left(\Delta\beta \frac{L_f}{2}\right)}{[1 - \exp(-\alpha L_f)]^2} \right\} \tag{F.18}$$

with

$$\Delta\beta(\nu_i, \nu_j, \nu_k) = \frac{2\pi\lambda^2}{c}(\nu_i - \nu_k)(\nu_j - \nu_k) \left\{ D(\lambda) + [(\nu_i - \nu_k) + (\nu_j - \nu_k)] \frac{\lambda^2}{2c} \frac{\partial D(\lambda)}{\partial \lambda} \right\}. \tag{F.19}$$

For SSMF transmission, the FWM efficiency is relatively low due to the high GVD parameter. With high GVD, it is hard to satisfy the phase-matching condition, as different signals at

different frequencies have different group velocities. Another way to reduce the FWM efficiency is by increasing the WDM channel spacing or by spacing the channels unequally [109].

For the degenerate case ($\nu_n = 2\nu_i - \nu_k$), let us assume that $\nu_k = \nu_i + \Delta\nu_{ch}$ and $\nu_n = \nu_i - \Delta\nu_{ch}$, where $\Delta\nu_{ch}$ is the WDM channel spacing. Using Eq. F.3, the phase-mismatch simplifies to $\Delta\beta = \beta_2 \cdot (\Delta\nu_{ch})^2$ [112]. Two conclusions can be drawn from the degenerate phase-mismatch: i) the FWM process is phase-matched, that is, the FWM efficiency is maximum when $\beta_2 = 0$ (null first-order GVD); and ii) the lower the channel spacing, the higher the FWM efficiency and thus, the higher the performance degradation from FWM-induced inter-channel crosstalk.

For the non-degenerate case ($\nu_i \neq \nu_j$), let us assume that frequencies ν_i, ν_j and ν_k ($\nu_j > \nu_i$, $\Delta\nu_{ch} = \nu_j - \nu_i$ and $\nu_k = \nu_i - \Delta\nu_{ch}$) generate $\nu_n = \nu_j + \Delta\nu_{ch}$. Initially, ν_k was also generated from ν_j and ν_i ($\nu_k = 2\nu_i - \nu_j$). If these frequencies represent the central frequencies of WDM channels, ν_i and ν_j were responsible for the generation of two new frequencies ν_k and ν_n. For equally-spaced WDM channels, the FWM-induced generation of frequencies ν_k and ν_n result in inter-channel crosstalk for the channels that will be centred at ν_k and ν_n. A scheme of this FWM process involving ν_i, ν_j, ν_k and ν_n is shown in Fig. F.3.

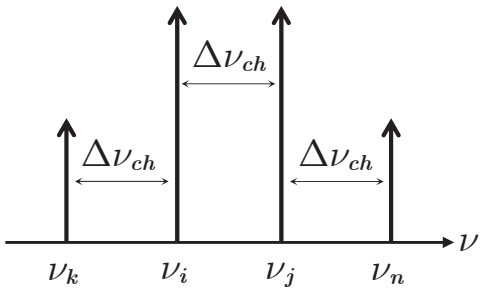

Figure F.3: Four-wave mixing principle.

Appendix G

Single-band and single-channel nonlinear transmission

In this appendix, as a preliminary study of the nonlinear crosstalk with virtual carrier (VC)-assisted orthogonal frequency-division multiplexing (OFDM) signals, the impact of the nonlinear fibre effects on the performance of VC-assisted direct-detection (DD) single sideband (SSB) multi-band (MB)-OFDM metro networks is evaluated through numerical simulation after the transmission of a set of pairs band-VC. Distortion powers with single pair and with five pairs band-VC are compared. Emphasis is placed on the evaluation of the average power limit for different number of fibre spans. The number of independent signal runs required to achieve accurate performance estimates is also assessed. A complete study of the nonlinear crosstalk considering several wavelength division multiplexing (WDM) channels (with each one carrying a MB-OFDM signal) is performed in chapter 4.

The work presented along this appendix is also published in [70].

G.1 System and parameters description

The system considered to analyse the impact of the nonlinear fibre effects on the performance of VC-assisted DD-SSB-MB-OFDM metro networks is illustrated in Fig. G.1. The system of Fig. G.1 can be seen as a simplified metro network with fibre transmission. The following simplifications are made: 1) optical and electrical noise are neglected in order to focus on the impact of the crosstalk due to the nonlinear transmission along the fibre; 2) each network node is represented by an erbium doped fibre amplifier (EDFA); 3) the optical distribution network

(ODN) is not considered as the node performing the extraction operation is directly connected to the optical network unit (ONU); and 4) transmission of a single optical channel carrying one SSB-MB-OFDM signal is employed.

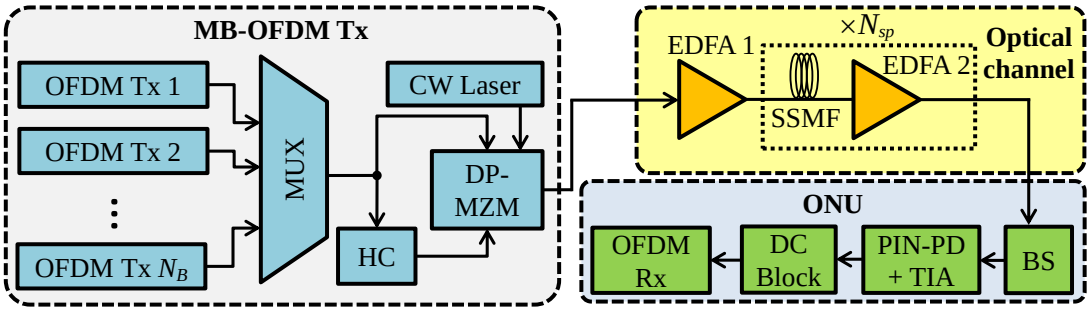

Figure G.1: Block diagram of the simplified VC-assisted DD-SSB-MB-OFDM metro network.

Each OFDM band is composed by 128 OFDM subcarriers mapped using 32-quadrature amplitude modulation (QAM); as a consequence, the bandwidth of each band, B_w, is 2.18 GHz. The overall bit rate of each band is 10.9 Gb/s and the Hilbert transform (HT) is obtained using a hybrid coupler (HC) (referred as HC1 in Fig. 3.5). The frequency disposition of the OFDM bands and VCs is similar to the one presented in Fig. 2.4. A virtual carrier-to-band power ratio (VBPR) of 9 dB is used to each pair band-VC to ensure that the signal-signal beat interference (SSBI) mitigation is performed correctly. The central frequencies of adjacent bands are separated in frequency by $\Delta f_b = 3.125$ GHz. A central frequency of the first band of 1.9 GHz is considered (as explained in section 3.3). The virtual carrier-to-band gap (VBG) considered for all pairs band-VC is proportional to the subcarrier spacing and is 34 MHz (see Tab. 3.1). Setting the same VBGs for all pairs band-VC guarantees that adjacent VCs are also separated in frequency by Δf_v equal to 3.125 GHz. A modulation index (MI) of 5% is employed, as considered in section 3.4.

EDFA 1 dictates the optical power level at the standard single mode fibre (SSMF) input. Propagation along the SSMF accounts for the effects of self phase modulation (SPM), cross phase modulation (XPM) and four wave mixing (FWM). The SSMF parameters are shown in Tab. 2.2. EDFA 2 compensates the losses of the preceding SSMF span. The set of N_{sp} loss-compensated SSMF spans represents the connections between the nodes of a metro network. Each SSMF span has 40-km length. At the ONU, the band selector (BS) is a second-order super-Gaussian (SG) optical filter. When selecting a certain pair band-VC, the BS is centred at a frequency 150 MHz higher than the frequency of the middle of that pair band-VC, and has a -3 dB bandwidth 150 MHz larger than the bandwidth of each OFDM band; these parameters (BS bandwidth and BS central frequency) guarantee minimum inter-band crosstalk due to non-ideal filtering.

G.2 Results and discussion

In this section, the performance of the MB-OFDM system in the presence of fibre dispersion and nonlinearity is evaluated through numerical simulation, and using the error vector magnitude (EVM) as figure of merit. The performance with nonlinear transmission is evaluated numerically using the split-step Fourier method (SSFM) with a fibre step size of 100 meters. Three different analysis are performed: 1) linear and nonlinear fibre regime with single-band (SB) transmission; 2) nonlinear fibre regime considering MB transmission, with and without time-synchronization between bands at the first span input; and 3) linear and nonlinear fibre transmission for a MB-OFDM signal with 5 bands (MB case).

G.2.1 Single-band nonlinear transmission

Fig. G.2 shows the EVM as a function of the average power at the SSMF input, P_{in}, for the SB case with linear and nonlinear transmission along the fibre, with different number of SSMF spans. Fig. G.2 shows that the EVM penalty while increasing the average power with linear transmission ($\gamma = 0$, only fibre dispersion is accounted) for SSB systems, is negligible. With nonlinear transmission ($\gamma = 1.3\ \mathrm{W}^{-1} \cdot \mathrm{km}^{-1}$), the EVM penalty increases rapidly and it is higher for a higher number of SSMF spans. The nonlinear transmission penalty is attributed mainly to intra-band FWM, as strong FWM occurs when transmitting dozens of narrowly-spaced subcarriers, which are interpreted as closely-spaced optical channels [84]. Inspection of Fig. G.2 also reveals that, to achieve the same performance after doubling the number of SSMF spans, the average power at the fibre input has to decrease 3 dB, which is in accordance with what is shown in [84]. Taking into account that an average EVM of -19.5 dB corresponds to approximately an average bit error ratio (BER) of 10^{-3} for 32-QAM systems, and assuming a margin of 1.5 dB to account for other system impairments, the highest acceptable EVM due to fibre transmission is assumed as -21 dB. Hence, the maximum average power allowed is around 10 dBm for 1 span and decreases to 2 dBm for 6 spans.

G.2.2 Single-channel multi-band nonlinear transmission

The following study aims at analysing the dependence of the nonlinear effects efficiency on the time-synchronization between different bands at the first span input. Fig. G.3 shows the EVM as a function of the average power at the SSMF input, for 32 independent signal runs of one

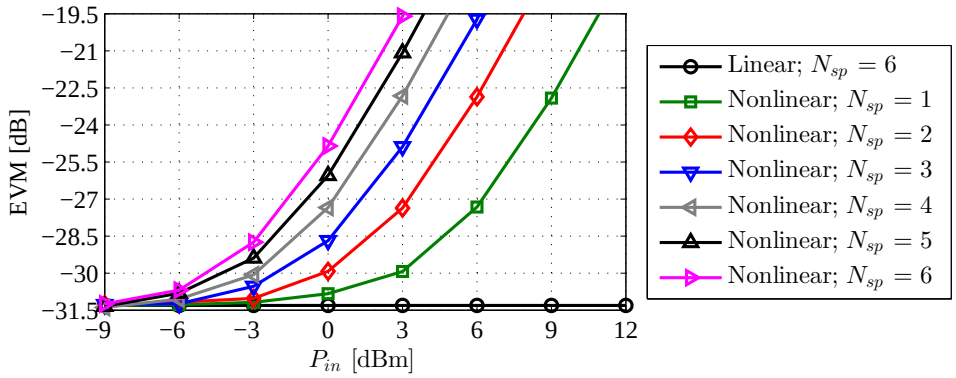

Figure G.2: EVM as a function of the average power at the SSMF input, for the SB case, with different number of spans and for linear and nonlinear SSMF transmission.

optical channel with a MB-OFDM signal with 5 bands. For each run, random delays and random binary sequences between OFDM bands are considered. EVM results are shown for bands 1 and 3 and for 3 and 6 spans. The average EVM of all the runs and EVMs where all the OFDM bands are time-synchronized at the first span input are also shown. Fig. G.3 shows that, from run to run, the EVM results vary considerably, especially when the degradation due to fibre nonlinearity is substantial. Therefore, to obtain accurate EVM estimates, the average EVM over the independent signal runs has to be performed. Inspection of Fig. G.3 shows that the average EVM value is usually lower than the EVM where all the OFDM bands are synchronized at the first span input, and that the difference between them reduces as the number of spans increases. Moreover, the time-synchronized case corresponds to the worst case EVM for lower number of spans, which indicates that synchronizing all the OFDM bands at the first span input corresponds to the case where the nonlinear effects are more efficient. With the increase of the number of spans, the total fibre dispersion also increases, and its interplay with the nonlinear effects causes a reduction between the EVM differences from run to run. Likewise, fibre dispersion induces synchronization reduction between the OFDM bands after several spans, which justifies why the synchronized case no longer presents the worst case EVM when $N_{sp} = 6$, as it can be verified in Fig. G.3(d). Fig. G.3 also reveals that the average EVM for low average powers is 3 to 4 dB worse than the EVM for low average powers of the SB case shown in Fig. G.2; this difference is attributed to the inter-band crosstalk due to the non-ideal filtering of the BS. Inspection of Fig. G.3 shows also a considerable EVM degradation in the MB case with increasing average power, when compared with the SB case; this is attributed to the presence of inter-band nonlinear effects.

As the average EVM over the independent signal runs has to be performed to achieve accurate EVM estimates, the minimum required number of independent signal runs has to be assessed.

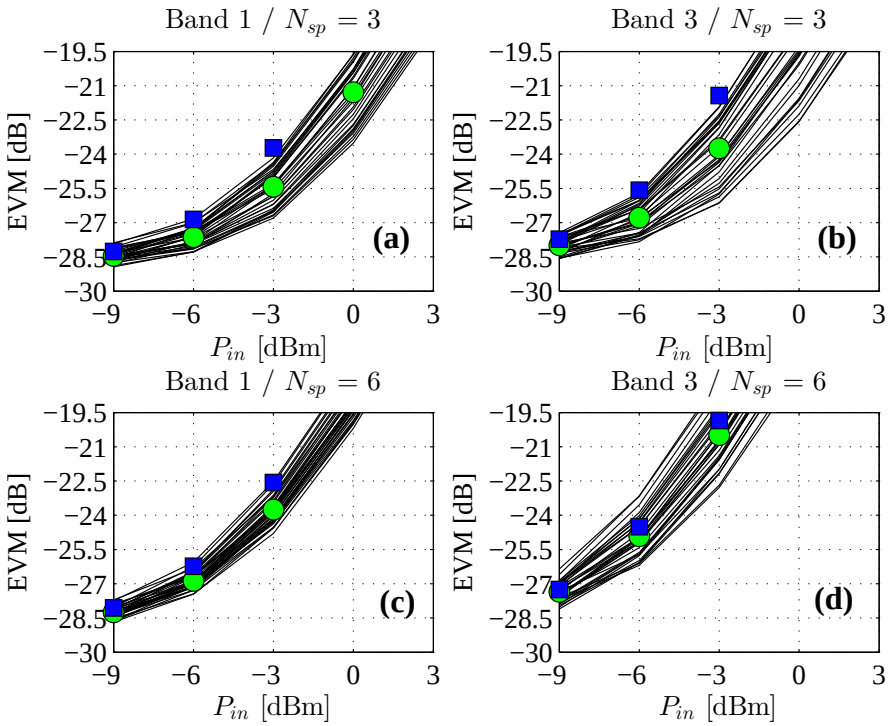

Figure G.3: EVM as a function of the average power at the SSMF input, for 32 independent signal runs of one channel with a MB-OFDM signal with 5 bands. EVM results are shown for (a) band 1 and $N_{sp} = 3$, (b) band 3 and $N_{sp} = 3$, (c) band 1 and $N_{sp} = 6$ and (d) band 3 and $N_{sp} = 6$. Average EVM of all the runs (○) and EVMs where all the OFDM bands are time-synchronized at the first span input (□) are also shown.

Fig. G.4 depicts the average EVM obtained over independent signal runs, for all bands of the MB-OFDM signal, when considering different number of fibre spans and average powers at the SSMF input. Fig. G.4 shows that, for the number of spans and average powers at the SSMF input considered, the average over 16 independent signal runs is enough to guarantee an EVM discrepancy not exceeding 0.5 dB from the average EVM obtained with 32 runs. These conclusions hold for 2, 4 and 6 SSMF spans and for average powers at the SSMF input between -9 and 6 dBm.

Fig. G.5 shows the average EVM over 32 independent signal runs for bands 1, 3 and 5 of a MB-OFDM signal with 5 bands, as a function of the average power at the SSMF input, for different number of spans and for linear and nonlinear transmission along the SSMF. Fig. G.5 shows that, with linear transmission, while increasing the average power at the SSMF input, the degradation is negligible, whereas with nonlinear transmission, the EVM degrades considerably with the average power increase. The maximum allowed average power (that is, when an EVM of -21 dB is reached) is set by the bands that suffer the most from inter-band crosstalk: for band 3 is around 3 dBm for 1 span and decreases to -2.5 dBm for 6 spans. Comparing the maximum average powers of the SB and MB cases, the power reduction for the MB case is 7 dB

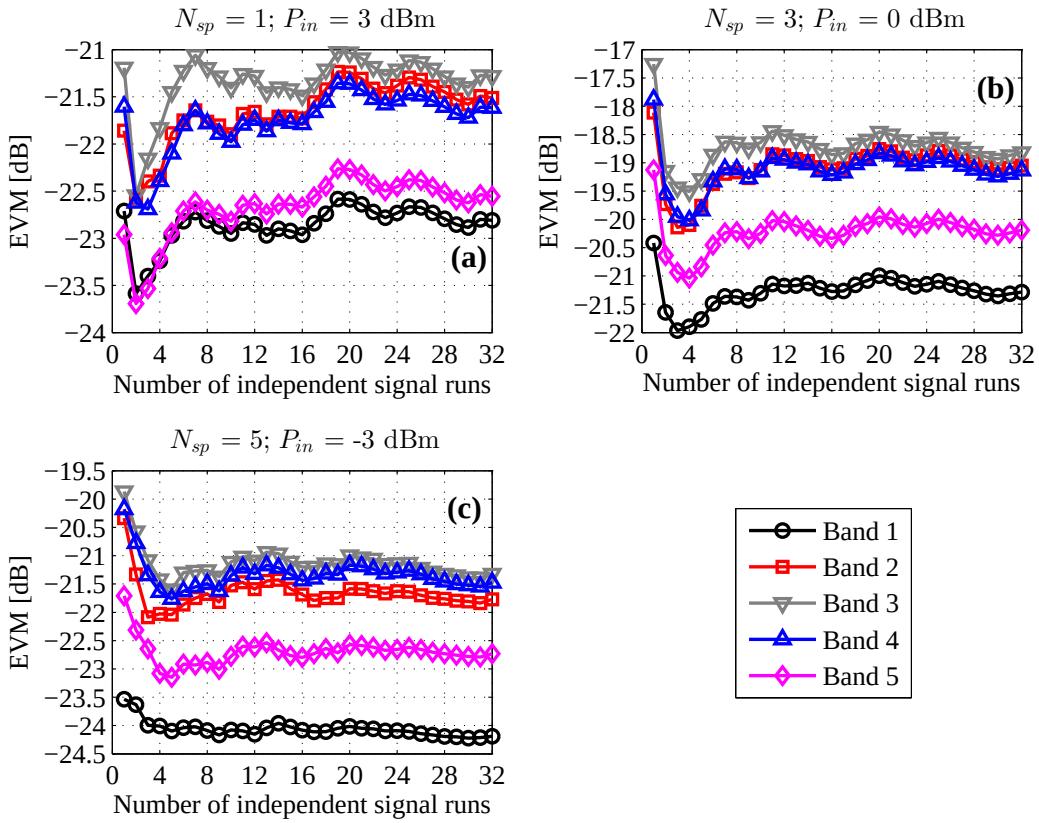

Figure G.4: Average EVM over independent signal runs, for all 5 bands of the MB-OFDM signal. Three different cases are shown: (a) $N_{sp} = 1$ and $P_{in} = 3$ dBm, (b) $N_{sp} = 3$ and $P_{in} = 0$ dBm and (c) $N_{sp} = 5$ and $P_{in} = -3$ dBm.

and 4.5 dB for 1 span and 6 spans, respectively. These power reductions are attributed to the presence of inter-band nonlinear effects, such as inter-band FWM. A lower power reduction with increasing number of spans indicates that the effectiveness of the nonlinear effects decreases with the increase of fibre dispersion. The higher accumulated dispersion increases the misalignment between symbols of different bands from one span to the other, reducing the strength of the inter-band nonlinear impairments. A direct consequence of this effect is that, with MB, in order to achieve the same EVM while doubling the number of spans, the required decrease of the average power at the SSMF input is less than 3 dB, which is different from the SB case which requires an average power decrease of 3 dB.

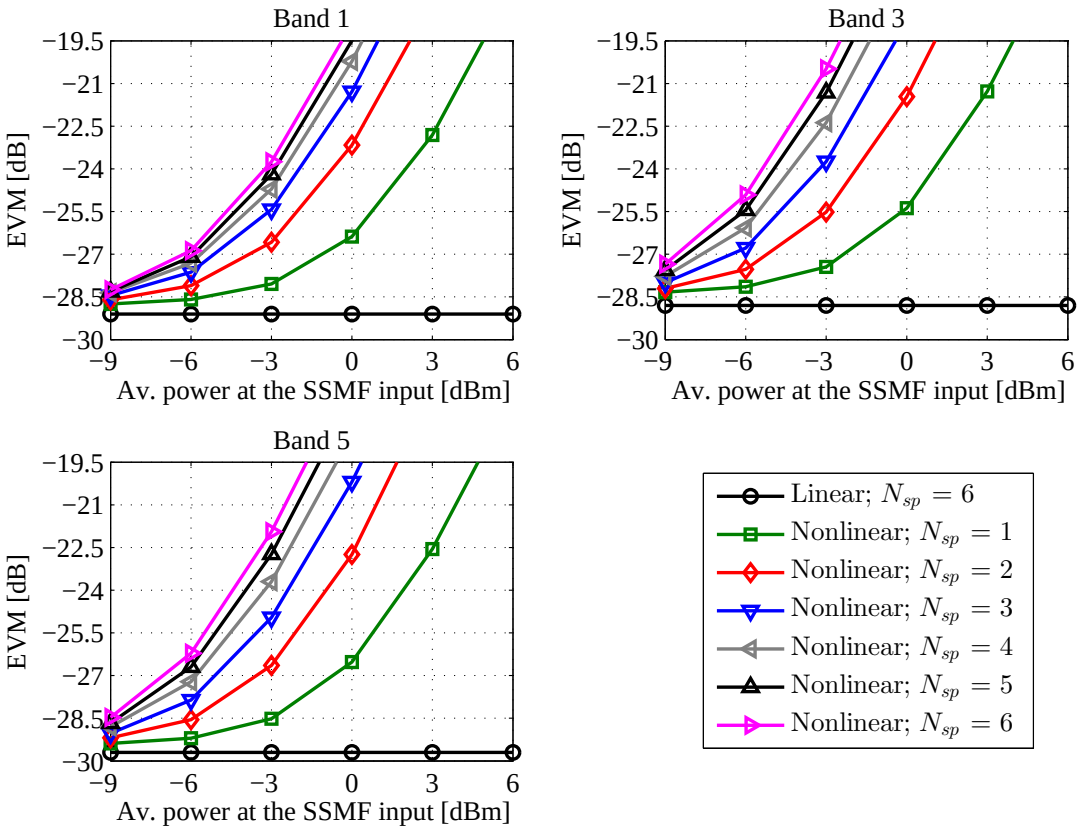

Figure G.5: Average EVM over 32 independent signal runs, for bands 1, 3 and 5 of a 5-band MB-OFDM signal, as a function of the average power at the SSMF input, for different number of spans and for linear and nonlinear transmission.

G.3 Conclusions

As MB-OFDM signals are composed by tight-spaced subcarriers and closely-spaced OFDM bands, the performance is limited by intra-band and inter-band FWM, which lead to high FWM efficiencies. Results have shown that an average over 16 independent signal runs is enough to guarantee an EVM discrepancy not exceeding 0.5 dB from the average EVM obtained with 32 independent signal runs, when nonlinear fibre effects are dominant. It was also verified that inter-band crosstalk due to nonlinear transmission of 5 bands over 240 km of SSMF limits the average power at the fibre input to levels not exceeding −2.5 dBm.

References

[1] Cisco. "The Zettabyte Era: Trends and Analysis". (June 2017) [Online]. Available: `https://www.cisco.com/c/en/us/solutions/collateral/service-provider/visual-networking-index-vni/vni-hyperconnectivity-wp.pdf`. Accessed on: Jan. 19, 2018.

[2] D. Qian, M. Huang, E. Ip, Y. Huang, Y. Shao, J. Hu, and T. Wang, "101.7 Tbit/s (370×294-Gb/s) PDM-128QAM-OFDM transmission over 3×55-km SSMF using pilot-based phase noise mitigation," in Proc. *Opt. Fiber Conf.*, paper PDPB5, Los Angeles, USA, Mar. 2011.

[3] J. Sakaguchi, Y. Awaji, N. Wada, A. Kanno, T. Kawanishi, T. Hayashi, T. Taru, T. Kobayashi, and M. Watanabe, "Space division multiplexed transmission of 109-Tb/s data signals using homogeneous seven-core fiber," *IEEE/OSA J. Lightw. Technol.*, vol. 30, no. 4, pp. 658-665, Feb. 2012.

[4] J. Senior, *Optical Fiber Communications - Principles and Practice*, 3rd ed. Essex, England, UK: Prentice Hall, 2009.

[5] L. Kazovsky, W. Shaw, D. Gutierrez, N. Cheng, and S. Wong, "Next-generation optical access networks," *IEEE/OSA J. Lightw. Technol.*, vol. 25, no. 11, pp. 3428-3442, Nov. 2007.

[6] S. Pato, N. Borges, and J. Pedro, "Capacity prospects of future high density metro-access networks," in Proc. *Int. Conf. Transp. Opt. Netw.*, Cartagena, Spain, 2013, paper We.B3.3.

[7] M. Ruffini, "Multidimensional convergence in future 5G networks," *IEEE/OSA J. Lightw. Technol.*, vol. 35, no. 3, pp. 535-549, Feb. 2017.

[8] T. Pfeiffer, "Converged heterogeneous optical metro-access networks," in Proc. *Eur. Conf. Opt. Commun.*, Torino, Italy, 2010, paper Tu.5.B.1.

[9] T. Alves, L. Mendes, and A. Cartaxo, "High granularity multiband OFDM virtual carrier-assisted direct-detection metro networks," *IEEE/OSA J. Lightw. Technol.*, vol. 33, no. 1, pp. 42-54, Jan. 2015.

[10] R. Davey, D. Grossman, M. Wiech, D. Payne, D. Nesset, A. Kelly, A. Rafael, S. Appathurai, and S. Yang, "Long-reach passive optical networks", *IEEE/OSA J. Lightw. Technol.*, vol. 27, no. 3, pp. 273-291, Feb. 2009.

[11] N. Cvijetic, M. Huang, E. Ip, Y. Huang, D. Qian, and T. Wang, "1.2 Tb/s symmetric WDM-OFDMA-PON over 90km straight SSMF and 1:32 passive split with digitally-selective ONUs and coherent receiver OLT", in Proc. *Opt. Fiber Conf.*, paper PDPD7, Los Angeles, USA, Mar. 2011.

[12] J. Altabas, D. Izquierdo, J. Lazaro, A. Lerin, F. Sotelo, and I. Garces, "1 Gbps full-duplex links for ultra-dense-WDM 6.25 GHz frequency slots in optical metro-access networks," *OSA Opt. Exp.*, vol. 24, no. 1, pp. 555-565, Jan. 2016.

[13] W. Shaw, G. Kalogerakis, S. Wong, Y. Hsueh, N. Cheng, S. Yen, M. Marhic, and L. Kazovsky, "MARIN: Metro-access ring integrated network," in Proc. *Global Telecommun. Conf.*, San Francisco, CA, 2006, pp. 1-5. doi: 10.1109/GLOCOM.2006.371

[14] H. Rohde and S. Randel, "Project PIEMAN: a European approach to a symmetrical 10 Gbit/s, 100 km, 32 λ and 512 split PON," *SPIE Proceedings*, Vol. 6353, Sept. 2006. doi: 10.1117/12.688820

[15] J. Prat, J. Lazaro, P. Chanclou, R. Soila, A. Gallardo, A. Teixeira, G. TosiBeleffi, and I. Tomkos, "Results from EU project SARDANA on 10G extended reach WDM PONs," in Proc. *Opt. Fiber Conf.*, San Diego, CA, 2010, paper OThG5.

[16] C. Zhang, Q. Zhang, C. Chen, N. Jiang, D. Liu, K. Qiu, S. Liu, and B. Wu, "Metro-access integrated network based on optical OFDMA with dynamic sub-carrier allocation and power distribution," *OSA Opt. Exp.*, vol. 21, no. 2, pp. 2474-2479, Jan. 2013.

[17] C. Zhang, W. Jin, Q. Zhang, C. Chen, and K. Qiu, "Polarization multiplexed OFDM band interleaving enabled metro-access integrated networks," *Opt. Fiber Technol.*, vol. 20, no. 2, pp. 130-136, Mar. 2014.

[18] N. Cvijetic, "OFDM for next-generation optical access networks," *IEEE/OSA J. Lightw. Technol.*, vol. 30, no. 4, pp. 384-398, Feb. 2012.

[19] J. Armstrong, "OFDM for optical communications," *IEEE/OSA J. Lightw. Technol.*, vol. 27, no. 3, pp. 189-204, Feb. 2009.

[20] B. Schmidt, A. Lowery, and J. Armstrong, "Experimental demonstrations of electronic dispersion compensation for long-haul transmission using direct-detection optical OFDM," *IEEE/OSA J. Lightw. Technol.*, vol. 26, no. 1, pp. 196-203, Jan. 2008.

[21] R. Llorente, T. Alves, M. Morant, M. Beltran, J. Perez, A. Cartaxo, and J. Marti, "Ultra-wideband radio signals distribution in FTTH networks," *IEEE Photon. Technol. Lett.*, vol. 20, no. 11, pp. 945-947, Jun. 2008.

[22] C. Lin, Y. Lin, J. Chen, S. Dai, P. Shih, P. Peng, and S. Chi, "Optical direct-detection OFDM signal generation for radio-over-fibre link using frequency doubling scheme with carrier supression," *OSA Opt. Exp.*, vol. 16, no. 9, pp. 6056-6063, Apr. 2008.

[23] J. Tang, P. Lane, and K. Shore, "30 Gbit/s transmission over 40 km directly modulated DFB laser-based SMF links without optical amplification and dispersion compensation for VSR and metro applications," in Proc. *Opt. Fiber Conf.*, paper JThB8, Anaheim, USA, Mar. 2006.

[24] B. Schmidt, A. Lowery, and J. Armstrong, "Experimental demonstration of 20 Gbit/s direct-detection optical OFDM and 12 Gbit/s with a colorless transmitter," in Proc. *Opt. Fiber Conf.*, paper PDP18, Anaheim, USA, Mar. 2007.

[25] S. Blouza, J. Karaki, N. Brochier, E. Rouzic, E. Pincemin, and B. Cousin, "Multi-band OFDM for optical networking," in Proc. *IEEE Int. Conf. Comput. Tool*, Lisbon, 2011. doi: 10.1109/EUROCON.2011.5929191

[26] K. Christodoulopoulos, I. Tomkos, and E. Varvarigos, "Elastic bandwidth allocation in flexible OFDM-based optical networks," *IEEE/OSA J. Lightw. Technol.*, vol. 29, no. 9, pp. 1354-1366, May 2011.

[27] R. Dischler, F. Buchali, and A. Klekamp, "Demonstration of bit rate variable ROADM functionality on an optical OFDM superchannel," in Proc. *Opt. Fiber Conf.*, paper OTuM7, San Diego, USA, Mar. 2010.

[28] W. Wei, D. Xu, D. Qian, P. Ji, T. Wang, and C. Qiao, "Demonstration of an optical OFDMA metro ring network with dynamic sub-carrier allocation," in Proc. *Opt. Fiber Conf.*, paper NTuA3, San Diego, USA, Feb. 2009.

[29] A. Lowery, L. Du, and J. Armstrong, "Orthogonal frequency division multiplexing for adaptive dispersion compensation in long haul WDM systems," in Proc. *Opt. Fiber Conf.*, Anaheim, CA, 2006, paper PDP39.

[30] W. Shieh, "OFDM for flexible high-speed optical networks," *IEEE/OSA J. Lightw. Technol.*, vol. 29, no. 10, pp. 1560-1577, May 2011.

[31] N. Cvijetic, M. Huang, E. Ip, Y. Shao, Y. Huang, M. Cvijetic, and T. Wang, "1.92 Tb/s coherent DWDM-OFDM-PON with no high-speed ONU-side electronics over 100 km SSMF and 1:64 passive split", *OSA Opt. Exp.*, vol. 19, no. 24, pp. 24540-24545, Nov. 2011.

[32] W. Peng, B. Zhang, K. Feng, X. Wu, A. Willner, and S. Chi, "Spectrally efficient direct-detection OFDM transmission incorporating a tunable frequency gap and an iterative detection techniques", *IEEE/OSA J. Lightw. Technol.*, vol. 27, no. 24, pp. 5723-5735, Dec. 2009.

[33] S. Kim, K. Seo, and J. Lee, "Spectral efficiencies of channel-interleaved bidirectional and unidirectional ultradense WDM for metro applications," *IEEE/OSA J. Lightw. Technol.*, vol. 30, no. 2, pp. 229-233, Jan. 2012.

[34] Z. Li, X. Xiao, T. Gui, Q. Yang, R. Hu, Z. He, M. Luo, C. Li, X. Zhang, D. Xue, S. You, and S. Yu, "432-Gb/s direct-detection optical OFDM superchannel transmission over 3040-km SSMF," *IEEE Photon. Technol. Lett.*, vol. 25, no. 15, pp. 1524-1526, Aug. 2013.

[35] T. Alves and A. Cartaxo, "Power budget of ultra-dense virtual-carrier-assisted DD MB-OFDM next-generation PON," *IEEE Photon. Technol. Lett.*, vol. 28, no. 13, pp. 1406-1409, Jul. 2016.

[36] T. Alves and A. Cartaxo, "100 Gb/s DD-MB-OFDM metro network with 11 Gb/s granularity and 2.85 GHz receiver," *IEEE Photon. Technol. Lett.*, vol. 27, no. 24, pp. 2551-2554, Dec. 2015.

[37] P. Cruz, T. Alves, and A. Cartaxo, "Theoretical analysis of the four-wave mixing effect in virtual carrier-assisted DD MB-OFDM ultradense WDM metropolitan networks," *IEEE/OSA J. Lightw. Technol.*, vol. 34, no. 23, pp. 5401-5411, Dec. 2016.

[38] W. Peng, I. Morita, H. Takahashi, and T. Tsuritani, "Transmission of high-speed (>100 Gb/s) direct-detection optical OFDM superchannel," *IEEE/OSA J. Lightw. Technol.*, vol. 30, no. 12, pp. 2025-2034, Jun. 2012.

[39] X. Zhang, Z. Li, C. Li, M. Luo, H. Li, C. Li, Q. Yang, and S. Yu, "Transmission of 100-Gb/s DDO-OFDM/OQAM over 320-km SSMF with a single photodiode," *OSA Opt. Exp.*, vol. 22, no. 10, pp. 12079-12086, May 2014.

[40] J. Yan, Y. Chen, K. Shen, and K. Feng, "A 1:128 high splitting ratio long reach PON based on a simple receiving design for ONU with 120-Gb/s double-sided multiband DDO-OFDM signal," in Proc. *Opt. Fiber Conf.*, Anaheim, USA, Mar. 2013, Paper JW2A.74.

[41] E. Giacoumidis, J. Karaki, E. Pincemin, C. Gosset, R. Bidan, E. Awwad, and Y. Jaouën, "100 Gb/s coherent optical polarization multiplexed multi-band-OFDM (MB-OFDM) transmission for long-haul applications," in Proc. *Int. Conf. Transp. Opt. Netw.*, Coventry, England, Jul. 2012, Paper We.B1.2.

[42] E. Pincemin, M. Song, J. Karaki, O. Zia-Chahabi, T. Guillossou, D. Grot, G. Thouenon, C. Betoule, R. Clavier, A. Poudoulec, M. Van der Keur, Y. Jaouën, R. Le Bidan, T. Le Gall, P. Gravey, M. Morvan, B. Dumas-Feris, M. Moulinard, and G. Froc, "Multi-band OFDM transmission at 100 Gbps with sub-band optical switching," *IEEE/OSA J. Lightw. Technol.*, vol. 32, no. 12, pp. 2202–2219, Jun. 2014.

[43] I. Cano, X. Escayola, P. Schindler, M. Santos, V. Polo, J. Leuthold, I. Tomkos, and J. Prat, "Experimental demonstration of a statistical OFDM-PON with multiband ONUs and elastic bandwidth allocation," *IEEE/OSA J. Opt. Commun. Netw.*, vol. 7, no. 1, pp. A73–A79, Jan. 2015.

[44] T. Alves, A. Alberto, and A. Cartaxo, "Direct-detection multi-band OFDM metro networks employing virtual carriers and low receiver bandwidth," in Proc. *Opt. Fiber Conf.*, paper Tu3G5, San Francisco, USA, Mar. 2014.

[45] A. Li, D. Che, X. Chen, Q. Hu, Y. Wang, and W. Shieh, "61 Gbits/s direct-detection optical OFDM based on blockwise signal phase switching with signal-to-signal beat noise cancellation", *OSA Opt. Lett.*, vol. 38, no. 14, pp. 2614-2616, Jul. 2013.

[46] R. Maher, T. Xu, L. Galdino, M. Sato, A. Alvarado, K. Shi, S. Savory, B. Thomsen, R. Killey, and P. Bayvel, "Spectrally shaped DP-16QAM super-channel transmission with multi-channel digital back-propagation," *Nature Sci. Rep.*, vol. 5, no. 8214, pp. 1-8, Feb. 2015. doi: 10.1038/srep08214

[47] X. Liu, A. Chraplyvy, P. Winzer, R. Tkach, and S. Chandrasekhar, "Phase-conjugated twin waves for communication beyond the Kerr nonlinearity limit," *Nature Photon.*, vol. 7, pp. 560-568, 2013.

[48] W. Shieh and I. Djordjevic, *OFDM for Optical Communications*, 2nd ed. San Diego, CA, USA: Academic Press, 2010.

[49] R. Ramaswami and K. Sivarajan, *Optical Networks: A Practical Perspective*, 2nd ed. San Diego, CA, USA: Academic Press, 2002.

[50] T. Schneider, *Nonlinear Optics in Telecommunications*, 1st ed. New York, NY, USA: Springer, 2004.

[51] A. Napoli, Z. Maalej, V. Sleiffer, M. Kuschnerov, D. Rafique, E. Timmers, B. Spinnler, T. Rahman, L. Coelho, and N. Hanik, "Reduced complexity digital back-propagation methods for optical communication systems," *IEEE/OSA J. Lightw. Technol.*, vol. 26, no. 20, pp. 3416–3425, Oct. 2008.

[52] E. Ip and J. Kahn, "Compensation of dispersion and nonlinear impairments using digital backpropagation," *IEEE/OSA J. Lightw. Technol.*, vol. 26, no. 20, pp. 3416–3425, Oct. 2008.

[53] D. Rafique, J. Zhao, and A. Ellis, "Digital back-propagation for spectrally efficient WDM 112 Gbit/s PM m-ary QAM transmission," *OSA Opt. Exp.*, vol. 19, no. 6, pp. 5219-5224, Mar. 2011.

[54] G. Gao, X. Chen, and W. Shieh, "Limitation of fiber nonlinearity compensation using digital back propagation in the presence of PMD," in Proc. *Opt. Fiber Conf.*, Los Angeles, CA, 2012, Paper OM3A.5.

[55] D. Rafique and A. Ellis, "Nonlinearity compensation via spectral inversion and digital back-propagation: a practical approach," in Proc. *Opt. Fiber Conf.*, Los Angeles, CA, 2012, Paper OM3A.1.

[56] I. Sackey, F. Da Ros, J. Fischer, T. Richter, M. Jazayerifar, C. Peucheret, K. Petermann, and C. Schubert, "Kerr nonlinearity mitigation: mid-link spectral inversion versus digital backpropagation in 5×28-GBd PDM 16-QAM signal transmission," *IEEE/OSA J. Lightw. Technol.*, vol. 33, no. 9, pp. 1821-1827, May 2015.

[57] M. Morshed, L. Du, and A. Lowery, "Mid-span spectral inversion for coherent optical OFDM systems: fundamental limits to performance," *IEEE/OSA J. Lightw. Technol.*, vol. 31, no. 1, pp. 58-66, Jan. 2013.

[58] S. Le, E. Giacoumidis, N. Doran, A. Ellis, and S. Turitsyn, "Phase-conjugated subcarrier coding for fibre nonlinearity mitigation in CO-OFDM transmission," in Proc. *Eur. Conf. Opt. Commun.*, Cannes, France, 2014, Paper We.3.3.2.

[59] H. Eliasson, P. Johannisson, M. Karlsson, and P. Andrekson, "Mitigation of nonlinearities using conjugate data repetition," *OSA Opt. Exp.*, vol. 23, no. 3, pp. 2392-2402, Feb. 2015.

[60] L. Du and A. Lowery, "Pilot-based XPM nonlinearity compensator for CO-OFDM systems," *OSA Opt. Exp.*, vol. 19, no. 26, pp. B862-B867, Dec. 2011.

[61] L. Du and A. Lowery, "Fiber nonlinearity precompensation for long-haul links using direct-detection optical OFDM," *OSA Opt. Exp.*, vol. 16, no. 9, pp. 6209-6215, Apr. 2008.

[62] P. Cruz, T. Alves, and A. Cartaxo, "Experimental assessment of 10 Gbit/s SSB OFDM IM-DD systems performance employing raised-cosine based symbol precoding," *IEEE/OSA J. Lightw. Technol.*, vol. 32, no. 8, pp. 1631-1638, Apr. 2014.

[63] P. Cruz, T. Alves, and A. Cartaxo, "Loss budget of ultra-dense 10 Gb/s per-user guaranteed direct-detection MB-OFDM metro-access networks," in Proc. *Int. Conf. Transp. Opt. Netw.*, Budapest, Hungary, Jul. 2015, Paper Tu.B1.4.

[64] P. Cruz, T. Alves, and A. Cartaxo, "Virtual carrier-assisted DD-MB-OFDM schemes for UDWDM metro-access networks with improved tolerance to four-wave mixing," *IEEE/OSA J. Lightw. Technol.*, vol. 35, no. 20, pp. 4468-4478, Oct. 2017.

[65] P. Cruz, T. Alves, and A. Cartaxo, "Analytical modeling for performance evaluation of ASE noise-impaired direct-detection single-sideband multi-band optical OFDM systems," in Proc. *Int. Conf. on Photon., Optics and Laser Technol.*, pp. 134-141, Lisbon, Portugal, Jan. 2014.

[66] P. Cruz, T. Alves, and A. Cartaxo, "Performance evaluation of optical noise-impaired multi-band OFDM systems through analytical modeling," Chapter in Proc. *Photoptics 2014 - Proceedings of the 2nd International Conference on Photonics, Optics and Laser Technology - Revised Selected Papers*, Eds. Paulo Ribeiro and Maria Raposo, Springer Proceedings in Physics, vol. 177, Springer International Publishing, Switzerland, 2016.

[67] P. Cruz, T. Alves, and A. Cartaxo, "Analytical modelling for performance evaluation of distortion-impaired direct-detection single-sideband optical OFDM systems employing virtual-carriers," in Proc. *Int. Conf. Transp. Opt. Netw.*, paper We.A1.6, Graz, Austria, Jul. 2014.

[68] L. Mendes, "Optimization of the degradation induced by the MZM and PIN nonlinear effects in MB-OFDM metropolitan networks," M. Sc. thesis in Electrical and Computer Engineering, Universidade de Lisboa, Instituto Superior Técnico, Lisbon, 2014.

[69] P. Cruz, J. Rosário, T. Alves, and A. Cartaxo, "Exhaustive Gaussian approach for performance evaluation of direct-detection OFDM systems employing square and cross QAM," in Proc. *Int. Telecommun. Symp*, São Paulo, Brazil, Aug. 2014. doi: 10.1109/ITS.2014.6947998

[70] P. Cruz, T. Alves, and A. Cartaxo, "Impact of inter-band crosstalk due to nonlinear fibre transmission on the performance of direct-detection single-sideband MB-OFDM metro networks", in Proc. *Int. Conf. Transp. Opt. Netw.*, paper Tu.B1.3, Budapest, Hungary, Jul. 2015.

[71] Y. Wu and W. Zou, "Orthogonal frequency division multiplexing: a multi-carrier modulation scheme", *IEEE Trans. on Consumer Electronics*, vol. 41, no. 3, pp. 392-399, 1995.

[72] H. Takahashi, A. Amin, S. Jansen, I. Morita, and H. Tanaka, "Highly spectrally efficient DWDM transmission at 7.0 b/s/Hz using 8 × 65.1-Gb/s coherent PDM-OFDM," *IEEE/OSA J. Lightw. Technol.*, vol. 28, no. 4, pp. 406-414, Feb. 2010.

[73] J. Cho, C. Xie, and P. Winzer, "Analysis of soft-decision FEC on non-AWGN channels," *OSA Opt. Exp.*, vol. 20, no. 7, pp. 7915-7928, Mar. 2012.

[74] T. Alves and A. Cartaxo, "Performance degradation due to OFDM-UWB radio signals transmission along dispersive single-mode fiber," *IEEE Photon. Technol. Lett.*, vol. 21, no. 3, pp. 158-160, Feb. 2009.

[75] D. Fonseca, A. Cartaxo, and P. Monteiro, "Modelling and experimental validation of an x-cut four phase modulators structure", *IEE Proceedings - Optoelectronics*, vol. 153, no. 4, pp. 145-151, 2006.

[76] T. Alves and A. Cartaxo, "Virtual carrier-assisted direct-detection MB-OFDM next-generation ultra-dense metro networks limited by laser phase noise," *IEEE/OSA J. Lightw. Technol.*, vol. 33, no. 19, pp. 4093-4100, Oct. 2015.

[77] J. Rosário, T. Alves, and A. Cartaxo, "ROADM cascade performance in DD multi-band OFDM metro networks employing virtual carriers," in Proc. *IEEE Photon. Conf.*, San Diego, CA, 2014, paper MG2.4.

[78] T. Strasser and J. Wagener, "Wavelength-selective switches for ROADM applications," *IEEE J. Sel. Topics Quantum Electron.*, vol. 16, no. 5, pp. 1150-1157, Sep.-Oct. 2010.

[79] C. Pulikkaseril, L. Stewart, M. Roelens, G. Baxter, S. Poole, and S. Frisken, "Spectral modelling of channel band shapes in wavelength selective switches", *OSA Opt. Exp.*, vol. 19, no. 9, pp. 8458-8470, Apr. 2011.

[80] Y. Benlachtar, G. Gavioli, V. Mikhailov, and R. Killey, "Experimental investigation of SPM in long-haul direct-detection OFDM systems," *OSA Opt. Exp.*, vol. 16, no. 20, pp. 15477-15482, Sept. 2008.

[81] T. Alves and A. Cartaxo, "Analytical characterization of four wave mixing effect in direct-detection double-sideband OFDM optical transmission systems," *OSA Opt. Exp.*, vol. 22, no. 7, pp. 8598-8616, Apr. 2014.

[82] A. Li, W. Shieh, and R. Tucker, "Wavelet packet transform-based OFDM for optical communications," *IEEE/OSA J. Lightw. Technol.*, vol. 28, no. 24, pp. 3519-3528, Dec. 2010.

[83] V. Pechenkin and I. Fair, "Correlation between peak-to-average power ratio and four-wave mixing in optical OFDM systems," *IEEE/OSA J. Opt. Commun. Netw.*, vol. 1, no. 7, pp. 636-644, Dec. 2009.

[84] A. Lowery, S. Wang, and M. Premaratne, "Calculation of power limit due to fiber nonlinearity in optical OFDM systems," *OSA Opt. Exp.*, vol. 15, no. 20, pp. 13282-13287, Oct. 2007.

[85] J. He, A. Li, X. Chen, and W. Shieh, "Fiber nonlinearity impact on direct-detection block-wise phase switched systems," *IEEE/OSA J. Lightw. Technol.*, vol. 32, no. 10, pp. 1872-1876, May 2014.

[86] K. Hill, D. Johnson, B. Kawasaki, and R. MacDonald, "CW three-wave mixing in single-mode optical fibers," *AIP J. Appl. Phys.*, vol. 49, no. 10, pp. 5098–5106, May 1978.

[87] K. Inoue, "Phase-mismatching characteristic of four-wave mixing in fiber lines with multi-stage optical amplifiers," *OSA Opt. Lett.*, vol. 17, no. 11, pp. 801–803, Jun. 1992.

[88] N. Shibata, R. Braun, and R. Waarts, "Phase-mismatch dependence of efficiency of wave generation through four-wave mixing in a single-mode optical fiber," *IEEE J. Quant. Electron.*, vol. 23, no. 7, pp. 1205–1210, Jul. 1987.

[89] P. Vitthaladevuni, M. Alouini, and J. Kieffer, "Exact BER computation of cross QAM constellations," *IEEE Trans. Wireless Commun.*, vol. 4, no. 6, pp. 3039-3050, Nov. 2005.

[90] Forward Error Correction for High Bit-Rate DWDM Submarine Systems, *ITU-T Recommendation G.975.1*, 2004, Appendix I.9.3.

[91] S. Le, M. McCarthy, N. Suibhne, M. Al-Khateeb, E. Giacoumidis, N. Doran, A. Ellis, and S. Turitsyn, "Demonstration of phase-conjugated subcarrier coding for fiber nonlinearity compensation in CO-OFDM transmission," *IEEE/OSA J. Lightw. Technol.*, vol. 33, no. 11, pp. 2206-2212, Jun. 2015.

[92] M. Shoreh, "Compensation of nonlinearity impairments in coherent optical OFDM systems using multiple optical phase conjugate modules," *IEEE/OSA J. Opt. Commun. Netw.*, vol. 6, no. 6, pp. 549-558, Jun. 2014.

[93] X. Li, W. Zhong, A. Alphones, and C. Yu, "Fiber nonlinearity tolerance of APSK modulated DFT-S OFDM systems," *IEEE Photon. Technol. Lett.*, vol. 25, no. 23, pp. 2304-2307, Dec. 2013.

[94] Y. Tang, W. Shieh, and B. Krongold, "DFT-spread OFDM for fiber nonlinearity mitigation," *IEEE Photon. Technol. Lett.*, vol. 22, no. 16, pp. 1250-1252, Aug. 2010.

[95] E. Ip, "Nonlinear compensation using backpropagation for polarization-multiplexed transmission," *IEEE/OSA J. Lightw. Technol.*, vol. 28, no. 6, pp. 939-951, Mar. 2010.

[96] B. Goebel, B. Fesl, L. Coelho, and N. Hanik, "On the effect of FWM in coherent optical OFDM systems," in Proc. *Opt. Fiber Conf.*, San Diego, CA, 2008, paper JWA58.

[97] A. Lowery, "Fiber nonlinearity mitigation in optical links that use OFDM for dispersion compensation," *IEEE Photon. Technol. Lett.*, vol. 19, no. 19, pp. 1556-1558, Oct. 2007.

[98] X. Liu, "Twin-wave-based optical transmission with enhanced linear and nonlinear performances," *IEEE/OSA J. Lightw. Technol.*, vol. 33, no. 5, pp. 1037-1043, Mar. 2015.

[99] J. Silva, A. Cartaxo, and M. Segatto, "A PAPR reduction technique based on a constant envelope OFDM approach for fiber nonlinearity mitigation in optical direct-detection systems," *IEEE/OSA J. Opt. Commun. Netw.*, vol. 4, no. 4, pp. 296-303, Apr. 2012.

[100] C. Ju, N. Liu, X. Chen, and Z. Zhang, "SSBI mitigation in A-RF-tone-based VSSB-OFDM system with a frequency-domain Volterra series equalizer," *IEEE/OSA J. Lightw. Technol.*, vol. 33, no. 23, pp. 4997-5006, Dec. 2015.

[101] Z. Li, M. Erkılınç, K. Shi, E. Sillekens, L. Galdino, B. Thomsen, P. Bayvel, and R. Killey, "SSBI mitigation and the Kramers-Kronig scheme in single-sideband direct-detection trans-

mission with receiver-based electronic dispersion compensation," *IEEE/OSA J. Lightw. Technol.*, vol. 35, no. 10, pp. 1887-1893, May 2017.

[102] R. Soeiro, T. Alves, and A. Cartaxo, "Inter-ring band-transfer limited by laser wavelength drift in DD MB-OFDM metro networks," *IEEE/OSA J. Lightw. Technol.*, vol. 34, no. 10, pp. 2473-2483, May 2016.

[103] T. Alves and A. Cartaxo, "Extension of the exhaustive Gaussian approach for BER estimation in experimental direct-detection OFDM setups," *Microw. Opt. Tech. Lett.*, vol. 52, no. 12, pp. 2772-2775, Dec. 2010.

[104] R. Shafik, M. Rahman, and A. Islam, "On the extended relationships among EVM, BER and SNR as performance metric," in Proc. *Int. Conf. on Elect. and Comput. Eng.*, Dhaka, Bangladesh, pp. 408-411, Dec. 2006.

[105] A. Cartaxo and T. Alves, "Performance evaluation methods of direct-detection OFDM systems," in Proc. *Int. Conf. Transp. Opt. Netw.*, Ponta Delgada, Azores, Portugal, 2009, Paper Tu.C5.2.

[106] W. Peng, K. Feng, A. Willner, and S. Chi, "Estimation of the bit error rate for direct-detected OFDM signals with optically preamplified receivers," *IEEE/OSA J. Lightw. Technol.*, vol. 27, no. 10, pp. 1340-1346, May 2009.

[107] T. Alves and A. Cartaxo, "Semi-analytical approach for performance evaluation of direct-detection OFDM optical communications systems," *Opt. Exp.*, vol. 17, no. 21, pp. 18714-18729, Oct. 2009.

[108] G. Agrawal, *Nonlinear Fiber Optics*, 4th ed. San Diego, CA, USA: Academic Press, 2007.

[109] M. Ferreira, *Nonlinear Effects in Optical Fibers*, 1st ed. Hoboken, NJ, USA: Wiley, 2011.

[110] G. Agrawal, *Lightwave Technology - Components and Devices*, 1st ed. Hoboken, NJ, USA: Wiley, 2004.

[111] C. Menyuk and A. Galtarossa, *Polarization Mode Dispersion*, 1st ed. New York, NY, USA: Springer, 2005.

[112] G. Agrawal, *Fiber-Optic Communication Systems*, 3rd ed. New York, NY, USA: Wiley, 2002.